AD_____

Award Number: W81 XWH-06-1-0482

TITLE: Targeting Therapy Resistant Tumor Vessels

PRINCIPAL INVESTIGATOR: Erkki Ruoslahti, M.D., Ph.D.

CONTRACTING ORGANIZATION: Burnham Institute
                                                     La Jolla, CA 92037

REPORT DATE: August 2008

TYPE OF REPORT: Final

PREPARED FOR: U.S. Army Medical Research and Materiel Command
          Fort Detrick, Maryland 21702-5012

DISTRIBUTION STATEMENT: Approved for Public Release;
                                             Distribution Unlimited

The views, opinions and/or findings contained in this report are those of the author(s) and should not be construed as an official Department of the Army position, policy or decision unless so designated by other documentation.

REPORT DOCUMENTATION PAGE

Form Approved
OMB No. 0704-0188

1. REPORT DATE (DD-MM-YYYY)	2. REPORT TYPE	3. DATES COVERED (From - To)
01-08-2008	Final	1 May 2006 - 31 AUG 2008

4. TITLE AND SUBTITLE

Targeting Therapy Resistant Tumor Vessels

5a. CONTRACT NUMBER

5b. GRANT NUMBER
W81XWH-06-1-0482

5c. PROGRAM ELEMENT NUMBER

6. AUTHOR(S)
Erkki Ruoslahti, M.D., Ph.D.

5d. PROJECT NUMBER

5e. TASK NUMBER

5f. WORK UNIT NUMBER

7. PERFORMING ORGANIZATION NAME(S) AND ADDRESS(ES)

Burnham Institute
La Jolla, CA 92037

8. PERFORMING ORGANIZATION REPORT NUMBER

9. SPONSORING / MONITORING AGENCY NAME(S) AND ADDRESS(ES)
U.S. Army Medical Research and Materiel Command
Fort Detrick, Maryland 21702-5012

10. SPONSOR/MONITOR'S ACRONYM(S)

11. SPONSOR/MONITOR'S REPORT NUMBER(S)

12. DISTRIBUTION / AVAILABILITY STATEMENT
Approved for Public Release; Distribution Unlimited

13. SUPPLEMENTARY NOTES

14. ABSTRACT

Anti-angiogenic therapy appears to eliminate immature blood vessels. This paradoxically leads to improvement of tumor blood supply, as the structure and function of mature tumor blood vessels, not specific for anti-angiogenic effect, is normalized. This is a serious limitation to the anti-angiogenic therapy. The goal of this project is to specifically distinguish these "normalized" therapy resistant vessels in breast cancer from those sensitive to anti-angiogenic treatment. To achieve this, we have developed tumor models for vascular normalization and are using in vivo phage display and isolation of peptides that specifically home to normalized tumor vessels resistant to anti-angiogenic therapy. The results obtained in this study will enable specific targeting and thus treatment of breast cancer vessels not responding to standard anti-angiogenic therapy.

15. SUBJECT TERMS
Anti-angiogenesis, phage display, tumor homing peptides

16. SECURITY CLASSIFICATION OF:			17. LIMITATION OF ABSTRACT	18. NUMBER OF PAGES	19a. NAME OF RESPONSIBLE PERSON USAMRMC
a. REPORT	b. ABSTRACT	c. THIS PAGE			19b. TELEPHONE NUMBER (include area code)
U	U	U	UU	106	

Standard Form 298 (Rev. 8-98)
Prescribed by ANSI Std. Z39.18

Table of Contents

Hoffman et al. Canc. Cell 2003
Inai et al. Amer. J. Pathol. 2004
Jarvinen and Ruoslahti., Amer. J.Path. 2007
Joyce et al., Cancer Cell 2003
Laakkonen et al., Nat. Med. 2002
Laakkonen et al., Proc. Natl Acad. Sci. 2004
Park et al, Adv. Matl. 2008
Simberg et al., Proc Natl Acad. Sci. 2007
Yau et al Canc. Res. 2006
Zhang et al Canc. Res. 2006

1. INTRODUCTION

The goal of this project was to identify peptides that selectively recognize breast cancer vessels that remain after anti-angiogenic treatment. Like all other tissues, cancerous tumors need a blood supply. To obtain blood supply, a tumor stimulates the growth of new blood vessels in a process known as angiogenesis. Preventing tumor angiogenesis has become a promising new form of cancer therapy, including that of breast cancer. However, researchers have found that such therapy preferentially destroys the immature tumor vessels, and leaves behind the more established vessels. These remaining vessels can keep providing the tumor with a blood supply. We are using *in vivo* phage display to target vessels that remain after anti-angiogenic therapy. Markers of such vessels will be useful in developing strategies for complete destruction of breast cancer vasculature, and in assessing the potential of anti-angiogenic therapy in individual patients.

2. PROGRESS REPORT

Summary

We developed three tumor models under this project: 4T1 mouse breast cancer and MDA-MB-435 human cancer xenograft tumors treated with anti-nucleolin, and 4T1 tumors treated with the kinase inhibitor, axitinib. We performed phage screening with these tumors using random peptide libraries and libraries of our previously isolated homing peptides. The latter approach was highly successful; we identified several peptides that effectively home to the treated tumors. In one case, the treatment increased the expression of the receptor for the peptide. This panel of peptides can now be used to design compounds that target the residual tumor after anti-angiogenic therapy.

Detailed report

Task 1. To develop two tumor models for anti-angiogenic therapy and subsequent phage library screening.

As originally proposed, we generated tumors with "normalized" vasculature by treating tumor-bearing mice with anti-nucleolin antibodies. The target tumor was 4T1 mouse breast cancer, and we also treated MDA-MB-435 human cancer xenograft tumors for comparison.

We originally proposed as MDA-MB-435 tumor treated with anti-VEGF as the second model, but changed the tumor type to 4T1 and used the kinase inhibitor axitinib for the treatment. The cell line change was prompted by studies that question the origin of the MDA-MB-435 cells as a breast cancer line. We switched to axitinib because Merck was interested in a collaboration, and we obtained a large supply of axitinib as a gift. Axitinb is in clinical trial, so the model is clearly relevant to the treatment of human cancer.

Data supportive of the normalization of tumor vessels as a result of anti-nucleolin treatment were provided in the 2007 annual report. We showed that the vessels remaining after the antibody treatment contain a pericyte coat, vessel architecture is normal, the diameter of the vessels is smaller (dilated, abnormal vessels are gone), a basement membrane is present, and tumor hypoxia is reduced. The changes in tumor vessels caused by axitinib have been characterized and published by others (Inai et al. 2004) and our results closely parallel theirs. An example of the abundance and morphology of blood vessels in treated and control tumors is shown in Figure 1.
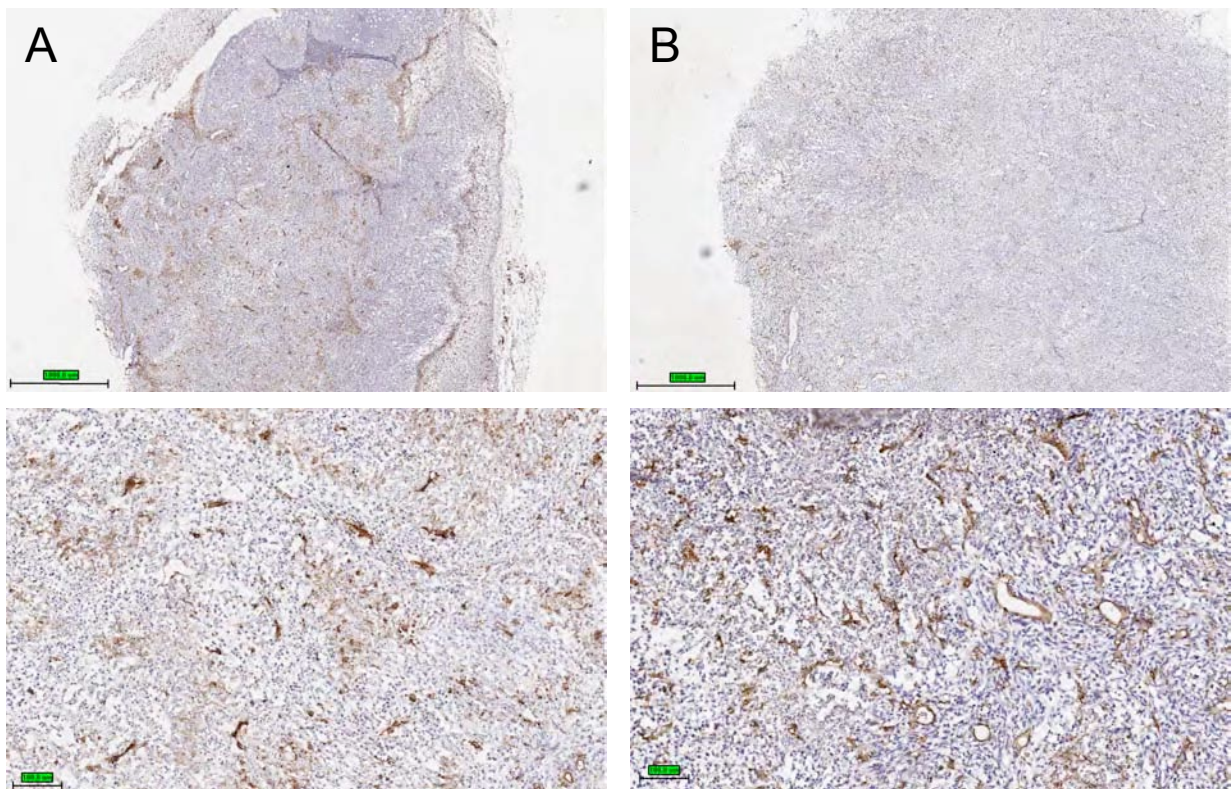

Fig. 1. Histological analysis of blood vessels in 4T1 tumors treated (A) with axitinib (25 mg/kg, daily intravenous injections for 7 days) or vehicle only (B). Note the CD31 staining pattern from deteriorated blood vessels in treated tumors (A).

Task 2. To screen phage libraries for peptides that specifically recognize vessels in tumors treated with anti-angiogenic therapy.

We experimented with a number of screening protocols in each tumor model. We screened both entirely random libraries and libraries composed of our previously identified tumor-homing peptides. We used both our standard *ex vivo/in vivo* screening protocols and we also devised a new *ex vivo* screening protocol, in which we used

tumor mice that had not been treated with anti-angiogenic agents. In this new protocol, we injected the mice with a phage library, perfused the mice to remove phage remaining in the circulation, collected the tumor, and isolated endothelial cells using an anti-CD31 antibody. We had used this procedure in our earlier phage work (e.g. Zhang et al., 2006). The new aspect was that we next removed those endothelial cells that come from the poorly developed (angiogenic) vessels, and then rescued the phage that had bound to (or become internalized by) the well-formed (mature) blood vessels. The logic was that these vessels would have remained after an anti-angiogenic treatment as the "normalized" vessels. We experimented with both anti-nucleolin and anti-integrin antibodies to remove the endothelial cells (and phage associated with them) that came from poorly formed vessels. The $\alpha5\beta1$ and $\alpha v\beta3$ integrins, which are highly expressed in tumor vessels, have been reported to be lost as a result of anti-angiogenic treatment (Yao et al. 2006). We had hoped that this procedure would greatly speed up and simplify the peptide identification, but ultimately the investment we made into this new screening method and the use of random libraries did not pan out. The successful approach turned out to be screening the libraries of previously identified peptides.

We made the homing peptide library using peptides from various sources and kept updating it as new peptides emerged. A total of about 40 peptides were screened. We used a format we have named "play off", where the peptides are identified and quantified by sequencing the phage inserts from the original pool (to obtain the ratios of the various phage in the input sample) and from the target (to see which phage had become enriched in the target tumor).   This method gave us several candidates from each of the tumor models, that were then tested individually as phage and as synthetic peptides. Figure 2 shows the results of a play off screen with axitinib-treated 4T1 tumors.
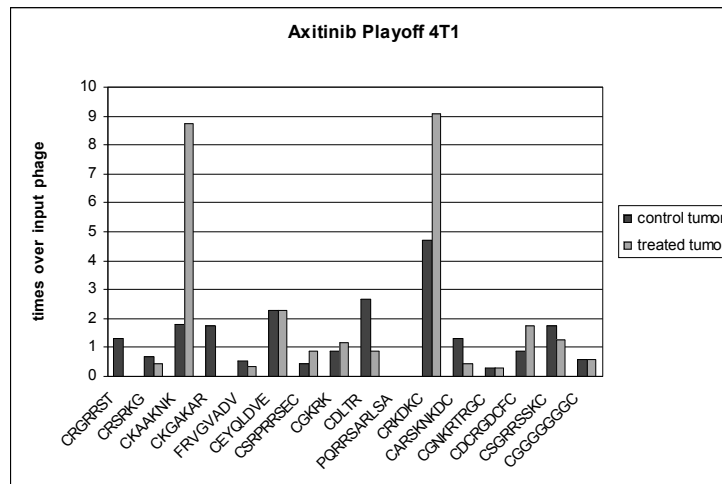

Fig. 2. A "play off" screen of a phage library composed of known tumor-homing peptides. The target was a 4T1 tumor from an axitinib-treated mouse or control-treated mouse. Peptides CKAAKNK and CRKDKC, and possibly CDCRGDCFC homed to the treated tumor (A) more than to the control tumor (B).

Task 3. To validate the specificity of the peptides isolated in the screening

We picked CKAAKNK, CRKDKC, and CGKRK as candidate peptides from the various play off screens for further testing. As the RGD-containing peptide CDCRGDCFC showed some promise, we included in this play off winner panel a newly discovered RGD peptide, CRGDKGPDC, which is a uniquely effective tumor-homing peptide that is internalized into the target cells and has been dubbed iRGD (Sugahara et al., in preparation). We also included CGNKRTRGC (LyP-1), although it did not score well in the play off. We suspected that, because this homes to tumor lymphatics and tumor cells, and not to blood vessels (Laakkonen et al., 2002; 2004), the play off format might not have done its justice.

It was interesting that the CKAAKNK and CRKDKC peptides showed up as candidate homing peptides for normalized vessels. CKAAKNK binds to tumor vessels in fully developed pancreatic islet cell tumor, but does not recognize the angiogenic vessels of premalignant lesions in this tumor model. Moreover, its localization in tumor vessels overlapped with the pericyte marker, NG2 (Joyce et al., 2003). These properties agree with the assumption that the peptide would preferentially recognize mature vessels. The CRKDKC peptide was discovered in wound-homing screens and shown to prefer the vessels at later stages of wound healing, again in agreement with a preference for vessels that are somewhat mature.

The αv integrins are the receptors for the RGD peptide, and it also binds to a cell surface protein that is responsible for the internalization of this peptide. The receptor for the LyP-1 peptide is a mitochondrial/cell surface protein known as p32 (Fogal et al., submitted). The receptors for the remaining peptides are not known.

We have confirmed the homing to treated tumors of the individual peptides in this panel. These tests were performed at 3 levels: phage (Fig. 3), free synthetic peptide (Fig. 4), and nanoparticles (Fig. 5). In each case, the homing to axitinib-treated 4T1 tumors was confirmed.

| iRGD phage | LyP-1 phage | KAA phage | CRK phage | CG₇C phage (control) |

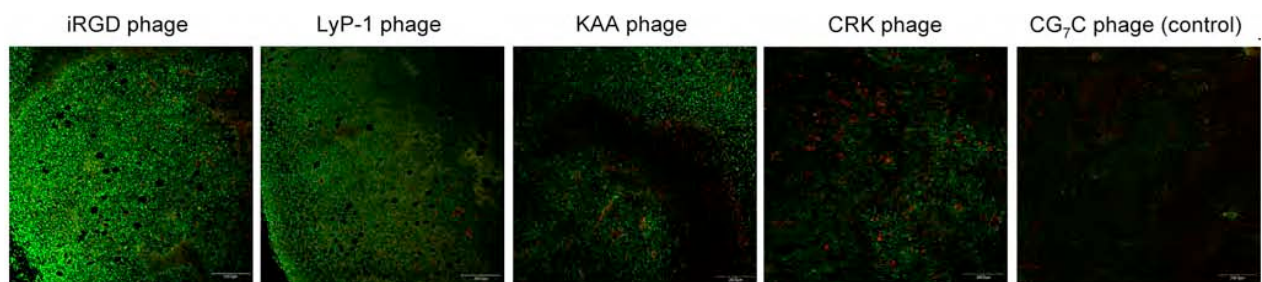Fig. 3. iRGD, LyP-1, KAAKNK (KAA), and CRKDKC (CRK) phage home to axitinib-treated 4T1 tumors. Balb/c mice bearing 4T1 tumors were treated with axitinib for 8 days and intravenously injected with peptide-displaying T7 phage. After 15 min of circulation, the mice were perfused with PBS containing 1% BSA, and tissues were collected for immunofluorescent staining with anti-T7 phage (green) and anti-CD31 (red).
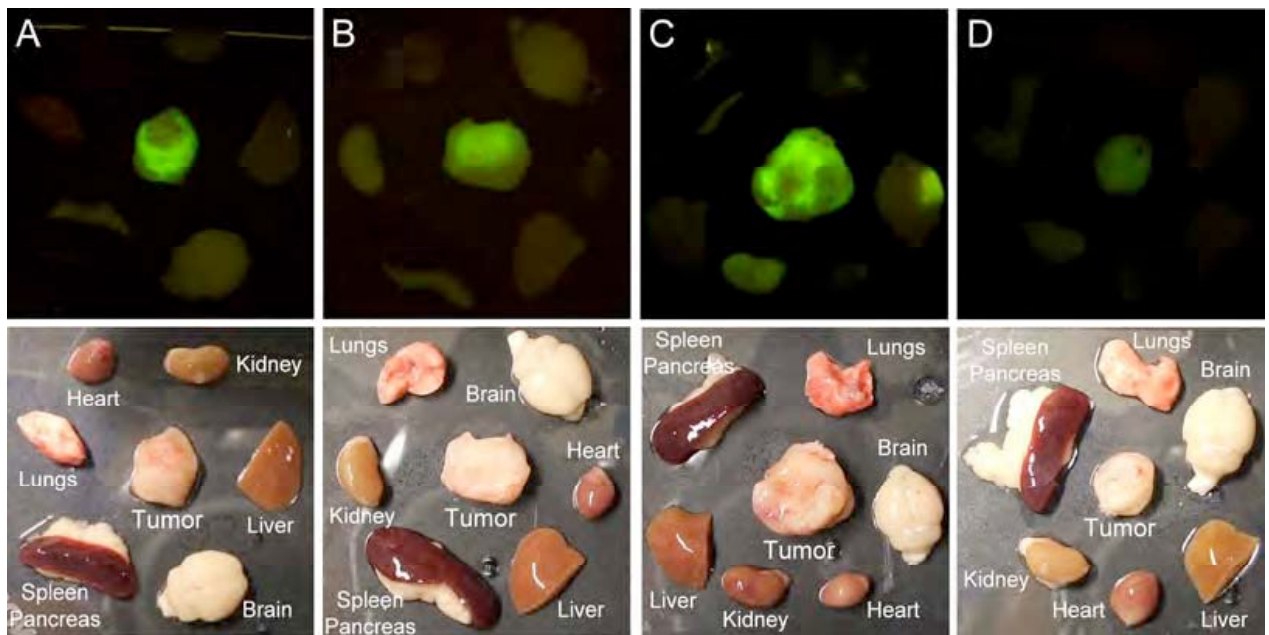
Fig. 4. iRGD, LyP-1, and CRKDKC peptides home to axitinib-treated 4T1 tumors. Balb/C mice bearing 4T1 tumors that were treated with axitinib were injected i.v. through the tail vein with approximately 150 mg of fluorescein-labeled iRGD (A), CRKDKC (B), LyP-1 (C) or a control peptide CG_7C (D). After 2 hours of circulation, the mice were perfused with PBS containing 1% BSA and organs of interest were harvested. Pictures of the organs taken under a fluorescent light table (upper panels) and corresponding bright field images (lower panels) are shown.
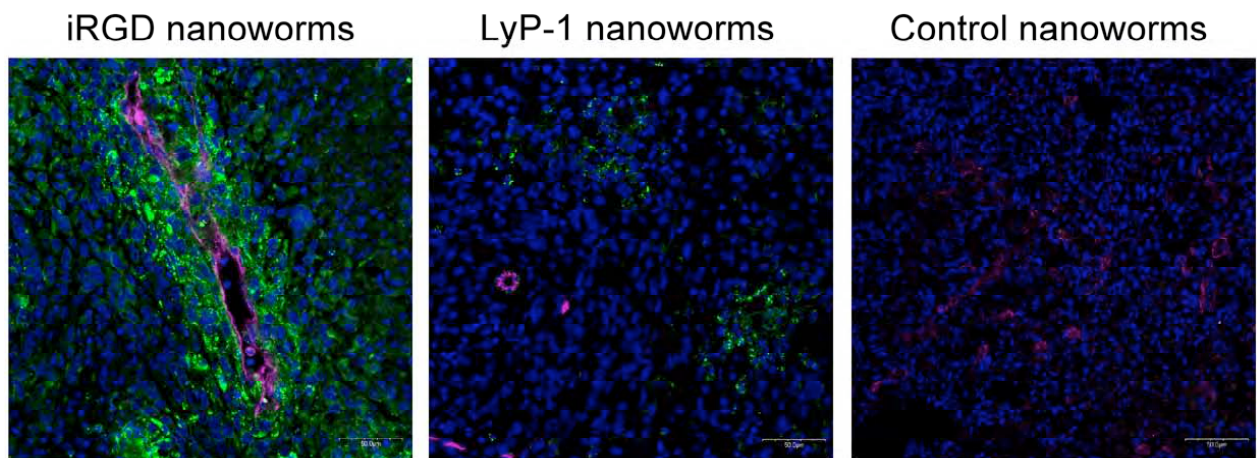
Fig. 5. iRGD and LyP-1 iron oxide nanoparicles home to axitinib-treated 4T1 tumors. Balb/C mice bearing 4T1 tumors twere treated with axitinib for 8 days and then intravenously injected with fluorescein-labeled iRGD, LyP-1, or control nanoworms (Park et al., 2008). The mice were pre-injected with nickel liposomes that prevent uptake of the nanoparticles by the liver (Simberg et al., 2007). After 5 hrs of circulation, the mice were perfused with Cy5-tomato lectin (magenta) to label patent blood vessels, followed by 4% paraformaldehyde and PBS, and tissues were collected for immunofluorescence studies. Images taken with a confocal microscope are shown. Note that iRGD-nanoworms target tumor blood

5

vessels and spread into the tumor tissue, whereas LyP-1 does not associate with blood vessels. Nuclei were stained with DAPI (blue).

The level of homing remains to be quantified, but visual inspection indicated the order: iRGD > Lyp-1 > CKAAKNK > CRKDKC (refer to Fig. 3). The iRGD and LyP-1 peptides, and their payload, effectively spread into the tumor tissue. The other peptides did less so. As expected from their target cell specificity, the peptides mostly concentrated around blood vessels, except that LyP-1 accumulated in areas that were positive for its receptor, p32, and for the lymphatic/myeloid marker podoplanin, but were low in blood vessels. Thus, this panel of peptides allows one to target different areas within tumors (Fig. 6). As the tumor specificity (lack of homing to normal tissues) of these peptides has been extensively documented in previous studies (cited above), we have not deemed it necessary to repeat those studies.
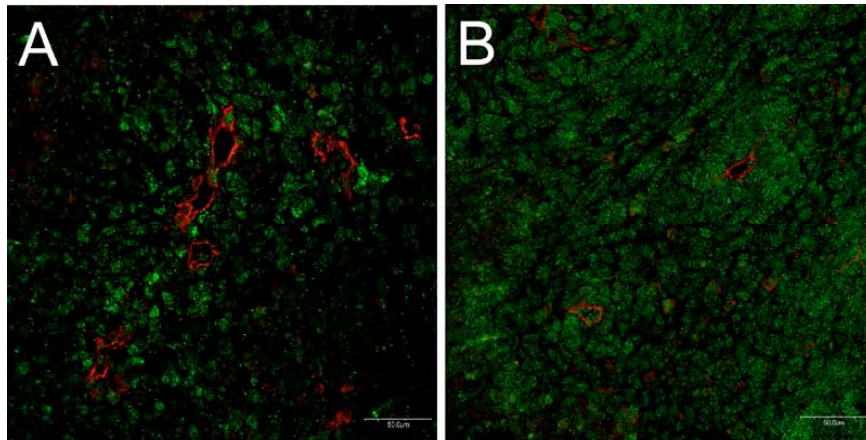

Figure 6. Homing of iRGD and LyP-1phage to axitinib-treated 4T1 tumors shows different patterns. Balb/C mice bearing 4T1 tumors were treated with axitinib for 8 days and intravenously injected with iRGD (A) or LyP-1 (B) phage. After 15 min of circulation, the mice were perfused with PBS containing 1% BSA, and tissues were collected and stained with anti-T7 phage (green) and anti-CD31 (red). Note that iRGD is detected in the area surrounding the blood vessels, whereas LyP-1 is widely dispersed and abundant in areas with few blood vessels.

The angiogenesis-related integrins have been reported to be lost in the vessels of axitinib-treated tumors (Yao et al., 2006). We have not studied integrin expression in the treated tumors, but iRGD also binds to a secondary receptor (the internalizing receptor, Teesalu and Sugahara et al., manuscripts in preparation), and this may sustain the tumor homing.

Interestingly, we found that p32, the LyP-1 receptor, is up-regulated in the treated tumors (Fig. 7) and may therefore be particularly well suited for the targeting of the residual tumor tissue that remains after axinitib therapy.
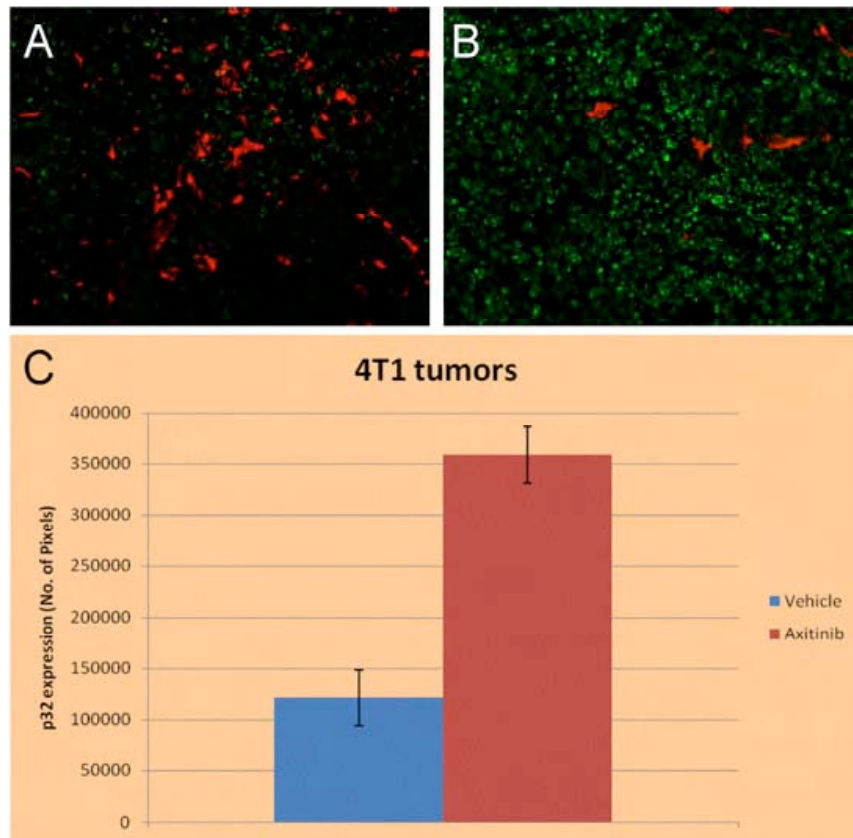
Fig. 7. The receptor for LyP-1, p32, is overexpressed in axitinib-treated 4T1 tumors. Five μm-thick cryosections of vehicle-treated (A) and axitinib-treated (B) 4T1 tumors were stained with anti-p32 (green) and anti-CD31 (red). Three tumors from each group were analyzed and images from 5 random fields per tumor were quantified for green fluorescence (p32) using the Image J software (C).

Some additional characterization of the peptides that we did not have time to perform under this grant will be necessary before publication: tumors that have been treated with anti-angiogenic therapies other than the ones used here need to be studied. Anti-VEGF treatment is obviously a high priority, because this drug is in clinical use (although not in breast cancer). We were previously deterred by the high cost of the antibody, but that should not be a problem now that we can focus only on a few peptides. Tumors other than the ones used here should be treated and studied. We already know that the LyP-1 peptide does not home to all tumors; fortunately breast cancers are the tumor type most likely to express the p32 receptor (18 out of 20 human clinical breast cancers were significantly positive for p32 expression, one had a trace, and one was negative; Fogal et al., submitted). CKAAKNK is also likely to be tumor-type specific (Joyce et al., 2003). More detailed quantification of the results will also be needed. These studies will be carried out under a DoD Innovator grant to the PI that is now being processed for funding.

3. KEY RESEARCH ACCOMPLISHMENTS

We have identified a panel of peptides that home to the vasculature of tumors of animals that have received anti-angiogenic therapy, but do not recognize normal blood vessels. In some cases, the treated tumors are recognized more robustly than untreated tumors. Pending some additional work, these results will be prepared for publication in the near future.

4. REPORTABLE OUTCOMES

Burnham Institute has filed patent applications of the peptides described in this report, and on their receptors, when known:

> *Methods and compositions for targeting gC1qR/p32; Filed: 07/12/2007; Legal Ref. No. 06-054-03PCT; Serial No. PCTUS2007/073372*

> *Methods and Compositions Related to Internalizing RGD Peptides; Filed 01/18/2008; Legal Ref. No. 08-009-02PR; Serial No. 61/022,131 Prov. Applic.).*

These new results will be added to the next version of these applications.

In addition, we have helped Dr. Pirjo Laakkonen (a former postdoc) in Helsinki with a project that relates to the theme of this grant. She has used *in vivo* phage screening to identify a peptide that recognizes co-opted blood vessels in a glioma model. A patent application, in which the Burnham Institute will be one of the assignees, is being prepared on this peptide:

> *Peptides That Home to Tumor Lymphatic Vasculature and Methods of Using Same: Filed 02/27/2007; Legal Ref. #02-006-07DIV; Serial No. 11/712,0434.*

5. CONCLUSIONS

We have successfully completed the main goal of this grant, identifying peptides that recognize the vasculature of breast cancer tumors treated with anti-angiogenic therapy. These peptides may be useful for targeting additional therapies to the residual tumor tissue that remains after treatment with anti-angiogenic compounds.

6. REFERENCES

Hoffman, J.A., Giraudo E., Singh, M., Inoue, M., Porkka, K., Hanahan, D., and Ruoslahti, E. Progressive vascular changes in a transgenic mouse model of squamous cell carcinoma. *Cancer Cell* . **4**:383-391 (2003).

Inai, T., Mancuso, M., Hashizume, H., Baffert, F., Haskell, A., Baluk, P., Hu-Lowe, D., Shalinsky, D.R., Thurston, G., Yancopoulos, G.D., McDonald, D.M. Inhibition of vascular endothelial growth factor (VEGF) signaling in cancer causes loss of endothelial fenestrations, regression of tumor vessels, and appeareance of basement membrane ghosts. Am. J. Path. **165**:35-52 (2004).

Jarvinen T. and Ruoslahti E. Molecular changes in the vasculature of injured tissues *Am. J. Path.,* **171**:702-711 (2007).

Joyce, J.A., Laakkonen P., Bernasconi, M., Bergers, G., Ruoslahti, E., and Hanahan, D. Stage-specific vascular markers revealed by phage display in a mouse model of pancreatic islet tumorigenesis. *Cancer Cell* **4**:393-403 (2003).

Laakkonen, P., Porkka, K., Hoffman, J. A., and Ruoslahti, E. A tumor-homing peptide with a lymphatic vessel-related targeting specificity. *Nature Med.* **8**: 743-751 (2002).

Laakkonen, P., Akerman, M.E., Biliran, H., Yang, M., Ferrer, F., Karpanen, T., Hoffman, R.M., and Ruoslahti, E. Antitumor activity of a homing peptide that targets tumor lymphatics and tumor cells. *Proc. Natl. Acad. Sci. U. S. A*. **101**:9381-9386 (2004).

Park, J. H., von Maltzahn, G., Zhang, L., Schwartz, M. P., Ruoslahti, E., Bhatia, S. N., and Sailor, M. J. Magnetic iron oxide nanoworms for tumor targeting and imaging. Adv. Mater. 20:1630-1635 (2008)

Simberg, D., Duza, T., Park, J. H., Essler, M., Pilch, J., Zhang, L., Derfus, A. M., Yang, M., Hoffman, R. M., Bhatia, S., Sailor, M. J., and Ruoslahti, E. Biomimetic amplification of nanoparticle homing to tumors. *Proc. Natl. Acad. Sci. U. S. A.* 104:932-936 (2007).

Yao, V.J., Ozawa, M.G., Varner, A.S., Kasman, I.M., Chanthery, Y.H., Pasqualini, R., Arap, W. and McDonald, DM. Antiangiogenic therapy decreases integrin expression in normalized tumor blood vessels. *Cancer Res.* 66:2639-2649 (2006).

Zhang, L. Giraudo, E., Hoffman, J.A., Hanahan, D. and Ruoslahti, E. Lymphatic zip codes in premalignant lesions and tumors. *Cancer Res.* 66: 5696-5706 (2006).

7. APPENDIX

List of Personnel Receiving Pay from the Research Effort:

Erkki Ruoslahti
Tambet Teesalu
Kazuki Sugahara
Miriam Wankell
Fernando Ferrer
Venkatu Ramana Kotamraju
Heli Matilainen
Valentina Fogal
Nicholas Zabatakis (lab manager)
Barry Rowan (lab manager)
Mike Nguyen (lab assistant)
Marcia Guillermina (lab assistant)
Nicole Hess (lab assistant)
Damon Conklin-Moragne (lab assistant)
Olga Volovnik (lab assistant)
Tiffany Santorian (lab assistant)
Adriana Hernandez (lab assistant)

Invention Report

Attached references

REPORT OF INVENTIONS AND SUBCONTRACTS
(Pursuant to "Patent Rights" Contract Clause) (See Instructions on back)

The public reporting burden for this collection of information is estimated to average 1 hour per response, including the time for reviewing instructions, searching existing data sources, gathering and maintaining the data needed, and completing and reviewing the collection of information. Send comments regarding this burden estimate or any other aspect of this collection of information, including suggestions for reducing the burden, to the Department of Defense, Executive Services Directorate (9000-0095). Respondents should be aware that notwithstanding any other provision of law, no person shall be subject to any penalty for failing to comply with a collection of information if it does not display a currently valid OMB control number.

PLEASE DO NOT RETURN YOUR COMPLETED FORM TO THE ABOVE ORGANIZATION. RETURN COMPLETED FORM TO THE CONTRACTING OFFICER.

1.a. NAME OF CONTRACTOR/SUBCONTRACTOR	2.a. NAME OF GOVERNMENT PRIME CONTRACTOR	3. TYPE OF REPORT (X one)
Erkki Ruoslahti	SAME	b. FINAL [X]
		a. INTERIM

1.b. ADDRESS (Include ZIP Code)	1.c. CONTRACT NUMBER	1.d. AWARD DATE (YYYYMMDD)	2.b. ADDRESS (Include ZIP Code)	2.c. CONTRACT NUMBER	2.d. AWARD DATE (YYYYMMDD)	4. REPORTING PERIOD (YYYYMMDD)
3119 Bio II, Burnham Institute for Med. Res. at UCSB	BC 051724	20060501	SAME	SAME	20060501	a. FROM 20060501
UC Santa Barbara, Santa Barbara, CA 93106-9610						b. TO 20080630

SECTION I - SUBJECT INVENTIONS

5. "SUBJECT INVENTIONS" REQUIRED TO BE REPORTED BY CONTRACTOR/SUBCONTRACTOR (If "None," so state)

a. NAME(S) OF INVENTOR(S) (Last, First, Middle Initial)	b. TITLE OF INVENTION(S)	c. DISCLOSURE NUMBER, PATENT APPLICATION SERIAL NUMBER OR PATENT NUMBER	d. ELECTION TO FILE PATENT APPLICATIONS (X)				e. CONFIRMATORY INSTRUMENT OR ASSIGNMENT FORWARDED TO CONTRACTING OFFICER (X)	
			(1) UNITED STATES		(2) FOREIGN		(a) YES	(b) NO
			(a) YES	(b) NO	(a) YES	(b) NO		
	(NONE)							

f. EMPLOYER OF INVENTOR(S) NOT EMPLOYED BY CONTRACTOR/SUBCONTRACTOR

(1) (a) NAME OF INVENTOR (Last, First, Middle Initial)	(2) (a) NAME OF INVENTOR (Last, First, Middle Initial)	g. ELECTED FOREIGN COUNTRIES IN WHICH A PATENT APPLICATION WILL BE FILED	
		(1) TITLE OF INVENTION	(2) FOREIGN COUNTRIES OF PATENT APPLICATION
(b) NAME OF EMPLOYER	(b) NAME OF EMPLOYER		
(c) ADDRESS OF EMPLOYER (Include ZIP Code)	(c) ADDRESS OF EMPLOYER (Include ZIP Code)		

SECTION II - SUBCONTRACTS (Containing a "Patent Rights" clause)

6. SUBCONTRACTS AWARDED BY CONTRACTOR/SUBCONTRACTOR (If "None," so state)

a. NAME OF SUBCONTRACTOR(S)	b. ADDRESS (Include ZIP Code)	c. SUBCONTRACT NUMBER(S)	d. FAR "PATENT RIGHTS"		e. DESCRIPTION OF WORK TO BE PERFORMED UNDER SUBCONTRACT(S)	f. SUBCONTRACT DATES (YYYYMMDD)	
			(1) CLAUSE NUMBER	(2) DATE (YYYYMM)		(1) AWARD	(2) ESTIMATED COMPLETION

SECTION III - CERTIFICATION

7. CERTIFICATION OF REPORT BY CONTRACTOR/SUBCONTRACTOR (Not required if: (X as appropriate)) SMALL BUSINESS or   NONPROFIT ORGANIZATION

I certify that the reporting party has procedures for prompt identification and timely disclosure of "Subject Inventions," that such procedures have been followed and that all "Subject Inventions" have been reported.

a. NAME OF AUTHORIZED CONTRACTOR/SUBCONTRACTOR OFFICIAL (Last, First, Middle Initial)	b. TITLE	c. SIGNATURE	d. DATE SIGNED
Freiser, Jean	Director of Sponsored Research		6/27/08

DD FORM 882, JUL 2005   PREVIOUS EDITION IS OBSOLETE.   FormFlow/Adobe Professional 6.0

Progressive vascular changes in a transgenic mouse model of squamous cell carcinoma

Jason A. Hoffman,[1,3,4] Enrico Giraudo,[2,4] Mallika Singh,[2,4,6] Lianglin Zhang,[1] Masahiro Inoue,[2,5,7] Kimmo Porkka,[1,5] Douglas Hanahan,[2,*] and Erkki Ruoslahti[1,*]

[1]Cancer Research Center, The Burnham Institute, 10901 North Torrey Pines Road, La Jolla, California 92037
[2]Department of Biochemistry and Biophysics and the Diabetes and Comprehensive Cancer Centers, University of California, San Francisco, 513 Parnassus Avenue, San Francisco, California 94143
[3]Program in Molecular Pathology, The Burnham Institute and Department of Pathology, University of California, San Diego, School of Medicine, 9500 Gilman Drive, La Jolla, California 92093
[4]These authors contributed equally to this work.
[5]These authors contributed equally to this work.
[6]Present address: Exelixis Inc., 170 Harbor Way, South San Francisco, California 94083.
[7]Present address: Osaka Medical Center for Cancer and Cardiovascular Diseases, Department of Biochemistry, 1-3-3 Nakamichi, Higashinari-ku, Osaka 537-8511, Japan.
*Correspondence: ruoslahti@burnham.org (E.R.); dh@biochem.ucsf.edu (D.H.)

Summary

Phage display was used to identify homing peptides for blood vessels in a mouse model of HPV16-induced epidermal carcinogenesis. One peptide, CSRPRRSEC, recognized the neovasculature in dysplastic skin but not in carcinomas. Two other peptides, with the sequences CGKRK and CDTRL, preferentially homed to neovasculature in tumors and, to a lesser extent, premalignant dysplasias. The peptides did not home to vessels in normal skin, other normal organs, or the stages in pancreatic islet carcinogenesis in another mouse model. The CGKRK peptide may recognize heparan sulfates in tumor vessels. The dysplasia-homing peptide is identical to a loop in kallikrein-9 and may bind a kallikrein inhibitor or substrate. Thus, characteristics of the angiogenic vasculature distinguish premalignant and malignant stages of skin tumorigenesis.

Introduction

Tumorigenesis is a multistage process that involves multiple cell types (Hanahan and Weinberg, 2000). One contributory cell type is the tumor endothelia that line blood and lymphatic vessels (Ruoslahti, 2002). These cells form a tumor's prerequisite blood vascular system during angiogenesis and also line the two routes used by tumor cells to metastasize. Angiogenesis is already apparent in the premalignant lesions of human tumors and transgenic mouse tumor models (Hanahan and Folkman, 1996). The new blood vessels in neoplasias are often structurally and functionally abnormal (Carmeliet and Jain, 2000; Pasqualini et al., 2002) and may be at different stages of normal maturation during physiological angiogenesis (Gee et al., 2003).

The K14-HPV16 transgenic tumor model expresses human papillomavirus type 16 (HPV16) oncogenes under control of the keratin-14 (K14) promoter. These mice express the HPV16 E6 and E7 oncogenes in the basal cells of their squamous epithelia (Arbeit et al., 1994); in the FVB/n strain background, they spontaneously develop epidermal squamous cell cancers (SCC) in a multistage fashion (Coussens et al., 1996). Their skin appears normal at birth but becomes hyperplastic within the first month, and focal dysplasias develop between 3 and 6 months of age. These focal dysplasias are angiogenic and by one year, these lesions develop into invasive SCCs in about half of the mice. Progression is accompanied by the upregulation of pro-angiogenic factors such as VEGF (Smith-McCune et al., 1997) and bFGF (Arbeit et al., 1996), and the model has called attention to the involvement of proteases from inflammatory mast cells (Coussens et al., 1999) and other bone marrow-derived cells (neutrophils and macrophages) in angiogenesis and tumor progression (Coussens et al., 2000).

In vivo phage display has revealed peptides that target tumor endothelial cells (Arap et al., 1998) or tumor pericytes (Burg et al., 1999). A combination of in vivo and ex vivo phage display (Hoffman et al., 2004) has further expanded the discriminatory

---

S I G N I F I C A N C E

Antiangiogenic therapies for the treatment of cancers have the promise of high efficacy and low toxicity. The complex responses to antiangiogenic therapy likely reflect our incomplete understanding of the alterations that blood vessels experience during tumor development and of how tumor types might molecularly differ in their neovascular parameters. We have discovered peptides that differentially recognize blood vessels at distinctive stages of tumor progression in squamous carcinogenesis, predicting neovascular heterogeneity between premalignant and malignant stages. These peptides present a means to define molecular determinants relevant to the varying responses to antiangiogenic therapies and could serve as vehicles for targeting imaging agents and therapeutics to tumor blood vessels in a tumor type- and stage-specific manner.

---

power of that methodology, yielding peptides that recognize a shared cell surface specificity among tumor blood vessels, tumor cells, and bone marrow cells (Porkka et al., 2002) or tumor lymphatic endothelium and tumor cells (Laakkonen et al., 2002).

The goal of the present study was to evaluate the molecular changes that occur in blood vessels as they develop from angiogenic vessels in dysplasias to tumor blood vessels. Our aim to compare the vasculature in premalignant and malignant lesions was motivated in part by studies in another mouse model (RIP-Tag) demonstrating that the efficacy of certain angiogenesis inhibitors varied as a function of stage: several inhibitors were most effective against angiogenic dysplasias (progenitors), whereas other compounds were more effective against later stages (Bergers et al., 1999, 2003). Thus the premalignant (and nascent tumor) vasculature may have distinctive qualities as compared to those of the mature tumor vasculature. Indeed, this study supports that proposition. Herein we isolate and describe three peptides in depth that home via the circulation to the neovasculature. One recognizes a binding moiety that is preferentially expressed in skin dysplasias, but is low or absent in tumors and in normal vasculature. Two other peptides homed to tumors and to a lesser extent to dysplastic skin vasculature of tumor-bearing mice. All three peptides variably home to other tumor types growing in or under the skin, but none recognize the vasculature of angiogenic dysplasias or tumors in the RIP-Tag transgenic mouse model of pancreatic islet carcinoma. These results, and those reported in the accompanying paper (Joyce et al., 2003 [this issue of *Cancer Cell*]) that similarly profiles the vasculature in the RIP-Tag model, show that the vessels of premalignant and fully malignant lesions are distinguishable and that different tumors express distinct repertoires of molecular markers in their vasculature.

Results

Selecting phage that home to dysplastic skin

We used a previously described library of T7 bacteriophage that display on their surface 9-mer cyclic peptides with seven degenerate positions (CX_7C) (Laakkonen et al., 2002). To isolate peptides specific for dysplasia, we performed two rounds of selection ex vivo and one round in vivo. For the ex vivo rounds, we incubated the phage with dispersed cells from dysplastic skin removed from the ears and chest of K14-HPV16 mice at 4–6 months of age. The biopsied lesions typically included a focal region of epidermal dysplasia flanked by adjacent hyperplastic epidermis, along with the underlying reactive stromal elements and angiogenic endothelium in the aberrant dermis. A portion of each tissue biopsy used for ex vivo or subsequent in vivo rounds of phage selection was fixed in formalin and, after conventional processing, examined histologically to assess the neoplastic grade. H&E-stained paraffin sections confirmed that the areas of skin used in these selection steps were largely comprised of focal dysplasias (data not shown). The sequential ex vivo selections on cell suspensions of dysplastic skin resulted in a 160-fold enrichment of phage relative to similar treatment with nonrecombinant phage that lack displayed peptides (Figure 1A, left); a greater than 10,000-fold enrichment resulted from the subsequent in vivo round (Figure 1A, right). Selection in vivo also produced a minor enrichment of phage that homed to the control tissues: brain, kidney, and hyperplastic skin. We performed DNA sequence analysis of 48 clones isolated in the

second ex vivo round and 48 clones from the subsequent in vivo round (data not shown) to identify the CX_7C peptides that had been selected. Nine peptides that appeared most frequently amongst the 96 phage display clones analyzed were chosen for further examination.

To test the homing specificity of these peptide sequences, we intravenously injected purified phage displaying a particular sequence into K14-HPV16 mice bearing protuberant tumors or alternatively presenting with multifocal dysplasias but no tumors. Both neoplastic tissues and normal control organs were collected and assayed for accumulation of phage. Phage displaying the peptide CRAKSKVAC, which appeared with the highest frequency in both the ex vivo (5 times) and in vivo sequence pools (15 times), were 1500-fold enriched in dysplastic skin relative to nonrecombinant control phage (data not shown). However, phage displaying this peptide accumulated with similar frequencies in skin, kidney, and brain (data not shown), indicating that the CRAKSKVAC sequence homes to an abundant signal in each of these organs and is not specific to the skin lesions of interest here. Six other of the dysplasia-selected clones also differentiated poorly between the control tissues and dysplastic skin in these tests. Altogether, 7 of the 9 dysplasia phage clones appeared to be responsible for the overall enrichment of the pool in the control tissues observed in the final in vivo round (Figure 1A, right) and were not considered suitable candidates for further study. The insert sequences in the two remaining phage clones were found to be highly selective for dysplastic skin and did not appreciably home to normal organs. One of these peptides, CNRRTKAGC, is closely related to a previously described peptide that homes to tumor lymphatic vessels (Laakkonen et al., 2002) and was not further analyzed here. The second dysplasia-homing peptide, CSRPRRSEC, was novel in our experience; it appeared three times amongst the 48 phage sequenced from the in vivo round, along with two variants: CSRPRRS<u>V</u>C and CSRPRRS<u>W</u>C that appeared one time each. Phage displaying the CSRPRRSEC peptide were enriched ∼350-fold in dysplastic skin and did not significantly accumulate in the control tissues (Figure 1C). When injected into a K14-HPV16 mouse bearing an ear tumor as well as multifocal skin dysplasias, the CSRPRRSEC phage effectively homed to dysplastic chest skin and dysplastic ear skin, but showed little homing to the tumor (Figure 1C). The peptide-bearing phage did not home to the normal skin of FVB/n mice in vivo (Figure 1C) and did not bind in ex vivo experiments to the hyperplastic skin of 1- to 2-month-old K14-HPV16 mice (data not shown). These results indicate that the CSRPRRSEC peptide selectively homes to dysplastic lesions; we infer that the CSRPRRSEC peptide binds to a molecule (a "receptor") that is present in skin dysplasias, but is essentially absent or inaccessible via the circulation in normal skin or in SCCs.

Tumor-specific homing phage

To isolate phage that home to SCCs in K14-HPV16 mice, we performed two rounds of ex vivo and two rounds of in vivo selections on tumors histologically confirmed as squamous cell carcinoma grades II–IV (Coussens et al., 1996). The enrichment rose from 6-fold in the second ex vivo round to greater than 70-fold in the second in vivo round (the fourth sequential round overall) (Figure 1B). Fifteen phage clones were selected for further analysis based on their frequent appearance amongst 192 sequenced clones (48 from ex vivo round 2, 48 from in vivo round
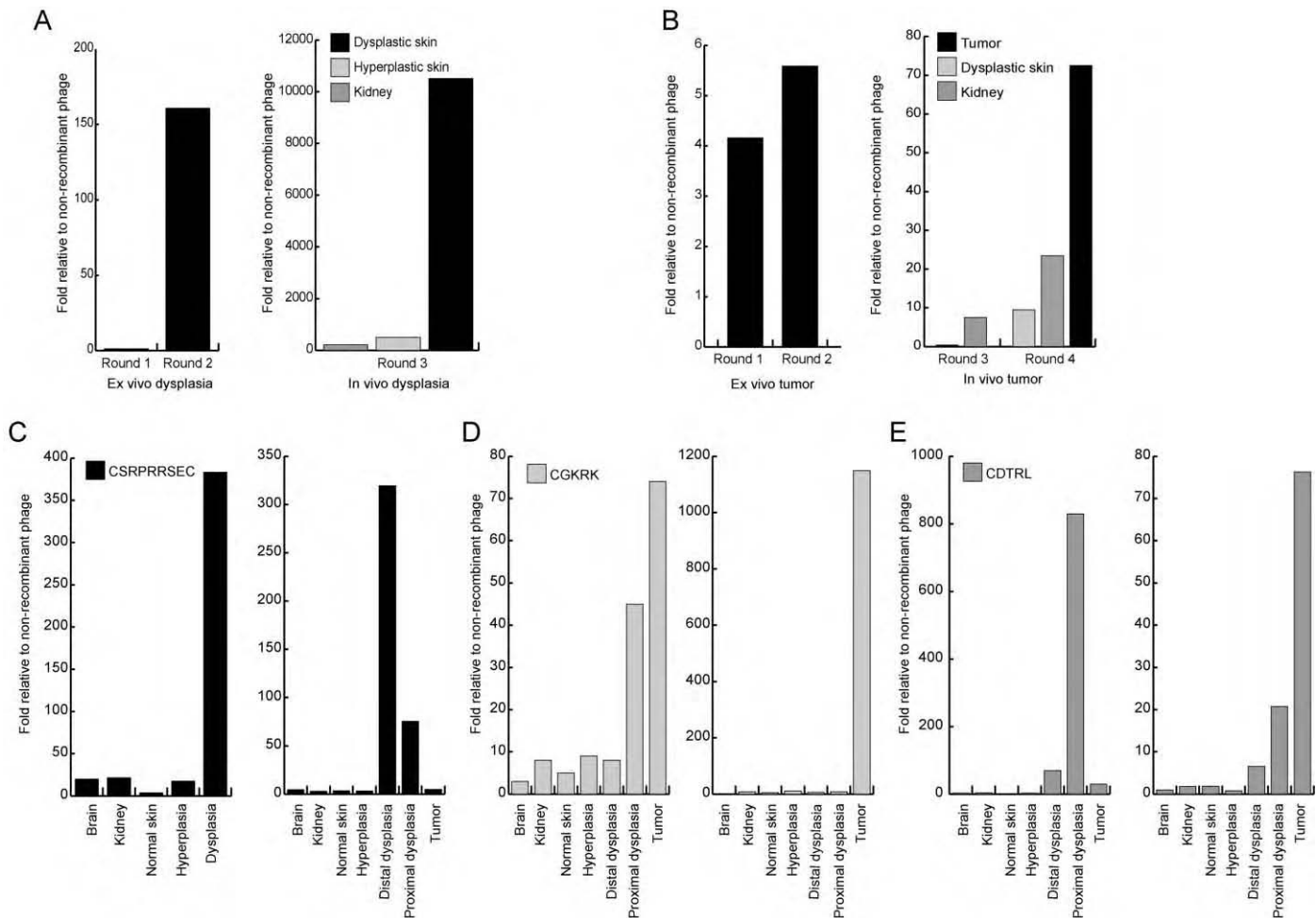
Figure 1. Phage-displayed peptides home to dysplastic skin lesions and tumors

Ex vivo and in vivo selections of phage for binding and homing to dysplastic skin lesions (**A**) or tumors (**B**).

C: In vivo homing of the CSRPRRSEC from the dysplastic skin screen to dysplastic skin lesions of a 4- to 6-month-old K14-HPV16 mouse (left) and to dysplastic skin lesions and tumor of a 9- to 12-month-old K14-HPV16 mouse (right).

In vivo homing of CGKRK (**D**) and CDTRL (**E**) peptides from tumor screening to tumors and other tissues in K14-HPV16 mice. Results from two different tumor-bearing mice are shown for each peptide. The normal skin values shown in **C–E** are from parallel experiments in wild-type FVB/n mice.

1, and 96 from in vivo round 2) and their increased appearance in the in vivo rounds. Of these, four clones with amino acid sequences CGKRK, CGTKRKC, CDTAVVEGL, and CDTRL bound to a K14-HPV16 tumor-derived cell suspension ex vivo. Phage-displayed CDTAVVEGL also homed in vivo 340-fold to tumors (data not shown), but we had difficulties with the CDTAVVEGL peptide in the subsequent steps, so we could not work further with the peptide. The remaining three phage-displayed peptides, CDTRL and the related CGKRK and CGTKRKC, were analyzed in depth.

When intravenously injected into tumor-bearing K14-HPV16 mice, the CGKRK phage showed a marked preference for the tumor, with an efficiency that varied from 80- to 1,000-fold in two experiments. Some homing to dysplastic lesions was observed in one of two experiments that showed an 80× enrichment in the tumor (Figure 1D). Normal and hyperplastic skin and various control organs also accumulated CGKRK phage but at very low levels (Figure 1D and data not shown). Similar analysis of the CDTRL phage revealed a variable preference for

SCCs and dysplastic lesions; in one experiment, the phage accumulated more effectively in dysplastic lesions than in a tumor, whereas the reverse was true in another experiment (Figure 1E). This phage showed little affinity for hyperplastic skin and no significant homing to normal skin from FVB/n mice (Figure 1E). Thus, phage displaying this peptide were variably selective for both dysplasias and squamous tumors of the epidermis, indicative of lesional heterogeneity in the moiety to which it binds. The squamous cancers that arise in the HPV16 model are heterogeneous, showing variations that can be scored by classical grading schemes for squamous tumors (Grades I–IV), as reported in Coussens et al. (1996); in addition, distinctive sebaceous cell carcinomas arise. Furthermore, the angiogenic dysplasias undergo morphological progression as the lesions progress from hyperplasia to low to high grade dysplasia, and thus it would not be surprising if there was variability in expression of certain binding moieties as a function of both premalignant and malignant progression.
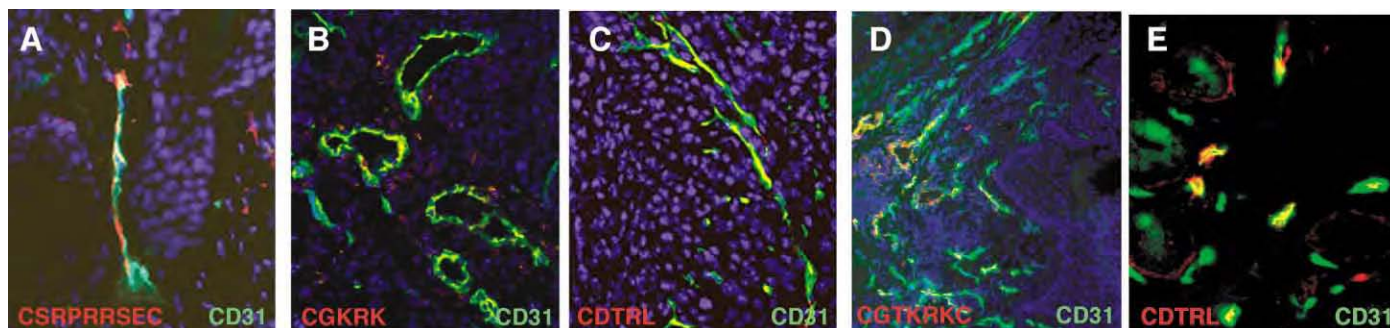
Figure 2. Vascular localization of homing phage

K14-HPV16 mice with dysplastic skin lesions or tumors were intravenously injected with individual homing phage, the mice were sacrificed 10 min later, and the phage were detected in tissue sections with rabbit anti-T7 phage (red; Alexa594). Blood vessels were stained with rat anti-mouse CD31 (green; Alexa488). **A:** CSRPRRSEC-displaying phage colocalizes with CD31 in the dysplastic skin lesions of 4- to 6-month-old dysplastic mice. **B–E:** The tumor-homing KRK-containing phage (**B** and **D**) and CDTRL (**C** and **E**) phage home to CD31-positive vessels in skin tumor (**B** and **C**) and dysplasia (**D** and **E**). Original magnifications: ×400 (**A** and **E**), ×200 (**B–D**).

Intra-tissue localization of homing peptides

To begin characterizing the nature of the selectivity of the dysplasia- and tumor-homing peptides for these neoplastic lesions, we sought to visualize their localization using histological procedures. K14-HPV16 mice were intravenously injected with cloned phage displaying a particular peptide or with the chemically synthesized, fluorescein-labeled peptide. We first evaluated the phage, intravenously injecting 4- to 6-month-old dysplasia-bearing mice with the dysplasia-homing phage, presenting CSRPRRSEC. In parallel, a set of 9- to 12-month-old tumor-bearing mice were infused with one or the other of the tumor-homing phage, CGTKRKC, CGKRK, or CDTRL. Various tissues were collected from each mouse and subjected to double label immunohistochemical staining, with an anti-T7 antibody to detect phage and with an anti-CD31 antibody that marks the endothelial cells of the vasculature. In each case, the phage colocalized with CD31-positive endothelial cells in the target tissue: CSRPRRSEC in dysplastic skin (Figure 2A) and CGKRK (Figure 2B) and CDTRL (Figure 2C) in tumors. The CGTKRKC phage was also detected to a lesser extent in the dysplastic skin of a tumor-bearing mouse (Figure 2D), and the positive vessels were often around what appeared to be concentric, nested clusters of keratinocytes, while the CDTRL phage was observed in large, dilated vessels throughout the dysplastic and hyperplastic skin (Figure 2E). Hematoxylin and eosin staining of serial sections adjacent to those used to visualize phage localization facilitated identification of the tissue structure to which the peptides were binding (see Supplemental Figure S1 at http://www.cancercell. org/cgi/content/full/4/5/383/DC1).

To further evaluate the homing specificity of the displayed peptides, we similarly analyzed pure peptides outside the context of the phage particles. We injected both younger dysplasia-bearing and older tumor-bearing K14-HPV16 mice with each of the fluorescein-labeled peptides. After 10 min, both normal and neoplastic tissues were collected; tissue sections were prepared and stained with antibodies to both CD31 and a second endothelial marker, the cell-surface antigen MECA32. Similar results were obtained with the two antibodies; the data for MECA32 are shown. Localizations of the intravenously infused peptides and the antibody were visualized by two-color fluorescence microscopy. The fluorescein-labeled peptides colocalized with

MECA32 in their target neoplastic tissue after an intravenous injection and were not detected in tissues where the corresponding phage did not home. Fluorescein-CSRPRRSEC colocalized with MECA32 in dysplastic skin vasculature from both non-tumor-bearing (Figure 3A) and tumor-bearing mice (Figure 3D, inset); notably, the peptide was not detected within the squamous tumor in the latter (Figure 3D), confirming its selectivity for the premalignant dysplastic vasculature. In contrast, the fluorescein-labeled CGKRK (Figure 3B) and CDTRL (Figure 3C) peptides were not detected in the dysplastic skin of younger non-tumor-bearing mice but were primarily detected in tumor vasculature (Figures 3E and 3F) and at lower levels in the dysplastic skin of these tumor-bearing mice (data not shown). Again, H&E staining of serial sections guided morphological evaluation of the binding patterns (see Supplemental Figure S2 on *Cancer Cell* website). A fluorescein-conjugated control peptide (NSSSVDK) did not home to any tissue. Taken together with the immunolocalization analyses of phage homing, the peptide localization data indicate that CGKRK and CDTRL home specifically to blood vessels in SCCs and in the dysplastic foci of tumor-bearing mice, but not to the vasculature of earlier stage dysplasias in non-tumor-bearing mice.

Tumor type specificity of peptide homing

The peptides identified by their binding to endothelial cells in skin dysplasias or skin tumors could in principle be selective for neoplasias in this tissue, neoplasias of this cell type, or neoplasias induced by these oncogenes or be general to neoplasias in various tissues and of various cell types and oncogenic transformations. To begin investigating this question, we asked whether the K14-HPV16 SCC-homing peptides, CGKRK and CDTRL, would home to the endothelium in tumors that are of different tissue origins and/or are resident in different anatomical locations. To this end, we examined three subcutaneous tumors arising from inoculated tumor cell lines, two other transgenic mouse models of organ-specific tumorigenesis, and subcutaneously transplanted matrigel pellets embedded with VEGF and bFGF. Each was assessed for selective binding to the neovasculature of intravenously injected fluorescein-labeled peptides (Figure 4; Supplemental Figure S3 on *Cancer Cell* website). We observed distinctive homing specificities for the two peptides
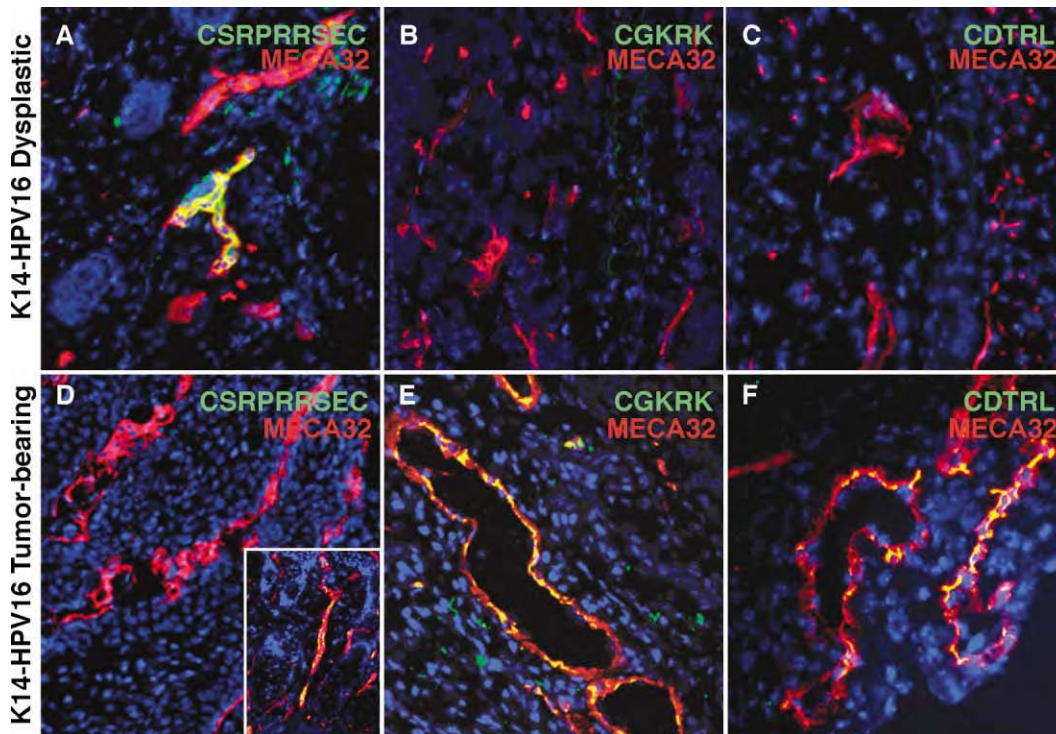
Figure 3. Fluorescein-labeled peptides colocalize with a vascular marker

Fluorescein-labeled peptides were intravenously injected into mice with dysplastic skin lesions or tumors, the mice were sacrificed 10 min later, and the peptide localization was examined in tissue sections. Fluorescein-CSRPRRSEC colocalizes with MECA32 in the vasculature of dysplastic skin (**A**) but not in tumor tissue (**D**). This peptide continues to recognize the vasculature of dysplastic skin in tumor-bearing mice (**D** inset). This peptide does not recognize premalignant lesions (angiogenic islets) in RIP1-Tag2 mice. Fluorescein-labeled CGKRK and CDTRL peptides were not detected in dysplastic skin from 4- to 6-month-old mice (**B** and **C**), but colocalized with MECA32 in tumor vasculature (**E** and **F**). Original magnifications: 200–400×.

in the various tumor microenvironments, but with one commonality: each homed to the neovasculature in subcutaneous matrigel pellets infused with a mixture of VEGF and bFGF. Neither peptide homed to angiogenic islets (dysplasias) or tumors in the RIP-Tag transgenic mouse model of pancreatic islet cell carcinoma (Hanahan, 1985) (Figures 4A and 4F), indicating that the binding moieties for these peptides are not present in normal, dysplastic, or pancreatic tumor vasculature. Interestingly, both CGKRK and CDTRL did home to breast carcinomas in another transgenic model, the MMTV-PyMT mice (Guy et al., 1992) (Figures 4B and 4G). Some of the positive cells appeared to be circulation-accessible tumor cells (Figure 4G; Chang et al., 2000), and they were negative for the Fcγ-II/III receptors (data not shown), suggesting that the peptide binding moiety can have broader representation beyond tumor endothelial cells. Both the CGKRK and CDTRL bind a range of cultured tumor cells (Supplemental Table S1 online) in addition to homing to tumor endothelial cells in vivo. Further, the activated endothelium in this type of mouse breast tumor shares molecular determinants with SCCs of the skin as detected by these peptides, ones that are not found in the RIP-Tag model of endocrine pancreatic cancer. This commonality is despite the fact that squamous tumorigenesis in the skin was induced by the E6 and E7 oncogenes of HPV16, while the islet tumors in RIP1-Tag2 were induced by the SV40 Tag oncogene, and the mammary tumors in MMTV-PyMT mice were induced by the polyoma middle T antigen.

The two tumor peptides showed different homing to three types of subcutaneously grown transplanted tumors. Fluorescein-CGKRK peptide homed to cells in each of the three transplant tumors (Figures 4C–4E), which arose from PDSC5, a K14-HPV16 tumor-derived cell line (Figure 4C), the MDA-MB-435 human breast cancer line (Figure 4D; Price et al., 1990), and the C8161 human melanoma line (Figure 4E; Bregman and Meyskens, 1986). In contrast, the CDTRL peptide was not present in the PDSC5 (Figure 4H) or MDA-MB-435 (Figure 4I) and only accumulated in the melanoma xenograft (Figure 4J) and in the skin overlying the melanoma xenograft tumor (Figure 4J inset). Fluorescein-CGKRK localized in the cytoplasm and nuclei of vascular cells identified as endothelial cells by their morphology and by immunostaining for CD31 and MECA32 (exemplified by Figure 4D). In addition, the peptide apparently extravasated out of the vessels and became distributed along tendril-like structures and in tumor cell nuclei; it also accumulated to some extent in avascular necrotic regions (exemplified by Figures 4B, 4C, and 4E). Given that all three tumors were growing subcutaneously, presumably by recruiting a neovasculature from the same normal vascular bed in the dermis, one can infer that cell type and/or oncogenic stimulus is imparting different qualities onto the vasculature and the tumor microenvironment, as revealed by the differential homing patterns seen with these peptides. Furthermore, it is apparent that the matrigel extracellular matrix in combination with VEGF and bFGF is sufficient to elicit expression of the binding moieties for these homing peptides;
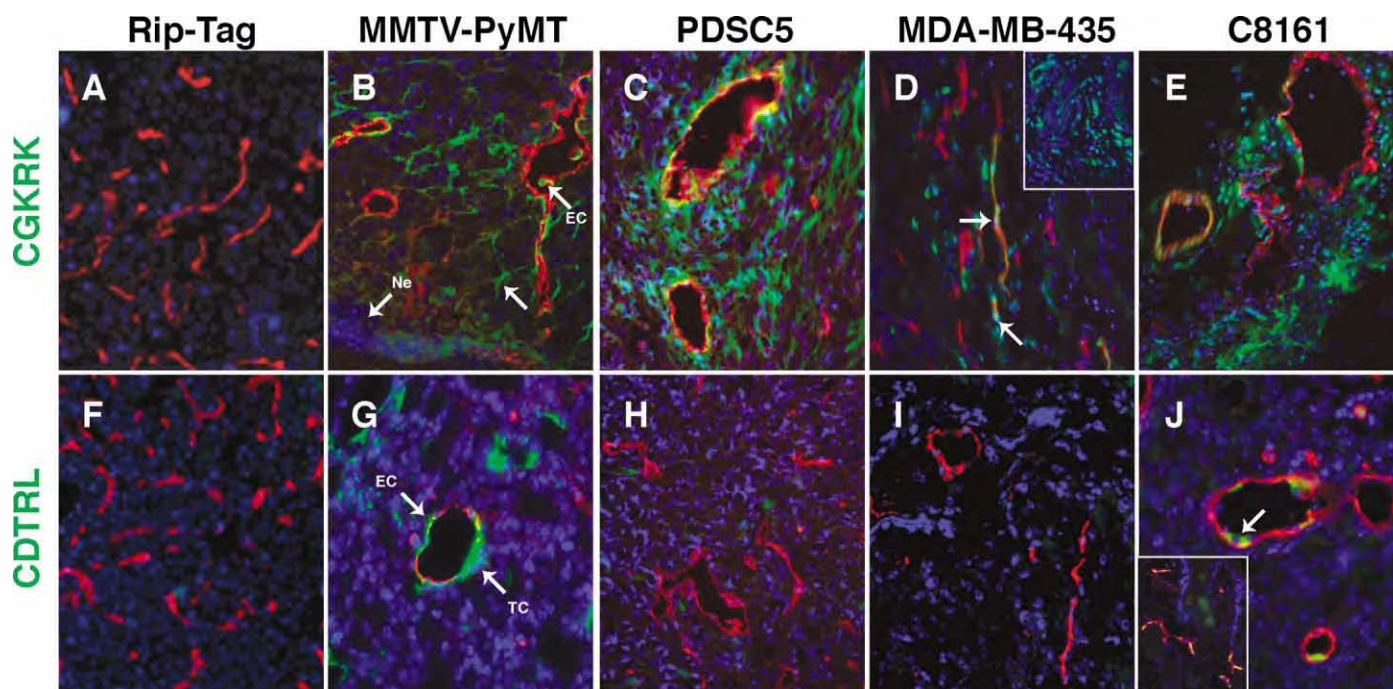
Figure 4. Localization of fluorescein-labeled peptides in other tumors

Mice bearing various tumors were intravenously injected with fluorescein-labeled peptides from the tumor-homing phage and examined as in Figure 3. The tissue sections were stained with MECA32 (shown with red fluorochrome) and CD31 (not shown). Fluorescein-CGKRK (**A–E**) was detected in 4 of the 5 tumor models examined; RIP1-Tag2 tumors (**A**) were negative. Some features are indicated by arrows, with the labels EC (for endothelial cell), TC (for tumor cell), and Ne (for necrotic region). The CGKRK peptide was seen in endothelial cells and tumor cells appearing both in the cytoplasm and nucleus (**B–E**; arrow in **D**). Fluorescein-CDTRL (**F–J**) was absent in the RIP1-Tag2 tumors (**F**), PDSCJ5 (**H**), and MDA-MB-435 (**I**), but present in MMTV-PyMT tumors (**G**) and C8161 xenografts (**J**) tumors. In the C8161 xenografts, the positive cells were CD31-positive cells that were adhering and spreading on the lumenal surface of the blood endothelial cells; the established endothelia were negative (indicated by the white arrow in **J**). The blood vessels in the skin surrounding the C8161 xenograft tumor are also positive for fluorescein-CDTRL (**J** inset). In the MMTV-PyMT, fluorescein-CDTRL colocalized with CD31 and MECA32 and also bound to cells within the vessel wall that were negative for MECA32, CD31, and the Fcγ-II/II receptors (**G**). Original magnifications: 200–400×.

notably, the neovasculature is again recruited from the dermis. Moreover, the two growth factors used in the matrigel assay have been implicated in the angiogenesis associated with squamouse carcinogenesis of the skin in the K14-HPV16 model (Arbeit et al., 1996; Coussens et al., 1999).

Discussion

In the study described herein, we have used phage libraries to profile the vascular changes that take place during squamous carcinogenesis of the skin in a transgenic mouse model involving the human papillomavirus type 16 oncogenes, which are implicated as causative agents in human squamous cancers. We describe three peptides that distinguish between the neo-vasculature in premalignant dysplastic lesions and malignant tumors. The peptides also distinguish both types of vasculature from normal skin vasculature. The in vivo binding patterns also reveal molecular diversity in the vasculature of tumors of different origins and anatomical locations, consistent with predictions based on evident morphological differences (Roberts et al., 1998).

The CSRPRRSEC peptide, obtained by screening for homing to dysplastic skin lesions, clearly differentiated this class of lesions from normal skin and from fully developed skin tumors. Moreover, because the peptide localized to the endothelial cells of the dysplastic lesions, the selectivity of its homing is attributable to vascular changes during the carcinogenic progression from normal skin to dysplasia to cancer. The accompanying paper (Joyce et al., 2003) describes peptides with different sequences that selectively recognize premalignant angiogenic islets in RIP1-Tag2 mice. Thus, the vasculature of premalignant lesions can be distinguished from that of malignant tumors of the same lineage in two different tumor systems.

The tumor-specific peptide CGKRK showed the broadest selectivity, homing to all tumors growing in or under the skin, while the CSRPRRSEC and CDTRL peptides were selective for two of the four tumors tested. The three tumor-selective phage did not home to normal skin vasculature and showed variable selectivity toward dysplasias of tumor-bearing mice. While all three homed to transplant tumors and the VEGF/bFGF matrigels, none accumulated in the angiogenic islet dysplasias or solid tumors in the RIP1-Tag2 model of pancreatic islet carcinogenesis. The strain of mice used did not seem to affect the homing of these peptides, as evidenced by their homing to tumors in different strains and their differential homing to tumors within the same strain. For example, the CGKRK peptide homed to tumors in FVB/b, C57B16, and Balb/c-*nu/nu*, while the CDTRL homed to C8161 but not MDA-MB-435 tumors, each growing in Balb/c-*nu/nu* mice. In the companion manuscript, Joyce et al. (2003) report a panel of peptides that home to the vasculature

of angiogenic islets and pancreatic islet carcinomas but not to the skin dysplasias or tumors in the HPV16 mice, nor to the vasculature in several subcutaneous transplant tumors or in s.c. matrigel plugs. Together, the data demonstrate that tumorigenesis in different organs involves the induction of distinctive vascular signatures as revealed by the selection of peptides displayed on circulating phage.

A database search revealed a homology between our CSRPRRSEC peptide and the $C_{220}SRPRR_{225}$ sequence in human kallikrein-9 (Yousef and Diamandis, 2000) and its mouse homolog (RIKEN Clone 1200016C12; Kawai et al., 2001), both proteases of the trypsin super family. These particular residues appear to be critical for the homing of the CSRPRRSEC peptide, as evidenced by the recovery of the CSRPRRS<u>V</u>C and CSRPRRS<u>W</u>C variants in our selection. The Cys220 to Arg225 sequence of human kallikrein-9 forms a loop that is part of the entrance to the active site; its conformation is variable between the different kallikreins and trypsin family members, affecting substrate specificity (Gomis-Ruth et al., 2002). Our cyclic peptide could structurally resemble and functionally mimic this loop. In the kallikreins, Cys220 forms a disulfide bond with Cys190, the cysteine next to the active site nucleophile Ser195, and all kallikreins close this loop with a kink introduced by the invariant Pro226. Our peptide closes the loop by forming a disulfide bond. Besides the sequence and structural identity, human kallikrein-9 is known to be expressed in the skin (Yousef and Diamandis, 2000), and the protein has been reported to be a favorable prognostic marker in ovarian cancer, implying that it antagonizes ovarian carcinogenesis (Yousef et al., 2001); moreover, several kallikreins are antiangiogenic (Diamandis et al., 2000). Thus, the receptor for the CSRPRRSEC peptide may be a kallikrein-9 substrate or inhibitor that is expressed or localized at elevated levels on the angiogenic endothelia of dysplastic skin lesions but then decreases with progression to squamous carcinomas. In analogy, PSA (prostate-specific antigen or human kallikrein-3) can cleave plasminogen to generate angiostatin (Heidtmann et al., 1999); kallikrein binding proteins like kallistatin are involved in angiogenesis (Miao et al., 2002) and kallikreins can exist as complexes with endogenous inhibitors on the surface of cells (Yayama et al., 2003). The possible functional involvement of this protease and its substrates and inhibitors in the HPV16 model squamous carcinogenesis deserves future investigation.

The CGKRK tumor-homing peptide was found in association with the luminal surface of the tumor endothelium, but also inside the tumor parenchyma after an intravenous injection. The localization of the peptide within the tumor tissues was not simply a result of leakiness of the tumor vasculature to labeled peptides because we did not see the same distribution with the other fluorescein-labeled peptides, and only the CGKRK peptide became localized to the nuclei of the tumor cells.

The CGKRK tumor-homing peptide has an overall charge of +3 and is essentially composed of basic residues. This peptide may bind by virtue of this charge and composition to cell surface heparan sulfates and to phosphatidylserine. An $\sim$60 nm in diameter T7 phage displaying 415 copies of this peptide would resemble a cationic liposome; cationic liposomes bind to and are used as a marker of tumor vasculature (Thurston et al., 1998). Cationic particles may bind to phosphatidylserine, an anionic phospholipid that is on the surface of tumor endothelial cells and is accessible to circulation (Ran et al., 2002). Phosphatidylserine is also a marker of apoptotic cells, and the

phosphatidylserine receptor on macrophages mediates engulfment (Fadok et al., 2000); this could explain CGKRK's uptake by the necrotic/apoptotic regions in the tumors (like shown in Figure 4B).

The KRK sequence is also found in exon 6 of human and mouse VEGF-A and other VEGF homologs like the endocrine gland-specific protein Bv8 (LeCouter et al., 2003). Exon 6 is present in the highly basic, cell-associated forms of VEGF ($VEGF_{189}$ and $VEGF_{206}$). Synthetic peptides corresponding to exon 6 release both FGF-2 and VEGF from the cell surface (Jonca et al., 1997) and inhibit VEGF binding and activity on HUVECs (Jia et al., 2001). A 24 residue basic peptide from exon 7 of $VEGF_{165}$ has been expressed on phage and shown to bind to heparan sulfate and home to the vasculature of subcutaneously growing CT26 colon and MATB-III mammary adenocarcinomas (El-Sheikh et al., 2002). The homing of heparin binding peptides to tumor vasculature may be explained by a greater accessibility to heparan sulfates or the expression of other specific glycosaminoglycans. Indeed there are known cases of glycosaminoglycans being preferentially expressed on the blood vessels of tumors (Smetsers et al., 2003; Qiao et al., 2003). The functional importance of this sequence in VEGF-A is suggested by the fact that mice engineered to express only $VEGF_{120}$, which lacks the ability to bind heparin, die within 2 weeks postpartum (Carmeliet et al., 1999). The CGKRK peptide may have a similar specificity, as it recognized the vessels in each of the subcutaneous tumors as well as the neovasculature induced in matrigel pellets implanted with VEGF and bFGF (Supplemental Figure S3 on *Cancer Cell* website).

Basic FGF binds to heparan sulfate and is also internalized by cells in a process that can be distinguished from internalization via FGF receptors (Roghani and Moscatelli, 1992), suggesting that heparan sulfate binding could be responsible for internalization of the CGKRK peptide. Finally, KRK is a known nuclear localization sequence (Craggs and Kellie, 2001; Zhou et al., 1991), potentially explaining the nuclear localization of the CGKRK peptide we observed. SCC induced in the skin by HPV oncogenes could therefore differ from islet cell tumors in the composition or presence of glycosaminoglycans like heparan sulfate, a possibility that deserves future investigation.

A similar shared specificity between tumor endothelial and tumor cells has been previously reported for two other tumor-homing peptides (Laakkonen et al., 2002; Porkka et al., 2002); these reported peptides are also internalized by cells and become localized to the nuclei. Tumor-homing peptides that penetrate into the tumor and are internalized by overt cancer cells or tumor endothelial cells may be particularly well suited for targeting therapeutic and imaging agents into tumors, leveraging their specificity and ability to accumulate substantively therein.

In summary, we describe peptides that target different stages of tumor development in the K14-HPV16 model of squamous cell carcinoma of the skin. These peptides further reveal molecular differences between tumor types. Peptides such as these and the receptor moieties they detect by their selective binding will contribute to our understanding of vascular heterogeneity and temporal changes that occur during multistage tumor development in different organs. This knowledge will provide avenues for developing improved diagnostic tools, including ones affording early detection of premalignant lesions and

asymptomatic early stage carcinomas, as well as for targeting therapeutics to those lesions.

Experimental procedures

Tumor-bearing and transgenic mice

To investigate homing to dysplasias, we used K14-HPV16 mice at 4–6 months of age and with no macroscopic evidence of tumors. Tumor-bearing K14-HPV16 mice were 9–12 months old with obvious ear or trunk tumors. RIP1-Tag2 mice were used at 12 weeks of age, when 100% had pancreatic islet tumors. MMTV-PyMT mice were 4–6 months old, bearing palpable mammary tumors. Cells for subcutaneous inoculation to produce the transplant tumors were cultured in 10% fetal calf serum (FCS) in Dulbecco's Modified Eagle's Media (DMEM). Tumors were generated by subcutaneously injecting 10^6 cells into the chest skin of FVB/n (PDSC5) or Balb/c nude (MDA-MB-435 and C8161) mice. We used mice bearing s.c. transplant tumors with an approximate diameter of 1 cm. PDSC5 tumors and MDA-MB-435 xenografts reached this size about 9 weeks post-injection while C8161 xenografts took 3 weeks post-injection. The matrigel angiogenesis bioassay involved inoculating Balb/c-nu/nu mice with a gelatinous plug composed of a mixture of 400 μl of Matrigel (Becton Dickinson, Bedford, Massachusetts), 100 ng of basic fibroblast growth factor, and 50 ng of vascular endothelial growth factor (R&D Systems, Minneapolis, Minnesota) in a 450 μl final volume. There were three experimental groups, one for each of the three peptides, comprised of three mice in each group. The mice were injected i.v. with 100 μg of fluorescein-peptide 9 days post-implantation. All animal experiments were approved by the Animal Research Committees at the Burnham Institute or University of California at San Francisco.

Ex vivo and in vivo phage selections

The selections were made with an NNK-encoded CX_7C peptide library displayed on Novagen's T7 415-1b phage vector. The library had a diversity of approximately 1×10^8. Phage selections and validations have been described (Hoffman et al., 2004; Laakkonen et al., 2002).

Immunofluorescence and immunohistochemistry

Areas of skin, tumors, and various organs were collected and either fixed in formalin, dehydrated through serial alcohols, and embedded in paraffin or directly embedded in OCT medium (Fisher Scientific). The K14-HPV16 dysplasia and tumors were graded by evaluating hematoxylin & eosin and anti-keratin staining on 5 μm paraffin sections under a light microscope (Coussens et al., 1996). Rat anti-mouse CD31, rat anti-mouse MECA32, and anti-CD16/CD32 (FcγRII and FcγRIII; BD Pharmingen) were used for vascular immunostaining on 10 μm frozen sections. The anti-phage stainings and biodistribution of fluorescein-labeled peptides were conducted as previously described (Hoffman et al., 2004; Laakkonen et al., 2002).

References

Arap, W., Pasqualini, R., and Ruoslahti, E. (1998). Cancer treatment by targeted drug delivery to tumor vasculature in a mouse model. Science *279*, 377–380.

Arbeit, J., Munger, K., Howley, P., and Hanahan, D. (1994). Progressive squamous epithelial neoplasia in K14-human papillomavirus type 16 transgenic mice. J. Virol. *68*, 4358–4368.

Arbeit, J., Olson, D., and Hanahan, D. (1996). Upregulation of fibroblast growth factors and their receptors during multi-stage epidermal carcinogenesis in K14-HPV16 transgenic mice. Oncogene *13*, 1847–1857.

Bergers, G., Javaherian, K., Lo, K., Folkman, J., and Hanahan, D. (1999). Effects of angiogenesis inhibitors on multistage carcinogenesis in mice. Science *284*, 808–812.

Bergers, G., Song, S., Meyer-Morse, N., Bergsland, E., and Hanahan, D. (2003). Benefits of targeting both pericytes and endothelial cells in the tumor vasculature with kinase inhibitors. J. Clin. Invest. *111*, 1287–1295.

Bregman, M., and Meyskens, F.J. (1986). Difluoromethylornithine enhances inhibition of melanoma cell growth in soft agar by dexamethasone, clone A interferon and retinoic acid. Int. J. Cancer *37*, 101–107.

Burg, M., Pasqualini, R., Arap, W., Ruoslahti, E., and Stallcup, W. (1999). NG2 proteoglycan-binding peptides target tumor neovasculature. Cancer Res. *59*, 2869–2874.

Carmeliet, P., and Jain, R. (2000). Angiogenesis in cancer and other diseases. Nature *407*, 249–257.

Carmeliet, P., Ng, Y.S., Nuyens, D., Theilmeier, G., Brusselmans, K., Cornelissen, I., Ehler, E., Kakkar, V.V., Stalmans, I., Mattot, V., et al. (1999). Impaired myocardial angiogenesis and ischemic cardiomyopathy in mice lacking the vascular endothelial growth factor isoforms VEGF164 and VEGF188. Nat. Med. *5*, 495–502.

Chang, Y.S., di Tomaso, E., McDonald, D.M., Jones, R., Jain, R.K., and Munn, L.L. (2000). Mosaic blood vessels in tumors: Frequency of cancer cells in contact with flowing blood. Proc. Natl. Acad. Sci. USA *97*, 14608–14613.

Coussens, L., Hanahan, D., and Arbeit, J. (1996). Genetic predisposition and parameters of malignant progression in K14-HPV16 transgenic mice. Am. J. Pathol. *149*, 1899–1917.

Coussens, L., Raymond, W., Bergers, G., Laig-Webster, M., Behrendtsen, O., Werb, Z., Caughey, G., and Hanahan, D. (1999). Inflammatory mast cells up-regulate angiogenesis during squamous epithelial carcinogenesis. Genes Dev. *13*, 1382–1397.

Coussens, L., Tinkle, C., Hanahan, D., and Werb, Z. (2000). MMP-9 supplied by bone marrow-derived cells contributes to skin carcinogenesis. Cell *103*, 481–490.

Craggs, G., and Kellie, S. (2001). A functional nuclear localization sequence in the C-terminal domain of SHP-1. J. Biol. Chem. *276*, 23719–23725.

Diamandis, E., Yousef, G., Luo, L., Magklara, A., and Obiezu, C. (2000). The new human kallikrein gene family: implications in carcinogenesis. Trends Endocrinol. Metab. *11*, 54–60.

El-Sheikh, A., Liu, C., Huang, H., and Edgington, T.S. (2002). A novel vascular endothelial growth factor heparin-binding domain substructure binds to glycosaminoglycans in vivo and localizes to tumor microvascular endothelium. Cancer Res. *62*, 7118–7123.

Fadok, V., Bratton, D., Rose, D., Pearson, A., Ezekewitz, R., and Henson, P. (2000). A receptor for phosphatidylserine-specific clearance of apoptotic cells. Nature *405*, 85–90.

Gee, M.S., Procopio, W.N., Makonnen, S., Feldman, M.D., Yeilding, N.M., and Lee, W.M.F. (2003). Tumor vessel development and maturation impose limits on the effectiveness of anti-vascular therapy. Am. J. Pathol. *162*, 183–193.

Gomis-Ruth, F.X., Bayes, A., Sotiropoulou, G., Pampalakis, G., Tsetsenis, T., Villegas, V., Aviles, F.X., and Coll, M. (2002). The structure of human prokallikrein 6 reveals a novel activation mechanism for the kallikrein family. J. Biol. Chem. *277*, 27273–27281.

Guy, C., Cardiff, R., and Muller, W. (1992). Induction of mammary tumors by expression of polyomavirus middle T oncogene: a transgenic mouse model for metastatic disease. Mol. Cell. Biol. *12*, 954–961.

Hanahan, D. (1985). Heritable formation of pancreatic beta-cell tumours in transgenic mice expressing recombinant insulin/simian virus 40 oncogenes. Nature *315*, 115–122.

Hanahan, D., and Folkman, J. (1996). Patterns and emerging mechanisms of the angiogenic switch during tumorigenesis. Cell 86, 353–364.

Hanahan, D., and Weinberg, R. (2000). The hallmarks of cancer. Cell 100, 57–70.

Heidtmann, H., Nettelbeck, D., Mingels, A., Jager, R., Welker, H., and Kontermann, R. (1999). Generation of angiostatin-like fragments from plasminogen by prostate-specific antigen. Br. J. Cancer 81, 1269–1273.

Hoffman, J., Laakkonen, P., Porkka, K., Bernasconi, M., and Ruoslahti, E. (2004). In vivo and ex vivo selections using phage-displayed libraries. In Phage Display: A Practical Approach, in press.

Jia, H., Jezequel, S., Lohr, M., Shaikh, S., Davis, D., Soker, S., Selwood, D., and Zachary, I. (2001). Peptides encoded by exon 6 of VEGF inhibit endothelial cell biological responses and angiogenesis induced by VEGF. Biochem. Biophys. Res. Commun. 283, 164–173.

Jonca, F., Ortega, N., Gleizes, P.-E., Bertr, N., and Plouet, J. (1997). Cell release of bioactive fibroblast growth factor 2 by exon 6-encoded sequence of vascular endothelial growth factor. J. Biol. Chem. 272, 24203–24209.

Joyce, J.A., Laakonen, Bernasconi, M., Bergers, G., Ruoslahti, E., and Hanahan, D. (2003). Stage-specific vascular markers revealed by phage display in a mouse model of pancreatic islet tumorigenesis. Cancer Cell 4, this issue, 393–403.

Kawai, J., Shinagawa, A., Shibata, K., Yoshino, M., Itoh, M., Ishii, Y., Arakawa, T., Hara, A., Fukunishi, Y., Konno, H., et al. (2001). Functional annotation of a full-length mouse cDNA collection. Nature 409, 685–690.

Laakkonen, P., Porkka, K., Hoffman, J., and Ruoslahti, E. (2002). A tumor-homing peptide with a targeting specificity related to lymphatic vessels. Nat. Med. 8, 751–755.

LeCouter, J., Lin, R., Tejada, M., Frantz, G., Peale, F., Kenneth, J.H., and Ferrara, N. (2003). The endocrine-gland-derived VEGF homologue Bv8 promotes angiogenesis in the testis: Localization of Bv8 receptors to endothelial cells. Proc. Natl. Acad. Sci. USA 100, 2685–2690.

Miao, R.Q., Agata, J., Chao, L., and Chao, J. (2002). Kallistatin is a new inhibitor of angiogenesis and tumor growth. Blood 100, 3245–3252.

Pasqualini, R., Arap, W., and McDonald, D. (2002). Probing the structural and molecular diversity of tumor vasculature. Trends Mol. Med. 8, 563–571.

Porkka, K., Laakkonen, P., Hoffman, J., Bernasconi, M., and Ruoslahti, E. (2002). A fragment of the HMGN2 protein homes to the nuclei of tumor cells and tumor endothelial cells in vivo. Proc. Natl. Acad. Sci. USA 99, 7444–7449.

Price, J., Polyzos, A., Zhang, R., and Daniels, L. (1990). Tumorigenicity and metastasis of human breast carcinoma cell lines in nude mice. Cancer Res. 50, 717–721.

Qiao, D., Meyer, K., Mundhenke, C., Drew, S.A., and Friedl, A. (2003). Heparan sulfate proteoglycans as regulators of fibroblast growth factor-2 signaling in brain endothelial cells. Specific role for glypican-1 in glioma angiogenesis. J. Biol. Chem. 278, 16045–16053.

Ran, S., Downes, A., and Thorpe, P.E. (2002). Increased exposure of anionic phospholipids on the surface of tumor blood vessels. Cancer Res. 62, 6132–6140.

Roberts, W., Delaat, J., Nagane, M., Huang, S., Cavenee, W., and Palade, G. (1998). Host microvasculature influence on tumor vascular morphology and endothelial gene expression. Am. J. Pathol. 153, 1239–1248.

Roghani, M., and Moscatelli, D. (1992). Basic fibroblast growth factor is internalized through both receptor-mediated and heparan sulfate-mediated mechanisms. J. Biol. Chem. 267, 22156–22162.

Ruoslahti, E. (2002). Specialization of tumour vasculature. Nat. Rev. Cancer 2, 83–90.

Smetsers, T.F., van de Westerlo, E.M., ten Dam, G.B., Clarijs, R., Versteeg, E.M., van Geloof, W.L., Veerkamp, J.H., van Muijen, G.N., and van Kuppevelt, T.H. (2003). Localization and characterization of melanoma-associated glycosaminoglycans: differential expression of chondroitin and heparan sulfate epitopes in melanoma. Cancer Res. 63, 2965–2970.

Smith-McCune, K., Zhu, Y.H., Hanahan, D., and Arbeit, J. (1997). Cross-species comparison of angiogenesis during the premalignant stages of squamous carcinogenesis in the human cervix and K14-HPV16 transgenic mice. Cancer Res. 57, 1294–1300.

Thurston, G., McLean, J., Rizen, M., Baluk, P., Haskell, A., Murphy, T., Hanahan, D., and McDonald, D. (1998). Cationic liposomes target angiogenic endothelial cells in tumors and chronic inflammation in mice. J. Clin. Invest. 101, 1401–1413.

Yayama, K., Kunimatsu, N., Teranishi, Y., Takano, M., and Okamoto, H. (2003). Tissue kallikrein is synthesized and secreted by human vascular endothelial cells. Biochim. Biophys. Acta 1593, 231–238.

Yousef, G., and Diamandis, E. (2000). The expanded human kallikrein gene family: locus characterization and molecular cloning of a new member, KLK-L3 (KLK9). Genomics 65, 184–194.

Yousef, G.M., Kyriakopoulou, L.G., Scorilas, A., Fracchioli, S., Ghiringhello, B., Zarghooni, M., Chang, A., Diamandis, M., Giardina, G., Hartwick, W.J., et al. (2001). Quantitative expression of the human kallikrein gene 9 (KLK9) in ovarian cancer: A new independent and favorable prognostic marker. Cancer Res. 61, 7811–7818.

Zhou, J., Doorbar, J., Sun, X., Crawford, L., McLean, C., and Frazer, I. (1991). Identification of the nuclear localization signal of human papillomavirus type 16 L1 protein. Virology 185, 625–632.

Inhibition of Vascular Endothelial Growth Factor (VEGF) Signaling in Cancer Causes Loss of Endothelial Fenestrations, Regression of Tumor Vessels, and Appearance of Basement Membrane Ghosts

Tetsuichiro Inai,* Michael Mancuso,*
Hiroya Hashizume,† Fabienne Baffert,*
Amy Haskell,* Peter Baluk,* Dana D. Hu-Lowe,‡
David R. Shalinsky,‡ Gavin Thurston,§
George D. Yancopoulos,§ and
Donald M. McDonald*

From the Cardiovascular Research Institute, Comprehensive Cancer Center, and Department of Anatomy, University of California, San Francisco, California; the Division of Microscopic Anatomy and Bio-Imaging,† Niigata University Graduate School of Medical and Dental Sciences, Niigata City, Japan; the Department of Research Pharmacology,‡ Pfizer Global Research and Development, San Diego, California; and Regeneron Pharmaceuticals,§ Tarrytown, New York*

Angiogenesis inhibitors are receiving increased attention as cancer therapeutics, but little is known of the cellular effects of these inhibitors on tumor vessels. We sought to determine whether two agents, AG013736 and VEGF-Trap, that inhibit vascular endothelial growth factor (VEGF) signaling, merely stop angiogenesis or cause regression of existing tumor vessels. Here, we report that treatment with these inhibitors caused robust and early changes in endothelial cells, pericytes, and basement membrane of vessels in spontaneous islet-cell tumors of RIP-Tag2 transgenic mice and in subcutaneously implanted Lewis lung carcinomas. Strikingly, within 24 hours, endothelial fenestrations in RIP-Tag2 tumors disappeared, vascular sprouting was suppressed, and patency and blood flow ceased in some vessels. By 7 days, vascular density decreased more than 70%, and VEGFR-2 and VEGFR-3 expression was reduced in surviving endothelial cells. Vessels in Lewis lung tumors, which lacked endothelial fenestrations, showed less regression. In both tumors, pericytes did not degenerate to the same extent as endothelial cells, and those on surviving tumor vessels acquired a more normal phenotype. Vascular basement membrane persisted after endothelial cells degenerated, providing a ghost-like record of pretreatment vessel number and location and a potential scaffold for vessel regrowth. The potent anti-vascular action observed is

evidence that VEGF signaling inhibitors do more than stop angiogenesis. Early loss of endothelial fenestrations in RIP-Tag2 tumors is a clue that vessel phenotype may be predictive of exceptional sensitivity to these inhibitors. *(Am J Pathol 2004, 165:35–52)*

Inhibitors of angiogenesis are now making their way through clinical trials.[1–3] Some results with inhibitors of vascular endothelial growth factor (VEGF) are promising,[4,5] but challenges are faced in selecting the right patients, determining effective doses, and evaluating responses. Patient selection is made difficult by lack of understanding of which tumors have drug-sensitive blood vessels, and limited information is available on the cellular changes tumor vessels undergo in response to angiogenesis inhibitors. Conventional measurements of microvascular density, one of the most common microscopic methods used to quantify angiogenesis in tumors,[6] is not always an accurate measure of efficacy because tumor mass may decrease in parallel with the number of blood vessels.[1] Other standard endpoints, such as tumor burden, provide little insight into whether drugs act on blood vessels or tumor cells and may not show whether tumor growth is stabilized by angiogenesis inhibition. Thus, new ways are needed for evaluating vascular effects of angiogenesis inhibitors.

Blood vessels in tumors have multiple abnormalities. Tumor vessels express unique proteins[7] and have bi-

zarre morphological features, including loss of arteriole-capillary-venule hierarchy, tortuosity, variable diameter, defective endothelial monolayer, and leakiness.[8,9] Even pericytes (mural cells) of tumor vessels are abnormal, as evidenced by altered gene expression and loss of intimate contact with endothelial cells.[10,11] Abnormalities of the basement membrane of tumor vessels are also present and reflect the disturbances of endothelial cells and pericytes.[12] We reasoned that a better understanding of these abnormalities and how they respond to treatment could give insight into the cellular effects of angiogenesis inhibitors.

One approach to blocking angiogenesis involves inhibition of VEGF.[4,13] VEGF and its receptors, VEGFR-1 (flt-1) and VEGFR-2 (flk-1/KDR), play key roles in the formation and growth of normal blood vessels and in tumor angiogenesis.[14] There is compelling evidence that VEGF is a survival factor for some tumor vessels and that the growth of some tumors is dependent on VEGF-induced angiogenesis. The strength of the evidence stems in part from the use of multiple different approaches to inhibit VEGF signaling, including neutralizing antibodies against VEGF[15] or VEGFR-2,[16] anti-sense VEGF cDNA,[17] conditional expression of the VEGF gene,[18] soluble VEGF receptors,[19,20] chimeric proteins consisting of the extracellular domain of VEGFR-1 and VEGFR-2 joined to the Fc portion of IgG,[21] adenoviral expression of soluble VEGF receptors[22] or dominant-negative VEGFR-2,[23] and small molecules that inhibit VEGF receptor tyrosine kinase phosphorylation.[24–27]

Inhibition of VEGF signaling not only blocks angiogenesis in tumors but can also change or destroy tumor vessels.[28–31] VEGF/VEGFR inhibition can decrease the diameter, tortuosity, and permeability of tumor vessels[28] and even transform surviving tumor vessels into a more normal phenotype.[32,33] Considering the important role of VEGF and its receptors in regulating vascular function, we sought to characterize the changes in tumor vessels produced by agents that block the action of this growth factor.

In the present studies, we examined the cellular effects of two inhibitors of VEGF signaling, VEGF-Trap and AG013736, on blood vessels in spontaneous pancreatic islet tumors in RIP-Tag2 transgenic mice[34] and implanted Lewis lung carcinoma (LLC) in syngeneic mice. VEGF-Trap is a decoy construct of VEGFR-1 and VEGFR-2 that inhibits VEGF signaling by selectively binding the ligand and has potent anti-angiogenic activity in preclinical tumor models.[21,31] AG013736 is a small molecule inhibitor of VEGFR-1, VEGFR-2, VEGFR-3, and related tyrosine kinase receptors that has potent anti-angiogenic and anti-tumor effects in mice.[27,35] We focused on changes occurring during the first week of treatment of established tumors to identify primary vascular effects of the inhibitors that precede or accompany the reduction in tumor growth documented by others.[21,27,31,33,35,36] Fluorescence, confocal, and electron microscopic approaches applied to tissues fixed *in situ* by vascular perfusion provided cellular and molecular readouts for assessing patency and blood flow of individual vessels, endothelial sprouts and fenestrations, VEGFR-2 and VEGFR-3 immu-

noreactivity, pericyte morphology, and changes in the vascular basement membrane. The orderly microvasculature of the mouse trachea was used to validate some of the methods in a simpler system.[37] Cellular changes observed as soon as 24 hours after the onset of treatment reflected drug activity and suggested novel features that may help to identify types of blood vessels that are sensitive to inhibition of VEGF signaling.

Materials and Methods

VEGF/VEGFR Inhibitors

VEGF-Trap (also called VEGF-Trap$_{R1R2}$), which consists of the second immunoglobulin (Ig) domain of VEGFR-1 and third Ig domain of VEGFR-2 fused to the constant region (Fc) of human IgG1,[21] was supplied by Regeneron Pharmaceuticals, Inc., Tarrytown, NY. AG013736, which is a potent small molecule inhibitor of VEGF/platelet-derived growth factor (PDGF) receptor tyrosine kinases (IC$_{50}$ = 1.2 nmol/L for VEGFR-1, 0.25 nmol/L for VEGFR-2, 0.29 nmol/L for VEGFR-3, 2.5 nmol/L for PDGFR-β, 2.0 for cKit, and 218 nmol/L for FGFR-1),[35] was supplied by Pfizer Global Research and Development, San Diego, CA.

Animals and Treatment

Tumor-bearing RIP-Tag2 transgenic mice[34] (C57BL/6 background, 10 to 12 weeks of age) were injected with VEGF-Trap (25 mg/kg in a volume of 5 μl/g i.p.) or its vehicle (5 μl/g; Chinese hamster ovary cell-derived human Fc domain in 40 mmol/L phosphate) on day 0 and studied on day 1 or 2 or were injected on days 0, 3, and 6 and studied on day 7. Alternatively, RIP-Tag2 mice were injected with AG013736 (25 mg/kg in a volume of 5 μl/g i.p.) or its vehicle (5 μl/g; 3 parts PEG 400 to 7 parts acidified H$_2$O, pH 2 to 3) twice daily for 1, 2, or 7 days or once daily for 7 or 21 days. In addition, wild-type C57BL/6 mice, 10 weeks of age, with a 1-mm³ piece of LLC tumor implanted under the dorsal skin for 4 to 6 days, were treated with AG013736 (25 mg/kg i.p.) or vehicle twice daily for 7 days. These intervention treatment regimens[38] examined the effects of the agents on established RIP-Tag2 tumors and LLC tumors. Normal wild-type mice (FVB/n background, 8 weeks of age) were treated with AG013736 (25 mg/kg i.p.) twice daily for <10 days, VEGF-Trap for 7 days, or vehicle for developing the model using the tracheal microvasculature.

Lectin Injection and Fixation by Vascular Perfusion

At the end of the treatment period, mice were anesthetized with ketamine (100 mg/kg i.m.) plus xylazine (10 mg/kg i.m.). In mice used for immunohistochemistry, blood flow and patency of individual tumor vessels were assessed by injection of 100 μg of fluorescein isothiocyanate-labeled *Lycopersicon esculentum* lectin in 0.9% NaCl

(100 μl into femoral vein; Vector Laboratories, Burlingame, CA).[8,11] Two minutes later the chest was opened rapidly, and the vasculature was perfused for 2 minutes at a pressure of 120 mmHg with fixative [1% paraformaldehyde in phosphate-buffered saline (PBS), pH 7.4, Sigma, St. Louis, MO] from an 18-gauge cannula inserted into the aorta via an incision in the left ventricle. Blood and fixative exited through an opening in the right atrium. Tissues were removed, immersed in fixative for 1 hour at 4°C, and then processed for immunohistochemistry. In mice used for transmission electron microscopy (TEM), tissues were fixed by vascular perfusion of fixative containing 3% glutaraldehyde in 75 mmol/L cacodylate buffer, pH 7.1, 4% polyvinylpyrrolidone, 0.05% $CaCl_2$, and 1% sucrose.[8,11] The fixative for scanning electron microscopy (SEM) contained 2% glutaraldehyde in 100 mmol/L phosphate buffer. Fixative was perfused at 120 mmHg for 2 minutes and then 100 mmHg for 3 minutes. Tissues were removed, immersed in fixative for at least 18 hours (4°C), and then processed for TEM or SEM.

Electron Microscopy

For TEM, RIP-Tag2 tumors, LLC tumors, pancreas, thyroid, and tongue were fixed by vascular perfusion and then were trimmed to a maximal dimension of 5 mm, embedded in 7% agarose, and 0.25- to 1-mm slices were cut with a tissue chopper or razor blade. Specimens measuring ~1 to 3 mm on a side were cut from the slices, rinsed with 100 mmol/L cacodylate buffer, fixed with OsO_4 (1% in 100 mmol/L cacodylate buffer at 4°C, 2 hours), rinsed with water, *en bloc* stained with uranyl acetate (2% aqueous for 48 hours at 38°C), dehydrated with acetone, and embedded in epoxy resin.[8,11] Sections 0.5 μm in thickness were stained with toluidine blue for light microscopy, and sections 60 to 80 nm in thickness were stained with lead citrate and examined with a Zeiss EM-10C electron microscope. For SEM, RIP-Tag2 tumors and thyroid glands were fixed by vascular perfusion, trimmed to a maximal dimension of 7 mm, and treated with 30% potassium hydroxide in distilled water for 8 minutes at 60°C to remove the extracellular matrix around blood vessels and tumor cells.[39] The specimens were stained with a solution of 2% tannic acid and 1% OsO_4, dehydrated with a graded series of ethanol, transferred to isoamyl acetate, and critical point-dried in liquid CO_2. Some tumors were cracked with fine forceps under a dissection microscope to expose blood vessels within the specimen. Dried specimens were put on aluminum stubs, coated with OsO_4 in an Osmium Plasma Coater (Vacuum Device Corp., Japan), and examined with a Hitachi S-4300N scanning electron microscope.

Immunohistochemistry

Endothelial cells of tumor vessels were evaluated by immunohistochemistry using six primary antibodies: rat monoclonal anti-CD31 (PECAM-1, clone MEC 13.3, 1:1000; Pharmingen, San Diego, CA), hamster monoclonal anti-CD31 (clone 2H8, 1:1000; Chemicon, Temecula,

CA), rabbit polyclonal anti-VEGFR-2 (VEGF receptor-2, antibody T014, 1:2000; gift from Rolf Brekken and Philip Thorpe, University of Texas Southwestern Medical Center), goat polyclonal anti-VEGFR-3 (VEGF receptor-3, 1:1000; R&D Systems, Minneapolis, MN), rat monoclonal anti-CD105 (endoglin, clone MJ7/18, 1:500; Pharmingen), and rat monoclonal anti-α_5 integrin [CD49e, clone 5H10-27 (MFR5), 1:400; Pharmingen]. Pericytes were examined with two primary antibodies: Cy3-conjugated mouse monoclonal anti-α-smooth muscle actin (SMA) (clone 1A4, 1:1000; Sigma Chemical Co., St. Louis, MO) and rat monoclonal anti-PDGFR-β (PDGF receptor-β, clone APB5, 1:2000; gift from Akiyoshi Uemura, Kyoto University, Japan). Vascular basement membrane was examined with rabbit polyclonal anti-type IV collagen antibody (1:10,000; Cosmo Bio Co., Tokyo, Japan).[12] Secondary antibodies were goat anti-rat IgG labeled with fluorescein isothiocyanate or Cy3 for rat CD31, CD105, α_5 integrin, and PDGFR-β antibodies; goat anti-hamster IgG labeled with fluorescein isothiocyanate for hamster CD31 antibody; donkey anti-rabbit IgG labeled with Cy3 for rabbit anti-VEGFR-2 antibody; donkey anti-goat IgG labeled with Cy3 for goat anti-VEGFR-3 antibody; and goat anti-rabbit IgG labeled with Cy3 or Cy5 for rabbit anti-type IV collagen antibody (1:400; Jackson ImmunoResearch, West Grove, PA).

After fixation by vascular perfusion, tracheas were removed, incised along the ventral midline, and processed as whole mounts to visualize the three-dimensional structure of the microvasculature.[37] Other organs and tumors were removed, rinsed several times with PBS, infiltrated with 30% sucrose, and frozen in OCT compound. Cryostat sections were cut 80 μm in thickness for all studies except for measurement of immunofluorescence intensity in which they were cut at 20 μm. Sections were dried on Superfrost Plus slides (Fisher Scientific, Pittsburgh, PA) for 1 to 2 hours (20-μm sections) or 12 to 15 hours (80-μm sections). Specimens were permeabilized with PBS containing 0.3% Triton X-100 (Lab Chem Inc., Pittsburgh, PA) and incubated in 5% normal serum (Jackson ImmunoResearch) in PBS+ [PBS containing 0.3% Triton X-100, 0.2% bovine serum albumin (Sigma), and 0.01% thimerosal (Sigma)] for 1 hour at room temperature to block nonspecific antibody binding. Sections were incubated with primary antibodies diluted in 5% normal serum in PBS+ for 2 hours (20-μm sections) or 12 to 15 hours (80-μm sections and trachea) at room temperature (20- and 80-μm sections) or 4°C (trachea). Most primary antibodies were used in combination with anti-CD31. Anti-CD31 was used alone to examine the distribution of lectin staining. Control specimens for immunofluorescence intensity analysis were incubated in 5% normal serum instead of primary antibody for the same period. After rinsing with PBS containing 0.3% Triton X-100, specimens were incubated for 1 hour (20-μm sections) or 4 to 6 hours (for 80-μm sections and trachea) at room temperature with fluorophore-conjugated (fluorescein isothiocyanate, Cy3 or Cy5) secondary antibodies diluted in 5% normal serum in PBS+. Specimens were rinsed with PBS containing 0.3% Triton X-100, fixed in 4% parafor-

maldehyde (PFA), rinsed again with PBS, and mounted in Vectashield (Vector Laboratories).

Fluorescence Imaging

Specimens were examined with a Zeiss Axiophot fluorescence microscope equipped with single, dual, and triple fluorescence filters and a low-light, externally cooled, three-chip charge-coupled device camera (480 × 640 pixel RGB-color images, CoolCam; SciMeasure Analytical Systems, Atlanta, GA) and with a Zeiss LSM 510 confocal microscope with argon, helium-neon, and UV lasers (512 × 512 or 1024 × 1024 pixel RGB-color images). In each mouse, four or five images were obtained from sections cut approximately through the midpoint of RIP-Tag2 tumors, ranging from 0.5 to 2 mm in diameter, or LLCs, measuring ~5 mm in diameter. Images were obtained from central and peripheral regions of tumors too large to be included in one image.

Fluorescence Intensity Measurements

Fluorescence intensity of blood vessels in 20-μm-thick cryostat sections of RIP-Tag2 and LLC tumors from mice treated with AG013736, VEGF-Trap, or vehicle for 7 days was measured on digital images (×20 objective, ×1 Optovar, tissue region 480 μm by 640 μm) of specimens stained for VEGFR-2, VEGFR-3, α_5-integrin, CD31, CD105, or PDGFR-β immunoreactivity. Measurements of mean vessel brightness involved four steps. 1) On the fluorescence microscope, the background fluorescence (nonspecific fluorescence of the tissue) of each image was set to a barely detectable level by adjusting the gain of the charge-coupled device camera, and then the image was captured. The brightness of blood vessel fluorescence was ignored in this step. 2) RGB images were converted to 8-bit gray scale images (fluorescence intensity range: 0 < 255) using ImageJ software (*http://rsb. info.nih.gov/ij*). 3) The intensity of the background fluorescence was measured on images of tissues (RIP-Tag2 and LLC tumors and normal pancreatic islets) stained with Cy3-labeled secondary antibody without a primary antibody. Analysis of these images showed that >97% of pixels had a fluorescence intensity of <15. A fluorescence intensity of 15 was thus established as the threshold for distinguishing pixels of the vasculature from those of the background. 4) The fluorescence intensity of the vasculature represented the average brightness of all vessel-related pixels. This value was calculated from all pixels with fluorescence intensities ≥15 as follows: the sum of the number of pixels at each fluorescence intensity times that fluorescence intensity was divided by the total number of pixels with brightness ≥15. The mean value was calculated for four images of tissue stained with a particular antibody from each mouse (*n* = 4 to 8 mice per group).

The distribution of VEGFR-2 intensity values of individual tumor vessels was measured to determine whether the treatment-related decrease in mean vessel brightness was because of selective pruning of vessels with the highest VEGFR-2 expression. For this purpose, the peak VEGFR-2 fluorescence intensity of 10 sequentially selected vessels was measured using the Plot Profile function of ImageJ on each of the digital images just described for RIP-Tag2 tumors with or without AG013736 treatment for 7 days (four images per mouse, *n* = 4 mice per group).

Tumor Vascularity

An index of area density (proportion of sectional area) was measured in fluorescence microscopic digital images to quantify tumor vessel blood flow (lectin staining of perfused blood vessels), endothelial cells (CD31 immunoreactivity), pericytes (α-SMA immunoreactivity), and vascular basement membrane (type IV collagen immunoreactivity) in 80-μm-thick cryostat sections of RIP-Tag2 and LLC tumors with or without treatment. Blood vessel fluorescence was analyzed in images (×10 objective, ×1 Optovar, tissue region 960 × 1280 μm) captured from sections of four to five tumors (RIP-Tag2) or four regions of tumor (LLC) in each mouse. Based on fluorescence intensities ranging from 0 to 255, blood vessels were distinguished from background by empirically determining threshold values that included only blood vessels in specimens from vehicle-treated mice (intensity value 40 to 55 for RIP-Tag2 tumors and 35 for LLC tumors). The threshold was constant for all measurements of a given marker in each experiment. The area density of blood vessels stained with lectin, CD31, α-SMA, or type IV collagen was calculated as the proportion of pixels having a fluorescence intensity value equal to or greater than the corresponding threshold. An average value was calculated for all tumors or regions of tumor in each mouse (*n* = 4 mice per group). The values were not true area densities because of the section thickness. Indeed, they overestimated the true area density because measurements were made on two-dimensional projections of three-dimensional (80-μm thick) specimens. However, by including more tissue, thicker specimens expanded the range of possible values and the sensitivity of the measurements. All specimens were handled identically. Curve fitting using a second order polynomial equation with data from 1-μm- to 32-μm-thick projections made from 1-μm confocal optical sections obtained from 80-μm physical sections showed that an area density index of 57.7%, as measured above, corresponded to a true area density of 15.9%. Thus, blood vessels occupied ~16% of untreated RIP-Tag2 tumors.

Vascularity of Thyroid and Tongue

Blood vessel profiles were quantified in 0.5-μm-thick, toluidine blue-stained epoxy sections of thyroid and tongue with or without treatment on real-time color brightfield video images by using a Zeiss Axiophot microscope with a three-chip charge-coupled device color video camera (model DXC 755; Sony, Tokyo, Japan) interfaced to a real-time color video digitizing card (DVA-4000; Video-Logic, Cambridge, MA) in a Compaq computer

(Houston, TX). Measurements were made with a digitizing tablet (Digipad, model 1111A; GTCO, Rockville, MD) and image analysis software developed in our laboratory. Vascular density in sections of thyroid viewed with a ×20 objective (×1 Optovar) was expressed as number of capillary profiles per millimeter of follicle perimeter (10 thyroid follicles per mouse; $n = 3$ mice per group). Blood vessel profiles in sections of tongue viewed with a ×40 objective (×1 Optovar) were counted in regions measuring 22,337 μm^2, and vascular density was expressed as number of vessel profiles per 10^4 μm^2 of lingual muscle in each mouse ($n = 3$ mice per group).

Number of Endothelial Fenestrations

Fenestrations in endothelial cells of blood vessels in RIP-Tag2 and LLC tumors, thyroid, and tongue smooth muscle with or without treatment were counted on TEM images (total magnification ×17,640, 10 blood vessel profiles per mouse, $n = 3$ to 4 mice per group). Fenestrations were identified as 60- to 90-nm diaphragm-covered openings in endothelial cells.[40] Vessel perimeters were measured with a digitizing tablet on TEM images at ×4480 or ×5600. Values are expressed as mean number of endothelial fenestrations per 100 μm of vessel perimeter.

Estimate of Tumor Vessel Diameter

The effect on vessel diameter of 7-day treatment with AG013736 was measured on printed fluorescent images of RIP-Tag2 tumors stained for VEGFR-2 immunoreactivity (×20 objective, ×1 Optovar, tissue region 480 μm by 640 μm). Three horizontal lines were drawn across each image. The diameter of 10 blood vessels that intersected these lines was measured with the digitizing tablet (four images per mouse, $n = 4$ mice per group).

Estimate of Tumor Size

The effect of treatment on tumor size was assessed by treating 10-week-old RIP-Tag2 mice with AG013736 or vehicle as above for 21 days ($n = 4$ mice per group). After fixation by vascular perfusion with 1% PFA, the pancreas was frozen, and 80-μm-thick cryostat sections were stained for type IV collagen immunoreactivity. Digital fluorescence microscopic images of all tumors visible in any of four sections cut at different levels of each pancreas were captured (×5 objective, ×1 Optovar, tissue region 1920 μm by 2560 μm), and then the sectional area of each tumor (8 to 20 tumors per mouse) was measured with ImageJ. Tumors too large to fit into a single image were recorded as multiple images and the data combined. The volume of each tumor was calculated from the sectional area with the assumption the tumors were spherical.

Statistics

The significance of differences between groups was assessed using analysis of variance followed by the Bonferroni-Dunn or Fisher's test for multiple comparisons. Values are expressed as means ± SE. P values <0.05 were considered significant except where lower values were indicated in Bonferroni-Dunn tests.

Results

Treatment with VEGF-Trap or AG013736 caused multiple changes in the blood vessels of spontaneous RIP-Tag2 tumors and implanted LLC tumors. Changes in endothelial cells of tumor vessels were evident as soon as 24 hours after the onset of treatment, demonstrating the rapid onset of vascular actions of these drugs (Table 1). Both agents had anti-vascular effects in the tumors, with more than 50% of the vessels undergoing regression within 7 days (Table 1).

Loss of Vessel Patency and Blood Flow before Endothelial Cell Regression

L. esculentum lectin injected into the bloodstream binds rapidly and uniformly to the luminal surface of the vasculature, thus marking blood vessels that are patent and perfused.[8,11] In the simple vascular network of the trachea, lectin staining uniformly co-localized with CD31 immunoreactivity (Figure 1, A and D). After 2 days of treatment with AG013736, some CD31-positive vessels lacked lectin staining (Figure 1, B and E), and after a week or more reductions in both markers were evident, indicative of vessel loss (Figure 1, C and F). Similarly, in untreated RIP-Tag2 tumors most blood vessels had uniform lectin staining and CD31 immunoreactivity (Figure 2; A, C, and E), showing the vessels were patent, perfused, and lined by endothelial cells. However, after 1 day of treatment with AG013736, some CD31-positive vessels in RIP-Tag2 tumors lacked lectin staining (Figure 2; B, D, and F). The discrepancy between CD31 immunoreactivity and lectin staining involved 30% of the tumor vasculature at 1 day and 57% at 2 days but was minimal at 7 days (Figure 2G). Similar changes were found with VEGF-Trap (Figure 2H). The amount of lectin staining and CD31 immunoreactivity decreased by more than 70% during the first week, indicative of the extensive vessel loss (Figure 2, G and H). At that point, the amounts of lectin staining and CD31 immunoreactivity were again matched, showing that the nonperfused vessels had degenerated, and vessels that survived treatment were patent and perfused.

Reduction of Endothelial Sprouts and Fenestrations

Endothelial sprouts, appearing as cell protrusions tipped by filopodia, were abundant on blood vessels in untreated RIP-Tag2 tumors (Figure 3A) but were rare on tumor vessels after 7 days of treatment with AG013736 (Figure 3B). Most blood vessels of tumors in RIP-Tag2 mice have abundant endothelial fenestrations, as do capillaries of pancreatic islets from which the tumors

Table 1. Effect of VEGF/VEGFR Inhibitors on Endothelial Fenestrations and Vascular Density

	Control	AG013736		VEGF-Trap	
		1 day	7 days	1 day	7 days
RIP-Tag2 tumor					
Endothelial fenestrations	68.0 ± 21.3	5.0 ± 3.0* (−93%)	1.1 ± 0.5* (−98%)	9.1 ± 3.7* (−87%)	13.7 ± 5.3* (−80%)
Vascular density	55.7 ± 1.7	33.7 ± 2.1* (−39%)	11.7 ± 0.6* (−79%)	37.6 ± 2.0* (−32%)	15.4 ± 1.2* (−72%)
Lewis lung carcinoma					
Endothelial fenestrations	0	–	0	–	–
Vascular density	23.3 ± 2.3	–	11.3 ± 1.2* (−52%)	–	–
Thyroid gland					
Endothelial fenestrations	52.6 ± 3.3	–	6.2 ± 2.7* (−88%)	–	34.4 ± 3.0 (−35%)
Vascular density	42.5 ± 3.2	–	19.2 ± 1.6* (−55%)	–	45.4 ± 2.0 (+7%)
Tongue muscle					
Endothelial fenestrations	0	–	0	–	–
Vascular density	24.9 ± 1.9	–	26.9 ± 0.3 (+8%)	–	–

Comparison of endothelial fenestrations and vascular densities in mice with or without treatment. Fenestrations (number per 100 μm of vessel perimeter) were quantified on TEM images of 10 blood vessel profiles per mouse. Vascular densities in tumors (area density index expressed as percent of tumor area) were measured on 80-μm-thick sections stained for CD31 immunoreactivity by calculating proportion of pixels with fluorescence intensity greater than threshold (see Materials and Methods). Vascular densities in thyroid (number of capillaries/mm perimeter of follicles) and in tongue (number of vessels per 10^4 μm^2 of muscle) were measured on toluidine blue-stained epoxy sections 0.5 μm in thickness. Percent change in relation to corresponding control value shown in parentheses.
*Significantly different from control value ($P < 0.05$). Values are mean ± SE; n = 3 to 4 mice per group.
–, Not examined.

arise.[8,41] Because VEGF is known to induce fenestrations in endothelial cells[40] and targeted deletion of VEGF in pancreatic islets results in nonfenestrated vessels,[41] we asked whether inhibition of VEGFR signaling would reduce the number of fenestrations in tumor vessels. Surprisingly, the reduction was rapid and almost complete in RIP-Tag2 tumor vessels (Figure 3; C to F). Treatment with VEGF-Trap for only 24 hours reduced the number of endothelial fenestrations by 87% (Table 1). Treatment with AG013736 reduced fenestrations by 93% after 1 day and by 98% after 7 days (Figure 3, D and F, and Table 1).

Next we asked whether the presence of endothelial fenestrations was an indicator of vessel sensitivity to the anti-vascular effects of AG013736 and VEGF-Trap. Two approaches were used. First, we examined LLC tumor vessels, which had no endothelial fenestrations (Table 1). The number of blood vessels in LLC tumors was reduced by 52% after 7 days of treatment with AG013736 (Table 1). Although still an appreciable reduction in tumor vascularity, the change in LLC tumors was significantly less than the 79% reduction found in RIP-Tag2 tumors (Table 1). Second, we examined the response of normal blood vessels with or without endothelial fenestrations to VEGF-Trap or AG013736. In blood vessels of the thyroid, which are heavily fenestrated, VEGF-Trap reduced the number of fenestrations by 35% and produced no reduction in vascularity (Table 1). However, treatment with AG013736 for 7 days reduced the number of fenestrations by 88% and caused a 55% reduction in vascularity (Table 1). These changes were not accompanied by weight loss or other obvious evidence of impaired health (data not shown). By contrast, the vasculature of tongue musculature, which had no endothelial fenestrations, showed no reduction in vessel number after treatment with

AG013736 (Table 1). Together, the findings suggest that some blood vessels with endothelial fenestrations are dependent on VEGF signaling for survival, and the magnitude of reduction in fenestrations may predict the amount of blood vessel destruction produced by VEGF/VEGFR inhibitors.

Decreased Endothelial Cell VEGFR-2 and VEGFR-3 Immunofluorescence

Because inhibition of VEGF signaling can decrease VEGFR-2 expression in certain types of blood vessels,[31,37,42] we asked whether VEGF/VEGFR blockade decreased receptor expression in our tumor models. We reasoned that the intensity of endothelial cell immunofluorescence in digital images could provide a measure of protein expression in blood vessels, if the brightness of vessel-related pixels was distinguished from the number of vessel-related pixels.

Fluorescence intensity was analyzed in microscopic images of blood vessels in immunohistochemically stained sections of RIP-Tag2 tumors, LLC tumors, and normal pancreatic islets after treatment for 7 days with AG013736, VEGF-Trap, or their respective vehicles. Blood vessels in these tissues were immunoreactive for VEGFR-2, VEGFR-3, α_5 integrin, CD31, and CD105 in endothelial cells and PDGFR-β in pericytes.

Treatment of RIP-Tag2 mice with AG013736 for 7 days had two effects on tumor vessel immunofluorescence. First, the number of vessel-related pixels decreased with all endothelial cell markers, because of the 79% decrease in number of tumor vessels. Second, the brightness of fluorescence of certain markers decreased in the
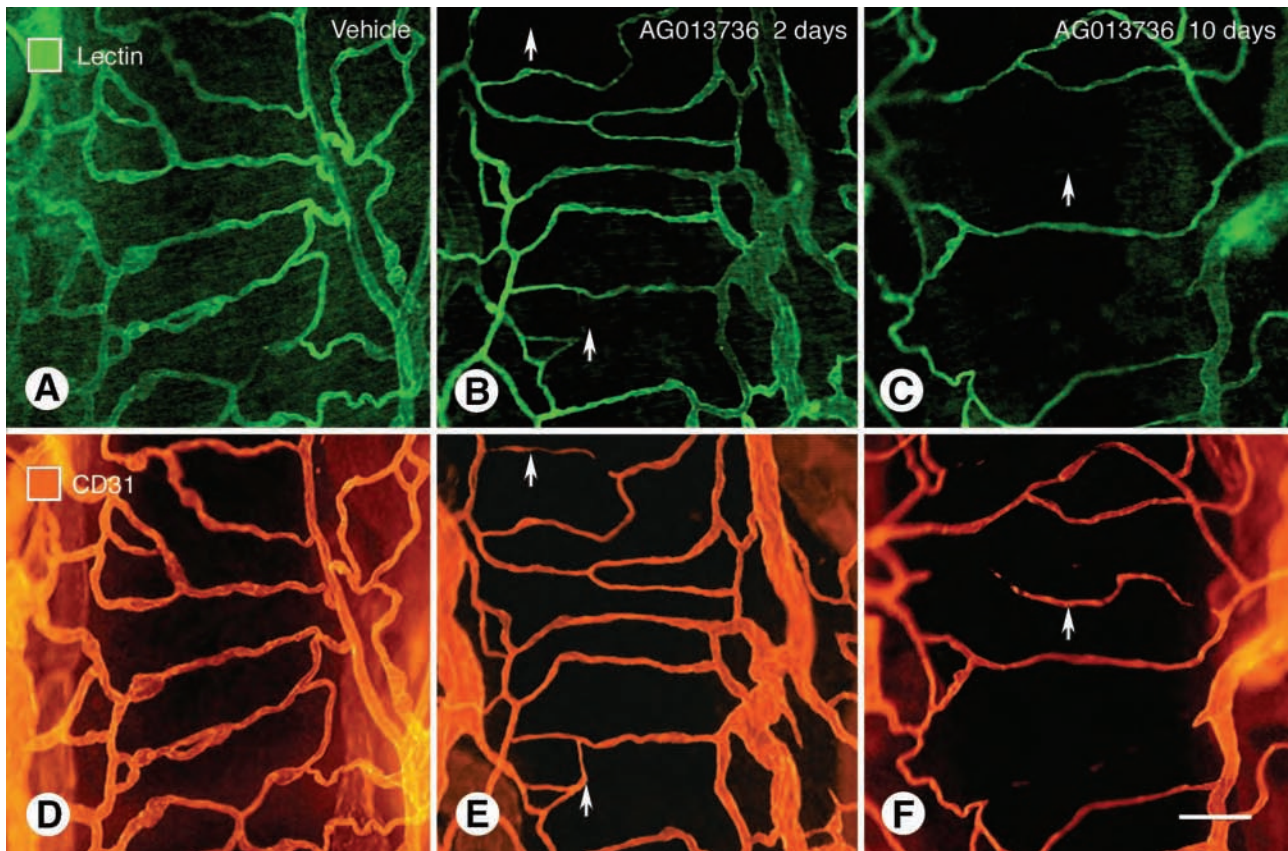
Figure 1. Loss of vessel patency in simple vascular network of trachea after inhibition of VEGF signaling. Fluorescence micrographs showing vasculature of mouse tracheas stained by intravenous injection of lectin (**A–C**) and same vessels stained for CD31 immunoreactivity (**D** and **E**). Three conditions are compared: **A** and **D**, normal state; **B** and **E**, after 2 days of treatment with AG013736; and **C** and **F**, after 10 days of treatment with AG013736. After 2 days of treatment the lectin stains fewer vessels than CD31 because vessel patency is lost and blood flow stops before the CD31 disappears as endothelial cells degenerate. At 10 days, fewer vessels are evident by either method. **Arrows** mark regions where the lectin staining and CD31 immunoreactivity do not match. Scale bar, 30 μm.

surviving vessels. VEGFR-2 immunofluorescence showed the largest change in brightness. Fluorescence microscopic images and surface plots of vessel fluorescence intensity showed conspicuous reductions in VEGFR-2 immunoreactivity in addition to the large decrease in vessel number (Figure 4; A to C). Tumors stained for CD105 immunoreactivity showed the same reduction in vessel number but no appreciable change in vessel brightness (Figure 4; D to F). Measurements confirmed that the reduction in brightness of VEGFR-2 immunofluorescence (−49%) was significant but that of CD105 immunofluorescence was not (−10%, Figure 4G).

To determine whether the decrease in VEGFR-2 immunofluorescence resulted from selective pruning of vessels with the highest receptor expression, thereby leaving vessels with low VEGFR-2 expression, we compared the range of fluorescence intensities of vessel populations in RIP-Tag2 tumors with or without treatment with AG013736. Because the treatment caused a 79% reduction in vascularity, leaving 21% of the vessels, we compared the dimmest 21% of vessels in untreated tumors to the mean brightness of the surviving vessels. Measurements of individual vessels showed that the fluorescence intensity of the 21% of vessels with least VEGFR-2 expression (intensity = 125 ± 3) in untreated tumors was significantly greater than the 21% of vessels still present

after treatment (intensity = 83 ± 4, n = 4 per group, P < 0.001). This finding suggests that the treatment not only reduced vessel number but also reduced vessel VEGFR-2 expression in RIP-Tag2 tumors. Further, the decrease in VEGFR-2 fluorescence appears to reflect a change in epitope density on individual vessels rather than reduced vessel caliber because there was no significant change in vessel size (mean diameter 9.7 μm after vehicle compared to 11.6 μm) after treatment with AG013736 for 7 days.

Other measurements showed that reductions in brightness of VEGFR-3 (−29%) and α_5-integrin (−21%) immunofluorescence were also significant (Figure 4G). However, changes in brightness of CD31 (−14%) and PDGFR-β (+5%) were not significant (Figure 4G). VEGF-Trap had a smaller effect in this assay, reducing brightness of VEGFR-2 immunofluorescence in RIP-Tag2 tumors by 18% (Figure 4H). Treatment of LLC tumors with AG013736 for 7 days caused a 52% decrease in vascularity but a much smaller decrease in brightness of VEGFR-2 immunofluorescence (−16%) than was found in RIP-Tag2 tumors (Figure 4; I to K).

Overall, the largest decrease in brightness of VEGFR-2 immunofluorescence in tumor vessels coincided with the largest reduction in vascularity (Table 1), suggesting that diminished immunofluorescence was indicative of robust
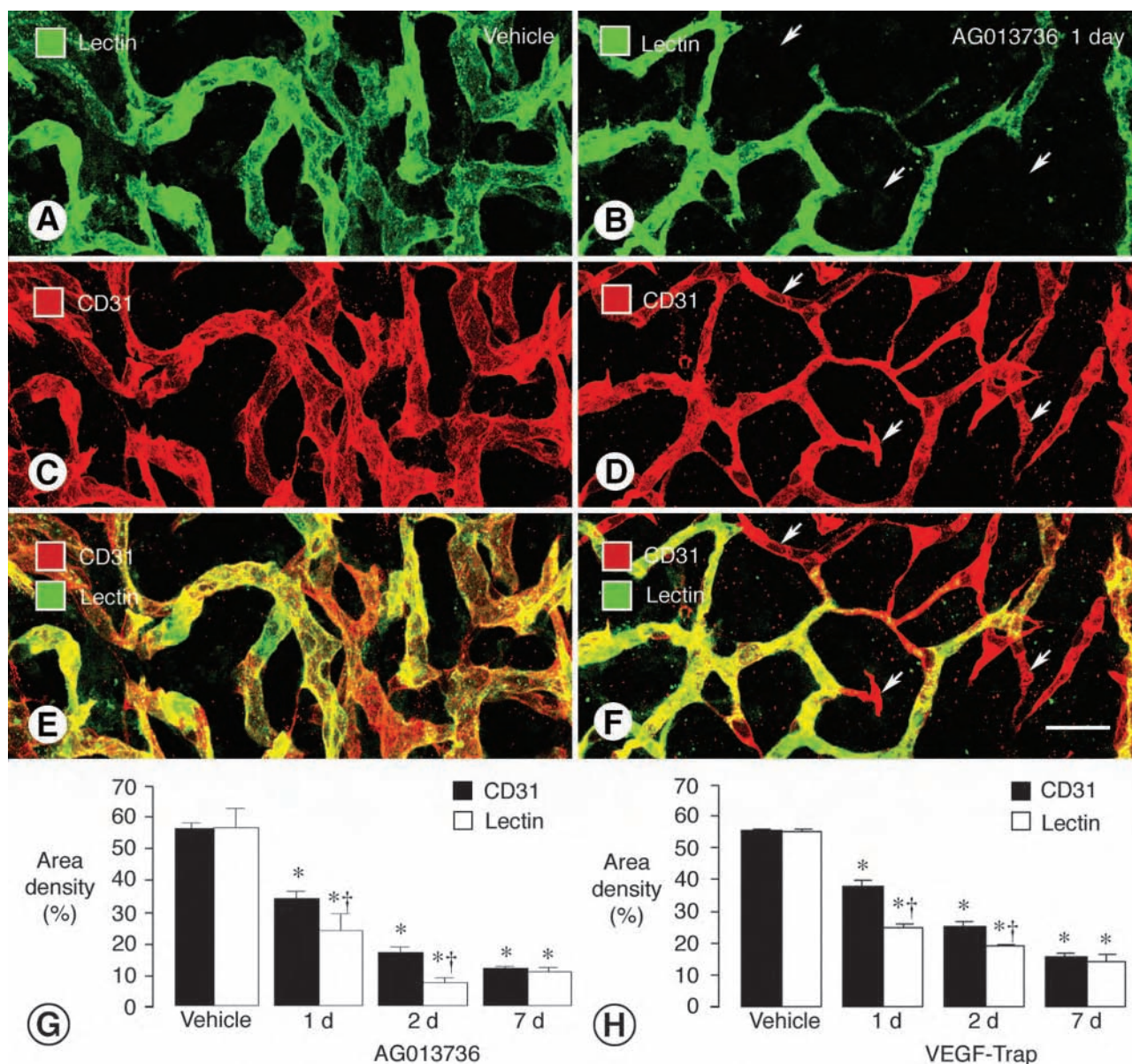
Figure 2. Reduction in tumor vessel patency and blood flow after inhibition of VEGF signaling. Confocal microscopic images of tumor vessels in RIP-Tag2 mice treated with vehicle (**A**, **C**, **E**) or AG013736 (**B**, **D**, **F**) for 1 day and injected with lectin before fixation by vascular perfusion. Lectin staining (**A**, green) of blood vessels in vehicle-treated tumor closely matches CD31 immunoreactivity (**C**, red). However, after treatment with AG013736, multiple vessels (**arrows**) lack lectin staining (**B**, green) but have CD31 immunoreactivity (**D**, red), indicating loss of vessel patency. Vessels without flow appear red in merged images (**E**, **F**). Bar graphs show area density (%) of lectin staining and CD31 immunoreactivity in vessels of RIP-Tag2 tumors after treatment for 1, 2, or 7 days with AG013736 (**G**) or VEGF-Trap (**H**) or their respective vehicle. After 1 or 2 days of treatment by either agent, the area density of lectin staining is significantly less than the amount of CD31 immunoreactivity. By 7 days, this discrepancy no longer exists, suggesting that the surviving vessels have blood flow. *, Different from vehicle ($P < 0.05$). †, Different from CD31 ($P < 0.05$). Scale bar, 25 μm.

action on tumor vessels. To the extent that brightness of fluorescence reflects amount of expression, vessels with the highest initial VEGFR-2 expression were most likely to be destroyed or transformed into vessels with lower VEGFR-2 expression.

Normalization of Pericytes on Tumor Vessels

Pericytes identified by α-SMA immunoreactivity are loosely associated with endothelial cells in RIP-Tag2 and LLC tumors.[11] Bizarre pericyte-endothelial cell relationships were particularly conspicuous in LLC tumors (Fig-

ure 5A). Similar abnormalities were present but less extreme in RIP-Tag2 tumors (Figure 5B).

α-SMA-positive pericytes underwent multiple changes after treatment with VEGF-Trap (data not shown) or AG013736 for 7 days (Figure 5, C and D). One population of pericytes became closely associated with surviving vessels in LLC tumors (Figure 5C) and RIP-Tag2 tumors (Figure 5D). These pericytes were more tightly apposed to endothelial cells than in untreated tumors (compare Figure 5, B and D). Unlike most pericytes in untreated tumors, some were oriented circumferentially around vessels (Figure 5E), resembling smooth muscle cells on
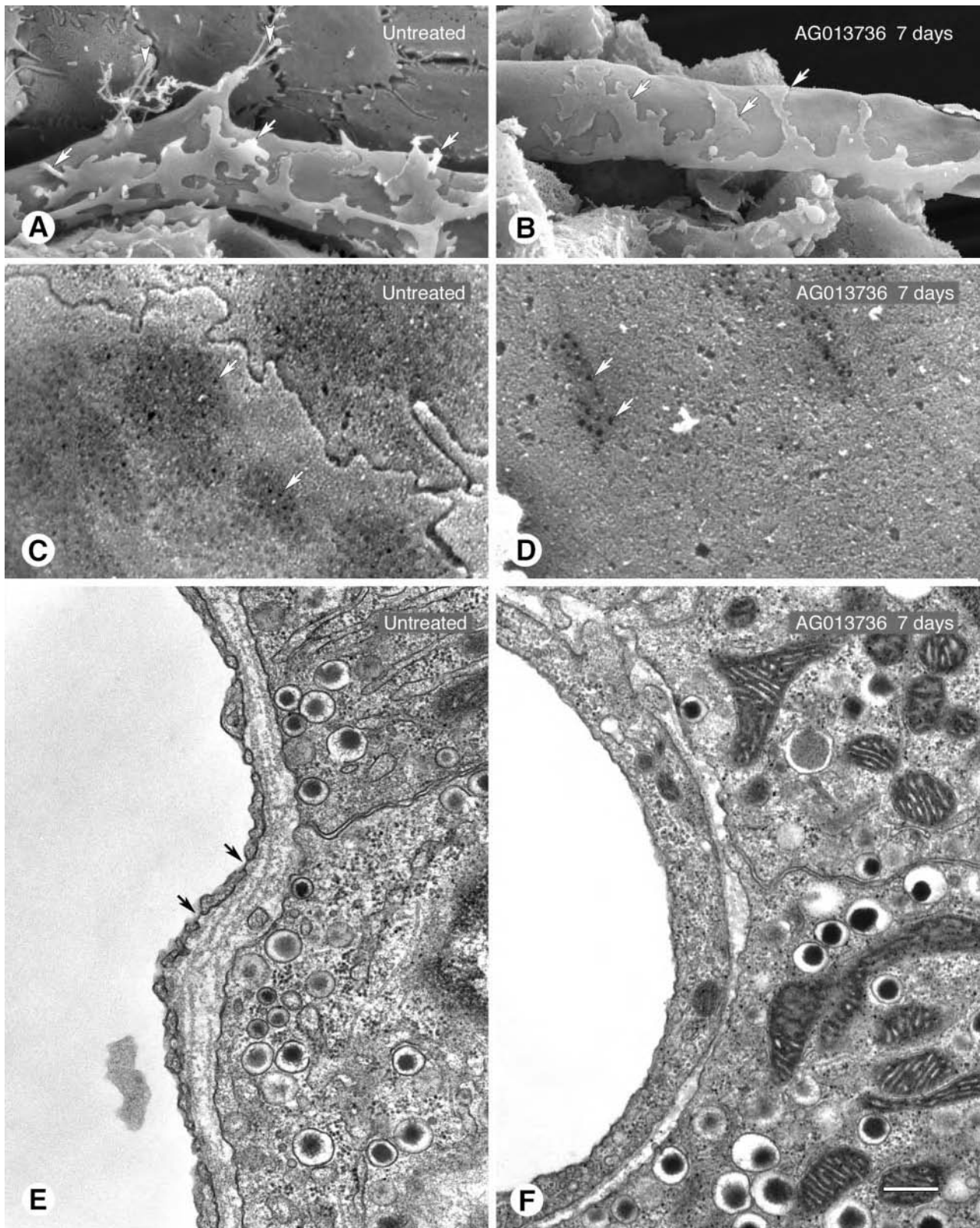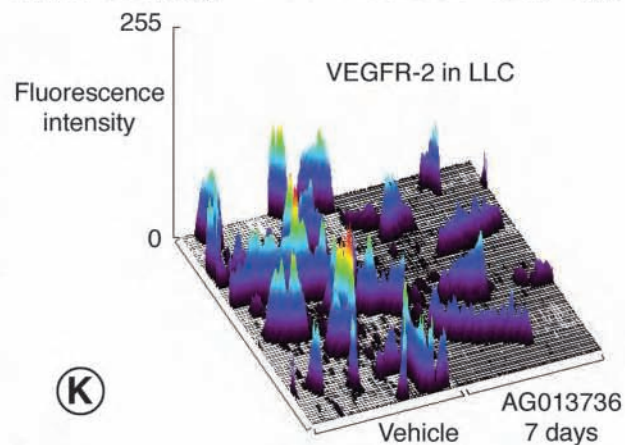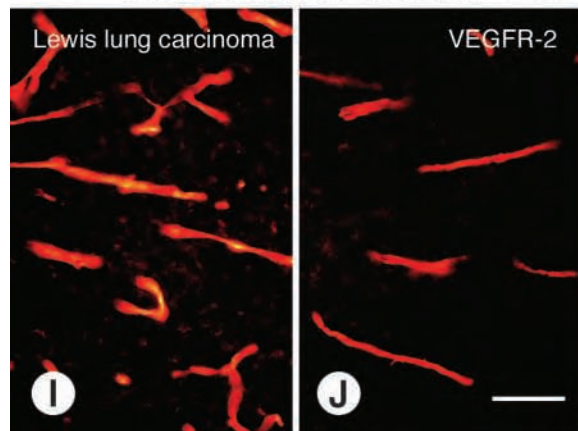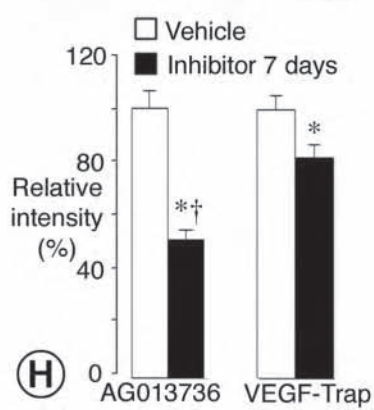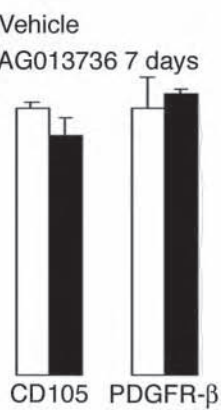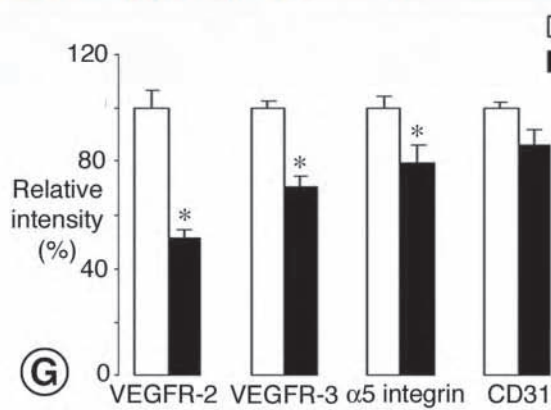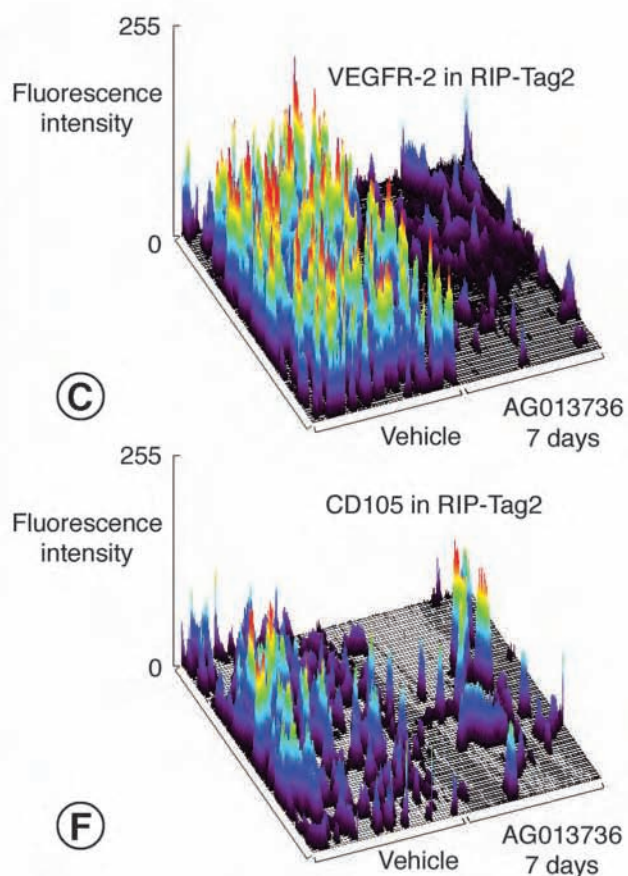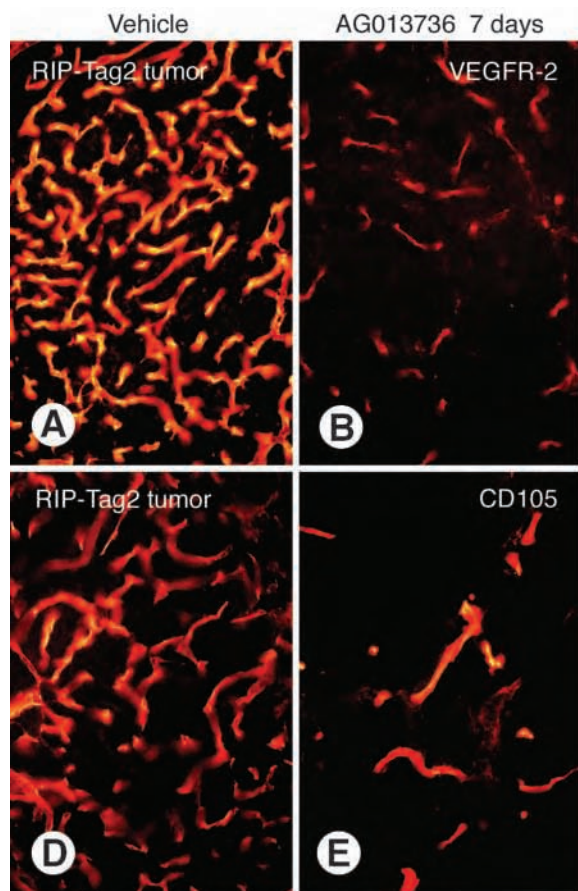
Figure 3. Reduction in endothelial sprouts and fenestrations in RIP-Tag2 tumors after inhibition of VEGF signaling. **A** and **B:** SEM of outer surface of tumor vessels showing endothelial sprouts (**arrowheads**) without treatment (**A**) but not after treatment with AG013736 for 7 days (**B**). Processes of pericytes are also visible (**arrows**), those without treatment being more loosely associated with the endothelium than after treatment. **C** and **D:** Higher magnification SEM showing much more abundant endothelial fenestrations (**arrows**) on abluminal surface of untreated tumor vessel (**C**) than after treatment (**D**, AG013736, 7 days). **E** and **F:** TEM showing abundance of endothelial fenestrations (**arrows**) in untreated tumor vessel (**E**) compared to none after treatment (**F**, AG013736, 1 day). In sections of tumor vessels examined by TEM, 63% and 83% had no fenestrations in the 1- and 7-day AG013736 groups, respectively, but only 7% had none without treatment. Scale bar: 5 μm (**A**, **B**); 1 μm (**C**, **D**); 0.5 μm (**E**, **F**).

Vehicle — **AG013736 7 days**

A. RIP-Tag2 tumor
B. VEGFR-2
C. Fluorescence intensity — VEGFR-2 in RIP-Tag2
D. RIP-Tag2 tumor
E. CD105
F. Fluorescence intensity — CD105 in RIP-Tag2
G. Relative intensity (%) — Vehicle / AG013736 7 days — VEGFR-2, VEGFR-3, α5 integrin, CD31, CD105, PDGFR-β
H. Relative intensity (%) — Vehicle / Inhibitor 7 days — AG013736, VEGF-Trap
I. Lewis lung carcinoma
J. VEGFR-2
K. Fluorescence intensity — VEGFR-2 in LLC

arterioles. Another population of α-SMA-positive cells had no apparent association with blood vessels (Figure 5; F and G). Many of these cells did not co-localize with the surviving CD31-positive blood vessels (Figure 5, F and G). As evidence of the greater impact of treatment on endothelial cells than pericytes, the reductions in CD31 immunoreactivity and lectin staining were more than double the reduction in α-SMA immunoreactivity (Figure 5H). Treatment with AG013736 for 7 days reduced staining of α-SMA-positive pericytes (-33%) to the same extent as type IV collagen in basement membrane (-32%) (Figure 5H). Despite their lack of vessel association, virtually all α-SMA-positive cells co-localized with type IV collagen (Figure 5I). Cells with PDGFR-β immunoreactivity had similar properties (data not shown).

Persistence of Vascular Basement Membrane after Blood Vessel Regression

The basement membrane of blood vessels that regress naturally during development may persist long after endothelial cells disappear.[43,44] We asked whether the same occurs in tumors after endothelial cell degeneration is triggered by angiogenesis inhibitors. Using CD31 and type IV collagen immunoreactivities as markers,[12] we compared the fates of endothelial cells and vascular basement membrane during blood vessel regression. Initially, the idea was tested in a simple system by comparing the distribution of the two markers in the simple, well-organized microvasculature of the mouse trachea. Under baseline conditions, type IV collagen staining consistently co-localized with CD31 staining of tracheal blood vessels (Figure 6A). However, after treatment with AG013736 for 7 days, distinct strands of type IV collagen unaccompanied by CD31 staining indicated the presence of empty sleeves of basement membrane (Figure 6B). These strands were in locations normally occupied by ~20% of capillaries. Strands were similarly numerous in tracheas treated with VEGF-Trap. Absence of lectin staining showed that the strands were not blood vessels without endothelial cells (data not shown).

As in the trachea, most CD31-positive blood vessels in untreated RIP-Tag2 tumors had type IV collagen immunoreactivity (Figure 6C), and the area densities of the two was essentially the same (56% *versus* 54%). By comparison, after treatment with AG013736 for 7 days, the conspicuous loss of CD31-positive vessels was not accompanied by a corresponding reduction in type IV collagen (Figure 6D). Numerous strands of type IV collagen, unaccompanied by CD31 immunoreactivity, interconnected the surviving blood vessels (Figure 6D). In LLC tumors,

some strands of type IV collagen were present in the absence of treatment (Figure 6E), but they were much more abundant after treatment with AG013736 (Figure 6F). Strands of type IV collagen that did not co-localize with CD31 resembled empty sleeves of basement membrane (Figure 6F).

After treatment of RIP-Tag2 tumors with AG013736 for 1, 2, or 7 days, CD31-positive staining decreased by 39%, 70%, and 79%, respectively, but type IV collagen staining decreased by only 11%, 10%, and 32% (Figure 6G). Once or twice daily treatment with AG013736 for 7 days had about the same effect on the tumor vasculature. Even after 21 days of once-daily treatment, there was still a large discrepancy between the reduction in CD31 (-68%) and the reduction in type IV collagen (-31%). The reduction in CD31-positive vessel density at 21 days tended to be less than at 7 days (Figure 6G), perhaps related to tumor shrinkage after longer treatment. However, the amount of type IV collagen was about the same as at 7 days, indicating persistence of vascular basement membrane for at least 21 days of treatment. Treatment of RIP-Tag2 tumors with VEGF-Trap for 1, 2, or 7 days resulted in qualitatively similar but quantitatively somewhat smaller reductions in type IV collagen and CD31 immunoreactivities (Figure 6H). Treatment of LLC tumors with AG013736 for 7 days reduced CD31 staining by 52% but decreased type IV collagen staining by only 3% (Figure 6I).

Treatment-Induced Decrease in Tumor Size

Treatment of RIP-Tag2 mice with AG013736 for 21 days resulted in a significant decrease in mean tumor size. In the AG013736-treated group, tumor sectional areas were reduced 54% (0.72 ± 0.12 *versus* 1.55 ± 0.29 mm^2) and corresponding calculated volumes were reduced 70% (0.65 ± 0.15 *versus* 2.20 ± 0.57 mm^3) in comparison to vehicle-treated mice.

Discussion

The goal of this study was to identify cellular changes in tumor vessels that reflect the action of VEGF/VEGFR inhibitors and show which vessels depend on VEGF signaling for survival. We used two inhibitors, AG013736 and VEGF-Trap, that block VEGF signaling by different mechanisms. The approach was to characterize changes in endothelial cells, pericytes, and basement membrane of blood vessels in mouse models of spontaneous and implanted tumors, with a focus on the first week of treat-

Figure 4. Reduction in brightness of receptor immunofluorescence and decrease in vessel number after inhibition of VEGF signaling. Fluorescence micrographs comparing high VEGFR-2 immunoreactivity and high vessel density in vehicle-treated RIP-Tag2 tumor (**A**) with low VEGFR-2 immunoreactivity and low vessel density after AG013736 treatment for 7 days (**B**). Reduced brightness of VEGFR-2 immunoreactivity is illustrated by lower peaks in the surface plot of fluorescence intensity (**C**). Reduced vessel number is indicated by fewer peaks (**C**). By contrast, after staining for CD105 immunoreactivity, vessel brightness is not reduced by the treatment, but vessel number is clearly reduced (**D–F**). Consistent with molecule-specific changes in expression levels indicated by brightness of fluorescence, intensity measurements show significant reductions in VEGFR-2, VEGFR-3, and α_5-integrin immunoreactivities of RIP-Tag2 tumor vessels after treatment with AG013736 for 7 days but little or no reduction in CD105, CD31, or PDGFR-β (**G**, values for vehicle normalized to 100%). VEGF-Trap for 7 days also reduced brightness of VEGFR-2 immunofluorescence in RIP-Tag2 tumor vessels, but the change was smaller (**H**, values for vehicle normalized to 100%). AG013736 had a smaller effect (-16%) on brightness of VEGFR-2 immunofluorescence in LLCs than found in RIP-Tag2 tumors, both in fluorescence micrographs (**I, J**) and surface plot (**K**). *, Different from corresponding vehicle ($P < 0.05$). †, Different from VEGF-Trap ($P < 0.05$). Scale bar, 80 μm.
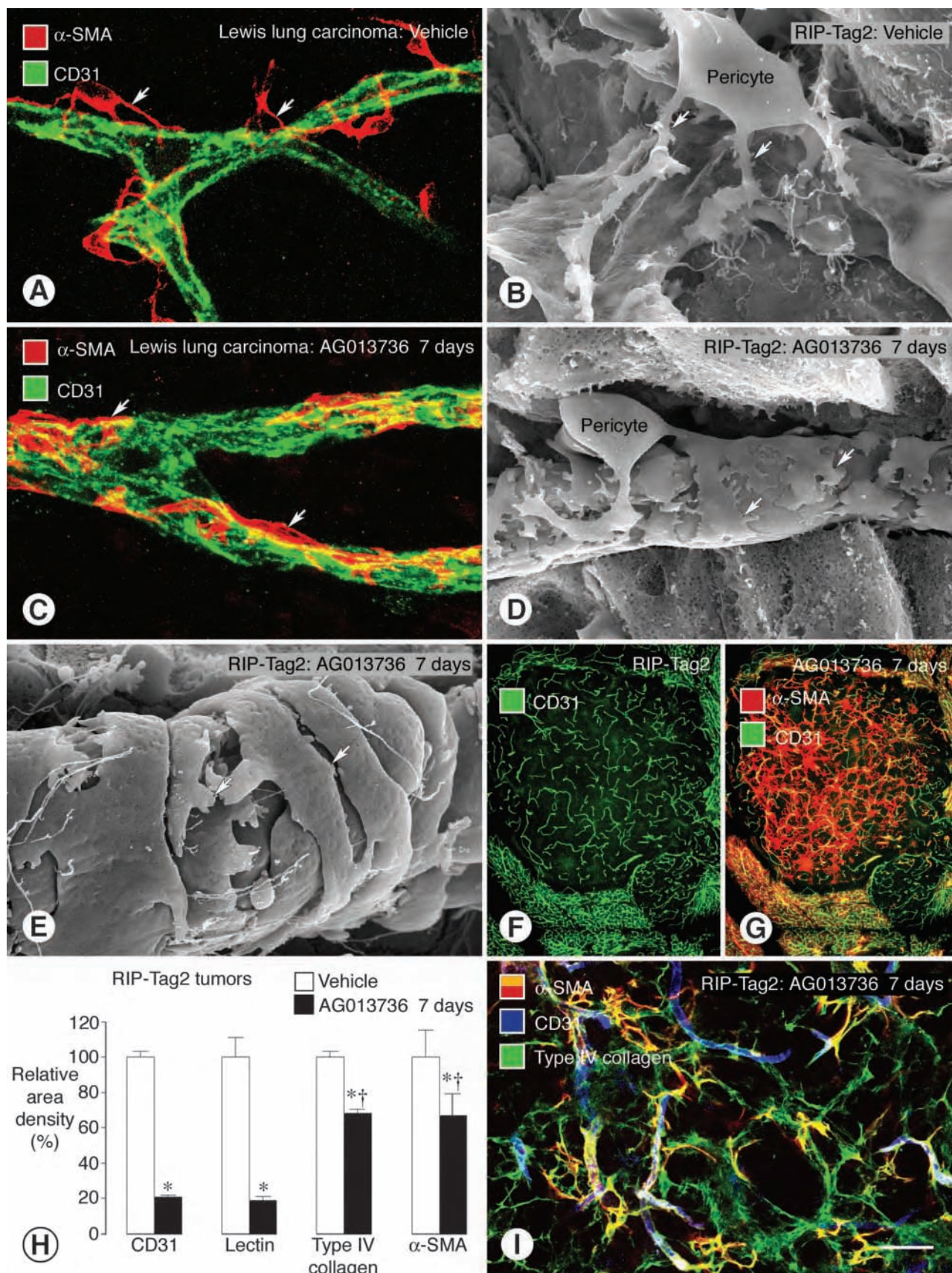
ment. Among the most conspicuous changes in tumor vessels were early loss of patency and blood flow, almost total disappearance of endothelial fenestrations and sprouts, eventual loss of endothelial cells, and appearance of empty sleeves of blood vessel-derived basement membrane. In RIP-Tag2 tumors, the ~20 to 30% of vessels that survived treatment for 7 days were distinctly different from those present at the outset. Surviving vessels had a superficially normal appearance and were accompanied by pericytes with a normalized phenotype, but the vessels lacked endothelial fenestrations typical of normal islet vessels and had reduced expression of VEGFR-2 and VEGFR-3. These features not only give insight into the process of blood vessel regression but also reflect the potent anti-vascular activity of VEGF/VEGFR inhibitors.

Loss of Vessel Patency and Blood Flow

Cessation of blood flow in selected blood vessels was an early sign of drug action in RIP-Tag2 tumors. The affected vessels were not stained by lectin in the bloodstream but did have CD31 immunoreactivity. Such vessels were rare before treatment, were abundant at 1 day, peaked at 2 days, and largely disappeared by 7 days. At the final time point, there was minimal mismatch between lectin staining and CD31 immunoreactivity despite the marked reduction in overall number of vessels. These results suggest that vessel closure precedes endothelial cell regression. Although the sequence of events during the first 24 hours still need to be determined, the results thus far are consistent with findings made in the developmentally transient capillary network in the papillary membrane of the eye, which regresses by synchronous apoptosis of endothelial cells after blood flow ceases.[45] The wave of apoptosis after cessation of flow may be mediated by VEGF deprivation.[46] VEGF/VEGFR inhibition can reduce tumor vessel diameter to the point where blood flow stops.[28] Cessation of flow would eliminate the shear stress that plays a role in endothelial cell survival.[47] Methods that detect changes in blood flow may prove useful in assessing early evidence of VEGF/VEGFR inhibition, but the effects would be restricted to responsive vessels, and overall tumor blood flow may not reflect the magnitude of changes in individual vessels.[32]

Loss of Endothelial Cell Fenestrations

Both VEGF-Trap and AG013736 sharply reduced endothelial fenestrations in blood vessels of RIP-Tag2 tumors within 24 hours and nearly eliminated them by 7 days. Considering that VEGF-Trap has selectivity for VEGF,[21]
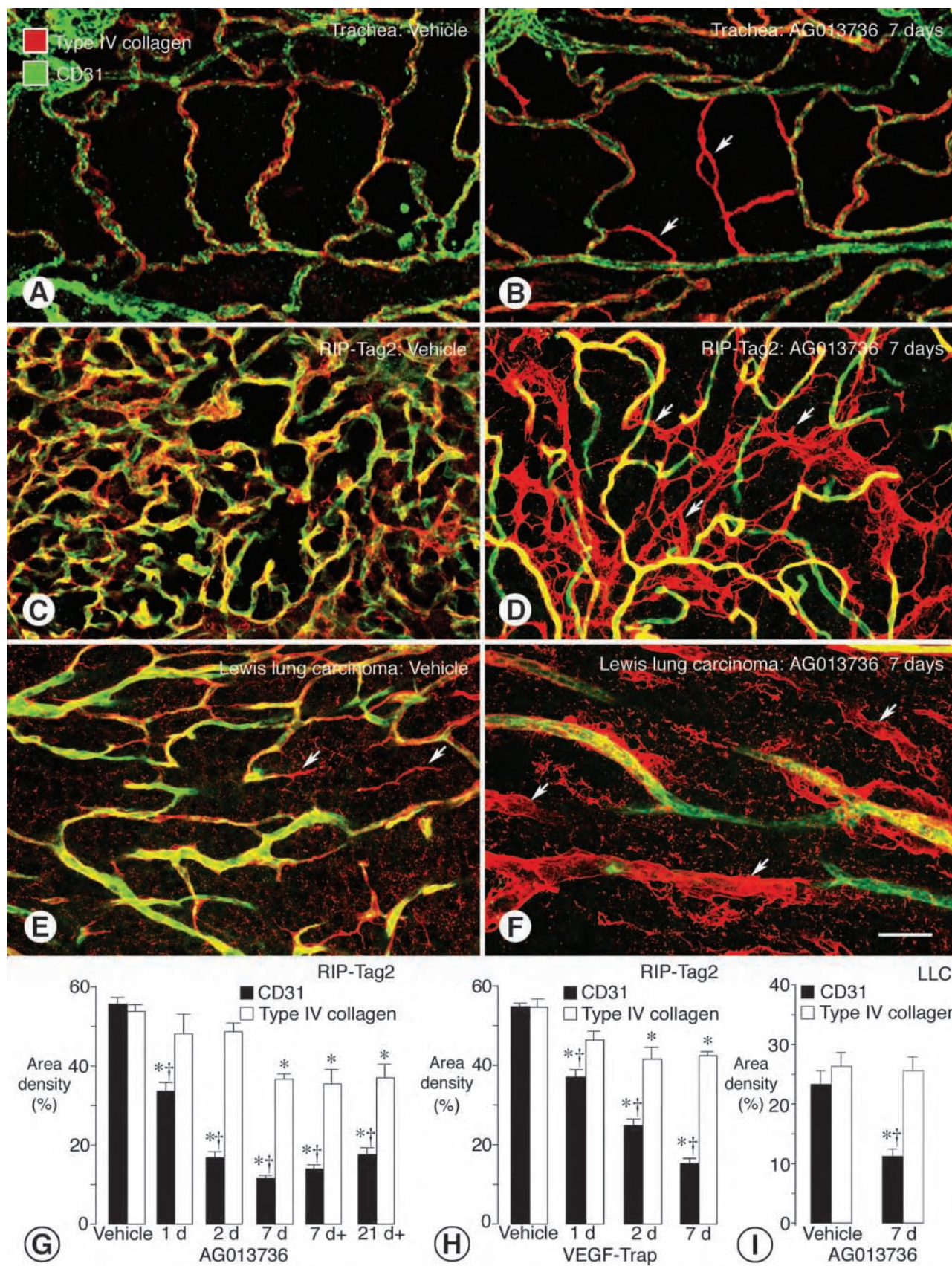
the similarity of the effect of the two agents suggests that the loss of fenestrations results from inhibition of a key action of VEGF on endothelial cells. Although AG013736 acts on multiple receptors, it is more potent for VEGFR than for PDGFR-β,[35] and the dose used in these studies was chosen to produce plasma concentrations in mice that favor greater inhibition of VEGFR signaling than PDGFR-β signaling (unpublished observations). These findings emphasize that endothelial fenestrations in tumor vessels are not only VEGF-dependent but also dynamic in nature. Topical application of VEGF can induce endothelial fenestrations within 10 minutes in normally nonfenestrated blood vessels of muscle.[40] The dynamic nature of endothelial fenestrations in tumor vessels makes these structures potentially useful as a biomarker for assessing the activity of VEGF/VEGFR inhibitors.

The magnitude of the reduction in fenestrations was consistent with extent of vessel loss, both in RIP-Tag2 tumors and normal thyroid. It is unclear whether differences in the magnitude of the effects of the two inhibitors on thyroid vessels reflect differences in local concentration, target specificity, or pharmacokinetics. As VEGF is a known survival factor for some blood vessels[18] and an inducer of fenestrations,[40] abundant endothelial fenestrations in tumor vessels may be a sign of exceptional susceptibility to VEGF/VEGFR inhibition. A link between endothelial fenestrations and sensitivity to VEGF/VEGFR inhibitors could be useful in identifying tumors that are likely to respond favorably to these agents. Yet presence of endothelial fenestrations is not the only criterion governing susceptibility because more than half of the nonfenestrated vessels in LLC tumors were destroyed by AG013736.

Reduced VEGFR-2 and VEGFR-3 Immunofluorescence

Treatment with AG013736 for 7 days reduced by half the intensity of VEGFR-2 immunofluorescence in blood vessels of RIP-Tag2 tumors but caused a smaller reduction in LLC tumors. VEGF-Trap had a similar but smaller effect on RIP-Tag2 tumors. These changes were superimposed on the large reduction in vessel number. Our experiments addressed the question of whether the intensity of immunofluorescence provides a meaningful index of expression of VEGFR-2, VEGFR-3, and other endothelial cell proteins. We reasoned that changes in receptor immunoreactivity might reflect treatment-induced changes in expression. Our results are consistent with evidence from *in situ* hybridization and immunofluorescence histochemistry showing that inhibition of VEGF signaling downregulates VEGFR-2 expression in tumor vessels and cer-

Figure 5. Tightening of pericytes on tumor vessels after inhibition of VEGF signaling. Confocal microscopic and SEM images show changes in pericyte-endothelial cell relationships (**arrows**) in tumor vessels. In vessels of LLC, α-SMA immunoreactive pericytes (**A**, red) are loosely attached to CD31-positive endothelial cells (green). A similar loose association of pericytes to endothelial cells is also evident by SEM in RIP-Tag2 tumor vessels (**B**). By comparison, after treatment with AG013736 for 7 days, α-SMA-positive pericytes are tighter on endothelial cells imaged by immunofluorescence (**C**) or SEM (**D**). Pericytes on some treated vessels acquire a smooth muscle-like phenotype (**E**). RIP-Tag2 tumor vessels still present after AG013736 for 7 days (**F**) are accompanied by a disproportionately large number of α-SMA-positive cells, many of which are not associated with blood vessels (**G**). After treatment with AG013736, reductions in α-SMA and type IV collagen immunoreactivities are about the same but are much less than corresponding reductions in CD31 and lectin (**H**, values for vehicle normalized to 100%). After the ~80% reduction in RIP-Tag2 tumor vessels treated with AG013736 for 7 days, most α-SMA-positive cells are still covered by type IV collagen basement membrane (**I**). *, Different from corresponding vehicle ($P < 0.05$). †, Different from CD31. Scale bar: 20 μm (**A, C**); 5 μm (**B, D**); 500 μm (**F, G**); 50 μm (**I**).

Type IV collagen
CD31

Trachea: Vehicle

Trachea: AG013736 7 days

RIP-Tag2: Vehicle

RIP-Tag2: AG013736 7 days

Lewis lung carcinoma: Vehicle

Lewis lung carcinoma: AG013736 7 days

RIP-Tag2

RIP-Tag2

LLC

tain normal capillaries.[31,37,42] Therefore, it may be feasible to monitor the action of VEGF/VEGFR inhibitors by following changes in receptor expression. These findings warrant further study of how angiogenesis inhibitors affect expression of their molecular targets.

Change in Pericyte Phenotype

Pericytes are present on >97% of blood vessels in the tumor models we studied, but they have multiple abnormalities including a loose association with endothelial cells.[11] Defective recruitment of pericytes to tumor vessels may result from disturbances in endothelial cell signaling. Blood vessels in mice deficient in PDGF-B or PDGFR-β do not recruit pericytes and have abnormalities reminiscent of those of tumor vessels.[10,48] Treatment with AG013736 or VEGF-Trap normalized the phenotype of some pericytes, as manifested by a tighter association with endothelial cells of surviving vessels. This change is consistent with previous reports of the normalization of tumor vessels by VEGF/VEGFR inhibition.[32,33] Because this change in pericyte phenotype was found not only with AG013736 but also with ligand-specific VEGF-Trap, it is likely to result from inhibition of VEGF signaling. Receptor tyrosine kinase inhibitors that target PDGFRs reportedly produce pericyte loosening[33] or detachment[36,49] from endothelial cells of tumor vessels, arguing against a direct role of PDGFR inhibition in the changes we observed.

Blood vessels in some tumors are reportedly susceptible to VEGF deprivation because they are immature as indicated by lack of pericytes.[50] This implies that VEGF/VEGFR inhibitors should eliminate pericyte-free vessels and leave ones with pericytes. However, this did not occur. Treatment with AG013736 or VEGF-Trap eliminated more than half of the vessels in RIP-Tag2 and LLC tumors despite the presence of pericytes.[11] SU5416 has a similar effect in RIP-Tag2 tumors.[36,51] VEGF-Trap eliminates most vessels, including those with pericytes, in intrarenal Wilms' tumors in mice.[31] These observations indicate that disruption of endothelial cell function by antagonism of VEGF signaling leads to altered pericyte function, consistent with the interdependency of endothelial cells and pericytes in angiogenesis.[52] They also suggest that functional abnormalities rather than absence of pericytes may contribute to susceptibility of tumor vessels to VEGF/VEGFR inhibition.

Blood vessels still present in RIP-Tag2 tumors after a 7-day treatment differed from those in untreated tumors and from those in normal pancreatic islets. Unlike their untreated counterparts, tumor vessels surviving treatment had almost no endothelial fenestrations and reduced expression of VEGFR-2 and VEGFR-3. Therefore, any normalization induced by treatment did not include reversion of vessels to their original phenotype. We cannot exclude that some of the remaining vessels always had these features and were revealed by pruning away the susceptible ones. But the new phenotype was more likely created by transformation of vessels during treatment, as evidenced by the disappearance of endothelial fenestrations within 24 hours, well before most of the responsive vessels degenerated, and reduction of VEGFR-2 expression to levels not normally found. In any case, the treatment created tumor vessels with a distinct phenotype. The appearance of such vessels in tumors is an indicator of response to VEGF/VEGFR inhibition and evidence of a type of vessel that may be resistant to this treatment.

After treatment with AG013736 or VEGF-Trap, fewer pericytes regressed than endothelial cells. Many surviving α-SMA-positive cells were not associated with tumor vessels, presumably because their endothelial cells had degenerated, but curiously, most were still enveloped by basement membrane. This feature favors the identification of these cells as pericytes instead of myofibroblasts. The similarly small reductions in pericytes and basement membrane raise the possibility that surviving pericytes contribute to the persistence of the vascular basement membrane after endothelial cells degenerate. This possibility suggests that targeting pericytes and/or vascular basement membrane concurrently with endothelial cells may augment the destruction of tumor vessels. The complementary effects of inhibiting VEGFR and PDGFR signaling are consistent with this idea.[33,36]

Vessel-Like Remnants of Basement Membrane

Our experiments showed that treatment with AG013736 or VEGF-Trap destroyed many blood vessels in RIP-Tag2 and LLC tumors, but the vascular basement membrane, reflected by type IV collagen immunoreactivity, persisted after endothelial cells regressed. These findings are consistent with observations in several other experimental models of vascular regression. The tunica vasculosa lentis, which is part of the hyaloid vasculature of the developing eye, regresses after birth. Regression of the cellular components of the blood vessels leaves sleeves of basement membrane designated intercapillary strands,[44] which appear identical to those we observed in tumors. Similarly, models of injury have shown that the basement membrane of capillaries as well as that of peripheral nerves, skeletal muscle fibers, and renal tu-

Figure 6. Persistence of vascular basement membrane after endothelial cells degenerate. Confocal micrographs show co-localization of CD31 immunoreactivity (green) and type IV collagen immunoreactivity (red) on simple vasculature of normal adult mouse trachea (**A**). After treatment with AG013736 for 7 days, sleeves of type IV collagen immunoreactivity devoid of CD31 immunoreactive endothelial cells are present among blood vessels of the tracheal mucosa (**B**, **arrows**). Similarly, in vehicle-treated RIP-Tag2 tumors, CD31 and type IV collagen immunoreactivities co-localize on most vessels (**C**), but after treatment with AG013736 for 7 days, empty sleeves of type IV collagen immunoreactivity are abundant (**D**, **arrows**). In LLC, some type IV collagen sleeves are present without treatment (**E**, **arrows**) but are much more numerous after treatment (**F**, **arrows**). Measurements show that area densities of CD31 and type IV collagen immunoreactivities were about the same in vehicle-treated RIP-Tag2 tumors, but after treatment with AG013736 for 1 to 21 days (d, twice daily; d+, once daily), CD31 immunoreactivity decreased much more than type IV collagen (**G**). This difference was detectable even at 1 day. A similar discrepancy was found after treatment with VEGF-Trap (**H**). In LLC, type IV collagen immunoreactivity remained essentially unchanged after treatment with AG013736 for 7 days despite the 52% reduction in CD31 staining (**I**). *, Different from corresponding vehicle (*P* < 0.05). †, Different from type IV collagen. Scale bar: 30 μm (**A**, **B**); 50 μm (**C–F**).

bules can persist after the parenchymal elements disappear.[43] Blood vessels in tumors and in patients with diabetes mellitus have multiple layers of basement membrane, suggesting that there are recurrent cycles of vascular degeneration and regeneration in chronic conditions.[12,43] In the systems we examined, the vascular basement membrane persisted for at least 10 days in the tracheal model and 21 days in RIP-Tag2 tumors. Together, these results suggest that basement membrane ghosts are a historical record of previously existing blood vessels. Thus, unlike loss of endothelial fenestrations that may be VEGF-dependent, the appearance of basement membrane sleeves may be a manifestation of blood vessel regression regardless of the mechanism.

The persistence of the vascular basement membrane after tumor vessels degenerate warrants careful consideration from a cancer therapeutic perspective because empty sleeves of basement membrane may provide a scaffold for vascular regrowth in tumors after cessation of treatment. Injury to a skeletal muscle can create capillaries with two layers of basement membrane, an outer layer formed before the injury and an inner layer formed after the injury,[43] suggesting that regenerating endothelial cells use the original outer basement membrane as a scaffold for angiogenesis and form a new inner basement membrane during regrowth. Vessels in RIP-Tag2 tumors appear to regrow along basement membrane strands after treatment is stopped (unpublished observations). The process resembles axonal regeneration in peripheral nerves. Moreover, because the longer isoforms of VEGF have a heparin-binding domain,[53] heparan sulfate proteoglycans in the vascular basement membrane may serve as a reservoir of VEGF. For these reasons it may be necessary to consider strategies for targeting basement membrane strands after endothelial cells have been destroyed by VEGF/VEGFR inhibitors.

Functional Significance of VEGF Dependence of Blood Vessels

A key question is whether the observed effects of AG013736 and VEGF-Trap on tumor vessels translate into therapeutic benefit. Both agents were selected because they are potent inhibitors of VEGF signaling and have documented efficacy in preclinical tumor models.[21,27,31,35] Although the main focus of the present studies was to analyze direct effects on tumor vessels during the first week, prolongation of treatment to 3 weeks was indeed accompanied by significant reduction in tumor mass. Further studies are needed to evaluate in depth the relationship between vascular changes and anti-tumor efficacy. Additional studies are also necessary to determine whether changes in tumor vessels similar to those we observed are produced by agents that inhibit angiogenesis through mechanisms unrelated to VEGF signaling.

Another important question raised by these studies is the functional significance of VEGF dependence of some normal capillaries in adult animals. A more complete understanding will require further studies, but previous experiments have shown that ~20% of normal capillaries

of the mouse trachea regress after VEGF/VEGFR inhibition and thus appear to depend on VEGF for survival.[37] This dependence is age-related but still present in 16-week-old mice.[37] The present studies revealed VEGF dependence of an even larger proportion (~50%) of normal thyroid capillaries in adult mice. In both the trachea and thyroid, all of the susceptible vessels were capillaries. In neither case was the loss of capillaries accompanied by weight loss or other evidence of impaired health,[37] but further investigations are warranted, including studies of the dose-response characteristics of normal vessels and tumor vessels to inhibitors of VEGF signaling.

Finally, it will be important to determine whether the presence of endothelial fenestrations in capillaries is a clue to unusual sensitivity to VEGF/VEGFR inhibition. If so, tumors with fenestrated blood vessels, such as those arising in endocrine glands or the gastrointestinal tract, may be particularly sensitive to VEGF/VEGFR inhibition. Novel surrogate markers of vessels with endothelial fenestrations may help to rationalize therapy by predicting which tumors are likely to respond to inhibitors of VEGF signaling.

Conclusions

These studies of cellular changes produced in blood vessels of two mouse tumor models by AG013736 and VEGF-Trap show that these inhibitors of VEGF signaling do much more than block growth of new tumor vessels. The agents had multiple effects that may prove useful in understanding the dependence of tumor vessels on VEGF for survival, the process of blood vessel regression, and the action of angiogenesis inhibitors. Within the first 24 hours, patency was lost and flow ceased in some tumor vessels. Most endothelial fenestrations and sprouts disappeared. Responsive vessels, representing as much as 80% of the tumor vasculature, were eliminated throughout the first week. Surviving vessels had a different phenotype, with no fenestrations and reduced VEGFR-2 and VEGFR-3 expression. Tumor vessels lacking fenestrations were less responsive to the inhibitors. Additional studies will be needed to determine whether all tumor vessels with endothelial fenestrations are dependent on VEGF for survival, but our findings suggest that this phenotype of tumor vessel is exceptionally responsive to VEGF/VEGFR inhibition. Endothelial cell regression occurred despite the presence of pericytes and was not accompanied by simultaneous loss of vascular basement membrane. Sleeves of type IV collagen remained as telltale markers of destroyed vessels. Because basement membrane remnants may serve as a scaffold for tumor revascularization, they provide another potential therapeutic target. These results will hopefully lead to a better understanding of the action of VEGF/VEGFR inhibitors on tumor vessels and stimulate the development of innovative ways to assess their *in vivo* action and predict which tumors will be most responsive.

References

1. Hlatky L, Hahnfeldt P, Folkman J: Clinical application of antiangiogenic therapy: microvessel density, what it does and doesn't tell us. J Natl Cancer Inst 2002, 94:883–893

2. Herbst RS, Mullani NA, Davis DW, Hess KR, McConkey DJ, Charnsangavej C, O'Reilly MS, Kim HW, Baker C, Roach J, Ellis LM, Rashid A, Pluda J, Bucana C, Madden TL, Tran HT, Abbruzzese JL: Development of biologic markers of response and assessment of antiangiogenic activity in a clinical trial of human recombinant endostatin. J Clin Oncol 2002, 20:3804–3814

3. Ellis LM: Antiangiogenic therapy: more promise and, yet again, more questions. J Clin Oncol 2003, 21:3897–3899

4. McCarthy M: Antiangiogenesis drug promising for metastatic colorectal cancer. Lancet 2003, 361:1959

5. Yang JC, Haworth L, Sherry RM, Hwu P, Schwartzentruber DJ, Topalian SL, Steinberg SM, Chen HX, Rosenberg SA: A randomized trial of bevacizumab, an anti-vascular endothelial growth factor antibody, for metastatic renal cancer. N Engl J Med 2003, 349:427–434

6. Weidner N: Intratumor microvessel density as a prognostic factor in cancer. Am J Pathol 1995, 147:9–19

7. St. Croix B, Rago C, Velculescu V, Traverso G, Romans KE, Montgomery E, Lal A, Riggins GJ, Lengauer C, Vogelstein B, Kinzler KW: Genes expressed in human tumor endothelium. Science 2000, 289:1197–1202

8. Hashizume H, Baluk P, Morikawa S, McLean JW, Thurston G, Roberge S, Jain RK, McDonald DM: Openings between defective endothelial cells explain tumor vessel leakiness. Am J Pathol 2000, 156:1363–1380

9. McDonald DM, Foss AJ: Endothelial cells of tumor vessels: abnormal but not absent. Cancer Metastasis Rev 2000, 19:109–120

10. Abramsson A, Berlin O, Papayan H, Paulin D, Shani M, Betsholtz C: Analysis of mural cell recruitment to tumor vessels. Circulation 2002, 105:112–117

11. Morikawa S, Baluk P, Kaidoh T, Haskell A, Jain RK, McDonald DM: Abnormalities in pericytes on blood vessels and endothelial sprouts in tumors. Am J Pathol 2002, 160:985–1000

12. Baluk P, Morikawa S, Haskell A, Mancuso M, McDonald DM: Abnormalities of basement membrane on blood vessels and endothelial sprouts in tumors. Am J Pathol 2003, 163:1801–1815

13. Ferrara N: Role of vascular endothelial growth factor in physiologic and pathologic angiogenesis: therapeutic implications. Semin Oncol 2002, 29:10–14

14. Ferrara N, Gerber HP, LeCouter J: The biology of VEGF and its receptors. Nat Med 2003, 9:669–676

15. Kim KJ, Li B, Winer J, Armanini M, Gillett N, Phillips HS, Ferrara N: Inhibition of vascular endothelial growth factor-induced angiogenesis suppresses tumour growth in vivo. Nature 1993, 362:841–844

16. Witte L, Hicklin DJ, Zhu Z, Pytowski B, Kotanides H, Rockwell P, Bohlen P: Monoclonal antibodies targeting the VEGF receptor-2 (Flk1/KDR) as an anti-angiogenic therapeutic strategy. Cancer Metastasis Rev 1998, 17:155–161

17. Im SA, Gomez-Manzano C, Fueyo J, Liu TJ, Ke LD, Kim JS, Lee HY, Steck PA, Kyritsis AP, Yung WK: Antiangiogenesis treatment for gliomas: transfer of antisense-vascular endothelial growth factor inhibits tumor growth in vivo. Cancer Res 1999, 59:895–900

18. Benjamin LE, Keshet E: Conditional switching of vascular endothelial growth factor (VEGF) expression in tumors: induction of endothelial cell shedding and regression of hemangioblastoma-like vessels by VEGF withdrawal. Proc Natl Acad Sci USA 1997, 94:8761–8766

19. Goldman CK, Kendall RL, Cabrera G, Soroceanu L, Heike Y, Gillespie GY, Siegal GP, Mao X, Bett AJ, Huckle WR, Thomas KA, Curiel DT: Paracrine expression of a native soluble vascular endothelial growth factor receptor inhibits tumor growth, metastasis, and mortality rate. Proc Natl Acad Sci USA 1998, 95:8795–8800

20. Davidoff AM, Leary MA, Ng CY, Vanin EF: Gene therapy-mediated expression by tumor cells of the angiogenesis inhibitor flk-1 results in inhibition of neuroblastoma growth in vivo. J Pediatr Surg 2001, 36:30–36

21. Holash J, Davis S, Papadopoulos N, Croll SD, Ho L, Russell M, Boland P, Leidich R, Hylton D, Burova E, Ioffe E, Huang T, Radziejewski C, Bailey K, Fandl JP, Daly T, Wiegand SJ, Yancopoulos GD, Rudge JS: VEGF-Trap: a VEGF blocker with potent antitumor effects. Proc Natl Acad Sci USA 2002, 99:11393–11398

22. Tseng JF, Farnebo FA, Kisker O, Becker CM, Kuo CJ, Folkman J, Mulligan RC: Adenovirus-mediated delivery of a soluble form of the VEGF receptor Flk1 delays the growth of murine and human pancreatic adenocarcinoma in mice. Surgery 2002, 132:857–865

23. Millauer B, Shawver LK, Plate KH, Risau W, Ullrich A: Glioblastoma growth inhibited in vivo by a dominant-negative Flk-1 mutant. Nature 1994, 367:576–579

24. Fong TA, Shawver LK, Sun L, Tang C, App H, Powell TJ, Kim YH, Schreck R, Wang X, Risau W, Ullrich A, Hirth KP, McMahon G: SU5416 is a potent and selective inhibitor of the vascular endothelial growth factor receptor (Flk-1/KDR) that inhibits tyrosine kinase catalysis, tumor vascularization, and growth of multiple tumor types. Cancer Res 1999, 59:99–106

25. Laird AD, Vajkoczy P, Shawver LK, Thurnher A, Liang C, Mohammadi M, Schlessinger J, Ullrich A, Hubbard SR, Blake RA, Fong TA, Strawn LM, Sun L, Tang C, Hawtin R, Tang F, Shenoy N, Hirth KP, McMahon G, Cherrington JM: SU6668 is a potent antiangiogenic and antitumor agent that induces regression of established tumors. Cancer Res 2000, 60:4152–4160

26. Drevs J, Muller-Driver R, Wittig C, Fuxius S, Esser N, Hugenschmidt H, Konerding MA, Allegrini PR, Wood J, Hennig J, Unger C, Marme D: PTK787/ZK 222584, a specific vascular endothelial growth factor-receptor tyrosine kinase inhibitor, affects the anatomy of the tumor vascular bed and the functional vascular properties as detected by dynamic enhanced magnetic resonance imaging. Cancer Res 2002, 62:4015–4022

27. Hu-Lowe D, Hallin M, Feeley R, Zou H, Rewolinski D, Wickman G, Chen E, Kim Y, Riney S, Reed J, Heller D, Simmons B, Kania R, McTigue M, Niesman M, Gregory S, Shalinsky D, Bender S: Characterization of potency and activity of the VEGF/PDGF receptor tyrosine kinase inhibitor AG013736. Proc Am Assoc Cancer Res 2002, 43:A5357

28. Yuan F, Chen Y, Dellian M, Safabakhsh N, Ferrara N, Jain RK: Time-dependent vascular regression and permeability changes in established human tumor xenografts induced by an anti-vascular endothelial growth factor/vascular permeability factor antibody. Proc Natl Acad Sci USA 1996, 93:14765–14770

29. Shaheen RM, Davis DW, Liu W, Zebrowski BK, Wilson MR, Bucana CD, McConkey DJ, McMahon G, Ellis LM: Antiangiogenic therapy targeting the tyrosine kinase receptor for vascular endothelial growth factor receptor inhibits the growth of colon cancer liver metastasis and induces tumor and endothelial cell apoptosis. Cancer Res 1999, 59:5412–5416

30. Bruns CJ, Liu W, Davis DW, Shaheen RM, McConkey DJ, Wilson MR, Bucana CD, Hicklin DJ, Ellis LM: Vascular endothelial growth factor is an in vivo survival factor for tumor endothelium in a murine model of colorectal carcinoma liver metastases. Cancer 2000, 89:488–499

31. Huang J, Frischer JS, Serur A, Kadenhe A, Yokoi A, McCrudden KW, New T, O'Toole K, Zabski S, Rudge JS, Holash J, Yancopoulos GD, Yamashiro DJ, Kandel JJ: Regression of established tumors and metastases by potent vascular endothelial growth factor blockade. Proc Natl Acad Sci USA 2003, 100:7785–7790

32. Jain RK: Normalizing tumor vasculature with anti-angiogenic therapy: a new paradigm for combination therapy. Nat Med 2001, 7:987–989

33. Erber R, Thurnher A, Katsen AD, Groth G, Kerger H, Hammes HP, Menger MD, Ullrich A, Vajkoczy P: Combined inhibition of VEGF and PDGF signaling enforces tumor vessel regression by interfering with pericyte-mediated endothelial cell survival mechanisms. EMBO J 2004, 18:338–340

34. Hanahan D: Heritable formation of pancreatic beta-cell tumours in transgenic mice expressing recombinant insulin/simian virus 40 oncogenes. Nature 1985, 315:115–122

35. Wickman G, Hallin M, Dillon R, Amundson K, Acena A, Grazzini M, Herrmann M, Vekich S, McTigue M, Kania R, Bender S, Shalinsky DR, Hu-Lowe DD: Further characterization of the potent VEGF/PDGF receptor tyrosine kinase inhibitor, AG013736, in preclinical tumor models for its antiangiogenesis and antitumor activity. Proc Am Assoc Cancer Res 2003, 44:A3780

36. Bergers G, Song S, Meyer-Morse N, Bergsland E, Hanahan D: Benefits of targeting both pericytes and endothelial cells in the tumor vasculature with kinase inhibitors. J Clin Invest 2003, 111:1287–1295

37. Baffert F, Thurston G, Rochon-Duck M, Le T, Brekken R, McDonald DM: Age-related changes in VEGF-dependency and angiopoietin-1 induced plasticity of adult blood vessels. Circ Res 2004, 94:984–992

38. Bergers G, Javaherian K, Lo KM, Folkman J, Hanahan D: Effects of angiogenesis inhibitors on multistage carcinogenesis in mice. Science 1999, 284:808–812

39. Hashizume H, Ushiki T: Three-dimensional cytoarchitecture of angiogenic blood vessels in a gelatin sheet implanted in the rat skeletal muscular layers. Arch Histol Cytol 2002, 65:347–357

40. Roberts WG, Palade GE: Increased microvascular permeability and endothelial fenestration induced by vascular endothelial growth factor. J Cell Sci 1995, 108:2369–2379

41. Lammert E, Gu G, McLaughlin M, Brown D, Brekken R, Murtaugh LC, Gerber HP, Ferrara N, Melton DA: Role of VEGF-A in vascularization of pancreatic islets. Curr Biol 2003, 13:1070–1074

42. Zhang W, Ran S, Sambade M, Huang X, Thorpe PE: A monoclonal antibody that blocks VEGF binding to VEGFR2 (KDR/Flk-1) inhibits vascular expression of Flk-1 and tumor growth in an orthotopic human breast cancer model. Angiogenesis 2002, 5:35–44

43. Vracko R: Basal lamina scaffold—anatomy and significance for maintenance of orderly tissue structure. Am J Pathol 1974, 77:314–346

44. Latker CH, Kuwabara T: Regression of the tunica vasculosa lentis in the postnatal rat. Invest Ophthalmol Vis Sci 1981, 21:689–699

45. Meeson A, Palmer M, Calfon M, Lang R: A relationship between apoptosis and flow during programmed capillary regression is revealed by vital analysis. Development 1996, 122:3929–3938

46. Meeson AP, Argilla M, Ko K, Witte L, Lang RA: VEGF deprivation-induced apoptosis is a component of programmed capillary regression. Development 1999, 126:1407–1415

47. Dimmeler S, Assmus B, Hermann C, Haendeler J, Zeiher AM: Fluid shear stress stimulates phosphorylation of Akt in human endothelial cells: involvement in suppression of apoptosis. Circ Res 1998, 83:334–341

48. Hellstrom M, Gerhardt H, Kalen M, Li X, Eriksson U, Wolburg H, Betsholtz C: Lack of pericytes leads to endothelial hyperplasia and abnormal vascular morphogenesis. J Cell Biol 2001, 153:543–553

49. Shaheen RM, Tseng WW, Davis DW, Liu W, Reinmuth N, Vellagas R, Wieczorek AA, Ogura Y, McConkey DJ, Drazan KE, Bucana CD, McMahon G, Ellis LM: Tyrosine kinase inhibition of multiple angiogenic growth factor receptors improves survival in mice bearing colon cancer liver metastases by inhibition of endothelial cell survival mechanisms. Cancer Res 2001, 61:1464–1468

50. Benjamin LE, Golijanin D, Itin A, Pode D, Keshet E: Selective ablation of immature blood vessels in established human tumors follows vascular endothelial growth factor withdrawal. J Clin Invest 1999, 103:159–165

51. Bergers G, Brekken R, McMahon G, Vu TH, Itoh T, Tamaki K, Tanzawa K, Thorpe P, Itohara S, Werb Z, Hanahan D: Matrix metalloproteinase-9 triggers the angiogenic switch during carcinogenesis. Nat Cell Biol 2000, 2:737–744

52. Gerhardt H, Betsholtz C: Endothelial-pericyte interactions in angiogenesis. Cell Tissue Res 2003, 314:15–23

53. Fairbrother WJ, Champe MA, Christinger HW, Keyt BA, Starovasnik MA: Solution structure of the heparin-binding domain of vascular endothelial growth factor. Structure 1998, 6:637–648

Vascular Biology, Atherosclerosis and Endothelium Biology

Molecular Changes in the Vasculature of Injured Tissues

Tero A.H. Järvinen* and Erkki Ruoslahti*†

From the Cancer Research Center, Burnham Institute for
Medical Research, La Jolla; and Burnham Institute for Medical
Research,† University of California, Santa Barbara, California*

We have explored molecular specialization of the vasculature of regenerating wound tissue in the skin and tendons to identify a different repertoire of markers from that obtained by studying tumor vasculature. We screened a phage-displayed peptide library for peptides that home to wounds in mice and identified two peptides that selectively target phage to skin and tendon wounds: CARSKNKDC (CAR) and CRKDKC (CRK). CAR is homologous to heparin-binding sites in various proteins and binds to cell surface heparan sulfate and heparin. CRK is similar to a segment in thrombospondin type 1 repeat. Intravenously injected CAR and CRK phage, as well as fluorescein-labeled CAR and CRK peptides, selectively accumulated at wound sites, where they partially co-localized with blood vessels. The CAR peptide showed a preference for early stages of wound healing, whereas the CRK favored wounds at later stages of healing. The CAR peptide was internalized into the target cells and delivered the fluorescent label into the cell nuclei. These results identify new molecular markers in wound tissues and show that the expression of these markers in wound vasculature changes as healing progresses. The peptides recognizing these markers may be useful in delivering treatments into regenerating tissues. *(Am J Pathol 2007, 171:702–711; DOI: 10.2353/ajpath.2007.061251)*

Tissue regeneration, inflammation, and tumors induce the growth of new blood vessels from pre-existing ones. This process, angiogenesis, is a vital requirement for wound healing because the formation of new blood vessels allows a variety of mediators, nutrients, and oxygen to reach the healing tissue.[1–3] Newly formed blood vessels differ in structure from pre-existing vasculature. Such differences have been extensively characterized by comparing tumor vasculature to normal vessels.[4–6] Angiogenic vessels in nonmalignant tissues and in premalig-

nant lesions share markers with tumor vessels,[7,8] but distinct markers also exist.[9,10]

Here, we use *in vivo* screening of phage-displayed peptide libraries to probe vascular specialization. This method has revealed a surprising degree of heterogeneity in the vasculature; tissue-specific homing peptides have been identified for a large number of normal organs and tissues,[11–13] and tumors and atherosclerotic lesions have been shown to carry their own vascular markers, both in the blood vessels and in lymphatics.[6,14,15] We reasoned that surveying nonmalignant angiogenesis might reveal a different repertoire of markers than has been obtained by studying tumor vasculature. We chose wounds as the target because wounds are one of the few nontumor locations where angiogenesis takes place in an adult organism.

In this study, we report on two peptides that specifically deliver the phage or peptide-coupled fluorophor to wound microvasculature after intravenous injection. These peptides seem to be different from previously described tumor-homing peptides and they reveal changes in the molecular profile of wound vasculature as the wound heals.

Materials and Methods

Materials

Heparinase I (*Flavobacterium heparinum*; heparin lyase, EC 4.2.2.7), heparinase III (*F. heparinum*; heparin-sulfate lyase,

EC 4.2.2.8), and heparin immobilized on acrylic beads were purchased from Sigma-Aldrich (St. Louis, MO).

Generation of Wounds

Wound experiments were performed in 6- to 8-week-old male Sprague-Dawley rats and BALB/c mice. Rats were anesthetized with an intraperitoneal injection of 50/50% ketamine-xylaxine, and an intraperitoneal injection of 2.5% avertin (Sigma-Aldrich) was used for mice. Skin was shaved, cleaned, and disinfected with povidone-iodine (Betadine; Sigma-Aldrich) and 70% alcohol. All animal experiments were approved by the Institutional Animal Care and Use Committee of Burnham Institute for Medical Research.

Two types of injuries were used with patellar tendons. For phage screening in rats, patellar tendons were exposed through small skin incisions placed on the lateral side of the joint, so that the skin wound and tendon wound were not in direct contact with each other. Six longitudinal, full-length incisions were made into the tendon. Full-thickness incision wounds, 1.5 cm in length, were made in skin on the back of the animal. The skin wounds were left uncovered without a dressing. For quantification of phage homing and peptide injections, two size 11 surgical scalpels were placed side-by-side and the central third of the patellar tendon was removed analogous to the graft used in anterior cruciate ligament reconstruction. Achilles tendons were wounded by making four longitudinal, full-length incisions into the tendon. Skin wounds were 8-mm circular, full-thickness excision wounds, made to the skin with a biopsy punch. None of the procedures prevented the animals from bearing weight and moving immediately after the operation and without a noticeable limp.

Phage Libraries, Library Screening, and Individual Phage Clones

The libraries were prepared by using NNK-oligonucleotides encoding a random library of cyclic peptides of the general structure CX_7C (C, cysteine; X, any amino acid). The oligonucleotide mixture was cloned into the T7Select 415-1 vector according to the manufacturer's instructions (Novagen, Madison, WI). This vector displays peptides in all 415 copies of the phage capsid protein as a C-terminal fusion. Libraries with this structure have yielded numerous high-affinity cell-binding peptides.[6,11,16,17]

The screening process involved three *in vivo* selection rounds, performed essentially as described.[17] Eight-week-old Sprague-Dawley rats were injected with the library [1 to 5×10^{11} phage in 1.5 ml of phosphate-buffered saline (PBS)] through the tail vein or intracardially and were perfused 12 minutes later through the heart with 1% bovine serum albumin in Dulbecco's modified Eagle's medium to remove unbound intravascular phage. The short circulation time focused the screening on the blood vessels because the intact phage cannot readily access extravascular tissue. It also minimized any neutralization or processing of the phage in the tissues. The first *in vivo* round included 19 animals with both patellar tendon and skin wounds, which were separately pooled. The second round used separate sets of three animals for tendon and skin wound screening, and the third round was performed with one wound of each kind.

The following primers, expressing the indicated peptides, were used to prepare phage: CAR, 5′-AATTCCT-GCGCGCGTTCGAAGAATAAGGATTGCTA-3′ and 5′-AGCTTAGCAATCCTTATTCTTCGAACGCGCGCAGG-3′; CRK, 5′-AATTCCTGCCGGAAGGATAAGTGCTA-3′ and 5′-AGCTTAGCACTTATCCTTCCGGCAGG-3′; CAQSNN-KDC, 5′-AATTCCTGCGCGCAGTCGAACAATAAGGAT-TGCTA-3′ and 5′-AGCTTAGCAATCCTTATTGTTCGACT-GCGCGCAGG-3′; CAR2, 5′-AATTCCTGCGCTAGGTCT-ACTGCTAAGACTTGCTA-3′ and 5′-AGCTTAGCAAGT-CTTAGCAGTAGACCTAGCGCAGG-3′; and CRASKC, 5′-AATTCCTGCCGGGCATCTAAGTGCTA-3′ and 5′-AGC-TTAGCACTTAGATGCCCGGCAGG-3′. To test single phage clones *in vivo*, 1×10^{10} phage in 1.5 ml of PBS were injected through the tail vein. After the circulation period and perfusion, tissue samples were harvested and weighed. Phage titers per mg of wet tissue were then determined, and the results were expressed as the ratio between the titer of the test clone and nonrecombinant control phage in the same tissue.

Peptides

Peptides were synthesized with an automated peptide synthesizer by using standard solid-phase fluorenylmethoxycarbonyl chemistry. During synthesis, the peptides were labeled with fluorescein using an amino-hexanoic acid spacer as described.[18] Each individual fluorescein-conjugated peptide was injected intravenously into the tail vein of rats or mice with wounds. The peptides were allowed to circulate for different periods of time, followed by heart perfusion. Tissues were embedded into OCT (Tissue-Tek; Sakura Finetek U.S.A., Inc., Torrance, CA) and processed for microscopy.

Immunohistochemistry

Frozen tissue sections were fixed in acetone for 10 minutes and incubated with 0.5% blocking reagent for 1 hour (NEN Life Sciences, Boston, MA). Tissue sections were incubated with the primary antibody overnight at 4°C. The following monoclonal antibodies (mAbs) and polyclonal antibodies (pAbs) were used: rabbit anti-T7-phage affinity-purified pAb (1:100),[17] rat anti-mouse CD31 mAb (1:200; BD Pharmingen, San Diego, CA) and rabbit anti-fluorescein isothiocyanate (FITC) pAb (1:200; Invitrogen, Carlsbad, CA). The primary antibodies were detected with labeled secondary antibodies, and each staining experiment included sections stained with species-matched immunoglobulins as negative controls. The sections were washed several times with PBS, mounted in Vectashield mounting medium with 4,6-diamidino-2-phenylindole (DAPI) (Vector Laboratories, Burlingame, CA) and visualized under an inverted fluorescent or light microscope.

Cell Culture

Chinese hamster ovary cells (CHO-K) were obtained from the American Type Culture Collection (Rockville, MD). The pgsA-745 mutant cell line,[19] which is derived from CHO-K, was kindly provided by Dr. J. Esko (University of California at San Diego, La Jolla, CA). Cells were maintained in α-minimal essential medium and Earle's salt supplemented with 10% fetal bovine serum, 100 μg/ml streptomycin sulfate, 100 U of penicillin G/ml, and 292 μg/ml L-glutamine (Invitrogen).

Cell Binding Assays

Cells were detached with 0.5 mmol/L ethylenediaminetetraacetic acid solution (Irvine Scientific, Santa Ana, CA), washed with PBS, and resuspended in 1% bovine serum albumin plus α-minimal essential medium. For the phage binding experiments, ~1 × 10^{10} phages were added to 15 ml of culture media containing ~1 × 10^6 cells in a test tube. The samples were rotated for 2 hours at +4°C. The cells were then washed six times and transferred to a new tube. After a final wash, the cells were counted and cell-bound phage titers were determined. Heparinase treatment of the CHO-K cells was performed using 1.5 IU/ml heparinase I and 1.25 IU/ml heparinase III in serum-free culture media for 2 hours.

Peptide binding to cells was studied essentially as described above for phage. Peptides were tested at 5 μmol/L concentration, with or without 5 × 10^9 phage. After incubation on ice for 30 minutes, the cells were washed and resuspended with PBS containing 2 μg/ml of propidium iodide (Invitrogen) and analyzed using a FACScan flow cytometer (BD Biosciences, San Jose, CA).

To study peptide internalization, CHO-K cells or human umbilical vein endothelial cells seeded on plastic coverslips were incubated with 10 μmol/L fluorescein-conjugated peptides for 30 minutes to 72 hours, washed three times with PBS, and fixed with 4% paraformaldehyde for 20 minutes at room temperature. After several washes with PBS, the nuclei were visualized by staining with DAPI, and the slides were mounted with ProLong Gold anti-fade reagent (Invitrogen). The images were acquired using Olympus IX81 inverted and Olympus Fluoview FV1000 confocal microscopes (Olympus, Melville, NY). Z-stack images were taken by confocal microscope every 1 μm through the cells.

Heparin Binding

To measure phage binding to heparin, heparin-coated acrylic beads 10% (v/v) were suspended in 20 mmol/L Na$_2$HPO$_4$ buffer, pH 7.2, containing 0.2 mol/L NaCl.[20] Approximately 5.0 × 10^9 phage particles were incubated with the beads for 1 hour at room temperature. The beads were washed, transferred to new tube, and bound phage was eluted with 1.2 mol/L NaCl (pH 7.2) and titrated.[20]

Statistical Analysis

Differences between the various treatments were statistically tested using the Student's unpaired *t*-test, whereas the phage homing to wounds versus sham-operated tissues was analyzed using the Student's paired *t*-test. For comparisons of multiple groups, statistical analysis was performed by two-way analysis of variance complemented by the Bonferroni post hoc test for pair-wise comparisons between the test groups. The possible difference in the homing of the different phage clones to wounds was assessed using the log-transformed variables. *P* values of less than 0.05 were considered statistically significant for all tests. The significance level shown refers to two-tailed test.

Results

Identification of Homing Peptides by Phage Display

To identify candidate peptides that home into the vasculature in healing wounds, we screened phage libraries *in vivo*. A T7-phage library (diversity 9 × 10^8) was intravenously injected into rats 5 days after wounding of the skin and tendons. The 5-day time point was chosen because the number of blood vessels in the healing wound peaks at that time.[21–24] Separate screens for phage that home to tendon or skin wounds yielded phage pools with increased affinity for the target tissues. Sequencing of individual phage clones revealed two candidate homing motifs in the selected pools. The sequence CARSKNKDC (referred to as CAR) and a related sequence CARSTKATC (CAR2) were obtained in a tendon wound screen. BLAST analysis[25] showed that the CAR sequence is similar to the main heparin-binding site (RARKKNKNC) of bone morphogenetic protein 4 (BMP4). Another peptide, CRKDKC, was identified once in each of two independent screens on skin wounds. The CRK sequence shows some similarity with sequences in thrombospondin type 1 and type 3 repeats, which are present in a large number of extracellular matrix proteins. The CRK sequence is shorter than the structure of the CX$_7$C library would predict; a modified peptide structure is a relatively common occurrence in phage screening.[9] The sequence contains a cysteine residue at both ends, which are likely to form a cyclizing disulfide bond. These clones were chosen for further analysis.

The CAR phage homed 100- to 140-fold more efficiently to wounds in the patellar and Achilles tendons and in the skin than nonrecombinant phage (Figure 1A, solid bars). In contrast, similar numbers of both the CAR phage and control phage were seen in liver, kidney, heart, lung, spleen, normal skin, and normal Achilles and patellar tendons (Figure 1A). Immunohistochemistry showed that the CAR phage primarily co-localized with blood vessels (Supplemental Figure 1, see *http://ajp.amjpathol.org*). CAR2 was less effective as a wound homing phage than CAR (see below).

To confirm the specificity of the homing for wound tissue, we induced wounds in the patellar and Achilles tendons of the left hind limb, while subjecting the tendon areas in the right hind limb to a sham operation. The sham operation consisted of a skin incision that exposed the tendon but left
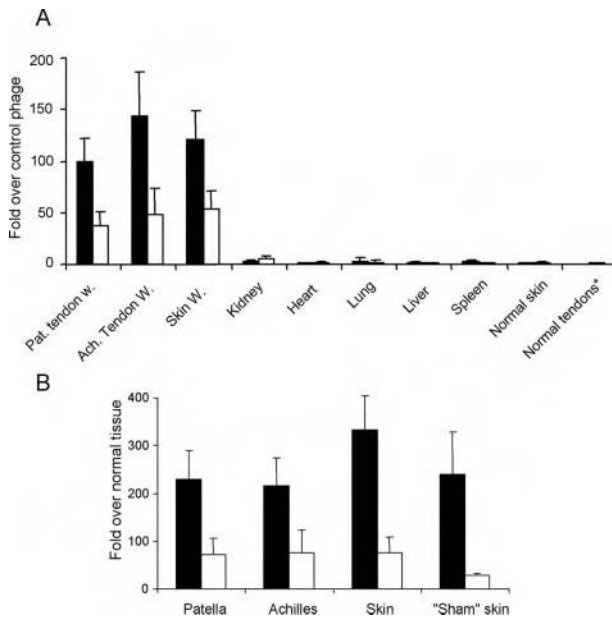
Figure 1. Homing specificity of two wound-homing phage clones. CAR phage (solid bars) or CRK phage (open bars) were injected into rats via tail vein, tissues were dissected 12 minutes later, and phage was recovered and quantified from wounds in patellar and Achilles tendons and skin. Sham-operated (exposed) tendon, normal skin, and other normal tissues were used as controls as indicated. Results are expressed as fold titers relative to that of similarly injected nonrecombinant T7 phage (**A**) or sham-operated contralateral tendon or normal skin after adjusting the output for the wet weight of the tissue samples (**B**). Sham skin refers to skin incision wounds made on the lateral side of the right knee, when the patellar tendon was exposed in the sham-operation. Error bars represent mean $\pm$ SEM of 11 experiments for wounds and 4 experiments for control tissues. **A:** Two-way analysis of variance; **B:** paired Student's *t*-test. Both the CAR and CRK phage homed to each of the wound tissues significantly more strongly ($P < 0.001$ or smaller) than the control (nonrecombinant) phage. The CAR phage showed significantly stronger homing than CRK phage to all wounds ($P < 0.01$ or smaller). Normal tendons* indicates combined data from normal Achilles and patellar tendons.

it otherwise intact. We compared *in vivo* phage homing to wounded tissue versus the corresponding normal tissue in the same animal in this model. On day 5 after wounding, the CAR phage homed 220- to 370-fold more to the wounded tendons compared with the contralateral intact tendons and to wounded skin compared with intact skin distant from the wound sites (Figure 1B, solid bars).

Intravenously injected CRK phage homed to 5-day tendon and skin wounds ~50 times more than nonrecombinant control phage (Figure 1A, open bars; and Supplemental Figure 2, see *http://ajp.amjpathol.org*). Comparison to the corresponding healthy tissues on the contralateral side showed nearly 80-fold preference for tendon and skin wounds (Figure 1B, open bars). In contrast, there were no significant differences between CRK phage and control phage in samples recovered from the liver, kidney, heart, lung, spleen, normal skin, or normal tendons (Figure 1A). Like the CAR phage, the CRK phage co-localized with blood vessels (Supplemental Figure 2, see *http://ajp.amjpathol.org*). Finally, we also recloned both the CAR and CRK sequences into the T7 vector and showed that the resulting phage clones homed to wounds as effectively as the original phage (the homing data obtained with the original and new phage clones have been pooled in Figure 1).

Sequence Specificity of Wound Homing by CAR and CRK

In the same tendon wound screen that produced the CAR sequence, we identified a peptide with a somewhat related sequence, CARSTKATC (CAR2). We generated a CAR mutant phage by changing two basic amino acids to neutral ones (CA*RSK*NKDC mutated to CA*QSN*NKDC). Both CAR2 and the mutant phage showed impaired wound-homing properties: the CAR2 phage had ~20% of the homing activity of CAR and the mutant phage was essentially inactive in homing (Supplemental Figure 3, A–C, see *http://ajp.amjpathol.org*). We also generated a mutant CRK phage by changing two amino acids (from CR*KD*KC to CR*AS*KC). The mutant phage had also almost completely lost the homing ability (Supplemental Figure 3, A–C, see *http://ajp.amjpathol.org*). The loss of activity as a result of the sequence changes emphasizes the role of the basic amino acids in the homing activity and attests to the specificity of the homing.

Synthetic CAR and CRK Peptides Accumulate in Wounds

We synthesized the CAR and CRK peptides as fluorescein (FITC) conjugates and tested their tissue distribution after intravenous injection to mice and rats with tendon and skin wounds. Both peptides produced strong fluorescent signal in the wounds that partially co-localized with CD31-positive cells at 4 and 8 hours after the injection (Figures 2 and 3). CAR2, even though slightly active at the phage-homing level, produced no accumulated fluorescence, and an unrelated five amino acid control peptide (KAREC) also gave no detectable signal in the wounds. Because of an autofluorescent background in wounds, the fluorescein-labeled peptides were also detected with an anti-FITC antibody, and the signal was thus amplified and converted to a nonfluorescent dye. The antibody staining confirmed the localization of the fluorescein label in the granulation tissue, particularly at later time points when the fluorescent signal was weak. The fluorescent signal produced by CAR and CRK in nontumor tissues (liver, kidney, lung, and spleen) did not differ from that of the fluorescein-labeled CAR2 or KAREC peptides used as controls (Supplemental Figure 4A, see *http://ajp.amjpathol.org*). In agreement with the phage results, no CAR or CRK peptide accumulated in normal skin (Supplemental Figure 4B, see *http://ajp.amjpathol.org*) or tendons (not shown).

Healing Stage-Dependent Changes in Phage Homing

To determine the extent our wound-homing peptides would home to wounds at times other than the 5-day time point, we injected individual phage clones at days 7, 10, and 14, after wounding. The total number of homing phage rescued from the wounds decreased by two orders of magnitude as wound healing progressed
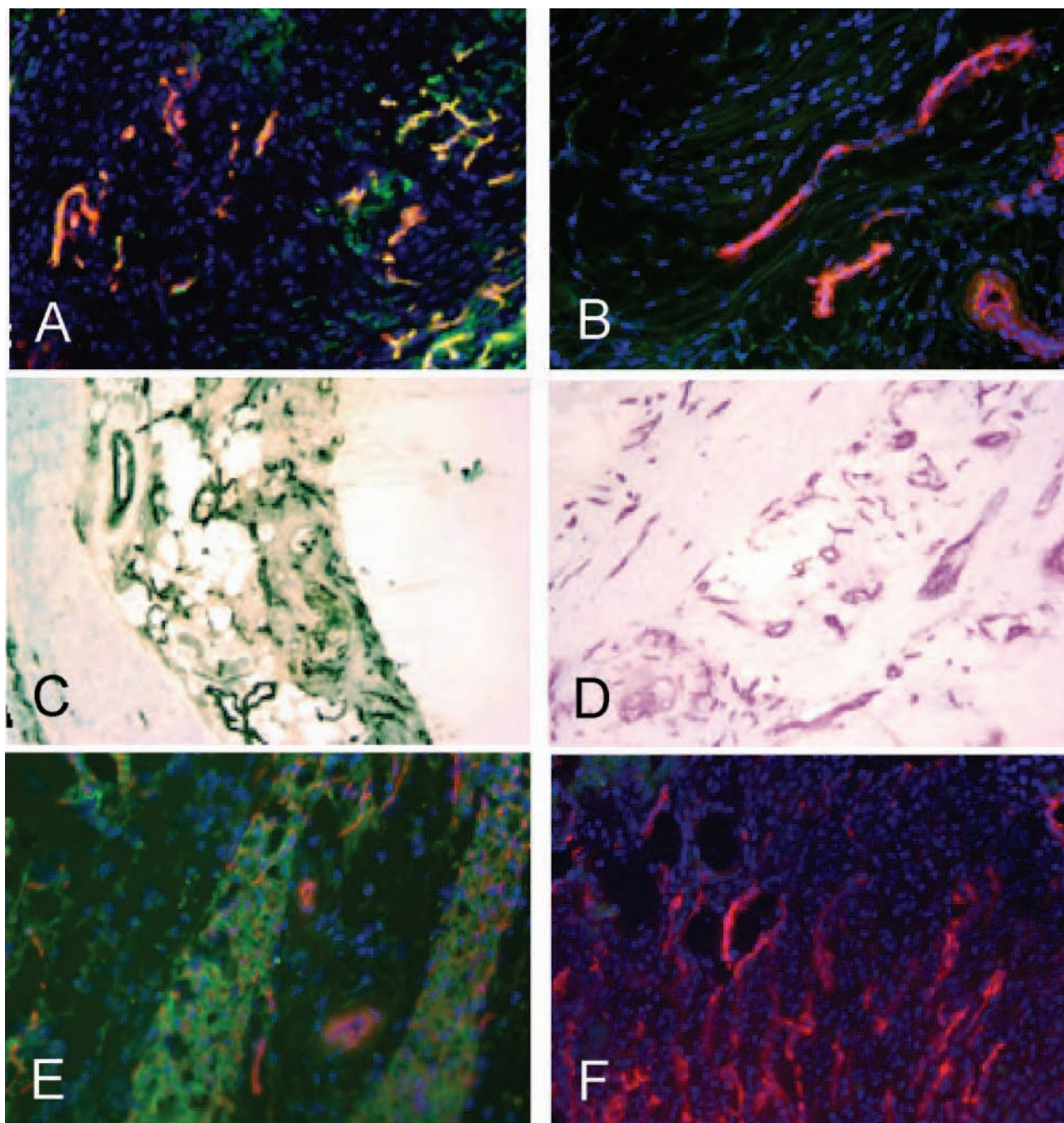
Figure 2. CAR peptide homes to blood vessels and granulation tissue in tendon and skin wounds. Fluorescein-conjugated peptides CAR (**A**, **C**, and **E**) or CAR2 (**B**, **D**, and **F**) were intravenously injected into rats (**A–D**) or mice (**E** and **F**) with 5-day-old wounds in Achilles tendons (**A–D**) or skin (**E** and **F**). Wound tissue was collected 4 hours later, which allowed the peptide to penetrate into the tissue, and examined for the presence of the peptides. In **A–D**, rabbit anti-FITC followed by FITC-conjugated (**A** and **B**) or biotin-conjugated anti-rabbit IgG and streptavidin peroxidase (**C** and **D**; brown), were used to detect the signal from the fluorescein-labeled peptide. Blood vessels were stained with CD-31 antibody (magenta in **C** and **D**) and the nuclei were stained with DAPI (blue). Original magnifications, ×200.

(not shown), presumably reflecting the pruning that occurs in wound vasculature during the maturation of granulation tissue into scar tissue.[3] However, comparison with control phage revealed selective homing even at the late (day 14) stages of wound healing (Figure 4). The CRK phage, which homed less strongly than CAR on day 5, was generally the more efficient homing peptide at the later stages of wound healing. Phage staining showed that both phage clones co-localized with blood vessels at all stages in wound healing (Supplemental Figures 1 and 2, see *http://ajp.amjpathol.org*), and in agreement with the phage homing data, little CAR phage was detected in 14-day wounds, whereas the CRK phage still gave relatively strong staining at this stage (Supplemental Figure 5, see *http://ajp.amjpathol.org*). The co-localization of the phage staining indicates that the molecular change reflected in the relative homing of CAR and CRK re-
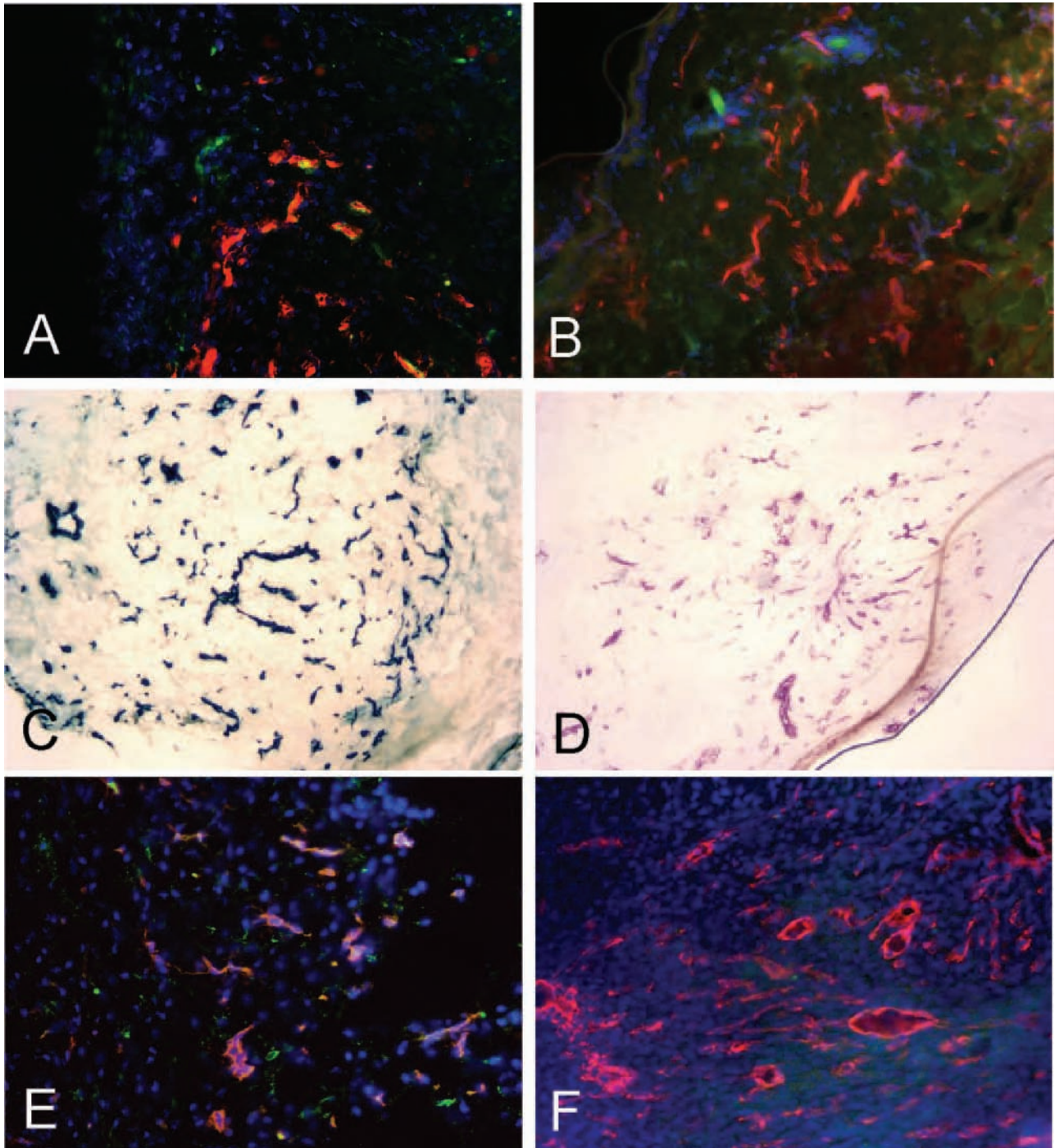
Figure 3. CRK peptide homes to blood vessels and granulation tissue in wounds. Fluorescein-conjugated peptides CRK (**A**, **C**, and **E**) or KAREC (control peptide: **B**, **D**, and **F**), were intravenously injected as in Figure 2 into rats (**A** and **B**) or mice (**C–F**) with 5-day-old wounds in the skin (**A–D**) or patellar tendons (**E** and **F**). The peptides, blood vessels, and nuclei were detected as in Figure 2. Original magnifications, ×200.

sides in the vasculature and that this change is related to the maturation of the vasculature in wounds.

Cell Surface Heparan Sulfate as the Target Molecule for CAR

The CAR sequence homology with the heparin-binding site of BMP4 and the presence in CRK of a classical heparin-binding motif (XBBXBX; where X denotes any amino acid and B basic residue), suggested that a particular form of a glycosaminoglycan, probably a heparan sulfate, might serve as the binding site for one or both of the peptides. We used Chinese hamster ovary cells (CHO-K) and the pgsA-745 mutant CHO line that is defective in glycosaminoglycan biosynthesis[19] to test the binding of CAR and CRK to cell surface
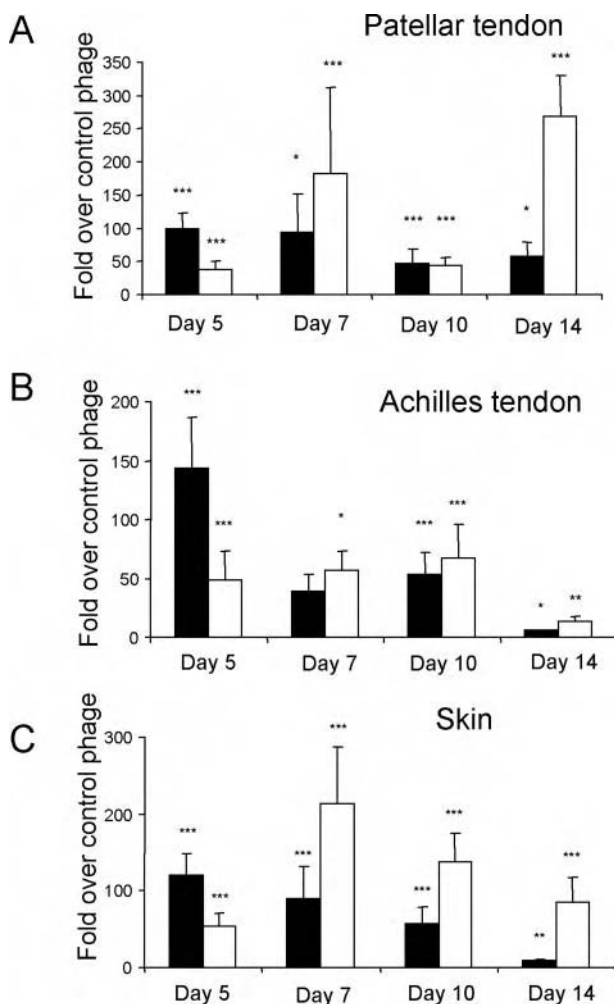
Figure 4. Healing stage dependence of phage homing to wounds. CAR phage (filled bars) or CRK phage (open bars) was intravenously injected into rats 5, 7, 10, and 14 days after wounding. The phage was recovered 12 minutes after the injection and quantified. Results are expressed as fold titers relative to that of similarly injected nonrecombinant T7 phage after adjusting the output to the wet weight of the tissue samples. **A:** Patellar tendon wounds; **B:** Achilles tendon wounds; **C:** skin wounds. The CAR and CRK phage homing shows a different healing time dependence. Error bars represent mean ± SEM for 11, four, seven, and five separate experiments at each time point. *$P < 0.05$, **$P < 0.01$, ***$P < 0.001$ versus nonrecombinant T7 phage, two-way analysis of variance.

Figure 5. Binding of CAR phage to cell surface heparan sulfate and heparin. **A:** CAR phage (filled bars) specifically binds to CHO-K cells, but not to the glycosaminoglycan-deficient pgsA-745 cells. CRK phage (open bars) does not bind significantly to either cell line. **B:** Heparinase treatment of the CHO-K cells (gray bar) suppresses the binding of the CAR phage to these cells. **C:** CAR phage, but not CRK phage, binds to heparin-coated beads. Error bars represent mean ± SEM for three or more separate experiments performed in duplicate. *$P < 0.05$; ***$P < 0.001$. **A** and **B:** Two-way analysis of variance; **C:** unpaired Student's *t*-test. Brackets indicate the difference between CAR and CRK phages.

glycosaminoglycans. CAR phage bound to the CHO-K cells 55-fold more than nonrecombinant control phage ($P < 0.0001$), but there was no specific binding to the glycosaminoglycan-deficient cells (Figure 5A). The CRK phage did not bind significantly to either cell line (Figure 5A). Pretreatment of the CHO-K cells with heparinase I and III decreased the binding of the CAR phage by almost 80% ($P < 0.0001$; Figure 5B). The CAR phage also bound to heparin-coated beads; 70-fold more CAR phage than nonrecombinant control phage was recovered from the beads ($P < 0.0001$; Figure 5C). CRK phage binding was only marginally higher than that of the control phage.

Fluorescence-activated cell sorting analysis also revealed strong binding of the synthetic CAR peptide to the CHO-K cells, but not to the pgsA-745 cells. An excess of unlabeled CAR 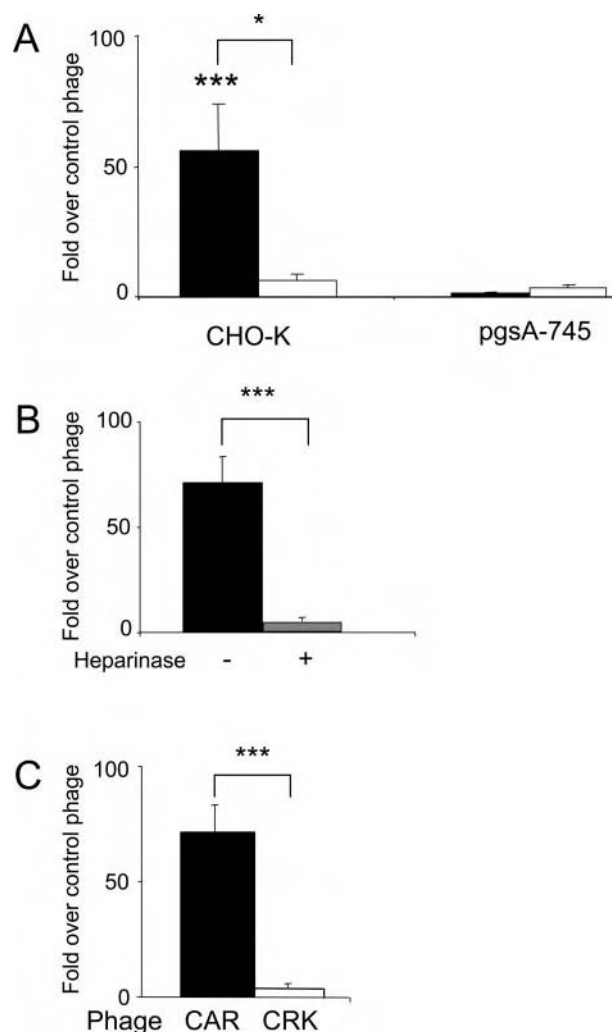peptide inhibited the binding in a dose-dependent manner. The binding could also be inhibited with the CAR phage. The CAR2 peptide bound only weakly to the CHO-K cells, and KAREC showed no binding to either the CHO-K or pgsA-745 cells (data not shown). These results indicate that CAR, but not CRK, has an active heparin-binding site, and that CAR binds to glycosaminoglycan moiety in cell surface heparan sulfate proteoglycans.

Cell-Penetrating Properties of CAR Peptide

Many of the best-characterized cell penetrating peptides contain basic residues, and heparan sulfate proteoglycans are thought to be involved in the internalization of these peptides.[26,27] This prompted us to study the cell-penetrating properties of the wound-
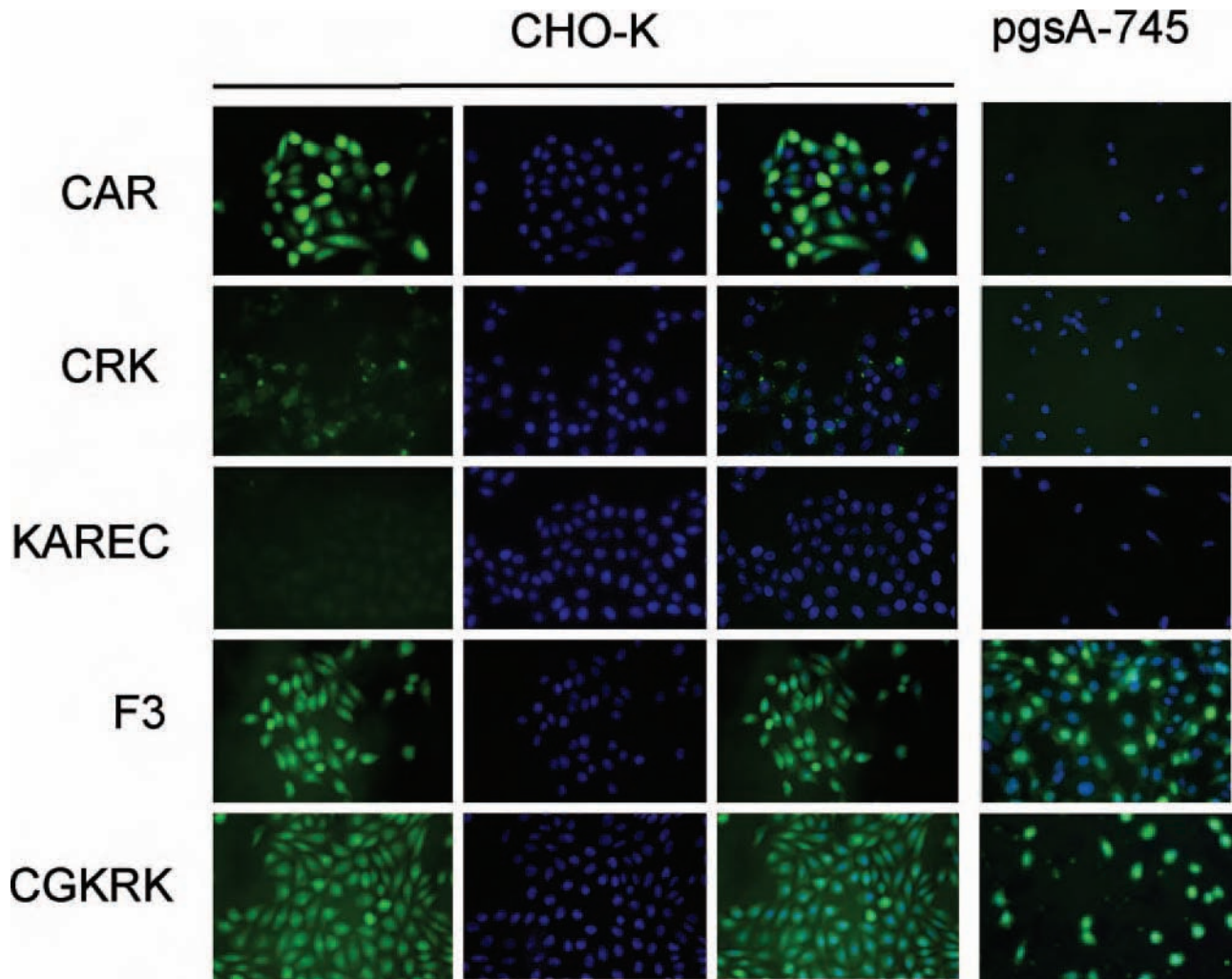
CHO-K   pgsA-745

Figure 6. The CAR peptide is internalized into CHO-K cells. Fluorescein-conjugated peptides as indicated were incubated at 10 μmol/L concentration with CHO-K and pgsA-745 cells for 24 hours. The cells were washed, fixed, stained with the nuclear stain DAPI (blue; CHO-K panels, middle), and examined for green fluorescence from the labeled peptides. The CAR peptide produces strong green fluorescence in the CHO-K cells that mostly overlaps with nuclear DAPI staining (right). This peptide does not appear in the glycosaminoglycan-deficient pgsA-745 cells. The CRK peptide binds weakly to the CHO-K cells. No overlap with nuclei is evident. KAREC control peptide gives no detectable cellular fluorescence, whereas F3 and CGKRK internalize in both CHO-K and pgsA-745 cells, overlapping with nuclei. Original magnifications, ×400.

homing peptides. Fluorescence from labeled CAR peptide incubated with CHO-K cells accumulated within 30 minutes inside the cells, overlapping with the nucleus (Figure 6). Confocal microscopy (not shown) confirmed the nuclear localization. The CRK peptide slightly bound to the cells but was not detectably internalized. The KAREC control peptide (Figure 6) or CAR2 (not shown) did not bind or become internalized. That the CAR peptide neither bound nor internalized into the glycosaminoglycan-deficient pgsA-745 cells (Figure 6), confirmed the specificity of the internalization and its dependence on the binding of the CAR peptide to its receptor. Thus, the CAR peptide seems to be a cell-penetrating peptide.

We have previously characterized two cell-penetrating peptides, CGKRK and F3, that specifically recognize angiogenic endothelial cells and tumor cells.[9,28] Each of these peptides contains basic residues, raising the question of whether they might bind to the same sites at the cell surface as the CAR peptide. F3 and CGKRK accumulated in the cytosol and nuclei of both the CHO-K and pgsA-745 cells (Figure 6), whereas CAR only bound to and was internalized by the CHO-K cells (and CRK did not bind avidly to either cell line). Moreover, a 10-molar excess of unlabeled F3 or CGKRK peptide did not detectably affect the uptake fluorescein-label from the CAR peptide by the CHO-K cells (not shown). Taken together with our previous demonstration that the receptor for the F3 peptide is cell surface-expressed nucleolin,[29] rather than heparan sulfate, these results show that the specificities of CAR and CRK are novel.

Discussion

We report here two novel peptides that specifically home to tendon and skin wounds, targeting both the vasculature and granulation tissue of the wounds. The target

molecule of one of the peptides seems to be a cell surface heparan sulfate structure. We use these peptides to provide evidence that the molecular profile of blood vessels in wounds changes as wounds mature.

In this work we used *in vivo* screening of phage libraries, which primarily probes the blood vessels.[6,11] Our approach was based on the notion that using wound-induced angiogenesis as a target might produce a different repertoire of vascular homing peptides than screening on other types of angiogenic lesions, such as tumors, which have been used extensively in similar screenings.[6] The hypothesis may have been correct, at least to the extent that the two peptides we have isolated seem to be unique. Our wound-homing peptides contain several basic residues, and highly basic peptides have been previously identified in tumor screens.[9,10,28,30] Moreover, the CAR and CKR peptides also recognize tumor vasculature (T.J. and E.R., unpublished results). However, the arrangement of the basic amino acids and other sequence features distinguish our new peptides from the previously described ones. They also differ in heparin binding and cell-type specificity. Among the earlier peptides, F3 and CGKRK bind to heparin, but as shown here, are equally effective in binding to cells that express cell surface heparan sulfate and cells that lack it. In contrast, CAR does not recognize the heparan sulfate-deficient cells, and CRK does not bind to heparin.

We performed the phage screening using wounds made in two tissues, tendon and skin. The CAR peptide came from a tendon screen and the CRK peptide was obtained in a skin screen. Despite their different origin, both peptides homed to wounds in both tissues, indicating that if vascular markers specific for individual tissues exist, our screening did not reveal such markers. However, our screening strategy of using the peak of angiogenesis might not have been ideal for revealing tissue-specific differences. Wounds that have healed sufficiently to regain elements of the original tissue may be more likely to reveal tissue-specific angiogenesis markers. In addition, the molecular changes detected by CAR and CRK may not be exclusively expressed in blood vessels; the fluorescein-labeled peptides, and to some extent the phage clones, spread into extravascular wound tissue, suggesting that cells in the granulation tissue may also express the receptors for these peptides.

The CAR and CRK peptides displayed an opposite homing preference with regard to the age of the wound; CAR favors early wounds and CRK prefers mature ones. Although the CAR peptide homing was clearly transient during wound healing, we did not follow the wounds long enough to see CRK homing disappear, but it seems likely that CRK homing is also transient. Because the phage almost exclusively accumulated in the wound blood vessels, we conclude that wound maturation is accompanied by changes in the profile of molecular markers in wound blood vessels. This conclusion parallels what has been observed in studies on tumor vasculature. Vascular markers can distinguish the blood vessels and lymphatics in premalignant lesions from those of fully malignant tumors in the same tumor system.[10,12] Furthermore, blood vessels in tumors at different stages of tumor development

and different stages of vessel maturation differ in their response to anti-angiogenic treatments.[31,32] Our results show that a similar maturation process takes place in wound vasculature. Individual vessels in a wound may not all be at the same stage in the maturation process because there were always some vessels in otherwise positive samples that did not bind the peptides.

The CAR peptide binds to heparin and cell surface heparan sulfate, suggesting that one or more heparan sulfate proteoglycans at the cell surface are the target molecules for this peptide. Heparan sulfate proteoglycans are ubiquitously expressed, but sequence variability in their heparan sulfate component makes possible tissue and cell type-specific interaction with proteins.[20,33–35] The specificity of the CAR peptide for wound vessels and tumor vessels suggests that this peptide may recognize a heparan sulfate sequence specific for wound and tumor angiogenesis. The CRK peptide showed some homology with sequences in thrombospondin type 1 and type 3 repeats, but it is unlikely that this peptide would bind to CD36, which is a known thrombospondin receptor in endothelial cells, because the CRK sequence shows no similarity with the thrombospondin sequence that binds CD36 (VTCG[36,37]); the receptor for CRK remains to be identified and is the subject of future studies.

Finally, the peptides we describe here may offer new therapeutic opportunities. Specific targeting of drugs and other therapeutic moieties to injured tissues may be a valuable option, especially when local treatment is not an option. We are exploring this aspect in ongoing work.

Acknowledgments

References

1. Folkman J: Angiogenesis. Annu Rev Med 2006, 57:1–18
2. Falanga V: Wound healing and its impairment in the diabetic foot. Lancet 2005, 366:1736–1743
3. Martin P: Wound healing—aiming for perfect skin regeneration. Science 1997, 276:75–81
4. Wickström S, Keski-Oja J, Alitalo K: Matrix reloaded to circulation hits the tumor target. Cancer Cell 2003, 3:513–514
5. St. Croix B, Rago C, Velculescu V, Traverso G, Romans KE, Montgomery E, Lal A, Riggins GJ, Lengauer C, Vogelstein B, Kinzler KW: Genes expressed in human tumor endothelium. Science 2000, 289:1197–1202
6. Ruoslahti E: Specialization of tumour vasculature. Nat Rev Cancer 2002, 2:83–90
7. Friedlander M, Theesfeld CL, Sugita M, Fruttiger M, Thomas MA, Chang S, Cheresh DA: Involvement of integrins $\alpha v\beta3$ and $\alpha v\beta5$ in ocular neovascular diseases. Proc Natl Acad Sci USA 1996, 93:9764–9769
8. Gerlag DM, Borges E, Tak PP, Ellerby HM, Bredesen DE, Pasqualini R, Ruoslahti E, Firestein GS: Suppression of murine collagen-induced arthritis by targeted apoptosis of synovial neovasculature. Arthritis Res 2001, 3:357–361

9. Hoffman JA, Giraudo E, Singh M, Zhang L, Inoue M, Porkka K, Hanahan D, Ruoslahti E: Progressive vascular changes in a transgenic mouse model of squamous cell carcinoma. Cancer Cell 2003, 4:383–391

10. Joyce JA, Laakkonen P, Bernasconi M, Bergers G, Ruoslahti E, Hanahan D: Stage-specific vascular markers revealed by phage display in a mouse model of pancreatic islet tumorigenesis. Cancer Cell 2003, 4:393–403

11. Rajotte D, Arap W, Hagedorn M, Koivunen E, Pasqualini R, Ruoslahti E: Molecular heterogeneity of the vascular endothelium revealed by in vivo phage display. J Clin Invest 1998, 102:430–437

12. Zhang L, Hoffman JA, Ruoslahti E: Molecular profiling of heart endothelial cells. Circulation 2005, 112:1601–1611

13. Kolonin MG, Sun J, Do KA, Vidal CI, Ji Y, Baggerly KA, Pasqualini R, Arap W: Synchronous selection of homing peptides for multiple tissues by in vivo phage display. FASEB J 2006, 20:979–981

14. Liu C, Bhattacharjee G, Boisvert W, Dilley R, Edgington T: In vivo interrogation of the molecular display of atherosclerotic lesion surfaces. Am J Pathol 2003, 163:1859–1871

15. Zhang L, Giraudo E, Hoffman JA, Hanahan D, Ruoslahti E: Lymphatic zip codes in premalignant lesions and tumors. Cancer Res 2006, 66:5696–5706

16. Koivunen E, Wang B, Ruoslahti E: Phage libraries displaying cyclic peptides with different ring sizes: ligand specificities of the RGD-directed integrins. Biotechnology 1995, 13:265–270

17. Laakkonen P, Porkka K, Hoffman JA, Ruoslahti E: A tumor-homing peptide with a lymphatic vessel-related targeting specificity. Nat Med 2002, 8:751–755

18. Laakkonen P, Akerman ME, Biliran H, Yang M, Ferrer F, Karpanen T, Hoffman RM, Ruoslahti E: Antitumor activity of a homing peptide that targets tumor lymphatics and tumor cells. Proc Natl Acad Sci USA 2004, 101:9381–9386

19. Esko JD, Stewart TE, Taylor WH: Animal cell mutants defective in glycosaminoglycan biosynthesis. Proc Natl Acad Sci USA 1985, 82:3197–3201

20. El-Sheikh A, Liu C, Huang H, Edgington TS: A novel vascular endothelial growth factor heparin-binding domain substructure binds to glycosaminoglycans in vivo and localizes to tumor microvascular endothelium. Cancer Res 2002, 62:7118–7123

21. Järvinen M: Healing of a crush injury in rat striated muscle. 3. A microangiographical study of the effect of early mobilization and immobilization on capillary ingrowth. Acta Pathol Microbiol Scand 1976, 84A:85–94

22. Thompson WD, Harvey JA, Kazmi MA, Stout AJ: Fibrinolysis and angiogenesis in wound healing. J Pathol 1991, 165:311–318

23. Dyson M, Young SR, Hart J, Lynch JA, Lang S: Comparison of the effects of moist and dry conditions on the process of angiogenesis during dermal repair. J Invest Dermatol 1992, 99:729–733

24. Paavonen K, Puolakkainen P, Jussila L, Jahkola T, Alitalo K: Vascular endothelial growth factor receptor-3 in lymphangiogenesis in wound healing. Am J Pathol 2000, 156:1499–1504

25. Altschul SF, Madden TL, Schaffer AA, Zhang J, Zhang Z, Miller W, Lipman DJ: Gapped BLAST and PSI-BLAST: a new generation of protein database search programs. Nucleic Acid Res 1997, 25:3389–3402

26. Joliot A: Transduction peptides within naturally occurring proteins. Sci STRE 2005, 313: pe54

27. Zorko M, Langel U: Cell penetrating peptides: mechanism and kinetics of cargo delivery. Adv Drug Deliv Rev 2005, 57:529–545

28. Porkka K, Laakkonen P, Hoffman JA, Bernasconi M, Ruoslahti E: A fragment of the HMGN2 protein homes to the nuclei of tumor cells and tumor endothelial cells in vivo. Proc Natl Acad Sci USA 2002, 99:7444–7449

29. Christian S, Pilch J, Akerman ME, Porkka K, Laakkonen P, Ruoslahti E: Nucleolin expressed at the cell surface is a marker of endothelial cells in angiogenic blood vessels. J Cell Biol 2003, 163:871–878

30. Zurita AJ, Troncoso P, Cardo-Vila M, Logothetis CJ, Pasqualini R, Arap W: Combinatorial screenings in patients: the interleukin-11 receptor as a candidate target in the progression of human prostate cancer. Cancer Res 2004, 64:435–439

31. Casanovas O, Hicklin DJ, Bergers G, Hanahan D: Drug resistance by evasion of antiangiogenic targeting of VEGF signaling in late-stage pancreatic islet tumors. Cancer Cell 2005, 8:299–309

32. Jain RK: Normalization of tumor vasculature: an emerging concept in antiangiogenic therapy. Science 2005, 307:58–62

33. van den Born J, Salmivirta K, Henttinen T, Ostman N, Ishimaru T, Miyaura S, Yoshida K, Salmivirta M: Novel heparan sulfate structures revealed by monoclonal antibodies. J Biol Chem 2005, 280: 20516–20523

34. Freeman C, Liu L, Banwell MG, Brown KJ, Bezos A, Ferro V, Parish CR: Use of sulfated linked cyclitols as heparin sulfate mimetics to probe the heparin/heparin sulfate binding specificity of proteins. J Biol Chem 2005, 280:8842–8849

35. Kreuger J, Spillmann D, Li JP, Lindahl U: Interactions between heparin sulfate and proteins; the concept of specificity. J Cell Biol 2006, 174:323–327

36. Dawson DW, Frieda S, Pearce A, Zhong R, Silverstein RL, Frazier WA, Bouck NP: CD36 mediates the in vitro inhibitory effects of thrombospondin-1 on endothelial cells. J. Cell Biol 1997, 138:707–717

37. Iruela-Arispe ML, Lombardo M, Krutzsch HC, Lawler J, Roberts DD: Inhibition of angiogenesis by thrombospondin-1 is mediated by 2 independent regions within the type 1 repeats. Circulation 1999, 100:1423–1431

Stage-specific vascular markers revealed by phage display in a mouse model of pancreatic islet tumorigenesis

Johanna A. Joyce,[1,3] Pirjo Laakkonen,[2,3,4] Michele Bernasconi,[2,5] Gabriele Bergers,[1,6] Erkki Ruoslahti,[2,*] and Douglas Hanahan[1,*]

[1]Department of Biochemistry and Biophysics, Diabetes and Comprehensive Cancer Centers, University of California, San Francisco, 513 Parnassus Avenue, San Francisco, California 94143
[2]Cancer Research Center, The Burnham Institute, 10901 North Torrey Pines Road, La Jolla, California 92037
[3]These authors contributed equally to this work.
[4]Present address: Molecular/Cancer Biology Laboratory, Biomedicum Helsinki, University of Helsinki, P.O.B. 63 (Haartmaninkatu 8), FIN-00014 Helsinki, Finland.
[5]Present address: Functional Genomics Unit, Divisions of Infectious Diseases and Oncology, The University Children's Hospital of Zürich, August-Forel Strasse 1 CH-8008 Zürich, Switzerland.
[6]Present address: Department of Neurological Surgery, University of California, San Francisco, 513 Parnassus Avenue, San Francisco, California 94143.
*Correspondence: dh@biochem.ucsf.edu (D.H.); ruoslahti@burnham.org (E.R.)

Summary

The vasculature in the angiogenic stages of a mouse model of pancreatic islet carcinogenesis was profiled in vivo with phage libraries that display short peptides. We characterized seven peptides distinguished by their differential homing to angiogenic progenitors, solid tumors, or both. None homed appreciably to normal pancreatic islets or other organs. Five peptides selectively homed to neoplastic lesions in the pancreas and not to islet β cell tumors growing subcutaneously, xenotransplant tumors from a human cancer cell line, or an endogenously arising squamous cell tumor of the skin. Three peptides with distinctive homing to angiogenic islets, tumors, or both colocalized with markers that identify endothelial cells or pericytes. One peptide is homologous with pro-PDGF-B, which is expressed in endothelial cells, while its receptor is expressed in pericytes.

Introduction

Angiogenesis, the formation of new blood vessels, is essential for tumor growth. The transition from normal to neoplastic vasculature during tumorigenesis has been termed the "angiogenic switch," and both positive and negative regulators of the switch have been identified (Hanahan and Folkman, 1996). The vascular anatomy of tumors is typically distinct from that of normal tissues (Carmeliet and Jain, 2000). In contrast to their normal counterparts, tumor vessels are tortuous and dilated and show reduced vessel integrity. Tumor vessels often have numerous fenestrae or discontinuities, loose interendothelial junctions, and a discontinuous or absent basement membrane, collectively resulting in vessel leakiness (Carmeliet and Jain, 2000; Hashizume et al., 2000).

We are only beginning to understand the molecular events underlying the pronounced abnormalities evident in the angiogenic vasculature of tumors and progenitor lesions. Previous studies have shown that a number of genes are upregulated during the transition from normal to tumor blood vessels, including the integrins $\alpha v\beta 3$, $\alpha v\beta 5$, and $\alpha 5\beta 1$; several matrix metalloproteinases; and various endothelial growth factor receptors (Hanahan and Folkman, 1996; Ruoslahti, 2002). Recently, St. Croix et al. further showed, using a comparative RNA expression profiling technology (SAGE), that a number of genes or EST's were selectively expressed or upregulated in the tumor endothelium of human colorectal cancer, relative to the corresponding normal colonic vasculature (St. Croix et al., 2000). This approach relied on substantive differences in gene expression to identify tumor-specific endothelial markers, which will likely only reveal a subset of alterations that distinguish normal and tumor blood vessels. Specific binding of phage from libraries that can display more than a billion random peptide sequences offers a complementary approach for comparative screening. In vivo phage display screening has proven to be a powerful method for un-

---

S I G N I F I C A N C E

While there is abundant evidence that tumor vasculature is functionally and morphologically aberrant, we show herein using a peptide epitope profiling technology that the angiogenic vasculature in premalignant lesions is distinguishable from normal as well as tumor vessels in a model of multistage tumorigenesis. Moreover, both angiogenic progenitor and tumor vessels in the pancreas have molecular signatures distinct from tumors growing in or under the skin, even of the analogous cell type. The stage and organ specificities of particular homing peptides may prove instructive about mechanisms regulating the neovasculature in different pathways of tumorigenesis, suggest means to detect and distinguish premalignant and malignant lesions noninvasively, and predict differential sensitivity to therapeutic agents targeting angiogenesis.
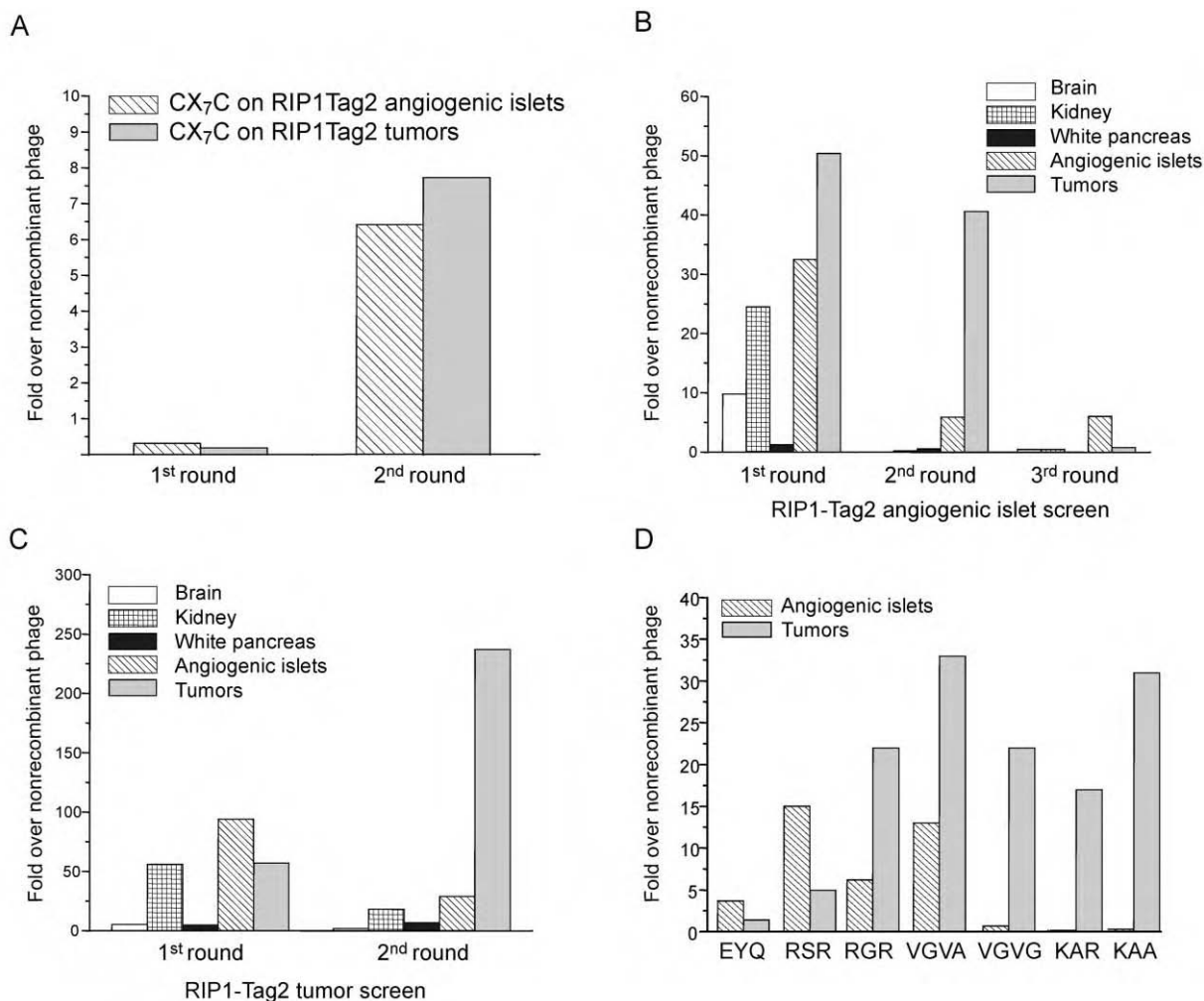

Figure 1. Isolation of stage-specific phage using ex vivo and in vivo phage display

A: Ex vivo screening on cells derived from RIP1-Tag2 angiogenic islets or tumors using the CX$_7$C peptide library displayed on T7 phage. The enriched phage pools were used for subsequent in vivo homing to RIP1-Tag2 angiogenic islets (three rounds of selection) (**B**) and tumors (two rounds of selection) (**C**). **D:** In vivo homing of individual phage to RIP1-Tag2 angiogenic islets and tumors.

covering differences among individual vascular beds in normal organs (Pasqualini and Ruoslahti, 1996; Rajotte et al., 1998) and has also yielded peptides that specifically home to blood vessels or lymphatics in tumors (Arap et al., 1998; Laakkonen et al., 2002; Porkka et al., 2002). The targets for these peptides in blood vessels include the $\alpha v\beta 3$ and $\alpha v\beta 5$ integrins (Arap et al., 1998) and aminopeptidase N (Pasqualini et al., 2000).

In this and a companion study (Hoffman et al., 2003 [this issue of *Cancer Cell*]), we set out to use phage-display profiling to ask whether additional levels of neoplastic vascular specialization might exist in tumor development. We sought to distinguish the vessels of premalignant angiogenic lesions from those of angiogenic solid tumors and to examine whether differences exist between angiogenic vessels of tumors developing in different organs. Previous studies have profiled differences between normal blood vessels and the vasculature of transplanted tumors in immunodeficient mice. Unlike these transplanted tumors, transgenic tumor models provide an opportunity to examine pre-neoplastic changes unfolding in different organs in a more physiologically relevant microenvironment.

We used a prototypical mouse model of multistage tumorigenesis, the RIP1-Tag2 transgenic model of islet cell carcinoma (Hanahan, 1985), to address our hypothesis that the vasculature of pre-neoplastic lesions differs from that of established tumors. RIP1-Tag2 transgenic mice express the SV40 T antigens (Tag) under the control of the insulin gene promoter, which elicits the sequential development of tumors in the islets of Langerhans over a period of 12–14 weeks. Hyperplastic islets begin to appear at around 4 weeks of age, and angiogenesis is activated a few weeks later in a subset of the hyperplastic islets, producing angiogenic (dysplastic) islets (Bergers et al., 1998; Folkman et al., 1989). Solid tumors form beginning at 9 to 10 weeks, initially presenting as small nodules that grow and progress to large islet tumors with well-defined margins, as well as two classes of invasive carcinoma (Lopez and Hanahan, 2002). We set out to identify stage-specific molecular markers accessible via the circulation, either on the surface of endothelial cells, their periendothelial support cells (pericytes and smooth muscle cells), or even tumor cells themselves (as a result of the hemorrhagic,

leaky angiogenic vasculature). We successfully selected phage pools that homed preferentially to different stages during RIP1-Tag2 tumorigenesis. In addition to "pan-angiogenic" markers shared by many types of tumors, we identified vascular target molecules that are characteristic of this tumor's tissue of origin and are not expressed in the vessels of several tumor types growing in or under the skin. We have begun to investigate the binding partners for these peptides and present evidence linking one peptide to a vascular signaling circuit involving PDGF ligands expressed in endothelial cells and their receptor PDGFRβ, expressed in pericytes of the angiogenic vasculature.

Results

Isolation of stage-specific phage from RIP1-Tag2 mice

RIP1-Tag2 mice develop multifocal angiogenic islet progenitors and then solid tumors in a stepwise manner, such that at 12 weeks of age, each mouse will typically have approximately 50 angiogenic islets and 2–6 small tumors. This circumstance allowed us to use 12-week-old mice to select for phage binding to angiogenic islet progenitors and/or tumors in the same mouse. In order to enrich for phage that bind to RIP1-Tag2 target cells (endothelial, perivascular, and tumor), we included a pre-selection step (Laakkonen et al., 2002; Porkka et al., 2002) on cell suspensions prepared from pancreatic lesions. Two rounds of ex vivo selection from a CX_7C peptide library on cell suspensions from angiogenic islets or solid tumors yielded phage pools that bound 7- to 8-fold over a control, nonrecombinant phage to their respective target cells (Figure 1A). These enriched phage pools were used in subsequent in vivo rounds to select for phage that would home specifically to either angiogenic islets or tumors in RIP1-Tag2 mice.

Three rounds of in vivo selection on angiogenic islets resulted in a phage pool that selectively homed to angiogenic islets. The homing to the islets was 7-fold higher than to tumors in the same mouse (Figure 1B). There was no homing to control organs. The tumor selection yielded a pool that showed an 8-fold preference for tumors versus angiogenic islets in the same mouse following two rounds of in vivo selection (Figure 1C).

Sequencing of phage from the selected pools identified a number of peptide sequences that were represented more than once, and these were tested for their ability to bind cell suspensions prepared from angiogenic islets and tumors. Six of the phage selected for further analysis were from the tumor screen (referred to as KAA, RGR, RSR, VGVA, VGVG, and KAR), and one (EYQ) was picked from the angiogenic screen. Peptide sequences corresponding to each of these peptide motifs are shown in Table 1. All of these peptides are linear, although the phage library used here (CX_7C) was designed to express peptides cyclized by a covalent bond between two cysteine residues. However, a library of this design does contain a minority of linear peptides. A stop codon occurring within the random insert will cause truncation of the peptide, and a frameshift mutation frequently changes the second cysteine into valine. It may be that the target molecules in the RIP1-Tag2 tumors selected for linear peptides. In the companion study (Hoffman et al., 2003), the same library yielded cyclic homing peptides. The RIP1-Tag2 homing phage fall into three classes based on their homing either to angiogenic islets or to tumors in vivo (Figure 1D) and their ex vivo binding patterns: tumor-selective phage

(KAA, KAR, and VGVG), angiogenic islet-selective phage (RSR and EYQ), and phage that home to both types of angiogenic lesions (VGVA and RGR). Some of the selected peptides that share similar peptide motifs also display similar homing patterns. For example, KAA and KAR (CKAAKNK and CKGAKAR = XBXXBXB, where B represents basic residues and X denotes uncharged residues) both preferentially home to tumors over angiogenic islets. However, other related peptides such as RGR and RSR (CRGRRST and CRSRKG = XBXBBX) have quite different homing capabilities. Interestingly, all of these peptides are distinct from those found previously in phage display screens of transplant tumors (Arap et al., 1998; Laakkonen et al., 2002; Porkka et al., 2002).

Stage-specific homing of fluorescein-conjugated peptides

To confirm that the selective phage homing was due to the displayed peptide sequences, we studied the localization of fluorescein-conjugated peptides after intravenous injection; one peptide from each homing class was selected for detailed analysis. We used 8-week-old RIP1-Tag2 mice to examine peptide localization during the angiogenic switch and 12-week-old RIP1-Tag2 mice to visualize both angiogenic islets and tumors.

The observed peptide localization profiles in each case closely mimicked that of the cognate phage, as shown in Figure 1D, with each peptide falling into the same of the three homing classes. Figure 2 illustrates the peptide localization for these three representative fluorescein-conjugated peptides: RSR (angiogenic-selective), KAA (tumor-selective), and RGR (angiogenic- and tumor-homing). RSR shows abundant accumulation in RIP1-Tag2 angiogenic islets (Figure 2B) but little or no localization in tumors (Figure 2C) or normal islets (Figure 2A). KAA shows abundant localization in RIP1-Tag2 tumors (Figure 2F) but little or no localization in angiogenic islets (Figure 2E) or normal islets (Figure 2D). Finally, RGR localizes in both RIP1-Tag2 angiogenic islets (Figure 2H) and tumors (Figure 2I) but there is little or no peptide in normal islets (Figure 2G). It was somewhat unexpected that RSR, which was selected from the tumor phage screening, preferentially bound to angiogenic islets. It seems that the epitope this peptide binds to is present both in tumors and angiogenic islets, but is more abundant in angiogenic islets. This result could also be indicative of the heterogeneity of the pools of angiogenic islets or tumors isolated by gross examination, in which there are multiple lesions of differing grades within each group. Hence, a gross selection of the tumor pool may in fact include some large, advanced angiogenic islets that can only be definitively distinguished by histological grading, which was performed in conjunction with the peptide homing to the different lesions.

Homing of the peptides to the pancreatic islet lesions was specific: little or no homing was detected in normal islets, brain, liver, lung, and spleen (Figures 2K and 2L and data not shown). Fluorescence was detected in kidney, presumably as a result of uptake from glomerular filtrate (Figure 2J). Representative figures of control tissues from a RIP1-Tag2 mouse injected with fluorescein-conjugated RGR peptide are shown in Figures 2J–2L. A similar absence of fluorescence in control tissues was observed for all other injected peptides (data not shown). In addition, control peptides did not show specific homing to any of the RIP1-Tag2 lesional stages or to a number of normal tissues.
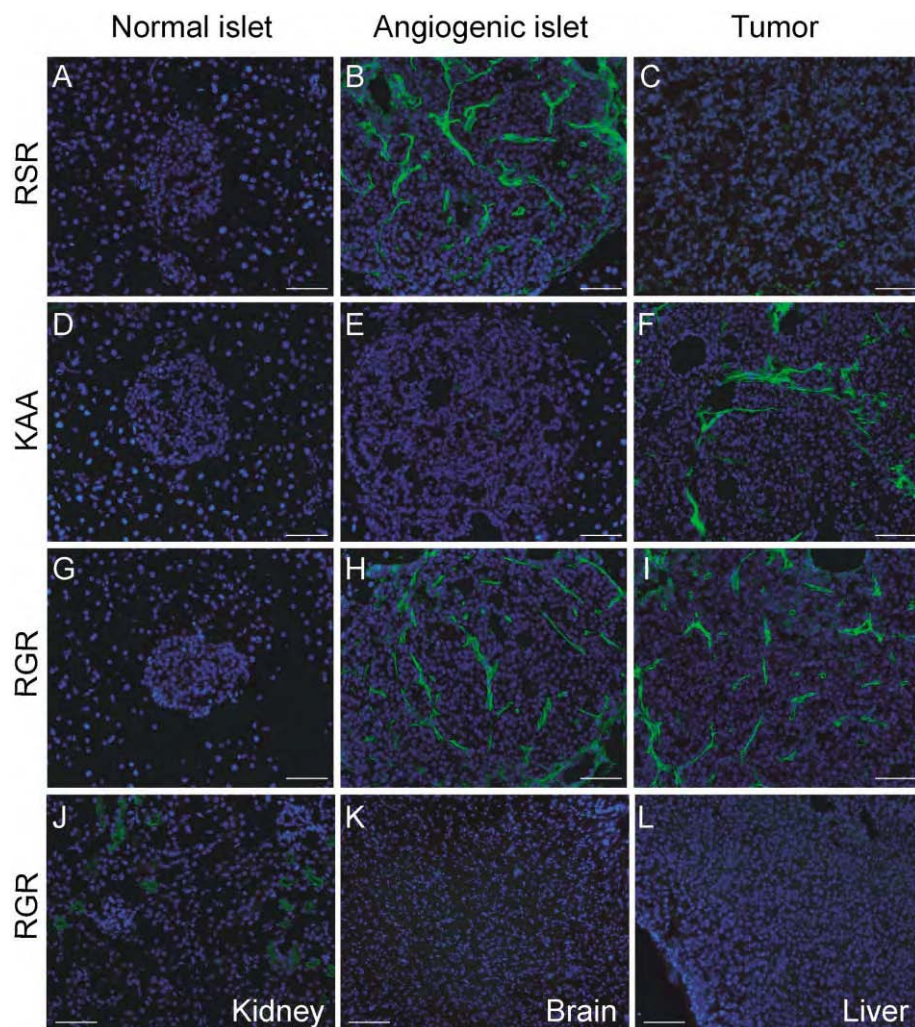
Figure 2. Stage-specific homing of fluorescein-conjugated peptides in RIP1-Tag2 model

Visualization of an angiogenic islet-selective peptide (RSR) homing is shown in normal islet (**A**), angiogenic islet (**B**), and tumor (**C**). Homing profiles are also shown for a tumor-selective peptide (KAA) to normal islet (**D**), angiogenic islet (**E**), and tumor (**F**), as well as of a peptide (RGR) that homes to both angiogenic islets and tumors (**G**, normal islet; **H**, angiogenic islet; and **I**, tumor). Control tissues (**J**, kidney; **K**, brain; and **L**, liver) from a RIP1-Tag2 mouse injected with fluorescein-conjugated RGR peptide are also presented. Similar absence of fluorescence in control tissues was observed for all other injected peptides, indicative of a lack of specific homing. The scale bar corresponds to 50 μM.

Fluorescein-conjugated peptides colocalize with vascular markers

We reasoned that intravenous administration of the phage libraries would select for phage carrying peptides that bind to endothelial molecules specific for the target vasculature. The expectation of endothelial selectivity is based upon the preferential exposure of phage to luminal cells of the vasculature, as well as the appreciable size of the phage and the short time the phage are allowed to circulate (Pasqualini and Ruoslahti, 1996). In order to test this expectation, tissues were collected following i.v. infusion with the various fluorescein-conjugated peptides, sectioned, and evaluated with endothelial cell markers. The primary analysis involved immunostaining with a mouse pan-endothelial cell antigen (MECA32) antibody that recognizes a dimer of 50–55 kDa protein subunits present on all endothelial cells (Hallman et al., 1995; Leppink et al., 1989) (Figures 3B, 3C, 3H, 3I, 3N, and 3O). Additional analyses (not shown) involved immunostaining to reveal CD31/PECAM or systemic infusion of a fluorescent-labeled lectin that binds to the endothelial lumen. In addition, tissue sections from peptide-infused mice were stained with an antibody recognizing NG2, a marker of the neovascular pericytes (Schlingemann et al., 1990, 1991) (Figures 3E, 3F, 3K, 3L, 3Q, and 3R). Remarkably, all three peptides (RSR, KAA, and RGR) show some colocalization both with endo-

thelial cell and pericyte markers, indicating that each homes to and binds moieties associated with both cell types (Figure 3 and data not shown). Again, there was no colocalization of these peptides with those same markers in the adjacent exocrine pancreas or in normal pancreatic islets; tissue sections stained with MECA32 and NG2 showed some colocalization, consistent with the proximity of endothelial cells and pericytes (Figures 3S–3U).

The apparent homing of peptides representing all three classes of stage specificity to both pericytes and endothelial cells was unexpected. It may be pertinent that the RIP1-Tag2 tumor vasculature is known to be leaky, as evidenced by extensive microhemorrhaging (Parangi et al., 1995) and morphometric analysis (Hashizume et al., 2000; Morikawa et al., 2002; Thurston et al., 1998), such that the circulating phage pool likely had access to the extraluminal vascular microenvironment, where receptors on pericytes and in the extracellular matrix could be accessible. It is known that the vasculature of both angiogenic islets and tumors is leaky (Morikawa et al., 2002). However, reciprocal homing of the peptides that recognize the angiogenic islet but not tumor vessels, and vice versa, excludes the possibility that the recognition of angiogenic islet versus tumor vessels would simply be caused by differences in the leakiness of the
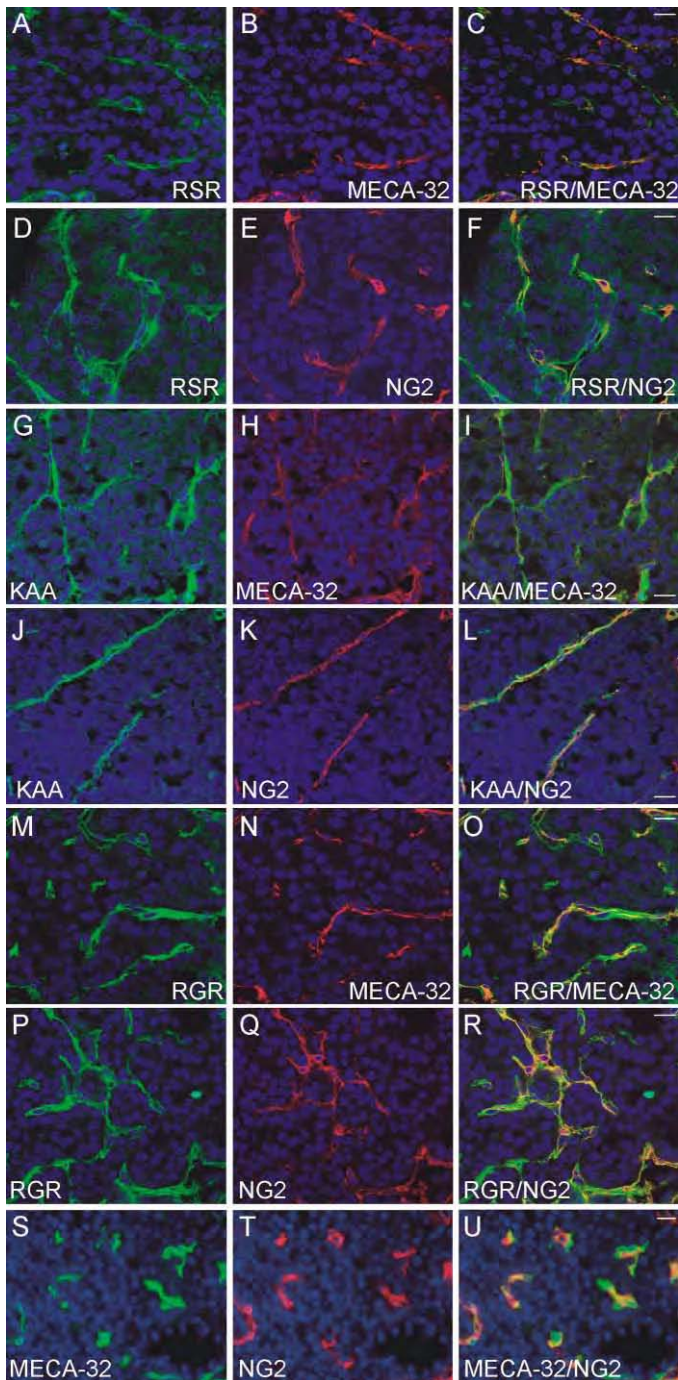
Figure 3. Colocalization of fluorescein-conjugated peptides with vascular markers in RIP1-Tag2 islet lesions

RSR peptide localization in an angiogenic islet is shown in (**A**) and (**D**) (green), while co-staining for MECA32 (red) and the merge are shown in (**B**) and (**C**). Co-staining for NG2 (red) is shown in (**E**), with the merge in (**F**). KAA peptide localization in a tumor is shown in (**G**) and (**J**) (green), while co-staining for MECA32 (red) and the merge are shown in (**H**) and (**I**). Co-staining for NG2 (red) is shown in (**K**), with the merge in (**L**). RGR peptide localization in an angiogenic islet is shown in (**M**) and (**P**) (green), while co-staining for MECA32 (red) and the merge are shown in (**N**) and (**O**). Co-staining for NG2 (red) is shown in (**Q**), with the merge in (**R**). Staining for endothelial cells (MECA32) (**S**) and pericytes (NG2) (**T**) in tumor sections demonstrated their close association (**U**). Scale bar: 10 μm.

vessels. The ex vivo pre-selection step we used to enrich for RIP1-Tag2-specific targets may have similarly selected for non-luminal endothelial binding partners, but it should be emphasized that any peptide selected ex vivo must also have been accessible via the circulation during the in vivo selections. Consistent with this logic, phage-displaying peptides that bind to the pericyte marker, NG2, have previously been shown to home to a transplant tumor in vivo (Burg et al., 1999).

Specificity of in vivo homing to islet tumors in the pancreas

Selection of phage that home to the vasculature of neoplastic lesions in RIP1-Tag2 mice can be envisioned to identify two classes of peptides: those whose cognate receptors are specific to angiogenic islets and/or tumors in the pancreas and those that also home to the angiogenic vasculature in other tumor types. Therefore, we asked whether phage and peptides selected in pancreatic neoplasias would home to two different transplant tumors growing subcutaneously or to de novo skin tumors induced in another transgenic mouse model.

βTC3 transplant tumors arise following subcutaneous inoculation of nude mice with cultured islet tumor-derived (βTC3) cells (Efrat et al., 1988), allowing the study of islet tumors and their vasculature outside of their natural environment in the pancreas. Because the vasculature of a subcutaneously grown βTC3 tumor derives from skin, we also tested another subcutaneous transplant tumor, arising from inoculation of the MDA-MB-435 human breast carcinoma cell line. Finally, K14-HPV16 mice, another well-studied transgenic mouse model of cancer that develop tumors of the squamous epithelial cells of the skin (Arbeit et al., 1994; Coussens et al., 1996), allowed us to compare RIP1-Tag2 islet tumors to a tumor with similar multistage pathogenesis arising in a different tissue. The relative homing efficiencies in the various tumor models of the phage from the RIP1-Tag2 tumor screen fall broadly into two categories: those that selectively home to RIP1-Tag2 tumors (KAA, RGR, VGVA) and those that show a more general homing to other tumors in addition to RIP1-Tag2 (VGVG, KAR) (Figure 4A). The phage homing data were supported by i.v. injection of fluorescein-conjugated peptides corresponding to the phage. Results for the three representative peptides are summarized in Figure 4B, and an example of the tissue fluorescence produced following injection of the KAR peptide in different tumors is shown in Figures 4C–4E.

Homing during non-tumor angiogenesis was examined using angiogenesis in subcutaneously implanted matrigel plugs. All peptides except one showed no homing to the matrigel plugs. The RGR peptide appeared in a punctate manner in some blood vessels. However, the intensity was much lower and the pattern quite different than in RIP-Tag lesions (data not shown). This indicates that this set of peptides are selective for neovascularization during tumorigenesis and are not general markers of neovessel formation.

Identification of candidate vascular receptors

The set of peptides homing to angiogenic neoplasias in the pancreas were applied to database searches, seeking to identify mouse proteins with sequences homologous to the peptides. Table 1 lists candidate proteins with such homologies that were deemed to be of interest. In theory, these proteins could correspond to putative ligands mimicked by the phage-displayed
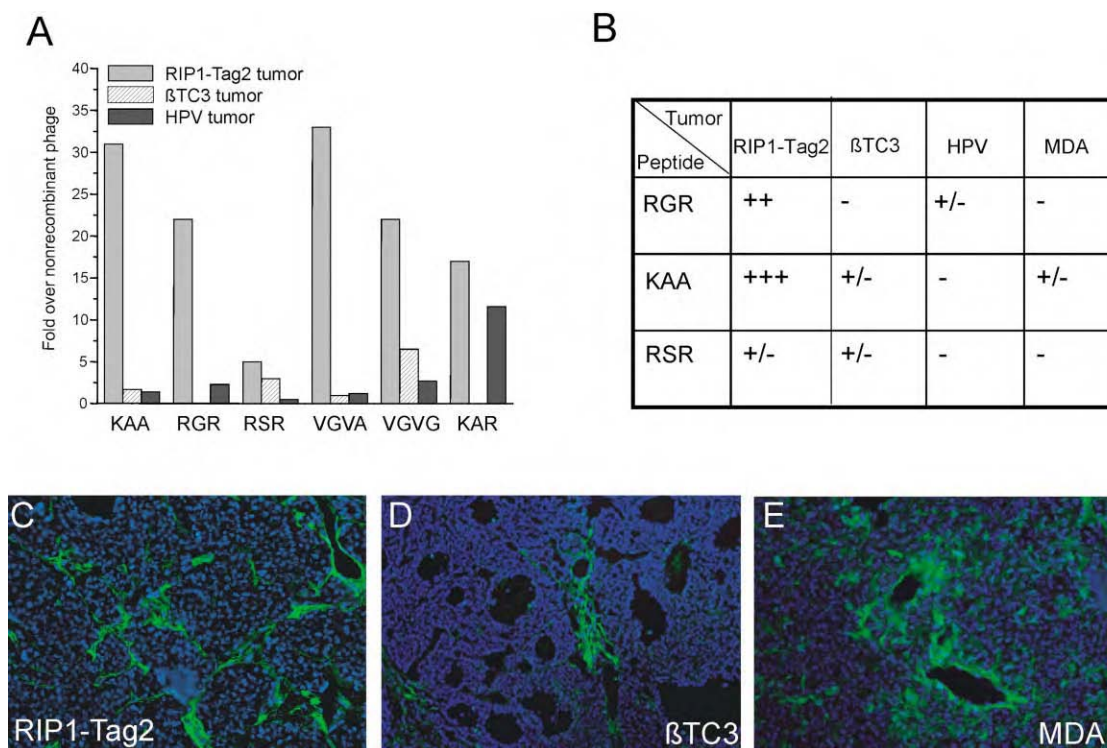
Figure 4. Evaluation of the neoplastic specificity of selected homing phage and peptides

A: Bar graph showing homing efficiency of individual phage to a pancreatic islet tumor in a RIP1-Tag2 mouse, a βTC3-derived subcutaneous transplant tumor in a nude mouse, and a squamous cell carcinoma in a K14-HPV16 mouse.

B: Table summarizing the relative homing of fluorescein-conjugated peptides to different tumor models. +++ indicates strong homing, as revealed by the fluorescent intensity of i.v. injected peptide, ++ indicates moderate homing, + indicates weak homing, - indicates absence of homing. Representative images of fluorescein-conjugated KAR peptide homing to a RIP1-Tag2 pancreatic islet tumor (**C**), a βTC3 subcutaneous tumor (**D**), and an MDA subcutaneous tumor (**E**) are also shown. Magnification 200×.

peptides. Many of the candidate proteins have been previously associated with the vasculature. One protein, collagen XII, was found to share homology with two peptides: KAR (CKGAKAR) and VGVA (FRVGVADV), though in different structural domains. It is interesting to note that collagen XII was also identified by gene expression profiling as a gene that is overexpressed in tumor endothelial cells (St. Croix et al., 2000; and http://mendel.imp.unvie.ac.at/SEQUENCES/TEMS/mainpgs/temtable.html).

It was somewhat surprising that homologies to peptide se-quences in two cell surface receptors, fibroblast growth factor receptor 1 (FGFR1) and Tie-1, were revealed by homology searching, as phage-displayed peptides have traditionally been thought to mimic ligands not receptors. However, in the case of FGFR1, the particular peptide sequence (YQLDV) has been reported to be in the ligand binding domain D2 (Plotnikov et al., 1999), suggesting the possibility that the phage displaying this peptide may in fact be binding to FGFR1 ligands, i.e., the fibro-blast growth factors (FGFs). It is well known that many of the

Table 1. Candidate mouse proteins sharing motifs with homing peptides

Peptide	Peptide sequence	Extended motif	Mouse protein with the motif	Accession number
RGR	CRGRRST	RGRRS	PDGF-B	P31240
		RGRR	Stromal interaction molecule 2	Q9P246
RSR	CRSRKG	CRSR-G	Cadherin EGF LAG receptor 1	O35161
KAA	CKAAKNK	CKA-K	WNT-2	NPO76142
KAR	CKGAKAR	CKGAKA	Collagen XII	Q60847
		AKAR	Collagen XII	Q60847
		GAKAR	Claudin 9	Q9ZOS7
VGVA	FRVGVADV	F-VGVADV	Collagen XII	Q60847
		RVGV	Collagen XII	Q60847
EYQ	CEYQLDVE	CEYQL	Semaphorin 4C	Q64151
		YQLDV	FGFR1	P16092
		YQLDV	Tie-1	Q06806

Peptides were analyzed using a BLAST (NCBI) search against the SWISSPROT database, using the option for short nearly exact matches, to identify mouse proteins with homologous sequences.

heparin binding FGFs are sequestered in the extracellular matrix and basement membrane by binding to heparan sulfate proteoglycans (Ornitz and Itoh, 2001), which is consistent with phage homing to these FGF depots in vivo. As the Tie-1 receptor is an orphan receptor tyrosine kinase, ligand binding information is not currently available; however, the peptide sequence homology is in the extracellular domain (Sato et al., 1993).

Another provocative homology was seen for the RGR peptide (CRGRRST), which is contained within the B chain of the pro-form of platelet-derived growth factor (PDGF-B), a known ligand for the transmembrane receptor tyrosine kinase PDGFRβ. The RGR sequence homology (RGRRS) spans the pro-peptide cleavage site of pro-PDGF-B (Johnsson et al., 1984). To investigate the hypothesis that the RGR peptide was homing to PDGFRβ by virtue of this homology, we transfected 293T cells with a fusion gene designed to overexpress PDGFRβ. The binding of RGR phage was 20-fold more efficient to PDGFRβ-transfected cells than nontransfected cells. In contrast, no binding above the background was detected toward cells transfected with vascular endothelial growth factor receptor 2 (VEGFR2) (Figure 5A). Moreover, when we tested the RSR phage, which has a peptide sequence similar to RGR, no specific binding was observed either to PDGFRβ- or VEGFR2-transfected cells (Figure 5A). The association of RGR with PDGFRβ was further substantiated when intravenously injected fluorescein-conjugated RGR peptide was shown to colocalize with PDGFRβ, visualized by subsequent immunostaining of tissue sections from RIP1-Tag2 tumors. Merging of the RGR-FITC image (Figure 5B, panel a) with the antibody staining for PDGFRβ (Figure 5B, panel b) revealed almost complete colocalization (Figure 5B, panels c and d).

Discussion

We set out in this and the companion study (Hoffman et al., 2003) to characterize the vasculature during the discrete stages of organ-specific carcinogenesis, using a profiling technology based on peptide libraries displayed on the surface of bacteriophage. Phage that display a peptide with an appropriate binding specificity home via the circulation to the site of binding affinity. As such, phage profiling can reveal differences in the composition and properties of the vasculature of different organs and pathological lesions. Using as a target the RIP1-Tag2 mouse model of multistage tumorigenesis involving the pancreatic islets of Langerhans, we have identified peptides that discriminate between the vasculature of the premalignant angiogenic islets and the fully developed tumors. Most of the identified homing peptides appear to selectively detect vascular changes induced during tumorigenesis in the endocrine pancreas, but not in other tumors growing in or under the skin. Remarkably, three peptides representing one of the distinctive homing classes (to angiogenic progenitors, to tumors, or to both) each colocalized with markers separately identifying endothelial cells and pericytes in the angiogenic lesions. The sequences of the homing peptides suggest candidate proteins containing homologous sequences that are mimicked by peptide binding to the angiogenic vasculature.

Insights into organ-specific differences in neoplastic vasculature

The influence of tissue microenvironment in tumor development is increasingly appreciated (Coussens and Werb, 2002; Liotta
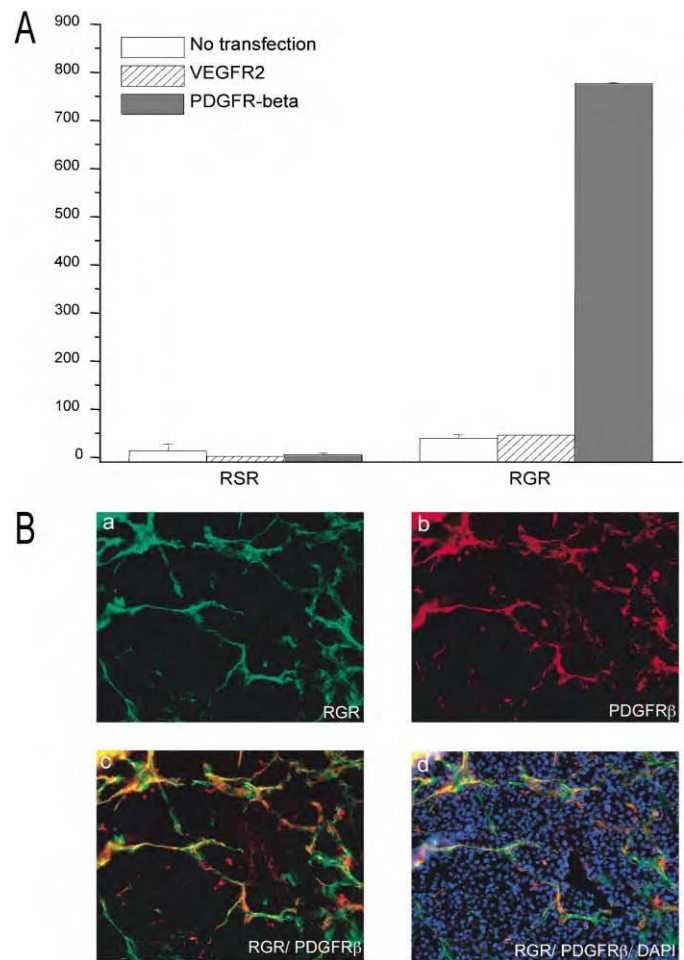

Figure 5. PDGFRβ is a candidate receptor for RGR peptide

A: Bar graph showing binding of RGR or RSR phage to 293T cells transfected with either the PDGFRβ, the related VEGFR2, or nontransfected cells. Y axis = fold over nonrecombinant phage.

B: Colocalization of fluorescein-conjugated RGR peptide (**a**, green) with the PDGFRβ antibody (**b**, red) and merged images (**c** and **d**) in RIP1-Tag2. Magnification 400×.

and Kohn, 2001). As developing neoplasias activate angiogenesis and recruit a neovasculature from the surrounding tissue microvascular bed, the organ microenvironment may influence the morphology and physiology of the tumor neovasculature. Evidence in support of organ-specific differences has come, for example, by comparing permeability in the vessels of transplant tumors as a function both of tumor type and the host tissue site (Hobbs et al., 1998; Roberts et al., 1998).

We asked whether tumors arising in their natural microenvironment are different from those developing in another "foreign" location by comparing endogenously arising RIP1-Tag2 tumors in the pancreas with βTC3 cell-derived tumors grown subcutaneously (the βTC3 cell line was established from a RIP1-Tag2 pancreatic islet tumor; Efrat et al., 1988). The results from both phage and peptide binding (Figure 4 and data not shown) indicate that some phage/peptides home to βTC3 subcutaneous tumors in addition to RIP1-Tag2 endogenous tumors, albeit less efficiently (e.g., VGVG). However, most of the other phage/

peptides do not show any appreciable homing to βTC3 tumors by comparison to RIP1-Tag2 tumors (e.g., KAA and VGVA), supporting the predominant role of the tissue microenvironment in influencing some of the receptors that are displayed on the cell surface.

Similar results were found for the two other tumor types we studied: squamous cell carcinomas of the epidermis arising in K14-HPV16 transgenic mice and subcutaneous xenograft tumors of the human MDA-MB-435 breast cancer cell line. KAR and VGVG were the only phage/peptides that homed appreciably to these models, whereas the other peptides showed a similar lack of homing, as for βTC3 tumors. Thus, the majority of phage-displayed and soluble peptides homed selectively to the tumor vasculature of RIP1-Tag2 tumors arising in their natural environment in the endocrine pancreas, showing little affinity for tumors growing subcutaneously or in the skin itself. By contrast, in the aforementioned study of tumor endothelial genes revealed by expression profiling (St. Croix et al., 2000), a number of the tumor-specific endothelial genes identified as upregulated in a colorectal cancer screen were also found in the tumor endothelium of other cancers (lung, brain, pancreas, and breast primary tumors; and a colorectal metastasis to the liver). Our method has clearly revealed a partially overlapping but distinctive set of markers. These results support the existence of both tumor-specific and tumor-generic vascular markers and may have implications for interpretation of data forthcoming from xenograft tumor models. If vascular markers are not recapitulated in transplant models representing a particular organ-specific cancer, then aspects of its phenotypic behavior and response to therapy (particularly targeted antiangiogenic and antivascular agents) may differ as well. Similar results have been seen in the companion study (Hoffman et al., 2003) comparing de novo epidermal squamous cell carcinomas in the K14-HPV16 mice with transplant tumors in the adjacent subcutaneous microenvironment.

Homing peptides revealing molecular anatomy of tumor vasculature

We have begun to investigate candidate binding moieties ("receptors") for the RIP1-Tag2 homing peptides, initially by searching protein databases for proteins that contain the homing peptide sequences and thus might represent the endogenous protein mimicked by the peptide. It is striking that a number of the candidate proteins revealed by the search have been implicated in some aspect of angiogenesis (PDGFs, WNTs, claudins, collagen XII, FGFR1, Tie-1). We chose to evaluate the PDGF-B homology in light of recent evidence implicating PDGF signaling in the angiogenic phenotype in the RIP-Tag2 model: three PDGF ligand genes are expressed in the tumor endothelial cells, while PDGF receptor β is expressed in tumor pericytes (Bergers et al., 2003). Pharmacological inhibition of PDGFR signaling in RIP1-Tag2 mice disrupted pericyte association with the tumor endothelium, inhibited angiogenesis, and reduced the vascularity of the islet tumors (Bergers et al., 2003). The results add to a knowledge base implicating PDGF signaling in pericyte-endothelial cell homeostasis, both in developing vessels (Betsholtz et al., 2001; Leveen et al., 1994; Lindahl et al., 1997; Soriano, 1994) and in tumors (Heldin and Westermark, 1999; Ostman and Heldin, 2001).

The evaluation of RGR in light of its homology to PDGF-B clearly suggests its homing is associated with PDGFR expres-

sion and/or signaling. The most compelling evidence comes from overexpressing PDGFRβ in cultured cells. There was a striking increase in the binding of the RGR phage to cells transfected with PDGFRβ, whereas transfection with a structurally related receptor tyrosine kinase, VEGFR2, had no effect on the binding. Moreover, systemically infused RGR colocalizes with virtually all of the PDGFRβ detected by immunostaining in angiogenic islets and tumors. Both lines of evidence support the model that RGR binds to PDGFRβ. There are, however, other data that complicate this simple conclusion. First, RGR colocalizes not only with a pericyte marker, NG2, consistent with PDGFRβ expression in pericytes, but also with an endothelial cell marker, MECA32, indicative of homing to endothelial cells (which do not typically express PDGFRβ—see Bergers et al., 2003). Second, the RGR peptide sequence overlaps the propeptide processing site and is thus only partially represented in mature PDGF-B ligand; moreover, the sequences for PDGF homo- and heterodimerization and for receptor binding are not at the N terminus of the mature ligand (Clements et al., 1991; Heldin and Westermark, 1999; Ostman et al., 1991). Thus it is not clear how RGR might bind either to PDGF ligands or receptors. These data lead us to suggest that RGR mimics a protein-protein interaction site in pro-PDGF-B that mediates its specific homing and mimics bona fide associations of pro-PDGF-B. One possible association for RGR is either with PDGFRβ itself or with a protein induced by its expression, given the enhanced binding seen in the transfected cells overexpressing PDGFRβ as well as the observed colocalization of RGR with PDGFRβ in angiogenic islets and tumors. It is interesting to note that a similar sequence is found in PDGF-D, a related PDGF ligand that also signals through PDGFRβ. The sequence RGRS is located in the secreted PDGF-D at the site of processing from the inactive to active form of PDGF-D (Bergsten et al., 2001; LaRochelle et al., 2001).

The additional colocalization of RGR with the endothelial cell marker MECA32 suggests that an RGR binding moiety is also expressed by endothelial cells or shared between pericytes and endothelial cells. While there is no obvious coimmunostaining of either endothelial cell marker (CD31, MECA32) with any of several pericyte markers (desmin, SMA, NG2) in the angiogenic islets or tumors (J.J. and G.B., unpublished observations), a small subset of FAC-sorted cells within RIP1-Tag2 tumors are positive for both CD31 and NG2 (G.B., unpublished observations). In addition, both cell types contribute to the vascular basement membrane and the extracellular matrix that separates and envelops them, and these structures could contain RGR binding motifs produced by one or both cell type and localized amongst them. Indeed, purified PDGF-B has been shown to bind various ECM and BM proteins, including collagens I–IV (Somasundaram and Schuppan, 1996), laminin-1, nidogen, and perlecan (Gohring et al., 1998). Another attractive candidate for RGR binding is the predicted prohormone processing enzyme that binds and cleaves pro-PDGF-B within the RGR homology. Interestingly, while the RGR phage and peptide homed effectively to angiogenic progenitor islets and solid tumors in RIP1-Tag2 mice, neither homed to angiogenic dysplasias or tumors in the HPV16 transgenic mice nor to the MDA-MB-435 subcutaneous tumors. These results suggest that PDGF signaling and the resultant vessel stabilization by pericytes may differ among tumors or that there are differences in pericyte activation and/or maturation (Morikawa et al., 2002). Alternatively, the blood

vessels in the squamous cell carcinomas, being less hemorrhagic, may limit the accessibility of the blood-borne phage and labeled peptides to the perivascular cells (see below).

Other homologies between homing peptides and endogenous proteins listed in Table 1 may also be significant. The fact that many of these proteins have been implicated in angiogenesis, or related biological processes, supports this prediction. For example, two of the peptides, KAR and VGVA, show homology to collagen XII, which is associated with blood vessels in the developing embryo (Bohme et al., 1995; Oh et al., 1993). Colocalization of both peptides with vascular markers (data not shown) is consistent with the predicted localization of collagen XII.

Lessons from profiling different tumor types

It is of interest to compare and contrast the results reported here to that of the companion study (Hoffman et al., 2003), which similarly used phage display libraries to profile the angiogenic dysplasias and squamous cell carcinomas that arise in the skin of K14-HPV16 transgenic mice. That study produced a series of homing peptides that were selective for angiogenic progenitors or solid tumors. And again, both tumor type-selective and tumor-generic phage were identified; their analysis focused on skin tumor-specific phage that did not home to the angiogenic vasculature in the stages of pancreatic islet carcinogenesis in RIP1-Tag2 mice. The skin-tumor homing peptides had different sequences from those identified herein, and their candidate cellular homologs (and prospective binding moieties) were distinctive. In sum, each study identified both tumor type-specific and stage-specific vascular homing peptides, further supporting the proposition that organ microenvironment imparts distinctive constraints on neoplastic development that affects the characteristics of the neovasculature induced to sustain tumor development and progression.

It is intriguing that the two organ sites of neoplastic development (skin and pancreas) preferentially selected phage with different cellular specificity. The HPV phage all homed exclusively to endothelial cells, whereas each of the RIP1-Tag2 phage representing the three homing classes (angiogenic progenitor, tumor, or both) chosen for analysis homed both to pericytes and to endothelial cells. This suggests significant differences in the vascular morphology and/or functionality in the skin and pancreas. One difference may be in vascular permeability. The islet tumors are blood red from hemorrhaging and the angiogenic vasculature is permeable to a variety of macromolecules (Hashizume et al., 2000; Thurston et al., 1998). By contrast, the skin tumors are white, indicative of less hemorrhagic vessels or higher interstitial pressure. Thus the phage population circulating through the vascular system in RIP1-Tag2 mice may have had ready access to the perivascular microenvironment, whereas the "tighter" vessels in the skin lesions may limit such accessibility. Future studies on the expression of the "receptors" identified by these distinctive classes of homing peptides should clarify whether their binding moieties are differentially expressed and/or differentially accessible via the vasculature in these distinctive tumor types and their angiogenic progenitor lesions, providing further insight into the dynamics and tissue-specific qualities of the angiogenic phenotype.

The selective accumulation of fluorescein-conjugated peptides in the RIP-Tag lesions indicates that a monovalent peptide-receptor interaction is robust enough to carry a payload to the target. As such, these peptides could be used as biomarkers or for imaging, particularly of pre-neoplastic lesions, which are notoriously difficult to detect. The peptides homing to angiogenic islets, for example, could be used both as markers of the angiogenic switch and to monitor therapeutic response to antiangiogenic agents, in much the same way as parameters such as microvessel density are currently employed. Future experiments will test the efficacy of targeting of imaging agents and active drugs to multiple stages of tumorigenesis.

In conclusion, we have used phage display to profile the vasculature during the distinctive stages of multistep tumorigenesis in a prototypical mouse model of cancer. We have identified three different classes of stage-specific peptides suggestive of distinctive characteristics of the neovasculature in premalignant and malignant lesions. We expect that the selectivity in peptide homing will help us understand the stage-specific differences in efficacy observed for angiogenesis inhibitor therapy in the RIP1-Tag2 model (Bergers et al., 1999). In addition, it may be possible to selectively target antitumor therapies to individual or multiple cell types during RIP-Tag tumorigenesis using these homing peptides conjugated to, for example, proapoptotic sequences, as previously reported (Ellerby et al., 1999). It will be of further interest to ask whether these homing peptides can similarly characterize the neovasculature of stages in human pancreatic islet carcinogenesis, as well as in other organ-specific cancers in mouse models and humans.

Experimental procedures

Generation of mice and tissue isolation

The generation of RIP1-Tag2 mice (Hanahan, 1985) and K14-HPV16 mice (Arbeit et al., 1994; Coussens et al., 1996) has been reported. Angiogenic islets were isolated from 8- and 12-week-old RIP1-Tag2 mice by collagenase digestion of the excised pancreas and selected based on their red, hemorrhagic appearance (Parangi et al., 1995). Tumors were microdissected from the excised pancreas of 12-week-old RIP1-Tag2 mice and the surrounding exocrine tissue was carefully removed. The synchronicity of tumorigenesis in the RIP1-Tag2 model allowed us to simultaneously isolate pools of angiogenic islets and tumors from the same mouse at 12 weeks of age, thus affording us the opportunity to directly compare homing of individual phage to different stages in an individual mouse/pancreas. Tumors were dissected from the ear or chest of K14-HPV16 mice. For the βTC3 allograft models, 10^6 βTC3 tumor cells (Efrat et al., 1988) were inoculated under the skin of the rear flank of nu/nu mice in a BALB/c background and allowed to grow until approximately 5 mm in size, and then used for experimental analysis. MDA-MB-435 xenograft models were generated by inoculating 10^6 tumor cells subcutaneously in the chest of nu/nu BALB/c mice. Tumors were used for the homing/binding experiments at 8–12 weeks after injection of the tumor cells. Matrigel plug angiogenesis was induced as previously described (Fulgham et al., 1999; Ngo et al., 2000; Yi et al., 2003). Briefly, 100 μl of Matrigel containing 80 ng/ml bFGF was injected subcutaneously in the abdominal area of BALB/c/nu/nu mice, and at day 8, the mice were injected with fluorescein-conjugated peptides as detailed below.

Phage libraries and library screening

The screening process involved two ex vivo selection rounds followed by 2–3 in vivo selection rounds. For the ex vivo selections, cell suspensions were prepared from the different RIP1-Tag2 lesions in 12-week-old RIP1-Tag2 mice and incubated overnight at 4°C with 10^9 plaque forming units (p.f.u.) of a T7 phage (Novagen) displayed CX_7C peptide library. The cells were washed to remove unbound phage and the bound phage rescued and amplified in *E. coli*. This procedure enriches for phage that bind to tumor, endothelial, and other stromal cells present in the suspension. The ex vivo pre-selected phage pool was injected intravenously into 12-week-old RIP1-Tag2 mice through the tail vein, allowed to circulate for 7 min, and heart-perfused with PBS to remove unbound intravascular phage. As the vascula-

ture is preferentially available for the phage to bind in this selection, there is an enrichment of phage that bind to the endothelium of the target tissue. The RIP1-Tag2 lesions and control tissues (brain, kidney, spleen, lung, "white" pancreas [i.e., not containing any hemorrhagic lesions], and liver) were excised to allow for comparison of homing efficiencies. Cell suspensions were prepared by mechanical disruption of the tissues, washed to remove unbound phage, and the bound phage rescued and amplified by adding *E. coli*. The phage pool was reinjected into mice at a similar disease stage, and the cycle repeated. In each experiment, nonrecombinant control phage was used as a control for relative selectivity. Sets of 96 phage clones were randomly collected from each homing phage population. The peptide-encoding DNA inserts were amplified by PCR, and the PCR products sequenced. Phage representing the most frequently appearing peptide motifs were individually tested for their ability to selectively home to the lesions on which they were selected, relative to other stages in the tumorigenesis pathway and to control organs. Fluorescein-conjugated peptides corresponding to these phage insert sequences were synthesized using an automated peptide synthesizer with standard solid-phase fluorenylmethoxycarbonyl (Fmoc) chemistry. One hundred micrograms of each individual fluorescein-conjugated peptide was injected intravenously into the tail vein of RIP1-Tag2 mice at 8 or 12 weeks of age and into normal BL/6 mice. The peptide was allowed to circulate for 7 min, followed by heart perfusion first with PBS and then with Zn-buffered formalin. The RIP1-Tag2 pancreas and control organs (brain, kidney, liver, lung, and spleen) were removed, fixed for 1 hr in formalin, washed with 1× PBS, placed in 30% sucrose for several hours, washed with 1× PBS, and embedded in OCT (Tissue-Tek). Each peptide was injected into at least three individual RIP1-Tag2 or normal mice at each of the different stages.

Histology and immunohistochemistry

To examine the localization of injected fluorescein-conjugated peptides, frozen sections (10 μm thick) were cut on a cryostat, mounted in Vectashield Mounting Medium with DAPI (Vector Laboratories), and visualized under an inverted fluorescent microscope or a confocal microscope (Zeiss LSM 510 META). For immunohistochemistry, frozen slides were preincubated with blocking buffer (1× PNB from NEN Biosciences) for 1 hr, washed several times in 1× PBS, and incubated with the primary antibody of interest overnight at 4°C. The cell-specific antibodies used were rat monoclonal anti-mouse CD31 (1:200; BD Pharmingen), rat monoclonal anti-mouse MECA32 (1:200; BD Pharmingen), rabbit polyclonal anti-mouse NG2 (1:200; Chemicon), and rat monoclonal anti-mouse PDGFRβ (CD140b) (1:200; eBioscience). The corresponding secondary antibodies; Cy-3 donkey anti-rabbit IgG and Rhodamine Red donkey anti-rat IgG (Jackson ImmunoResearch), were used at a 1:200 dilution and incubated for 1 hr at room temperature. The following species-matched immunoglobulins were used as negative controls: rabbit IgG (Vector Laboratories) and rat IgG (Jackson ImmunoResearch) at a 1:200 dilution. The slides were washed several times in 1× PBS and mounted in Vectashield Mounting Medium with DAPI (Vector Laboratories). Hematoxylin and eosin (H&E) staining was performed for histological grading of adjacent sections by standard methods, and lesions were graded as previously described (Lopez and Hanahan, 2002).

Transfection and phage binding assay

293T cells were transfected with plasmids encoding PDGFRβ or VEGFR2 (Borges et al., 2000) using Fugene transfection reagent (Roche Diagnostics). Briefly, 10 μg of plasmid was mixed with 700 μl of DMEM without serum and 30 μl of Fugene and incubated for 15 min at room temperature before adding the mixture to the cells. Forty-eight hours posttransfection, the cells were detached from the culture plates using EDTA and washed 1× with PBS. RSR, RGR, and the control nonrecombinant phage (about 1×10^9 pfu) were incubated with the transfected cells for 2 hr at 4°C, followed by five washes with 1% BSA in PBS to remove the unbound phage. The bound phage were rescued by adding bacteria, and the binding efficiencies were determined by plaque assay.

References

Arap, W., Pasqualini, R., and Ruoslahti, E. (1998). Cancer treatment by targeted drug delivery to tumor vasculature in a mouse model. Science *279*, 377–380.

Arbeit, J., Munger, K., Howley, P.M., and Hanahan, D. (1994). Progressive squamous epithelial neoplasia in K14-human papillomavirus type 16 transgenic mice. J. Virol. *68*, 4358–4368.

Bergers, G., Hanahan, D., and Coussens, L.M. (1998). Angiogenesis and apoptosis are cellular parameters of neoplastic progression in transgenic mouse models of tumorigenesis. Int. J. Dev. Biol. *42*, 995–1002.

Bergers, G., Javaherian, K., Lo, K.M., Folkman, J., and Hanahan, D. (1999). Effects of angiogenesis inhibitors on multistage carcinogenesis in mice. Science *284*, 808–812.

Bergers, G., Song, S., Meyer-Morse, N., Bergsland, E., and Hanahan, D. (2003). Benefits of targeting both pericytes and endothelial cells in the tumor vasculature with kinase inhibitors. J. Clin. Invest. *111*, 1287–1295.

Bergsten, E., Uutela, M., Li, X., Pietras, K., Ostman, A., Heldin, C.-H., Alitalo, K., and Eriksson, U. (2001). PDGF-D is a specific protease-activated ligand for the PDGF β-receptor. Nat. Cell Biol. *3*, 512–516.

Betsholtz, C., Karlsson, L., and Lindahl, P. (2001). Developmental roles of platelet-derived growth factors. Bioessays *23*, 494–507.

Bohme, K., Li, Y., Oh, P.S., and Olsen, B.R. (1995). Primary structure of the long and short splice variants of mouse collagen XII and their tissue-specific expression during embryonic development. Dev. Dyn. *204*, 432–445.

Borges, E., Jan, Y., and Ruoslahti, E. (2000). Platelet-derived growth factor receptor beta and vascular endothelial growth factor receptor 2 bind to the beta 3 integrin through its extracellular domain. J. Biol. Chem. *275*, 39867–39873.

Burg, M.A., Pasqualini, R., Arap, W., Ruoslahti, E., and Stallcup, W.B. (1999). NG2 proteoglycan-binding peptides target tumor neovasculature. Cancer Res. *59*, 2869–2874.

Carmeliet, P., and Jain, R. (2000). Angiogenesis in cancer and other diseases. Nature *407*, 249–257.

Clements, J.M., Bawden, L.J., Bloxidge, R.E., Catlin, G., Cook, A.L., Craig, S., Drummond, A.H., Edwards, R.M., Fallon, A., Green, D.R., et al. (1991). Two PDGF-B chain residues, arginine 27 and isoleucine 30, mediate receptor binding and activation. EMBO J. *10*, 4113–4120.

Coussens, L.M., and Werb, Z. (2002). Inflammation and cancer. Nature *420*, 860–867.

Coussens, L.M., Hanahan, D., and Arbeit, J.M. (1996). Genetic predisposition and parameters of malignant progression in K14–HPV16 transgenic mice. Am. J. Pathol. *149*, 1899–1917.

Efrat, S., Linde, S., Kofod, H., Spector, D., Delannoy, M., Grant, S., Hanahan, D., and Baekkeskov, S. (1988). Beta-cell lines derived from transgenic mice expressing a hybrid insulin gene-oncogene. Proc. Natl. Acad. Sci. USA *85*, 9037–9041.

Ellerby, H.M., Arap, W., Ellerby, L.M., Kain, R., Andrusiak, R., Rio, G.D., Krajewski, S., Lombardo, C.R., Rao, R., Ruoslahti, E., et al. (1999). Anti-cancer activity of targeted pro-apoptotic peptides. Nat. Med. *5*, 1032–1038.

Folkman, J., Watson, K., Ingber, D., and Hanahan, D. (1989). Induction of

angiogenesis during the transition from hyperplasia to neoplasia. Nature *339*, 58–61.

Fulgham, D.L., Widhalm, S.R., Martin, S., and Coffin, J.D. (1999). FGF-2 dependent angiogenesis is a latent phenotype in basic fibroblast growth factor transgenic mice. Endothelium *6*, 185–195.

Gohring, W., Sasaki, T., Heldin, C.H., and Timpl, R. (1998). Mapping of the binding of platelet-derived growth factor to distinct domains of the basement membrane proteins BM-40 and perlecan and distinction from the BM-40 collagen-binding epitope. Eur. J. Biochem. *255*, 60–66.

Hallman, R.D., Mayer, D.N., Berg, E.L., Broermann, R., and Butcher, E.C. (1995). Novel mouse endothelial cell surface marker is suppressed during differentiation of the blood brain barrier. Dev. Dyn. *202*, 325–332.

Hanahan, D. (1985). Heritable information of pancreatic beta-cell tumors in transgenic mice expressing recombinant insulin/simian virus 40 oncogenes. Nature *315*, 115–122.

Hanahan, D., and Folkman, J. (1996). Patterns and emerging mechanisms of the angiogenic switch during tumorigenesis. Cell *86*, 353–364.

Hashizume, H., Baluk, P., Morikawa, S., McLean, J.W., Thurston, G., Roberge, S., Jain, R.K., and McDonald, D.M. (2000). Openings between defective endothelial cells explain tumor vessel leakiness. Am. J. Pathol. *156*, 1363–1380.

Heldin, C.H., and Westermark, B. (1999). Mechanism of action and in vivo role of platelet-derived growth factor. Physiol. Rev. *79*, 1283–1316.

Hobbs, S.K., Monsky, W.L., Yuan, F., Roberts, W.G., Griffith, L., Torchilin, V.P., and Jain, R.K. (1998). Regulation of transport pathways in tumor vessels: Role of tumor type and microenvironment. Proc. Natl. Acad. Sci. USA *95*, 4607–4612.

Hoffman, J.A., Giraudo, E., Singh, M., Zhang, L., Inoue, M., Porkka, K., Hanahan, D., and Ruoslahti, E. (2003). Cancer Cell *4*, this issue, 383–391.

Johnsson, A., Heldin, C.H., Wasteson, A., Westermark, B., Deuel, T.F., Huang, J.S., Seeburg, P.H., Gray, A., Ullrich, A., Scrace, G., et al. (1984). The c-*sis* gene encodes a precursor of the B chain of platelet-derived growth factor. EMBO J. *3*, 921–928.

Laakkonen, P., Porkka, K., Hoffman, J.A., and Ruoslahti, E. (2002). A tumor-homing peptide with a targeting specificity related to lymphatic vessels. Nat. Med. *8*, 751–755.

LaRochelle, W.J., Jeffers, M., McDonald, W.F., Chillakuru, R.A., Giese, N.A., Lokker, N.A., Sullivan, C., Boldog, F.L., Yang, M., Vernet, C., et al. (2001). PDGF-D, a new protease-activated growth factor. Nat. Cell Biol. *3*, 517–521.

Leppink, D.M., Bishop, D.K., Sedmak, D.D., Henry, M.L., Ferguson, R.M., Streeter, P.R., Butcher, E.C., and Orosz, C.G. (1989). Inducible expression of an endothelial cell antigen on murine myocardial vasculature in association with interstitial cellular infiltration. Transplantation *48*, 874–877.

Leveen, P., Pekny, M., Gebre-Medhin, S., Swolin, B., Larsson, E., and Betsholtz, C. (1994). Mice deficient for PDGF-B show renal, cardiovascular and hematological abnormalities. Genes Dev. *8*, 1875–1887.

Lindahl, P., Johansson, B.R., Leveen, P., and Betsholtz, C. (1997). Pericyte loss and microaneurysm formation in PDGF-B deficient mice. Science *277*, 242–245.

Liotta, L.A., and Kohn, E.C. (2001). The microenvironment of the tumour-host interface. Nature *411*, 375–379.

Lopez, T., and Hanahan, D. (2002). Elevated levels of IGF-1 receptor convey invasive and metastatic capability in a mouse model of pancreatic islet tumorigenesis. Cancer Cell *1*, 339–353.

Morikawa, S., Baluk, P., Kaidoh, T., Haskell, A., Jain, R.K., and McDonald, D.M. (2002). Abnormalities in pericytes on blood vessels and endothelial sprouts in tumors. Am. J. Pathol. *160*, 985–1000.

Ngo, C.V., Gee, M., Akhtar, N., Yu, D., Volpert, O., Auerbach, R., and Thomas-Tikhonenko, A. (2000). An in vivo function for the transforming Myc protein: elicitation of the angiogenic phenotype. Cell Growth Differ. *11*, 201–210.

Oh, S.P., Griffith, C.M., Hay, E.D., and Olsen, B.R. (1993). Tissue-specific expression of type XII collagen during mouse embryonic development. Dev. Dyn. *196*, 37–46.

Ornitz, D.M., and Itoh, N. (2001). Fibroblast growth factors. Genome Biol. *2*, 3005.1–3005.12.

Ostman, A., and Heldin, C.H. (2001). Involvement of platelet-derived growth factor in disease: development of specific antagonists. Adv. Cancer Res. *80*, 1–38.

Ostman, A., Andersson, M., Hellman, U., and Heldin, C.H. (1991). Identification of three amino acids in the platelet-derived growth factor (PDGF) B-chain that are important for binding to the PDGF-β receptor. J. Biol. Chem. *266*, 10073–10077.

Parangi, S., Dietrich, W., Christofori, G., Lander, E.S., and Hanahan, D. (1995). Tumor suppressor loci on mouse chromosomes 9 and 16 are lost at distinct stages of tumorigenesis in a transgenic model of islet cell carcinoma. Cancer Res. *55*, 6071–6076.

Pasqualini, R., and Ruoslahti, E. (1996). Organ targeting *in vivo* using phage display peptide libraries. Nature *380*, 364–366.

Pasqualini, R., Koivunen, E., Kain, R., Lahdenranta, J., Sakamoto, M., Stryhn, A., Ashmun, R.A., Shapiro, L.H., Arap, W., and Ruoslahti, E. (2000). Aminopeptidase N is a receptor for tumor-homing peptides and a target for inhibiting angiogenesis. Cancer Res. *60*, 722–727.

Plotnikov, A.N., Schlessinger, J., Hubbard, S.R., and Mohammadi, M. (1999). Structural basis for FGF receptor dimerization and activation. Cell *98*, 641–650.

Porkka, K., Laakkonen, P., Hoffman, J.A., Bernasconi, M., and Ruoslahti, E. (2002). A fragment of the HMGN2 protein homes to the nuclei of tumor cells and tumor endothelial cells *in vivo*. Proc. Natl. Acad. Sci. USA *99*, 7444–7449.

Rajotte, D., Arap, W., Hagedorn, M., Koivunen, E., Pasqualini, R., and Ruoslahti, E. (1998). Molecular heterogeneity of the vascular endothelium revealed by *in vivo* phage display. J. Clin. Invest. *102*, 430–437.

Roberts, W.G., Delaat, J., Nagane, M., Huang, S., Cavenee, W.K., and Palade, G.E. (1998). Host microvasculature influence on tumor vascular morphology and endothelial gene expression. Am. J. Pathol. *153*, 1239–1248.

Ruoslahti, E. (2002). Specialization of tumour vasculature. Nat. Rev. Cancer *2*, 83–90.

Sato, T.N., Qin, Y., Kozak, C.A., and Audus, K.L. (1993). Tie-1 and Tie-2 define another class of putative receptor tyrosine kinase genes expressed in early embryonic vascular system. Proc. Natl. Acad. Sci. USA *90*, 9355–9358.

Schlingemann, R.O., Rietveld, F.J., de Waal, R.M., Ferrone, S., and Ruiter, D.J. (1990). Expression of the high molecular weight melanoma-associated antigen by pericytes during angiogenesis in tumors and in healing wounds. Am. J. Pathol. *136*, 1393–1405.

Schlingemann, R.O., Rietveld, F.J., Kwaspen, F., van de Kerkhof, P.C., de Waal, R.M., and Ruiter, D.J. (1991). Differential expression of markers for endothelial cells, pericytes, and basal lamina in the microvasculature of tumors and granulation tissues. Am. J. Pathol. *138*, 1335–1347.

Somasundaram, R., and Schuppan, D. (1996). Type I, II, III, IV, V, and VI collagens serve as extracellular ligands for the isoforms of platelet-derived growth factor (AA, BB, and AB). J. Biol. Chem. *271*, 26884–26891.

Soriano, P. (1994). Abnormal kidney development and hematological disorders in PDGFβ-receptor mutant mice. Genes Dev. *8*, 1888–1896.

St. Croix, B., Rago, C., Velculescu, V., Traverso, G., Romans, K.E., Montgomery, E., Lal, A., Riggins, G.J., Lengauer, C., Vogelstein, B., and Kinzler, K.W. (2000). Genes expressed in human tumor endothelium. Science *289*, 1197–1202.

Thurston, G., McLean, J.W., Rizen, M., Baluk, P., Haskell, A., Murphy, T.J., Hanahan, D., and McDonald, D.M. (1998). Cationic liposomes target angiogenic endothelial cells in tumors and chronic inflammation in mice. J. Clin. Invest. *101*, 1401–1413.

Yi, M., Sakai, T., Fassler, R., and Ruoslahti, E. (2003). Antiangiogenic proteins require plasma fibronectin or vitronectin for in vivo activity. Proc. Natl. Acad. Sci. USA, in press.

A tumor-homing peptide with a targeting specificity related to lymphatic vessels

Pirjo Laakkonen[1], Kimmo Porkka[1], Jason A. Hoffman[2] & Erkki Ruoslahti[1]

[1]Cancer Research Center, The Burnham Institute, La Jolla, California, USA
[2]Program in Molecular Pathology, The Burnham Institute and Department of Pathology, University of California San Diego School of Medicine, La Jolla, California, USA
Correspondence should be addressed to E.R.; email: ruoslahti@burnham.org

Blood vessels of tumors carry specific markers that are usually angiogenesis-related[1,2]. We previously used phage-displayed peptide libraries *in vivo* to identify peptides that home to tumors through the circulation and that specifically bind to the endothelia of tumor blood vessels[3,4]. Here we devised a phage screening procedure that would favor tumor-homing to targets that are accessible to circulating phage, but are not blood vessels. Screening on MDA-MB-435 breast carcinoma xenografts yielded multiple copies of a phage that displays a cyclic 9-amino-acid peptide, LyP-1. Homing and binding to tumor-derived cell suspensions indicated that LyP-1 also recognizes an osteosarcoma xenograft, and spontaneous prostate and breast cancers in transgenic mice, but not two other tumor xenografts. Fluorescein-labeled LyP-1 peptide was detected in tumor structures that were positive for three lymphatic endothelial markers and negative for three blood vessel markers. LyP-1 accumulated in the nuclei of the putative lymphatic cells, and in the nuclei of tumor cells. These results suggest that tumor lymphatics carry specific markers and that it may be possible to specifically target therapies into tumor lymphatics.

We combined *ex vivo* and *in vivo* phage selections[5] to search for peptides that recognize tumor-specific vessels other than blood vessels. We selected phage from a cyclic peptide library for binding to cell suspensions prepared from MDA-MB-435 breast cancer xenografts. To increase the likelihood of obtaining new kinds of homing peptides, we reduced the number of blood vessel endothelial cells by treating the cell suspension with anti-CD31 magnetic beads before recovering and amplifying bound phage. Blood-vessel endothelial cells express high levels of CD31, whereas lower levels are expressed by lymphatic endothelial cells[6,7] (and this study). Three rounds of *ex vivo* selection yielded a phage pool that bound to the primary tumor-derived cells approximately 350-fold over control, non-recombinant phage. Subsequent *in vivo* selections of this pool in a nude mouse bearing an MDA-MB-435 tumor resulted in 30-fold enrichment in the tumor relative to non-recombinant phage.

One of the peptide sequences enriched in the selected phage pool was CGNKRTRGC. The phage displaying this peptide bound to primary MDA-MB-435 tumor-derived cell suspensions about 7,000 times more than non-recombinant phage (Fig. 1*a*). The synthetic CGNKRTRGC peptide (LyP-1) inhibited the binding of the phage (data not shown). The LyP-1 phage bound cultured MDA-MB-435 cells on average about 100-fold over

non-recombinant phage. The LyP-1-displaying phage also bound to cell suspensions prepared from KRIB osteosarcoma xenografts, and from transgenic mouse mammary carcinomas (Fig. 1*a*). This phage did not to bind to cell suspensions from HL-60 leukemia or C8161 melanoma xenografts (Fig. 1*a*). Two permutations (CGEKRTRGC and CGNKRTRG**V**) arose spontaneously during the phage amplification and were recognized because of an altered plaque size. They did not significantly bind to MDA-MB-435 tumor-derived cell suspensions.

The LyP-1-displaying phage homed to the MDA-MB-435 and KRIB tumors *in vivo*. On the average, the mean phage titer in tumor tissue was 60-fold greater than non-recombinant phage in MDA-MB-435 tumors and 15-fold in KRIB tumors (Fig. 1*b*). In agreement with the cell-binding data, the phage did not home *in vivo* to HL-60 or C8161 xenografts (Fig. 1*b*), nor to brain, spleen, skin, kidneys and lungs; there may have been some homing to normal breast tissue (Fig. 1*c*). The MDA-MB-435 homing of the variant CGEKRTRGC-displaying phage was only 10% of the homing of the LyP-1.

When we treated MDA-MB-435 tumor-derived cells with 0.5% NP-40 before recovering homed phage, we found 10–20 times more LyP-1 phage than without the detergent, suggesting that the phage was internalized by cells. *In vitro* experiments showed that cultured MDA-MB-435 cells internalized fluorescein-conjugated LyP-1 peptide. The labeled peptide initially appeared in the cytoplasm and, with time, increasingly in the nucleus (Fig. 1*d*). There was no detectable cellular uptake of a fluorescein-labeled control peptide (ARALPSQRSR), which like CGNKRTRGC has three basic residues (data not shown).

Intravenously (i.v.) injected LyP-1 phage localized to vessel-like structures and to some single cells within the MDA-MB-435 tumors. The vessels containing the phage were negative for CD31 (Fig. 2*a*). Fluorescein-conjugated synthetic LyP-1 peptide, when injected into the tail vein of MDA-MB-435 tumor-bearing mice, also localized to vessel-like structures and to individual cells within the tumor mass. The peptide-stained vessels did not appear to be blood vessels, because they were negative for MECA-32 staining (Fig. 2*b*). In addition, there was a lack of colocalization with blood vessels labeled by i.v.-injected tomato lectin[8]. When the peptide and lectin fluorescence were captured in the same microscopic field, they were separate (Fig. 2*c*), and many fields contained only peptide fluorescence (Fig. 2*d*) or only lectin fluorescence (Fig. 2*e*). Fluorescein-conjugated LyP-1 localized to MDA-MB-435 tumors regardless of whether the tumors were grown subcutaneously or in the mammary fat pad,
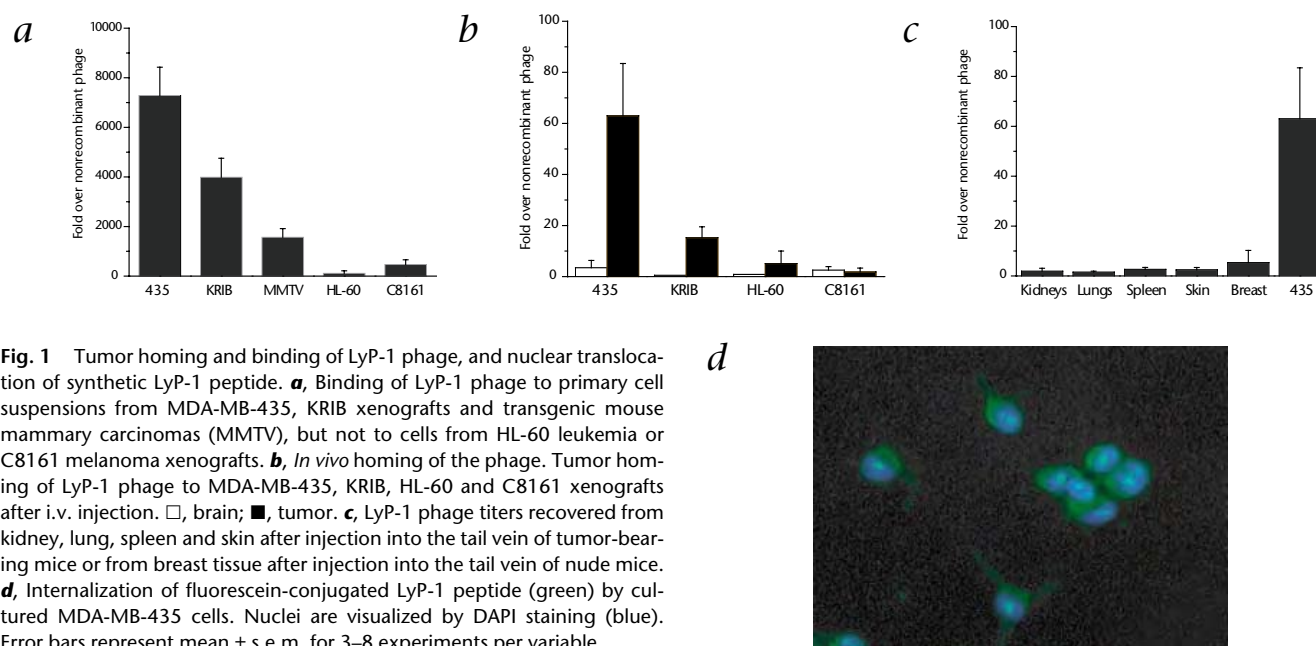
a

b

c

d

Fig. 1 Tumor homing and binding of LyP-1 phage, and nuclear translocation of synthetic LyP-1 peptide. *a*, Binding of LyP-1 phage to primary cell suspensions from MDA-MB-435, KRIB xenografts and transgenic mouse mammary carcinomas (MMTV), but not to cells from HL-60 leukemia or C8161 melanoma xenografts. *b*, *In vivo* homing of the phage. Tumor homing of LyP-1 phage to MDA-MB-435, KRIB, HL-60 and C8161 xenografts after i.v. injection. □, brain; ■, tumor. *c*, LyP-1 phage titers recovered from kidney, lung, spleen and skin after injection into the tail vein of tumor-bearing mice or from breast tissue after injection into the tail vein of nude mice. *d*, Internalization of fluorescein-conjugated LyP-1 peptide (green) by cultured MDA-MB-435 cells. Nuclei are visualized by DAPI staining (blue). Error bars represent mean ± s.e.m. for 3–8 experiments per variable.

but more fluorescence accumulated in the subcutaneous tumors (data not shown). The fluorescein-conjugated peptide also homed to transgenic prostate carcinomas (TRAMP), again failing to colocalize with tomato lectin (Fig. 2*f*). Among several normal tissues studied, fluorescence was only seen in kidney tubuli, presumably as a result of uptake of free fluorescein-conjugated LyP-1 from the glomerular filtrate. Fluorescence from the labeled control peptide also localized in kidney tubuli (data not shown).

Our data suggested that the vessel-like structures targeted by LyP-1 were not blood vessels, so we hypothesized that they might be lymphatic vessels. To investigate whether LyP-1 homed to tumor lymphatics, we stained MDA-MB-435 tumor sections with lymphatic markers: lymphatic vessel endothelial hyaloronic acid receptor-1 (LYVE-1), a transmembrane hyaluronic acid receptor[9,10]; podoplanin, a glomerular podocyte membrane protein[11]; and vascular endothelial growth factor receptor-3 (VEGFR-3)[12–14]. In accordance with earlier results[13–15], antibodies against each of these markers stained vessel-like structures in the MDA-MB-435 tumors. These structures frequently lacked a detectable lumen. The staining rarely overlapped with lectin staining, indicating that few, if any, of these vessels were blood vessels.

Fluorescein-conjugated LyP-1 injected into the tail vein of tumor-bearing mice colocalized with LYVE-1 (Fig. 3*a*), podoplanin (Fig. 3*b* and *c*) and VEGFR-3 (Fig. 3*d* and *e*) in vessel-like structures within MDA-MB-435 tumor tissue. Some of these structures appeared to be vessels filled with tumor cells (Fig. 3*f*). LyP-1 also accumulated outside the structures positive for the lymphatic markers, including the tumor cells, individual VEGFR3-positive cells and what appeared to be connective tissue between tumor cells. However, LyP-1 fluorescence typically centered around the structures detected with the lymphatic marker antibodies, implicating the lymphatic structures as the likely primary site of LyP-1 recognition. High-magnification images (Fig. 3*c* and *g*) show that fluorescein-conjugated LyP-1 accumulated in the nuclei of cells lining vessel-like structures, while the lymphatic marker antibodies (anti-podoplanin in Fig. 3*c*) stained the plasma membranes of the same cells. We also injected i.v. mice

with monoclonal antibody to podoplanin, and could detect the antibody in tissues. The injected antibody colocalized with LYVE-1 (Supplementary Fig. A online), and LyP-1 (Fig. 3*h*), but not with MECA-32 (data not shown).

The LyP-1 phage did not recognize C8161 xenografts in homing or cell-binding assays, but these tumors did contain vessel-like structures that stained positive for both LYVE-1 and podoplanin, but not for the tomato lectin (Supplementary Fig. B online). These results indicate that LyP-1 recognizes lymphatic vessel-associated structures in some tumors but not in others.

Previous *in vivo* phage-screening experiments have yielded peptides that recognize markers that are selectively expressed in tumor vasculature[3,4]. The structures recognized by LyP-1 in the target tumors seem to be related to lymphatic vessels, rather than blood vessels, as shown by colocalization of LyP-1 with three lymphatic markers and lack of colocalization with three blood-vessel markers. Probes for lymphatic vessels that require transport of the probe through the lymphatic vessels have generally revealed such vessels around, but not within tumors[16–18]. However, the use of molecular markers for lymphatic endothelial cells has revealed lymphatic structures inside many tumors[9,13–15].

Each of the lymphatic markers that we used colocalized with LyP-1 in the MDA-MB-435 tumors. None of these markers are completely specific for lymphatic endothelial cells[19,20], but the presence of all three markers in the LyP-1-positive structures strongly suggests that these structures are lymphatic vessels. These LyP-1-binding cells are not tumor cells, because they stained with antibody against mouse VEGFR-3 and with antibodies against mouse major histocompatibility complex (MHC) antigen H-2K^d (data not shown). The VEGFR-3 antibody is known not to recognize human VEGFR-3 (K. Alitalo and H. Kubo, pers. comm.).

LyP-1 often colocalized with lymphatic markers in structures that appeared in tissue sections as thin strands that form loops. These structures may be collapsed lymphatic vessels. Moreover, the reticular architecture with numerous ill-defined lumina described for tumor lymphatics in the recent study of human head and neck cancers is similar to ours[15]. Alternatively, these struc-
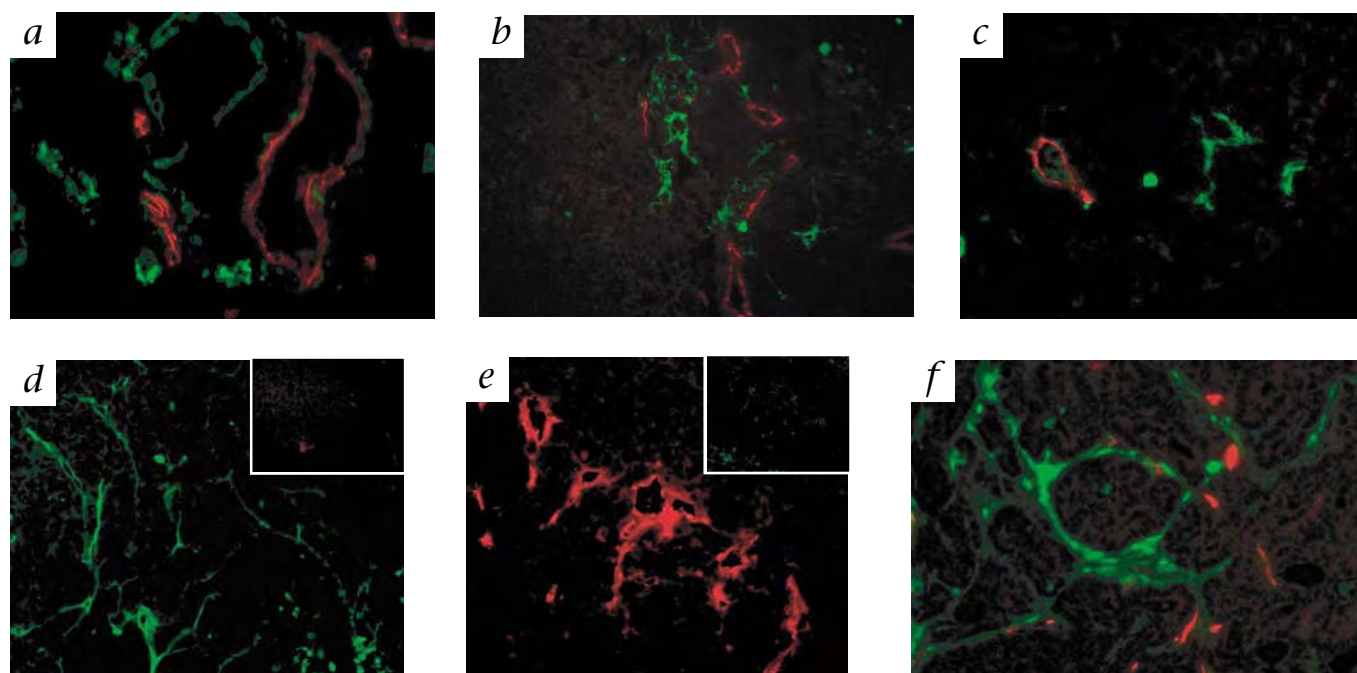
Fig. 2 LyP-1 phage and LyP-1 peptide do not colocalize with blood vessel markers. **a–e**, LyP-1 phage (*a*) or fluorescein-conjugated LyP-1 peptide (*b–e*) injected into the tail vein of a mouse bearing an MDA-MB-435 tumor. *a*, Tumor blood vessels were stained with anti-CD31 antibody (red) and phage was visualized using anti-T7 antibody followed by fluorescein-conjugated anti-rabbit IgG (green). *b–e*, Tumor blood vessels (red) were detected with MECA-32 (*b*) or i.v. injected, biotinylated tomato lectin (*c–e*). The green color shows the localization of LyP-1 peptide. *c*, A microscopic field containing both LyP-1 peptide and lectin fluorescence. *d*, Areas where peptide staining was abundant were often devoid of blood vessels. (the *inset*, blood vessel staining in the same microscopic field) *e*, Other areas of the tumor contained numerous blood vessels, but no peptide (inset, peptide staining in the same microscopic field). *f*, LyP-1 peptide (green) homed also to the transgenic mouse prostate tumor (TRAMP). Blood vessels (red) were detected with i.v. injected biotinylated tomato lectin. *d*, *e* and the insets in *d* and *e* are single color images. Magnification, ×400 in *a*, *c*, and *e*; ×200 in *b*, *d* and *f*.

tures could be dilated lymphatic vessels filled with tumor. It may be that most intra-tumor lymphatics are not patent vessels functional in transporting lymph. Because we access the tumor lymphatics through blood circulation, the accumulation of our phage and peptide in these structures may not be dependent on functionality of the targeted lymphatics.

Although these results strongly suggest that LyP-1 binds to tumor lymphatics, we cannot exclude the possibility that the
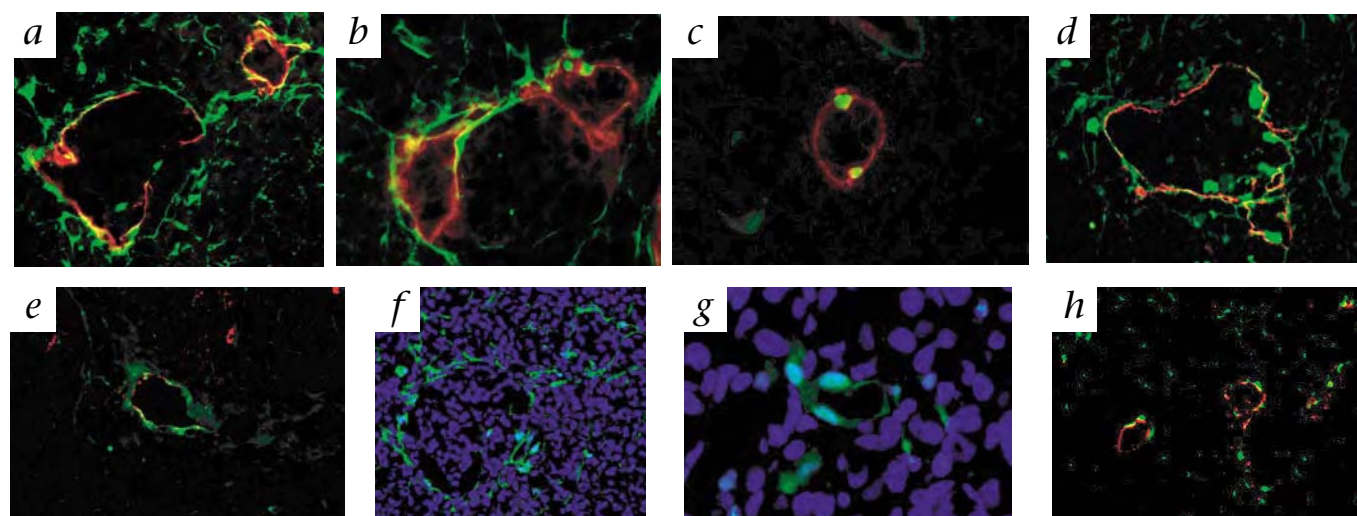
Fig. 3 Colocalization of LyP-1 with lymphatic markers. Fluorescein-conjugated LyP-1 peptide was injected into the tail vein of mice bearing MDA-MB-435 xenografts. **a–e**, LyP-1 (green) colocalizes with red staining for the lymphatic vessel markers LYVE-1 (*a*), podoplanin (*b* and *c*) and VEGFR-3 (*d* and *e*) in reticular and vessel-like structures within the tumor tissue. Some of the peptide fluorescence accumulates in the nuclei of the cells lining the vessels positive for the lymphatic markers and LyP-1, as shown by examination at a higher magnification (podoplanin costaining; *c*) and by using blue counter staining of nuclei with DAPI (*f* and *g*). *h*, LyP-1 fluorescence also partially colocalized with i.v. injected anti-podoplanin antibody in tumor tissue. Magnification, ×200 in *a–d* and *h*; ×400 in *g* and *f*.

target cell would be a transitional cell in between the lymphatic and blood vessel endothelial lineages[6]. There are also some similarities in the distribution of LyP-1 and periodic acid Shiff (PAS)-positive structures in melanomas, which may represent alternate vascular channels[21].

The binding of LyP-1 to putative tumor lymphatics and tumor cells is not universal for all tumors. Although we found LyP-1 to recognize two xenograft tumors and three transgenic mouse tumors, a leukemia (HL-60) and a melanoma (C8161) xenograft were negative. This was the case despite the fact that the C8161 tumors contained lymphatics as identified by positive staining for LYVE-1 and podoplanin and the lack of staining for a blood vessel marker. As the binding of LyP-1 to the cultured tumor cells correlated with its ability to recognize the putative tumor lymphatics in the xenografts, it may be that the tumor cells induce the expression of the LyP-1 binding molecule in the intratumoral lymphatic cells.

Our results suggest that tumor lymphatics may be specialized in a way similar to what has been shown for tumor blood vessels[3,4,22,23]. Moreover, the LyP-1 peptide may make it possible to specifically target tumor lymphatics and their adjacent tumor tissues for destruction. The nuclear localization of fluorescein coupled to LyP-1 suggests that LyP-1 could be a particularly effective carrier of drugs that act inside the nucleus. Given the importance of the lymphatic route in metastasis, such a treatment may destroy the most deadly parts of tumors.

Methods

Mice, cell lines and tumors. MDA-MB-435, KRIB and C8161 cell lines were maintained in DMEM supplemented with 10% FBS. Nude BALB/c mice were subcutaneously injected with 1×10^6 tumor cells, and tumor-bearing mice were used to prepare cell suspensions and for homing experiments at 3–6 weeks (KRIB or C8161) or 9–12 weeks (MDA-MB-435) post-injection. The animal experimentation was approved by the Burnham Institute Animal Research Committee.

Phage libraries and screening. The libraries were prepared as described[5]. NNK-oligonucleotides encoding a random library of cyclic peptides of the general structure CX_7C (ref. 24) were cloned into the T7Select 415-1 vector according to the manufacturer's instructions (Novagen, Madison, Wisconsin). This vector displays peptides in all 415 copies of the phage capsid protein as a C-terminal fusion.

Tumor-homing phage were isolated from the phage library by combining *ex vivo* and *in vivo* screening. For the *ex vivo* screening, tumor-cell suspensions were prepared from human MDA-MB-435 breast carcinoma xenograft tumors using collagenase (0.5 mg/ml, Sigma) to disperse the tissue. A cell suspension was incubated with the phage library (3.7×10^{10} plaque-forming units (p.f.u.)) overnight at 4 °C and unbound phage were removed by serially washing with 1% BSA in DMEM. Magnetic beads (Dynal, Oslo, Norway) coated with anti-mouse CD31 (MEC 13.3; Pharmingen, San Diego, California) were used to preferentially deplete the tumor-derived cell suspension of blood vessel endothelial cells. Phage bound to the CD31-deficient cell population were rescued and amplified. The phage selection process was repeated 3 times. The *ex vivo* pre-selected phage pool was then subjected to an *in vivo* selection round by injecting it (1.7×10^9 p.f.u.) into the tail vein of a nude mouse bearing an MDA-MB-435 tumor. 48 individual clones were then picked from this *in vivo*–selected, tumor-homing pool and their peptide-encoding inserts were sequenced. Nine peptides appearing more than once were amplified and their ability to bind to cultured cells and tumor-derived cell suspensions was tested[5]. The 5 individual phage that bound better to cell suspensions from MDA-MB-435 tumors than to cultured MDA-MB-435 cells were tested for their ability to home to tumors *in vivo*. In some experiments, the phage were rescued from tissues by treating the tissue with 0.5% NP-40 in PBS.

Peptide synthesis. Peptides were synthesized in our peptide synthesis facility using Fmoc chemistry in a solid-phase synthesizer. The peptides were purified by HPLC, and their sequence and structure was confirmed by mass spectrometry. Fluorescein-conjugated peptides were synthesized as described[25].

Antibodies and immunohistology. To produce antibodies to T7, New Zealand White rabbits were immunized with 10^{10} p.f.u. of T7 nonrecombinant phage (Novagen). The initial immunization was done in complete Freund's adjuvant and boosters were with incomplete Freund's adjuvant. The antibody titer was estimated by using ELISA, and the antiserum was absorbed against BLT5615 bacterial and mouse liver lysates. The LYVE-1 antibody was produced by immunizing New Zealand White rabbits with a peptide encoding the 19 C-terminal residues of mouse LYVE-1 (ref. 10) conjugated to keyhole limpet hemocyanin (KLH; Pierce, Rockford, Illinois). The initial immunization was done in complete Freund's adjuvant and boosters were with incomplete Freund's adjuvant. The antibodies were affinity purified with the peptide coupled to Sulfolink Gel (Pierce) and tested for tissue reactivity by immunofluorescence, where they gave a characteristic lymphatic staining pattern. The specificity of this antibody and that of an antibody against the ectodomain of LYVE-1 (ref. 10) have been reported to be similar[7]. Other primary antibodies used in immunohistochemistry were rat anti-mouse VEGFR-3 (ref. 12) (provided by K. Alitalo and H. Kubo), rat anti-mouse podoplanin[11] (provided by T. Petrova), rat anti-mouse MECA-32 (Pharmingen), rat anti-mouse CD31 (Pharmingen), and biotin anti-mouse H-2Kd, clone SF1-1.1 (Pharmingen).

Tissue distribution of fluorescein-labeled peptides was examined by i.v. injection of the peptide (100 µg in 200 µl PBS) into the tail vein of a mouse. Blood vessels were visualized by i.v. injection of *Lycopersicon esculentum* (tomato) lectin conjugated either to fluorescein or biotin (100 µg in 200 µl of PBS; Vector, Burlingame, California). The biotinyated lectin was detected with streptavidin-conjugated Alexa-594 (red). In some experiments, the anti-podoplanin antibody was similarly injected. The injected materials were allowed to circulate for 5–15 min and the mouse was perfused with 4% paraformaldehyde through the heart. Tissues were removed and frozen in OCT embedding medium (Tissue-Tek, Elkhart, Indiana). The biotin-conjugated lectin was detected with streptavidin-conjugated Alexa-594 (Molecular Probes, Eugene, Oregon) and the anti-podoplanin antibody with goat anti-rat Alexa-488 or Alexa-594 (Molecular Probes).

Note: Supplementary information is available on the Nature Medicine *website.*

1. Hanahan, D. & Folkman, J. Patterns and emerging mechanisms of the angiogenic switch during tumorigenesis. *Cell* **86**, 353–364 (1996).
2. Ruoslahti, E. Specialization of tumour vasculature. *Nature Rev. Cancer* **2**, 83–90 (2002).
3. Arap, W., Pasqualini, R. & Ruoslahti, E. Cancer treatment by targeted drug delivery to tumor vasculature in a mouse model. *Science* **279**, 377–380 (1998).
4. Porkka, K., Laakkonen, P., Hoffman, J.A., Bernasconi, M. & Ruoslahti, E. A fragment of the HMGN2 protein homes to the nuclei of tumor cells and tumor endothelial cells *in vivo. Proc. Natl. Acad. Sci. USA* (in the press).
5. Hoffman, J.A., Laakkonen, P., Porkka, K., Bernasconi, M. & Ruoslahti, E. *In vivo* and *ex vivo* selections using phage-displayed libraries. in *Phage Display: A Practical Approach* (eds. Clackson, T. & Lowman, H.) (Oxford University Press, Oxford, UK, in the press).

6. Oliver, G. & Detmar, M. The rediscovery of the lymphatic system: old and new insights into the development and biological function of the lymphatic vasculature. *Genes Dev.* **16**, 773–783 (2002).
7. Makinen, T. *et al.* Isolated lymphatic endothelial cells transduce growth, survival and migratory signals via the VEGF-C/D receptor VEGFR-3. *EMBO J.* **20**, 4762–4773 (2001).
8. Chang, Y.S. *et al.* Mosaic blood vessels in tumors: frequency of cancer cells in contact with flowing blood. *Proc. Natl. Acad. Sci.USA* **97**, 14608–14613 (2000).
9. Jackson, D.G., Prevo, R., Clasper, S. & Banerji, S. LYVE-1, the lymphatic system and tumor lymphangiogenesis. *Trends Immunol.* **22**, 317–321 (2001).
10. Prevo, R., Banerji, S., Ferguson, D.J., Clasper, S. & Jackson, D.G. Mouse LYVE-1 is an endocytic receptor for hyaluronan in lymphatic endothelium. *J. Biol. Chem.* **276**, 19420–19430 (2001).
11. Breiteneder-Geleff, S. *et al.* Angiosarcomas express mixed endothelial phenotypes of blood and lymphatic capillaries: Podoplanin as a specific marker for lymphatic endothelium. *Am. J. Pathol.* **154**, 385–394 (1999).
12. Kubo, H. *et al.* Involvement of vascular endothelial growth factor receptor-3 in maintenance of integrity of endothelial cell lining during tumor angiogenesis. *Blood* **96**, 546–553 (2000).
13. Stacker, S.A. *et al.* VEGF-D promotes the metastatic spread of tumor cells via the lymphatics. *Nature Med.* **7**, 186–191 (2001).
14. Skobe, M. *et al.* Induction of tumor lymphangiogenesis by VEGF-C promotes breast cancer metastasis. *Nature Med.* **7**, 192–198 (2001).
15. Beasley, N.J.P. *et al.* Intratumoral lymphangiogenesis and lymph node metastasis in head and neck cancer. *Cancer Res.* **62**, 1315–1320 (2002).
16. Mandriota, S.J. *et al.* Vascular endothelial growth factor-C-mediated lymphangiogenesis promotes tumour metastasis. *EMBO J.* **20**, 672–682 (2001).
17. Leu, A.J., Berk, D.A., Lymboussaki, A., Alitalo, K. & Jain, R.K. Absence of functional lymphatics within a murine sarcoma: a molecular and functional evaluation. *Cancer Res.* **60**, 4324–4327 (2000).
18. Karpanen, T. *et al.* Vascular endothelial growth factor C promotes tumor lymphangiogenesis and intralymphatic tumor growth. *Cancer Res.* **61**, 1786–1790 (2001).
19. Carreira, C.M. *et al.* LYVE-1 is not restricted to the lymph vessels: Expression in normal liver blood sinusoids and down-regulation in human liver cancer and cirrhosis. *Cancer Res.* **61**, 8079–8084 (2001).
20. Valtola, R. *et al.* VEGFR-3 and its ligand VEGF-C are associated with angiogenesis in breast cancer. *Am. J. Pathol.* **154**, 1381–1390 (1999).
21. Maniotis, A.J. *et al.* Vascular channel formation by human melanoma cells *in vivo* and *in vitro*: Vasculogenic mimicry. *Am. J. Pathol.* **155**, 739–752 (1999).
22. Brooks, P.C. *et al.* Integrin αvβ3 antagonists promote tumor regression by inducing apoptosis of angiogenic blood vessels. *Cell* **79**, 1157–1164 (1994).
23. St Croix, B. *et al.* Genes expressed in human tumor endothelium. *Science* **289**, 1197–202 (2000).
24. Smith, G.P. & Scott, J.K. Libraries of peptides and proteins displayed on filamentous phage. *Methods Enzymol.* **217**, 228–257 (1993).
25. Wender, P.A. *et al.* The design, synthesis, and evaluation of molecules that enable or enhance cellular uptake: peptoid molecular transporters. *Proc. Natl. Acad. Sci. USA* **97**, 13003–13008 (2000).

Antitumor activity of a homing peptide that targets tumor lymphatics and tumor cells

Pirjo Laakkonen*[†], Maria E. Åkerman*[‡], Hector Biliran*[§], Meng Yang[¶], Fernando Ferrer*, Terhi Karpanen[†], Robert M. Hoffman[¶], and Erkki Ruoslahti*[‖]

*The Burnham Institute, La Jolla, CA 92037; [†]Molecular/Cancer Biology Laboratory, Biomedicum Helsinki, University of Helsinki, P.O.B. 63 (Haartmaninkatu 8), FIN-00014 Helsinki, Finland; [‡]Department of Bioengineering, University of California at San Diego, La Jolla, CA 92093; and [¶]AntiCancer, Inc., San Diego, CA 92111

LyP-1 is a peptide selected from a phage-displayed peptide library that specifically binds to tumor and endothelial cells of tumor lymphatics in certain tumors. Fluorescein-conjugated LyP-1 and a related peptide, LyP-1b, strongly accumulated in primary MDA-MB-435 breast cancer xenografts and their metastases from i.v. peptide injections, allowing visualization of orthotopic tumors in intact mice. The LyP peptide accumulation coincided with hypoxic areas in tumors. LyP-1 induced cell death in cultured human breast carcinoma cells that bind and internalize the peptide. Melanoma cells that do not bind LyP-1 were unaffected. Systemic LyP-1 peptide treatment of mice with xenografted tumors induced with the breast cancer cells inhibited tumor growth. The treated tumors contained foci of apoptotic cells and were essentially devoid of lymphatics. These results reveal an unexpected antitumor effect by the LyP-1 peptide that seems to be dependent on a proapoptotic/cytotoxic activity of the peptide. As LyP-1 affects the poorly vascularized tumor compartment, it may complement treatments directed at tumor blood vessels.

phage display | tumor targeting | live imaging | therapy

Tumor blood vessels express molecular markers that distinguish them from normal blood vessels. Many of these tumor vessel markers are related to angiogenesis, but some are selective for certain tumors (1). Markers that distinguish the vasculature of tumors at the premalignant stage from the vasculature of fully malignant tumors in the same tumor system have also been described (2, 3). Recent data from our laboratory indicate that lymphatic vessels in tumors are also specialized, because a cyclic 9-amino acid peptide, LyP-1, binds to the lymphatic vessels in certain tumors, but not to the lymphatics of normal tissues (4).

The lymphatic system is an important route of tumor metastasis. Many cancers preferentially spread through the lymphatics. Recent discoveries of growth factors and molecular markers for lymphatic endothelial cells have made possible detailed studies of the relationship of tumor cells and the lymphatic vasculature of tumors (5–9). The use of marker proteins such as LYVE-1 (6), podoplanin (5), and Prox-1 (10) has shown that lymphatic vessels are abundant in the periphery of tumors and that many tumors also contain lymphatics within the tumor mass (4, 11). However, the intratumoral lymphatic vessels are generally not functional in transporting tissue fluid (12) and are often filled with tumor cells (4, 13). Recent experimental and clinical data strongly suggest that the number of lymphatics in a tumor, perhaps their size as well, and the expression of lymphangiogenic growth factors are important determinants in the ability of a tumor to metastasize (14–18).

Thus, it may become possible to reduce metastasis by specifically targeting tumor lymphatics (and the tumor tissue adjacent to these vessels) for destruction. The LyP-1 peptide, which specifically binds to tumor lymphatics (4), provides one potential avenue for developing reagents that can specifically destroy tumor lymphatics. This peptide also binds to the tumor cells in tumors that contain LyP-1-positive lymphatics, further expanding the potential of this peptide.

We show here that i.v. injected LyP-1 strongly and specifically accumulates in breast cancer xenografts over time, localizing preferentially in hypoxic areas. We also report that LyP-1 has a proapoptotic/cytotoxic effect on tumor cells and that systemic administration of the LyP-1 peptide inhibits breast cancer xenograft growth in mice. The treated tumors contain foci of apoptotic cells and reduced numbers of lymphatic vessels. These findings suggest that LyP-1 may provide a starting point for the development of new antitumor agents.

Materials and Methods

Cell Lines and Tumors. MDA-MB-435 human breast carcinoma cells and C8161 human melanoma cells were maintained in DMEM supplemented with 10% FCS. Nude BALB/c *nu/nu* mice were injected s.c. or into the mammary fat pad with 1×10^6 tumor cells to induce tumors. A vascular endothelial growth factor (VEGF)-C-transfected MDA-MB-435 cell line was prepared as previously reported for MCF7 cells (13).

Antibodies and Immunohistology. Blood vessels were visualized by staining tissue sections with monoclonal antibodies against CD-31, CD-34, or MECA-32 (all rat anti-mouse antibodies from Pharmingen). A polyclonal rabbit anti-mouse LYVE-1 antibody (4) and a rat monoclonal anti-mouse podoplanin antibody (provided by Kari Alitalo, University of Helsinki) were used to visualize lymphatic vessels. The primary antibodies were detected with goat anti-rabbit or anti-rat Alexa 594 (Molecular Probes).

Biodistribution of fluorescein-conjugated peptides was examined after i.v. injection (100 μl of 1 mM peptide solution in 200 μl of PBS) into the tail vein of a mouse. The peptide was allowed to circulate for various periods of time, and the mouse was perfused through the heart with 4% paraformaldehyde. Tissues were removed, soaked in 30% sucrose in PBS overnight, and frozen in OCT embedding medium (Tissue-Tek). Alternatively, tumor-bearing mice were i.v. injected with 500 μl of 1 mM fluorescein-conjugated peptide in PBS, and the peptide was allowed to circulate for 16–20 h.

The whole-body imaging was done under a blue light, by using the imaging system of a fluorescence stereo microscope (model LZ12; Leica, Deerfield, IL) equipped with a mercury 50-W lamp (19).

Determination of Vessel Density in Tissues. Frozen tumor sections were stained with antibodies against CD-34 and podoplanin (5) to visualize the tumor-associated blood and lymphatic vessels. Using ×200 magnification, each microscopic field in the hori-

---

MEDICAL SCIENCES

zontal and the vertical directions was counted for the presence of the two types of vessels.

Hypoxia. Hypoxic areas in the tumor were visualized by i.v. injection of a hypoxia marker 2-nitroimidazole (EF5) (20) into tumor-bearing mice (10 μl of 10 mM EF5 per g), followed by Cy3-conjugated mouse anti-EF5 (provided by Randall S. Johnson, University of California at San Diego). Cultured MDA-MB-435 cells were grown on coverslips and incubated overnight at 37°C to allow for attachment and spreading of the cells. Half of the cells were transferred to a hypoxia chamber (0.1% oxygen/5% CO$_2$) and incubated overnight under hypoxic conditions. Fluorescein-conjugated peptides (10 μM) were added to the cells in 1% BSA in DMEM and incubated for 3 h, followed by fixation with 4% paraformaldehyde in PBS. The coverslips were mounted on glass slides by using Vecta-Shield mounting media with 4′,6-diamidino-2-phenylindole (Vector Laboratories).

Cytotoxicity Assay. Cytotoxic efficacy of the different peptides was judged by measuring the release of a cytoplasmic enzyme, lactate dehydrogenase, from damaged cells into the supernatant by using a colorimetric assay Cytotoxicity Detection Kit (LDH assay; Roche Diagnostics). MDA-MB-435 cells were plated on 96-well plates (6,000 cells per well) and incubated overnight at 37°C to allow for attachment and spreading of the cells. Cells were washed once with PBS, and 50 μl of 2% BSA in DMEM was added to the cells. Peptides were added in 50 μl of H$_2$O and incubated for 24–72 h at 37°C. After the incubation, the cells were spun down (1,000 rpm, 10 min), and the supernatant was transferred to a new plate. The color reaction was added to the cells and incubated for 25 min before the absorbance was read at 492 nm. Cells incubated with 50 μl of H$_2$O and 50 μl of 2% BSA in DMEM served as a background control, and cells incubated with 1% Nonidet P-40 showed the maximal cytotoxic value. The cytotoxicity was determined as a percentage of the maximal value after the subtraction of the background.

Tumor Treatment Studies. Tumor-bearing mice were treated with i.v. injections of peptides beginning 4 weeks after tumor cell inoculation. The injections were administered twice a week for 4–5 weeks. Tumor volumes were measured once a week and were calculated according to the formula $V = $ width $\times$ height $\times$ depth/2, derived from the formula for the volume of an ellipsoid (21). Student's t test was used for statistical analysis of the results. The animal experiments reported here were approved by The Burnham Institute Animal Research Committee.

Synthesis of Fluorescein-Conjugated Peptides. Peptides were synthesized by using Fmoc-protected amino acids (Nova Biochem) and HATU (PE Biosystems, Foster City, CA) as a coupling reagent in dimethylformamide activated with diisopropylethylamine. All peptides were amide-capped at the C terminus by the use of Fmoc-PAL-PEG-PS resin (PE Biosystems). The peptides were conjugated with fluorescein at the N terminus by reacting with fluorescein isothiocyanate isomer (FITC, Aldrich) in dimethylformamide for 20 h in the presence of diisopropylethylamine.

Results

Fluorescein-Conjugated Homing Peptides Accumulate in Tumor Tissue. Intravenously injected LyP-1 peptide was observed to home to tumor-associated lymphatic vessels and tumor cells in MDA-MB-435 xenografts and some other tumors (4). In this earlier work, the peptide was allowed to circulate for <20 min. To optimize the accumulation of LyP-1 in these tumors, we studied the distribution of the peptide for longer periods of time. We found striking accumulation of fluorescein-conjugated LyP-1 in tumors several hours after the injection. At 16–20 h, the tumors of the LyP-1-injected mice were brightly fluorescent in whole-body fluorescent imaging (19) of intact mice (Fig. 1A). Tumors from the mice injected with a control peptide showed no fluorescence (Fig. 1B). Imaging of dissected tumors and organs from the same animals revealed strong fluorescence in tumors from mice injected with LyP-1, whereas no fluorescence was detectable in the tumors from the control peptide-injected mice. Other tissues showed no specific fluorescence with either peptide (Fig. 1 C and D).

We then confirmed the tumor-specificity of LyP-1 by quantifying the fluorescence in the dissected tissues. Tumor fluorescence from the control peptide injection was too low to be accurately distinguished from the background, but LyP-1 concentration was at least 15- to 40-fold higher in the tumors than that of the control peptide, whereas fluorescence in other tissues was not significantly different from the background (Fig. 1E). A peptide closely related to LyP-1 (CNKRTRGGC; H.B., J. A. Hoffman, P.L., and E.R., unpublished data) also strongly accumulated in the tumors (LyP-1b in Fig. 1E). These results show that the LyP-1 peptides accumulate in the MDA-MB-435 tumors with extraordinary efficiency and that the accumulation is specific. The LyP-1 fluorescence was mainly present in tumor cell nuclei (Fig. 1F), whereas the control peptide was essentially negative in tumor tissue (Fig. 1G). No fluorescence was detected in other tissues with any of the peptides (shown for LyP-1 in brain tissue in Fig. 1H).

LyP-1 Recognizes Metastatic Lesions. MDA-MB-435 tumor cells transfected with the lymphangiogenic growth factor VEGF-C produce tumors with increased number of lymphatic vessels and enhanced propensity to metastasize into regional lymph nodes and the lungs (13, 16, 22). In agreement with the ability of LyP-1 to recognize tumor lymphatics, LyP-1 accumulation in the VEGF-C-expressing tumors seemed to be stronger than in the parental-line tumors (data not shown). LyP-1 peptide also homed to the metastatic lymph nodes of the MDA-MB-435/VEGF-C tumor mice (Fig. 2 A–E), colocalizing with lymphatic endothelial markers (arrows in Fig. 2C) and tumor cells (Fig. 2E) within the lymph nodes. No LyP-1 fluorescence was detected in the vessels of normal lymph nodes; the nuclei of a few isolated cells that appeared to be leukocytes were positive (Fig. 2B Inset). Metastatic foci in lungs were also positive for Lyp-1 (Fig. 2F). These results show that metastases can retain the LyP-1 binding of the primary tumor and that the same tumor can induce the LyP-1-binding epitope in the lymphatic vessels of more than one tissue.

LyP-1 Peptide Recognizes Hypoxic Areas in Tumors. The tumor cells that accumulated LyP-1 formed clusters within the tumors, and these clusters contained few blood vessels (Fig. 3A) but were positive for lymphatic endothelial markers (Fig. 3B). The LyP-1-positive tumor cell clusters were strikingly similar to clusters of tumor cells revealed by uptake of hypoxia markers (23). This similarity, and the lack of blood vessels, led us to examine a possible connection between LyP-1 binding and hypoxia. Intravenously injected hypoxia reagent EF5 and fluorescein-labeled LyP-1 accumulated in the same areas in the tumors, but the staining for the two markers seemed to be mutually exclusive at the level of individual cells (Fig. 3 C and D). If EF5 was injected first, the homing of LyP-1 was reduced (Fig. 3C) and vice versa (Fig. 3D). Moreover, injecting LyP-1 or EF5 alone gave a stronger tumor signal for both compounds than the coinjections. In contrast, the accumulation of EF5 in C8161 melanoma xenografts, which are not recognized by LyP-1 (4), was unaffected by coinjecting LyP-1 (data not shown). These results
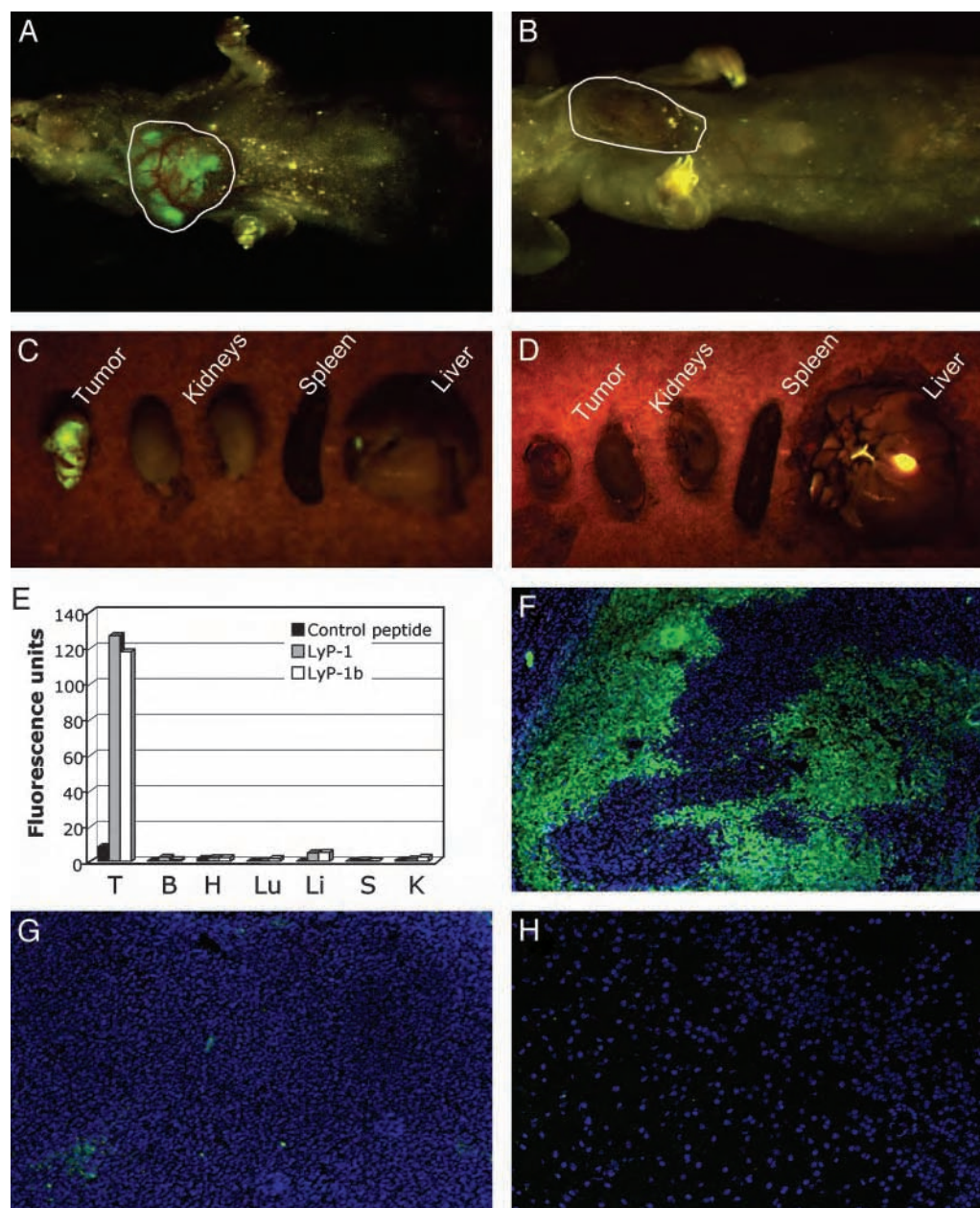
Fig. 1. Specific accumulation of lymphatic homing peptides in tumors. Mice bearing orthotopic MDA-MB-435 xenograft tumors were i.v. injected with fluorescein-conjugated LyP-1 (*A*) or a fluorescein-conjugated control peptide (ARALPSQRSR) (*B*). The mice were anesthetized 16–20 h later and examined for fluorescence under blue light. Tumor fluorescence of a LyP-1-injected tumor mouse is shown in *A*. No fluorescence was detected in tumors of mice injected with the control peptide (*B*). After the external examination, the mice were killed, and tumor, kidneys, spleen, and liver were excised and examined for fluorescence. LyP-1 produced intense fluorescence in the tumor, whereas no fluorescence was detectable in other organs (*C*). Even when imaged directly, no fluorescence was observed in the control peptide-injected tumor (*D*). The gallbladder is autofluorescent and appears as a green spot in *C* and *D*. *E* shows quantification of the imaging results for LyP-1 and for LyP-1b, which was analyzed in similar experiments. Mice that did not receive any fluorescent compound were used to determine the level of autofluorescence in tissues, and this background was subtracted from the experimental values. The graph shows a representative experiment of three. (*F–H*) Mice injected with peptides as in *A* and *B* were perfused through the heart, and their tumors were examined microscopically. Strong LyP-1 fluorescence is seen in the nuclei (visualized by 4′,6-diamidino-2-phenylindole staining) of tumor cells (*F*). No appreciable fluorescence from the control peptide is seen in tumor tissue (*G*), and all normal tissues tested were negative for all peptides (the result for LyP-1 in the brain is shown in *H*). T, tumor; B, brain; H, heart; Lu, lungs; Li, liver; S, spleen; K, kidneys. Magnification: *F* and *G*, ×100; *H*, ×200.

indicate that LyP-1 preferentially localizes in hypoxic parts of tumors and that LyP-1 and EF5 specifically affect one another's recognition of hypoxic tumor cells.

Serum Starvation Increases Binding of Fluorescein-Conjugated LyP-1 to Cultured MDA-MB-435 Cells. We next sought to reproduce the effect of hypoxia on tumor cell recognition *in vitro*. We cultured

MDA-MB-435 cells under hypoxic conditions but detected no increase in the number of cells that were positive for fluorescein-conjugated LyP-1 (data not shown). However, we did see an increase in the number of cells that had taken up LyP-1 when we maintained the cells in low serum (compare Fig. 3 *E* and *F*). Counting of LyP-1-positive cells showed that the difference was 2.5-fold. These results suggest that LyP-1 homing to tumors may
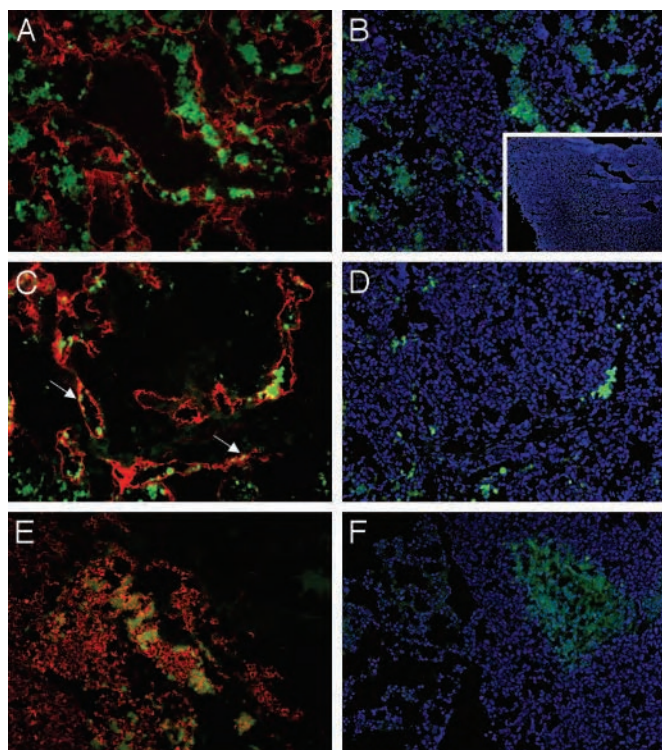
Fig. 2. Lymphatic homing peptide recognizes metastases of VEGF-C-expressing tumors. Fluorescein-conjugated LyP-1 peptide was i.v. injected into mice bearing orthotopic VEGF-C-expressing MDA-MB-435 tumors and allowed to circulate for 15 min. The tumor, lymph nodes, lungs, kidneys, and liver were removed and prepared for immunohistology. Lymphatic vessels in lymph node metastases (*A–D*) were visualized by staining with anti-LYVE-1 antibodies followed by goat anti-rabbit Alexa 594 (red, *A* and *C*). Nuclei were visualized by 4′,6-diamidino-2-phenylindole staining (blue, *B* and *D*). *A* and *B* and *C* and *D* show the same microscopic fields with different staining. LyP-1 peptide (green) is present in the nuclei of cells in and around enlarged lymphatic vessels in lymph node metastases. These cells are tumor cells as judged by their intense staining with anti-VEGF-C antibody (red, *E*). The peptide is also seen in the nuclei of lymphatic endothelial cells (arrows in *C*). No LyP-1 accumulated in a tumor-free lymph node (*B Inset*). A metastatic lung tumor also accumulates LyP-1 (*F*; LyP-1, green; nuclei, blue). Magnification, ×200; *Inset*, ×50.

Fig. 3. LyP-1 peptide recognizes cell clusters that lack blood vessels but contain lymphatics. Fluorescein-conjugated LyP-1 peptide was i.v. injected into MDA-MB-435 tumor-bearing mice and allowed to circulate for 15 min. LyP-1 peptide was seen in cell clusters throughout the tumor (green, *A* and *B*). These areas did not contain blood vessels, as judged by staining with the blood vessel endothelial marker, MECA-32 (red, *A*) but were often positive for the lymphatic endothelial markers, LYVE-1 (red, *B*) and podoplanin (not shown). The hypoxia marker EF5 (red), injected 8 h before LyP-1 (green), localized in the LyP-1-positive patches within the tumors (*C*). Reversing the order of the injections reduced the amount of EF5 in the LyP-1-positive patches (*D*). The presence of the two compounds at the cellular level seemed to be mutually exclusive. (*E* and *F*) LyP-1 binding to cultured cells is increased by serum starvation. Fluorescein-conjugated LyP-1 peptide was added to MDA-MB-435 cells cultured either in 10% (*E*) or 0.1% (*F*) serum, and the binding and uptake of the peptide by the cells was determined 3 h later. Serum starvation increased the number of LyP-1-positive cells (LyP-1, green; nuclei, blue). Magnification: *A–D*, ×200; *E* and *F*, ×100.

not be directly related to hypoxia but may result from the attendant nutrient starvation.

LyP-1 Binding and Internalization Induce Cell Death. Studying the internalization of the fluorescein-conjugated LyP-1 peptide in cultured cells, we noticed that the LyP-1 positive cells tended to round up, and the morphology of their nuclei frequently suggested apoptosis. To investigate whether LyP-1 caused cell death, we incubated MDA-MB-435 cells with unlabeled LyP-1 and monitored cell lysis. Incubation with LyP-1 resulted in a concentration-dependent increase in cell lysis with an IC$_{50}$ of ≈66 μM (Fig. 4*A*). C8161 human melanoma cells, which do not bind LyP-1 (4), were not affected by the peptide. Control peptides that resemble LyP-1 in their amino acid composition and/or cyclic structure (CRVRTRSGC, Fig. 4*A*) and two other peptides [CG**E**KRTRGC, a variant of LyP-1, which has no cell-binding activity (4); and KECQSRLLSCP, (data not shown)] had no effect on the viability of either cell line. Thus, LyP-1 specifically kills cells that bind this peptide.

Systemic Treatment with LyP-1 Inhibits Tumor Growth and Reduces the Number of Tumor Lymphatics. Given that LyP-1 had an *in vitro* cytotoxic effect on the MDA-MB-435 tumor cells, we examined
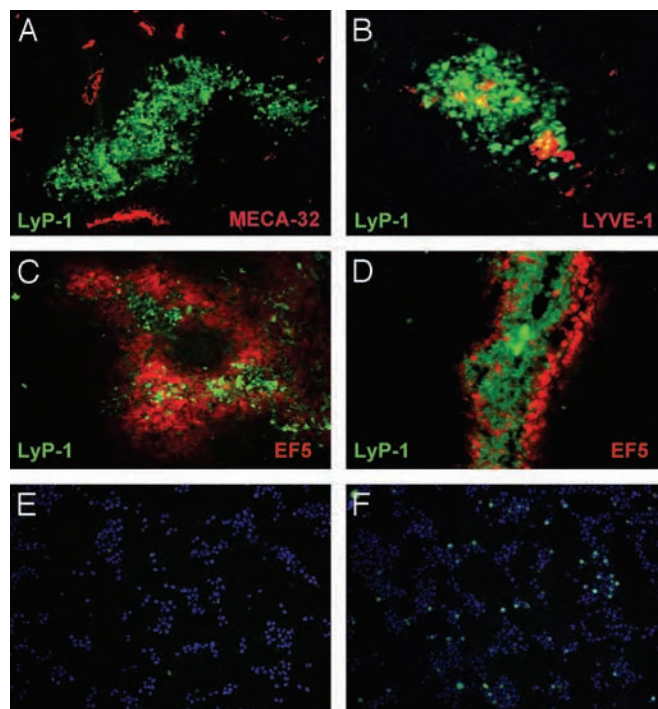
the effect of LyP-1 on tumor growth *in vivo*. We gave MDA-MB-435 or MDA-MB-435/VEGF-C tumor mice biweekly i.v. injections of the LyP-1 peptide, starting after the mice had established palpable tumors. Fig. 4*B* shows one of three similar treatment experiments. The LyP-1 peptide inhibited tumor growth formed by both cell lines. The average reduction of tumor volume relative to the control-treated mice was ≈50% and highly significant ($P < 0.005$). Increasing the dose of the LyP-1 peptide did not improve the efficacy of the compound (data not shown). The tumors of the LyP-1-treated animals contained numerous TUNEL-positive cells, indicating apoptosis, whereas little apoptosis was detected in the tumors of the control-treated mice (Fig. 4 *C* and *D*). The increased apoptosis in the LyP-1 group was specific for the tumor tissue; other tissues did not contain significant numbers of TUNEL-positive cells (data not shown).

LyP-1-treatment selectively reduced the number of lymphatic vessels in the tumors, while having a less prominent effect on the blood vessel density in the same tumors (Fig. 5). These results are in agreement with the *in vivo* homing pattern of the fluorescein-conjugated LyP-1 peptide to the lymphatics in MDA-MB-435 tumor-bearing mice (4). It seems that the lymphatic endothelial cells in the tumor are also susceptible to LyP-1.
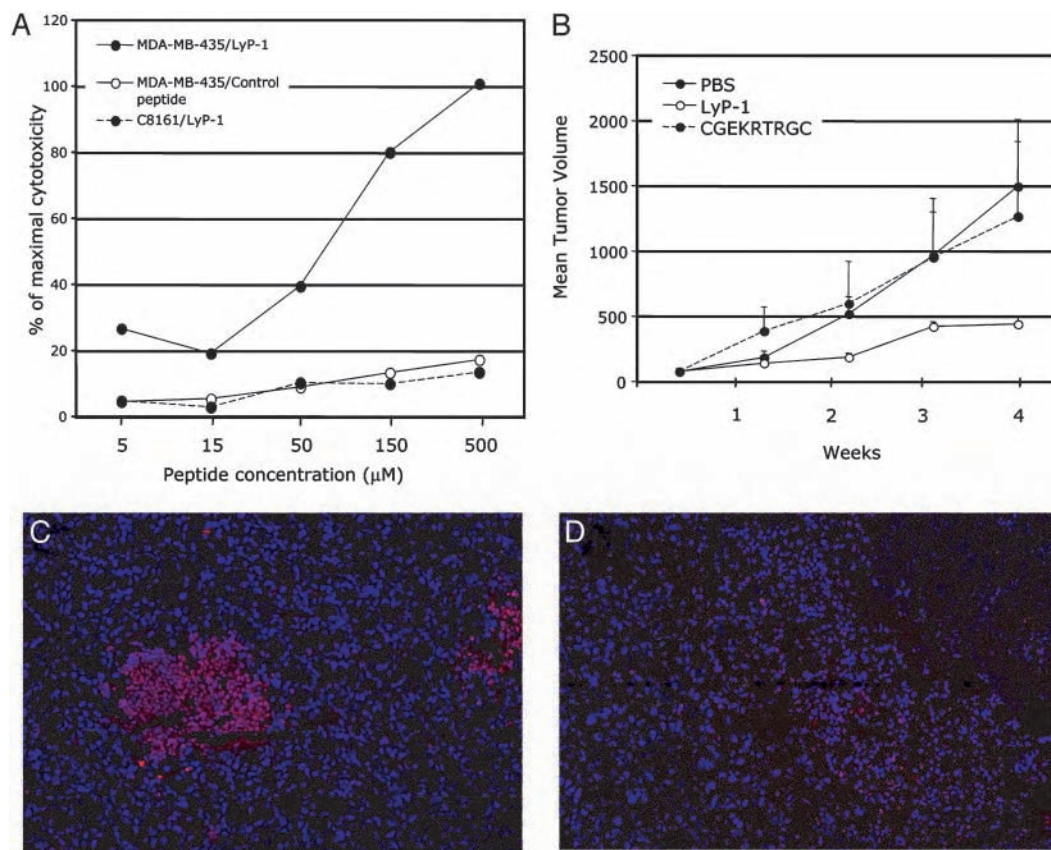
Fig. 4. LyP-1 peptide causes cell death *in vitro* and inhibits tumor growth *in vivo*. (*A*) LyP-1 (●, solid line) causes a dose-dependent release of lactate dehydrogenase from the cultured MDA-MB-435 cells, whereas a control peptide (CRVRTRSGC, ○) has no effect. LyP-1 does not release lactate dehydrogenase from human C8161 melanoma cells (●, dotted line). (*B*) Mice bearing MDA-MB-435 tumors were injected twice a week with 60 μg of LyP-1 or its inactive variant (CGEKRTRGC), or with PBS. There were five mice/group; the treatment was started 4 weeks after the inoculation of the tumor cells (1–2 weeks after the tumors became palpable) and lasted 4 weeks. One experiment of three is shown. LyP-1 reduced the mean tumor volume by an average of 50% (*P* < 0.05). (*C* and *D*) TUNEL staining (red) reveals clusters of apoptotic cells in the LyP-1-treated (*C*), but not control-treated (*D*), tumors. Blue, 4′,6-diamidino-2-phenylindole staining of nuclei. Magnification, ×200. The error bars in *B* show SEM.

Discussion

We report here that LyP-1, a peptide that specifically binds to tumor lymphatics and tumor cells, strongly accumulates in breast
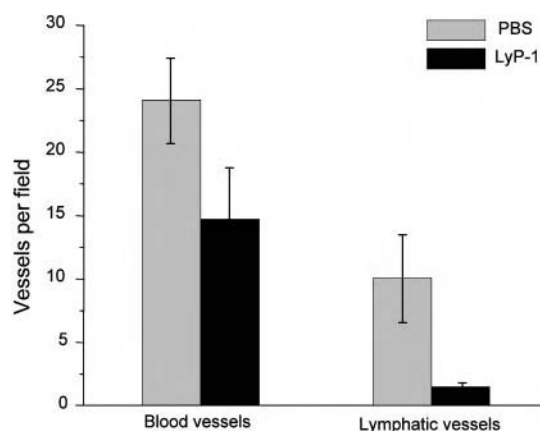
Fig. 5. LyP-1 peptide reduces the number of tumor lymphatics. Tumor sections were stained with antibodies against CD-34 and podoplanin to visualize and count tumor-associated blood vessels and lymphatics. LyP-1 reduced the number of lymphatic vessels by an average of 85% (three experiments). Blood vessel density in the same tumors was affected less (average reduction, 39%). The error bars show SD.

cancer xenografts after an i.v. injection. The peptide and a closely related variant of it preferentially localize in hypoxic areas within the tumors. We also show that systemically administered LyP-1 causes tumor cell apoptosis, reduces the number of tumor lymphatics, and inhibits tumor growth in mice bearing breast cancer xenografts. These results suggest that it may be possible to develop LyP-1-based cancer therapies.

The LyP-1 peptide shows strong accumulation in the MDA-MB-435 tumors, including metastases from these tumors. The efficacy and specificity of this peptide was sufficient to allow us to visualize orthotopic tumors in intact mice based on fluorescence. Although fluorescence-based imaging of tumors formed by GFP-producing cells in intact animals is possible (19), achieving it with an i.v. injected material may be unique. The remarkable tumor-homing efficiency of the LyP-1 peptide may be because of the propensity of this peptide to become internalized by cells. Cells that bind the LyP-1 peptide transport it across the cell membrane, into the cytoplasm and the nucleus. In this regard, LyP-1 is similar to the Tat peptide and other cell-penetrating peptides, which are also taken up by cells (24). An important difference is that our LyP-1 peptides are cell type-specific and deliver a payload to specific target cells: the lymphatic endothelial and tumor cells in tumors that display the "receptor" for these peptides. The internalization is likely to contribute to the effectiveness of these peptides in becoming concentrated in the targeted tumors. If this efficacy can be reproduced in clinical settings, LyP-1-directed targeting of contrast agents may become useful in tumor detection.

Our results show that treatment of tumor cells with the LyP-1 peptide causes cell death. This effect is specific because cells that do not bind LyP-1 were not affected. The tumor cell apoptosis we observed *in vivo* indicates that the LyP-1-binding cells die by apoptosis.

Whereas the mechanism whereby LyP-1 kills cells remains to be elucidated, the proapoptotic effect seems to be directed against tumor cells that are under stress, as LyP-1 colocalized with a tissue hypoxia marker *in vivo*, and serum starvation enhanced LyP-1 binding and internalization by cultured tumor cells *in vitro*. It will be important to identify the molecule (receptor) to which LyP-1 binds at the cell surface (and that may mediate the proapoptotic effect of LyP-1). Our efforts to isolate a LyP-1 receptor by affinity chromatography and various cloning methods have not yet been successful.

Treatment of tumor-bearing mice with the LyP-1 peptide suppressed tumor growth. It also drastically reduced the expression of lymphatic endothelial markers in the treated tumors. This latter result suggests that LyP-1 is also cytotoxic/proapoptotic for lymphatic endothelial cells in tumors. As tumor lymphatics have not been shown to be important for tumor growth (25), it is likely that the antitumor activity of LyP-1 is related to its effect on tumor cells rather than tumor lymphatics. However, given the demonstrated role of tumor lymphatics in metastasis (15, 16, 22), destroying tumor lymphatics with LyP-1 may be particularly effective in curtailing lymphatic spread of tumors. As lymphatics appear to be the first target of LyP-1 in tumors (4), the antitumor effect of LyP-1 may be particularly pronounced on tumor cells within and close to the lymphatics, which are likely to be the cells most probable to spread through the lymphatic system.

Hypoxia enhances metastasis (23, 26), and LyP-1 selectively targets tumor cells in the hypoxic areas of tumors. This may be another pathway through which LyP-1 could suppress metastasis. MDA-MB-435 tumors are highly metastatic, and the VEGF-C-expressing cells are even more aggressive in that regard. In this study, we evaluated the effects of LyP-1 on established primary tumors. As metastasis had already occurred at the time the treatment began, we could not evaluate the effect of LyP-1 on the metastatic spread. Studies to determine the effects of LyP-1 on metastasis are underway. Nonetheless, the data already at hand define this peptide as a potentially unique tool for tumor diagnosis and treatment.

1. Ruoslahti, E. (2002) *Nat. Rev. Cancer* **2,** 83–90.
2. Hoffman, J. A., Giraudo, E., Singh, M., Zhang, L., Inoue, M., Porkka, K., Hanahan, D. & Ruoslahti, E. (2003) *Cancer Cell* **4,** 383–391.
3. Joyce, J. A., Laakkonen, P., Bernasconi, M., Bergers, G., Ruoslahti, E. & Hanahan, D. (2003) *Cancer Cell* **4,** 393–403.
4. Laakkonen, P., Porkka, K., Hoffman, J. A. & Ruoslahti, E. (2002) *Nat. Med.* **8,** 751–755.
5. Breiteneder-Geleff, S., Soleiman, A., Kowalski, H., Horvat, R., Amann, G., Kriehuber, E., Diem, K., Weninger, W., Tschachler, E., Alitalo, K. & Kerjaschki, D. (1999) *Am. J. Pathol.* **154,** 385–394.
6. Banerji, S., Ni, J., Wang, S. X., Clasper, S., Su, J., Tammi, R., Jones, M. & Jackson, D. G. (1999) *J. Cell Biol.* **144,** 789–801.
7. Wigle, J. T. & Oliver, G. (1999) *Cell* **98,** 769–778.
8. Achen, M. G., Jeltsch, M., Kukk, E., Makinen, T., Vitali, A., Wilks, A. F., Alitalo, K. & Stacker, S. A. (1998) *Proc. Natl. Acad. Sci. USA* **95,** 548–553.
9. Jeltsch, M., Kaipainen, A., Joukov, V., Meng, X., Lakso, M., Rauvala, H., Swartz, M., Fukumura, D., Jain, R. K. & Alitalo, K. (1997) *Science* **276,** 1423–1425.
10. Wigle, J. T., Harvey, N., Detmar, M., Lagutina, I., Grosveld, G., Gunn, M. D., Jackson, D. G. & Oliver, G. (2002) *EMBO J.* **21,** 1505–1513.
11. Jackson, D. G., Prevo, R., Clasper, S. & Banerji, S. (2001) *Trends Immunol.* **22,** 317–321.
12. Leu, A. J., Berk, D. A., Lymboussaki, A., Alitalo, K. & Jain, R. K. (2000) *Cancer Res.* **60,** 4324–4327.
13. Karpanen, T., Egeblad, M., Karkkainen, M. J., Kubo, H., Yla-Herttuala, S., Jaattela, M. & Alitalo, K. (2001) *Cancer Res.* **61,** 1786–1790.
14. Pepper, M. S. (2001) *Clin. Cancer Res.* **7,** 462–468.
15. Stacker, S. A., Caesar, C., Baldwin, M. E., Thornton, G. E., Williams, R. A., Prevo, R., Jackson, D. G., Nishikawa, S., Kubo, H. & Achen, M. G. (2001) *Nat. Med.* **7,** 186–191.
16. Mandriota, S. J., Jussila, L., Jeltsch, M., Compagni, A., Baetens, D., Prevo, R., Banerji, S., Huarte, J., Montesano, R., Jackson, D. G., *et al.* (2001) *EMBO J.* **20,** 672–682.
17. Valtola, R., Salven, P., Heikkila, P., Taipale, J., Joensuu, H., Rehn, M., Pihlajaniemi, T., Weich, H., deWaal, R. & Alitalo, K. (1999) *Am. J. Pathol.* **154,** 1381–1390.
18. Saharinen, P., Tammela, T., Karkkainen, M. J. & Alitalo, K. (2004) *Trends Immunol.*, in press.
19. Yang, M., Baranov, E., Jiang, P., Sun, F. X., Li, X. M., Li, L., Hasegawa, S., Bouvet, M., Al-Tuwaijri, M., Chishima, T., *et al.* (2000) *Proc. Natl. Acad. Sci. USA* **97,** 1206–1211.
20. Lord, E. M., Harwell, L. & Koch, C. J. (1993) *Cancer Res.* **53,** 5721–5726.
21. Schueneman, A. J., Himmelfarb, E., Geng, L., Tan, J., Donnelly, E., Mendel, D., McMahon, G. & Hallahan, D. E. (2003) *Cancer Res.* **63,** 4009–4016.
22. Skobe, M., Hawighorst, T., Jackson, D. G., Prevo, R., Janes, L., Velasco, P., Riccardi, L., Alitalo, K., Claffey, K. & Detmar, M. (2001) *Nat. Med.* **7,** 192–198.
23. Rofstad, E. K., Rasmussen, H., Galappathi, K., Mathiesen, B., Nilsen, K. & Graff, B. A. (2002) *Cancer Res.* **62,** 1847–1853.
24. Lundberg, P. & Langel, U. (2003) *J. Mol. Recognit.* **16,** 227–233.
25. He, Y., Kozaki, K., Karpanen, T., Koshikawa, K., Yla-Herttuala, S., Takahashi, T. & Alitalo, K. (2002) *J. Natl. Cancer Inst.* **94,** 819–825.
26. Zhong, H., De Marzo, A. M., Laughner, E., Lim, M., Hilton, D. A., Zagzag, D., Buechler, P., Isaacs, W. B., Semenza, G. L. & Simons, J. W. (1999) *Cancer Res.* **59,** 5830–5835.

ADVANCED MATERIALS

Magnetic Iron Oxide Nanoworms for Tumor Targeting and Imaging**

By *Ji-Ho Park, Geoffrey von Maltzahn, Lianglin Zhang, Michael P. Schwartz, Erkki Ruoslahti, Sangeeta N. Bhatia,* and *Michael J. Sailor**

The application of nanotechnology to medicine is providing new approaches for the diagnosis and treatment of diseases.[1–14] Ultrasensitive imaging for early detection of cancers and efficient delivery of therapeutics to malignant tumors are two primary goals in cancer bionanotechnology; however, the development of nontoxic, functional nanoparticles that can successfully home to tumors presents some significant challenges. Dextran-coated magnetic iron oxide (IO) nanoparticles are of particular interest because they show relatively low toxicity and long circulation, and dramatically enhance hydrogen T_2 relaxation in magnetic resonance imaging (MRI).[5,11,15–20] The clinical power of these materials may be amplified by improving MRI relaxivity, blood circulation times, and the homing of such nanoparticles to tumors. Efforts to increase MRI sensitivity have focused on development of new magnetic core materials,[6,12] or on improvements in nanoparticle size[21] or clustering.[7,22] However, most efforts to improve the morphological characteristics of these nanoparticles have resulted in materials with relatively short circulation half-lives owing to incomplete additional hydrophilic coatings.[6,12,21]

An emerging theme in nanoparticle research is to control biological behavior and/or electromagnetic properties by controlling shape. The manipulation of electrical, magnetic, and optical properties by controlling the shape of nanomaterials has been demonstrated in many areas.[23–25] There are, however, limited studies that point to a shape dependence of the in vitro or in vivo behavior of nanomaterials.[14,26–28] One of the most important pathways for clearance of nanoparticles in vivo is the mononuclear phagocytic system (MPS). At the micrometer scale, particle shape is known to play a dominant role in particle uptake by phagocytes.[26] Some types of elongated nanoparticles have been shown to exhibit low MPS uptake and, as a result, prolonged blood half-life relative to spherical shapes.[13,14,29] For example, spherical micelles are taken up by phagocytes more readily than micelles that have been extended into filaments by shear flow.[14] Conversely, for targeted materials, elongation enhances the surface-to-volume ratio, allowing polyvalent binding to amplify particle affinity for cell surface receptors.[13,30]

In this work, we hypothesized that a nanostructure with an elongated assembly of IO cores (referred to here as nanoworms, NWs) would improve the ability of the nanoparticles to circulate, target, and image tumors. The synthetic strategy is inspired by the previous observation that magnetic nanoparticles can become aligned along strands of high-molecular-weight dextran.[31] We find that the geometry of the nanoparticles (elongated versus spherical) influences their efficacy both in vitro and in vivo by enhancing their magnetic relaxivity in MRI, increasing their ability to attach to tumor cells in vitro owing to enhanced multivalent interactions between peptide-modified NW and cell receptors, and amplifying their passive accumulation in vivo over spherical nanoparticle controls.

The NW synthesis is similar to the typical preparation of magnetic IO nanospheres (NSs), involving the reaction of Fe(II) and Fe(III) salts in the presence of dextran.[32] In order to prepare the wormlike morphology, the concentrations of iron salts are higher and the molecular weight of dextran is larger (20 kDa). The nanostructure appears in the transmission electron microscopy (TEM) image (Fig. 1a) as a string of IO cores (ca. 5 nm diameter) with an overall length on the order of 50 nm. The mean hydrodynamic size, measured by dynamic light scattering (DLS) is 65 nm (Table 1). It is not clear from the data if the IO cores are in contact with each other or merely in close proximity. When higher-molecular-mass dextran (40 kDa) is used, highly branched IO cores, with a larger size (~100 nm) and a broader size distribution (Supporting Information Fig. 1) are obtained.

[*] Prof. M. J. Sailor, J.-H. Park, Dr. M. P. Schwartz
Materials Science and Engineering Program
Department of Chemistry and Biochemistry
University of California, San Diego
9500 Gilman, La Jolla, CA 92093 (USA)
E-mail: msailor@ucsd.edu

G. von Maltzahn, Prof. S. N. Bhatia
Harvard–MIT Division of Health Sciences and Technology
Massachusetts Institute of Technology
77 Massachusetts Avenue, Cambridge, MA 02139 (USA)

Dr. L. Zhang, Prof. E. Ruoslahti
Burnham Institute for Medical Research at UCSB
University of California, Santa Barbara
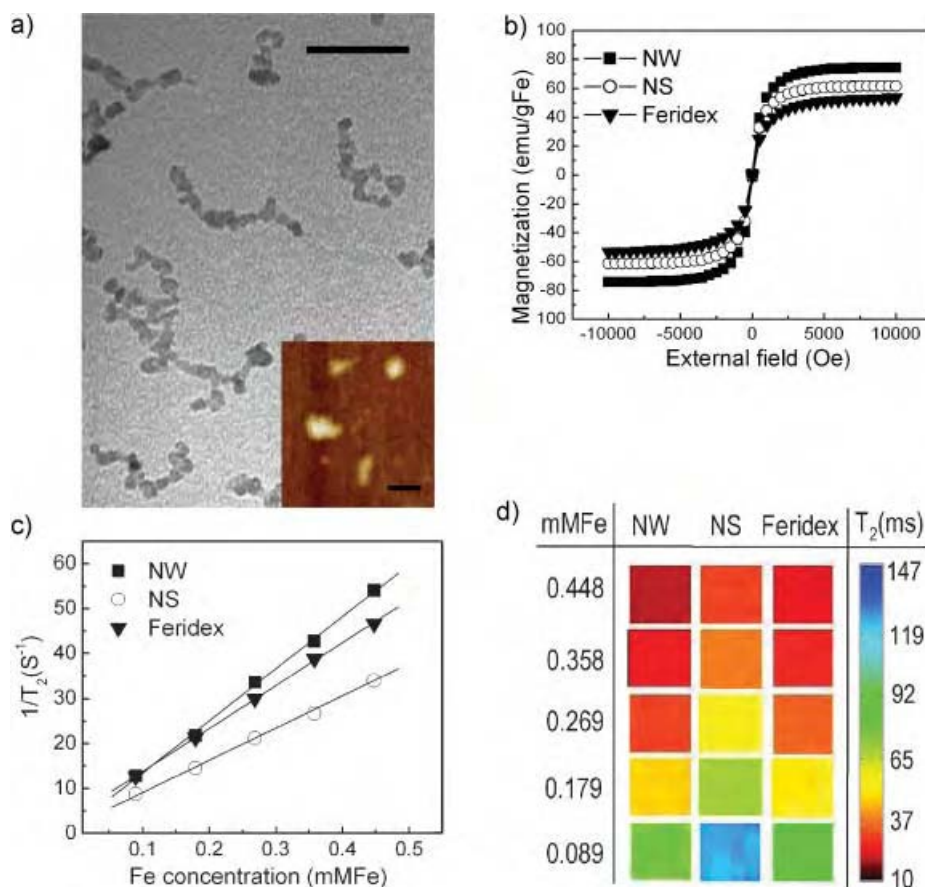1105 Life Sciences Technology Bldg., Santa Barbara, CA 93106 (USA)

Figure 1. Physical properties of magnetic NWs and conventional spherical nanoparticles (nanospheres; NSs) preparations. a) TEM image showing the wormlike nanostructure. More than 80% of the particles have a contorted linear appearance with a hydrodynamic length of 50–80 nm. Scale bar is 30 nm. (Inset: atomic force microscopy image showing the elongated shape. Scale bar is 100 nm). b) Magnetization curves for NWs, NSs, and Feridex. c) T_2 relaxation rates as a function of iron concentration (mM Fe) for NWs, NSs, and Feridex. d) T_2-weighted MR images of NWs, NSs, and Feridex with different concentrations.

and Supporting Information Fig. 2a).[15–18,32] NWs are characterized as elongated, dextran-coated particles composed of a linear aggregate of 5–10 IO cores (50–80 nm) while NSs are spherical, dextran-coated particles containing 1–2 IO cores (25–35 nm). NWs display a slightly larger saturation magnetization value (74.2 emu g_{Fe}^{-1} versus 61.5 emu g_{Fe}^{-1} Fe and 53.5 emu g_{Fe}^{-1}) and higher MR contrast ($R_2 = 116$ mMFe^{-1} S^{-1} versus $R_2 = 70$ mMFe^{-1} S^{-1} and $R_2 = 95$ mMFe^{-1} S^{-1}) than NSs and the commercially available Feridex (Fig. 1b–d). The elongated structure of the NWs apparently enhances the orientation of the magnetic moments of the individual nanoparticle constituents, increasing the net magnetization.[33,34] The increased MR contrast observed for NWs is thought to be due to enhanced spin–spin relaxation of water molecules caused by the slightly larger magnetization value[12,21] and the 1D assembly.[22,35]

The efficiency of peptide-targeted cellular internalization of NW relative to NS was tested on MDA-MB-435 tumor cells in vitro. Conceptually, the elongated shape of the NWs is expected to provide a larger number of interactions between the targeting ligands and their cell-surface receptors compared with spherical nanoparticles (Fig. 2a). For this study, the internalizing peptide, F3, was used

To provide comparison, nanospheres were synthesized using a published procedure.[32] They exhibited physical sizes and shapes, magnetic responses, and biological properties similar to what has been previously reported (Fig. 1, Table 1,

Table 1. Characteristics of nanoworms (NWs) and nanospheres (NSs).

Sample [a]	Size [b] [nm]	Blood $T_{1/2}$ [c] [min]	Amine [per NW/NS]	Peptide [per NW/NS]	Peptide [per g Fe ($\times 10^{20}$)]
NS	30.3	1060	0	0	0
NS-7-F	39.2		7	5	2.6
NS-30-F	39.6		30	10	5.3
NS-59-F	41.0		59	12	6.3
NW	65.8	990	0	0	0
NW-42-F	73.7		42	23	1.7
NW-P42-F	87.3		42	16	1.2
NW-175-F	76.6		175	69	5.1
NW-P175-F	88.2		175	48	3.0
NW-350-F	76.1		350	83	6.2
NW-P350-F	90.8		350	59	4.4

[a]The number after the letter identifier designates the number of amine groups per particle. The letter P indicates a poly(ethylene glycol) spacer is used. The –F suffix denotes F3-conjugated particle. [b]Hydrodynamic size based on DLS measurement (mean size resulting from three measurements). [c]Relative error in these measurements is ±10%.
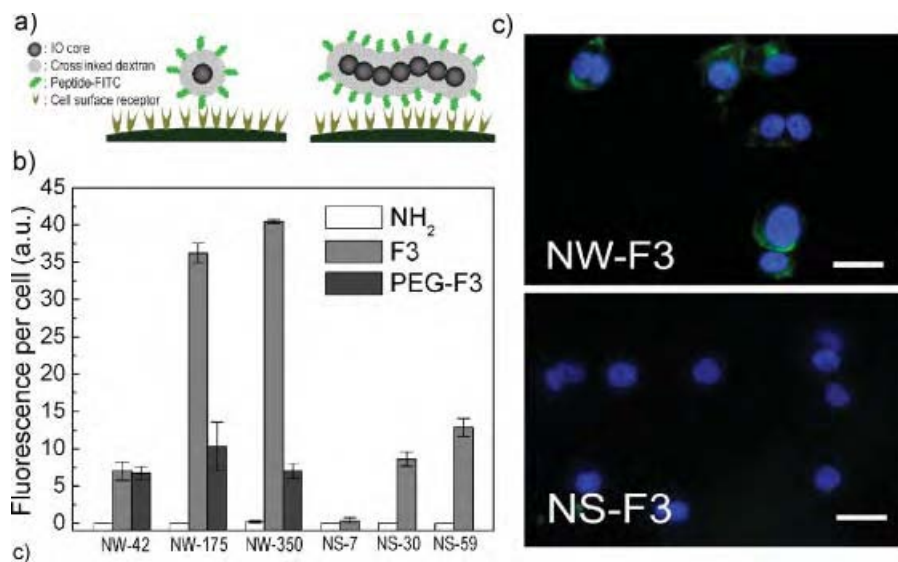
Figure 2. Internalization of nanoworms (NWs) and nanospheres (NSs) conjugated with F3 peptides into MDA-MB-435 cells. a) Conceptual scheme illustrating the increased multivalent interactions expected between receptors on a cell surface and targeting ligands on a NW compared with a NS. b) Fluorescence data comparing the efficiency of cellular internalization for various functionalized NW and NS systems. NH$_2$, F3, and PEG-F3 indicate aminated NW/NS, F3-conjugated NW/NS and PEGylgated F3-conjugated NW/NS, respectively. c) Fluorescence microscope images of cells 3 h after incubation with F3(FITC)-conjugated NW (NW-175-F) or F3(FITC)-conjugated NS (NS-30-F) (green). Nuclei are visualized with a DAPI stain (blue). Scale bar is 20 μm.

as the targeting species. F3 selectively targets cell-surface nucleolin in tumor cells and tumor endothelial cells, and is known to have cell-penetrating properties.[36–38] The number of peptides coupled to the particles was controlled by varying the extent of amination of the dextran coating (Table 1). Superconducting quantum interference device (SQUID) and fluorescence data indicate that internalization of F3-conjugated NWs (NW-F) is enhanced relative to F3-conjugated NS (NS-F) on a per-iron basis (Fig. 2b and Supporting Information Fig. 3a and b). For either NWs or NSs, the degree of internalization increases with the number of F3 peptides attached and incubation time, and dextran-coated NWs or NSs that do not contain targeting peptides display no evidence of internalization. Incorporation of a poly(ethylene glycol) (PEG) linker between the F3 targeting peptide and the NW reduces cellular uptake of NW (Fig. 2b). In a competition study, equal amounts (iron basis) of NW-175-F and NS-30-F were co-incubated, and NWs were found to inhibit cellular uptake of NSs (Supporting Information Fig. 3c). NWs recovered 24 h after internalization in cells retained their original shape (Supporting Information Fig. 3d).

Circulation in the blood stream for a long period of time is a key requirement for in vivo target-specific reporting and drug delivery with nanomaterials.[20,39] We tested the blood circulation times of unmodified NWs and NSs with an injection dose of 3 mg Fe kg^{-1} body mass in mice. Both exhibited similar long circulation times (blood half-lives: 15–18 h) with a first-order elimination rate (Fig. 3a and Table 1).[17] NWs extracted

from the bloodstream after 24 h retained their original shape (Supporting Information Fig. 4) and they showed a slight increase in hydrodynamic size (from ca. 65 to ca. 80 nm by DLS), attributed to protein binding during circulation.

The biodistribution of NWs in the mouse 24 h post injection is similar to that reported previously for NSs.[17] These particles both display a tendency to undergo MPS clearance in the liver, spleen, and lymph nodes (Fig. 3b). However, there are some differences in the biodistribution of NWs relative to NSs. The fraction of injected particles in the kidney is lower relative to the liver for NWs compared with NSs, whereas the spleen:liver particle concentration ratio is higher for NW.

In circulation nanoparticles tend to passively accumulate in tumors, since tumor vessels are generally found to be more permeable than the vessels of healthy tissues.[2] Passive tumor uptake of NWs in mouse xenograft MDA-MB-435 tumors was greater than NS (Fig. 3c). Interestingly, NWs remain in the tumor 48 h after injection, whereas NS are almost completely eliminated within this time period. The clearance behavior of NS is similar to that observed with RGD-conjugated quantum dots, which are of a comparable size.[9] The data indicate that once NW extravasate into tumor tissue from the blood vessels, they become physically trapped and do not readily re-enter the blood stream. Thus more effective diagnostic imaging or drug delivery may be possible with NW than with NS.

High-aspect-ratio nanomaterials such as carbon nanotubes and worm micelles have been found to circulate long enough to enable homing to biological targets despite their micrometer-sized length.[13,14,29] In addition, pseudo-1D assemblies of nanocrystals can display desirable optical or magnetic properties not found in the isodimensional materials.[40] The linear aggregation of IO cores increases MRI sensitivity as shown in this study, suggesting that NWs may offer an improved ability to image very small or poorly vascularized tumors.

The mechanism by which iron cores become linearly aggregated during synthesis requires further study, although the key factor seems to the molecular mass of the dextran polymer. Several methods to construct 1D assemblies of nanocrystals have been reported in recent years, for example involving the use of molecular coatings or biotemplates.[40–42] These approaches provide a means to control the chain-like nanostructures more precisely, although in vivo properties of such materials have not yet been characterized.
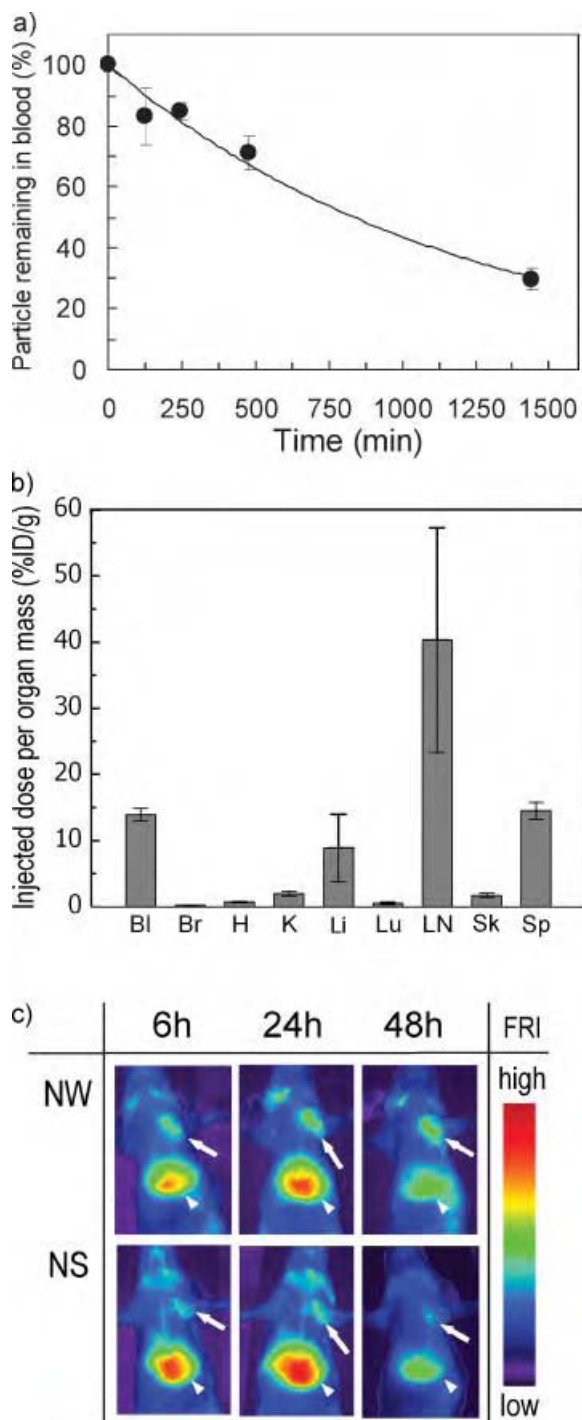
COMMUNICATION

Figure 3. In vivo behavior of untargeted nanoworms (NWs) in the mouse. a) Percentage of NW remaining in circulation as a function of time with an injection dose (ID) of 3 mgFe kg^{-1}. The solid line represents an exponential fit. b) Biodistribution of NW 24 h post injection. Bl, blood; Br, brain; H, heart; K, kidneys; Li, liver; Lu, lungs; LN, lymph node; Sk, skin; and Sp, spleen. c) Fluorescence images of mice bearing MDA-MB-435 tumors, obtained 6, 24, and 48 h after injection of NW or NS with an ID of 1 mg Fe kg^{-1}. Arrows and arrowheads point to the tumors and the livers, respectively.

There have been many studies comparing the targeting ability of multivalent with monovalent ligands on nanomaterials.[30,43,44] Here we have investigated the effect of nanoparticle morphology on intracellular delivery while attempting to maintain comparable surface chemical characteristics. For a constant ratio of attached targeting peptides per iron atom, NWs display a greater ability to be taken up by cultured tumor cells than NSs. The data suggest that the enhanced polyvalency of NWs versus NSs allows particles to bind to tumor cells with a higher avidity. No significant uptake is observed if the NWs or NSs contain no targeting peptides.

When shape and surface charge are held constant, the blood circulation time of nanoparticles is generally observed to decrease with increasing size.[39] However, nanomaterials that are elongated along one dimension seem to be better able to evade the organism's natural elimination processes.[13,14,29] This study clearly demonstrates that nanoparticle size can be increased along one dimension without sacrificing circulation time. The geometric alignment of cores within NW provides two key advantages over spherical counterparts: the elongated shape, with its larger surface area, presents multiple targeting ligands that can cooperatively interact with cell surfaces and linearly aggregated IO cores generate improved T_2 relaxivity for MR imaging. In addition, the nanomaterial is robust enough to retain its shape during circulation in vivo and after cell internalization. This is in contrast to softer structures, such as elongated filomicelles, which fragment into smaller particles in the cells and during circulation.[14] Overall, these results indicate that magnetic NWs represent an improved nanomaterial platform for targeting and imaging tumors in vivo. In addition to imaging, NWs may also facilitate more efficient delivery of therapeutics to biological targets because of their large surface area, multiple attachment points, and long blood half-life. These findings are important for the design of in vivo multifunctional nanoprobes applicable to the diagnosis and treatment of a range of human diseases.

Experimental

Nanoworms (NWs) were synthesized using a modification of the published preparation of dextran-coated IO nanoparticles [32]. For the NW synthesis, a higher concentration of iron salts and a higher molecular weight dextran (M_W 20,000 or 40,000, Sigma) were used. NWs or NSs with different numbers of free amines were prepared for peptide conjugation by reacting them with different concentrations of aqueous ammonia at room temperature for 48 h [16–18]. The amine number per NW or NS was measured using the SPDP assay [16]. The amine number per NW was calculated assuming that the molecular weight of a NW is 7 times higher than a NS, based on the mean number of aggregated IO cores for one NW observed in the TEM images and supported by the DLS data. The sizes and shapes of NWs, NSs or Micromod were characterized using TEM, AFM, and DLS. The magnetic properties of NWs, NSs, or Feridex were determined using a SQUID magnetometer. The surface charges of NWs or NSs were measured using a Malvern Instruments Zetasizer equipped with an autotitrator. MRI signals of NWs or NSs were analyzed using a Bruker 4.7 T magnet system.

One targeting peptides were used with the NW or NS samples: KDEPQRRSARLSAKPAPPKPEPKPKKAPAKK (F3), which

preferentially binds to blood vessels and tumor cells in various tumors [36]. The fluorescein (FITC)-conjugated peptides were synthesized using Fmoc chemistry in a solid-phase synthesizer, and purified by preparative HPLC. Their sequence and composition were confirmed by mass spectrometry. An extra cysteine residue was added to the N-terminus to allow conjugation to the aminated dextran coating of the NWs or NSs. For NIR fluorescence imaging, NWs or NSs were first labeled with Cy5.5/Cy7 (one Cy5.5/Cy7 dye per one IO core). The remaining free amines were used for conjugation with the targeting peptides. The number of FITC-peptides or Cy5.5/Cy7 dyes per single NW or NS was determined from the absorbance spectrum. For the cell uptake study, NW-42-F, NW-175-F, and NW-350-F display similar numbers of F3 targeting peptides per iron atom compared with NS-7-F, NS-30-F, and NS-59-F, respectively. Additionally, peptide conjugation to the particles through PEG chains resulted in fewer peptides per particle (Table 1).

For cell internalization tests, MDA-MB-435 cells were seeded into 24-well plates (10,000 per well) and cultured overnight. The cells were then incubated with Cy7-labeled NW-F or NS-F (40 μg (total Fe content) per well) for 30 min, 1 h, or 2 h at 37 °C in the presence of 10% FBS. The wells were rinsed three times with cell media and then imaged in the Cy7 channel (750 nm excitation/800 nm emission) with a NIR fluorescence scanner (LI-COR biosciences). The total number of attached Cy7 dye molecules was controlled to yield the same fluorescence intensity on a per-iron basis for both types of particles. The relative fluorescence of the images (each well) was analyzed using the ImageJ (NIH) or OsiriX (Apple) programs.

NW or NS in PBS (100 μL) were intravenously injected into mice (3 mg Fe kg^{-1}). Blood samples were extracted at several different times and magnetization and fluorescence intensities were analyzed by SQUID or by NIR fluorescence, respectively. The blood half-lives of NW and NS were calculated by fitting the fluorescence or magnetization data to a single-exponential equation using a one-compartment open pharmacokinetic model [17]. To determine tissue bio-distribution of the unmodified NW, percentages of injected dose per wet weight of each organ were quantified in healthy tumor-bearing mice.

For *in vivo* passive tumor targeting, mice bearing MDA-MB-435 tumors were anesthetized with intraperitoneal Avertin, and NW or NS (1 mg Fe kg^{-1} body weight in 100 μL PBS) were injected into the tail vein. For real-time observation of tumor/liver uptake, the mice were imaged under anesthesia using NIR fluorescence imaging (Siemens). To quantify NW or NS homing, tumors collected 24 h post injection were analyzed for magnetization using SQUID [45]. All animal work was reviewed and approved by the Burnham Institute's Animal Research Committee (see Supporting Information for details).

[1] M. E. Akerman, W. C. W. Chan, P. Laakkonen, S. N. Bhatia, E. Ruoslahti, *Proc. Natl. Acad. Sci. USA* **2002**, *99*, 12617.

[2] X. H. Gao, Y. Y. Cui, R. M. Levenson, L. W. K. Chung, S. M. Nie, *Nat. Biotechnol.* **2004**, *22*, 969.

[3] M. Ferrari, *Nat. Rev. Cancer* **2005**, *5*, 161.

[4] S. Sengupta, D. Eavarone, I. Capila, G. L. Zhao, N. Watson, T. Kiziltepe, R. Sasisekharan, *Nature* **2005**, *436*, 568.

[5] R. Weissleder, K. Kelly, E. Y. Sun, T. Shtatland, L. Josephson, *Nat. Biotechnol.* **2005**, *23*, 1418.

[6] W. S. Seo, J. H. Lee, X. M. Sun, Y. Suzuki, D. Mann, Z. Liu, M. Terashima, P. C. Yang, M. V. McConnell, D. G. Nishimura, H. J. Dai, *Nat. Mater.* **2006**, *5*, 971.

[7] J. H. Lee, Y. W. Jun, S. I. Yeon, J. S. Shin, J. Cheon, *Angew. Chem. Int. Ed.* **2006**, *45*, 8160.

[8] O. C. Farokhzad, J. J. Cheng, B. A. Teply, I. Sherifi, S. Jon, P. W. Kantoff, J. P. Richie, R. Langer, *Proc. Natl. Acad. Sci. USA* **2006**, *103*, 6315.

[9] W. B. Cai, D. W. Shin, K. Chen, O. Gheysens, Q. Z. Cao, S. X. Wang, S. S. Gambhir, X. Y. Chen, *Nano Lett.* **2006**, *6*, 669.

[10] J. D. Lewis, G. Destito, A. Zijlstra, M. J. Gonzalez, J. P. Quigley, M. Manchester, H. Stuhlmann, *Nat. Med.* **2006**, *12*, 354.

[11] D. Simberg, T. Duza, J. H. Park, M. Essler, J. Pilch, L. L. Zhang, A. M. Derfus, M. Yang, R. M. Hoffman, S. Bhatia, M. J. Sailor, E. Ruoslahti, *Proc. Natl. Acad. Sci. USA* **2007**, *104*, 932.

[12] J. H. Lee, Y. M. Huh, Y. Jun, J. Seo, J. Jang, H. T. Song, S. Kim, E. J. Cho, H. G. Yoon, J. S. Suh, J. Cheon, *Nat. Med.* **2007**, *13*, 95.

[13] Z. Liu, W. B. Cai, L. N. He, N. Nakayama, K. Chen, X. M. Sun, X. Y. Chen, H. J. Dai, *Nat. Nanotechnol.* **2007**, *2*, 47.

[14] Y. Geng, P. Dalhaimer, S. Cai, R. Tsai, M. Tewari, T. Minko, D. E. Discher, *Nat. Nanotechnol.* **2007**, *2*, 249.

[15] T. Shen, R. Weissleder, M. Papisov, A. Bogdanov, T. J. Brady, *Magn. Reson. Med.* **1993**, *29*, 599.

[16] L. Josephson, C. H. Tung, A. Moore, R. Weissleder, *Bioconjugate Chem.* **1999**, *10*, 186.

[17] P. Wunderbaldinger, L. Josephson, R. Weissleder, *Bioconjugate Chem.* **2002**, *13*, 264.

[18] L. Josephson, M. F. Kircher, U. Mahmood, Y. Tang, R. Weissleder, *Bioconjugate Chem.* **2002**, *13*, 554.

[19] M. G. Harisinghani, J. Barentsz, P. F. Hahn, W. M. Deserno, S. Tabatabaei, C. H. van de Kaa, J. de la Rosette, R. Weissleder, *N. Engl. J. Med.* **2003**, *348*, 2491.

[20] R. Weissleder, A. Bogdanov, E. A. Neuwelt, M. Papisov, *Adv. Drug Delivery Rev.* **1995**, *16*, 321.

[21] Y. W. Jun, Y. M. Huh, J. S. Choi, J. H. Lee, H. T. Song, S. Kim, S. Yoon, K. S. Kim, J. S. Shin, J. S. Suh, J. Cheon, *J. Am. Chem. Soc.* **2005**, *127*, 5732.

[22] H. Ai, C. Flask, B. Weinberg, X. Shuai, M. D. Pagel, D. Farrell, J. Duerk, J. M. Gao, *Adv. Mater.* **2005**, *17*, 1949.

[23] Y. W. Jun, J. S. Choi, J. Cheon, *Angew. Chem. Int. Ed.* **2006**, *45*, 3414.

[24] Y. N. Xia, N. J. Halas, *MRS Bull.* **2005**, *30*, 338.

[25] A. H. Fu, W. W. Gu, B. Boussert, K. Koski, D. Gerion, L. Manna, M. Le Gros, C. A. Larabell, A. P. Alivisatos, *Nano Lett.* **2007**, *7*, 179.

[26] J. A. Champion, S. Mitragotri, *Proc. Natl. Acad. Sci. USA* **2006**, *103*, 4930.

[27] B. D. Chithrani, A. A. Ghazani, W. C. W. Chan, *Nano Lett.* **2006**, *6*, 662.

[28] B. D. Chithrani, W. C. W. Chan, *Nano Lett.* **2007**, *7*, 1542.

[29] R. Singh, D. Pantarotto, L. Lacerda, G. Pastorin, C. Klumpp, M. Prato, A. Bianco, K. Kostarelos, *Proc. Natl. Acad. Sci. USA* **2006**, *103*, 3357.

[30] M. Mammen, S. K. Choi, G. M. Whitesides, *Angew. Chem. Int. Ed.* **1998**, *37*, 2755.

[31] D. Walsh, L. Arcelli, T. Ikoma, J. Tanaka, S. Mann, *Nat. Mater.* **2003**, *2*, 386.

[32] S. Palmacci, L. Josephson, *US Patent 5262176*, **1993**.

[33] C. Petit, V. Russier, M. P. Pileni, *J. Phys. Chem. B* **2003**, *107*, 10333.

[34] I. A. Banerjee, L. Y. M. Shima, T. Yoshino, H. Takeyama, T. Matsunaga, H. Matsui, *Adv. Mater.* **2005**, *17*, 1128.

[35] J. M. Perez, L. Josephson, T. O'Loughlin, D. Hogemann, R. Weissleder, *Nat. Biotechnol.* **2002**, *20*, 816.

[36] K. Porkka, P. Laakkonen, J. A. Hoffman, M. Bernasconi, E. Ruoslahti, *Proc. Natl. Acad. Sci. USA* **2002**, *99*, 7444.

[37] S. Christian, J. Pilch, M. E. Akerman, P. Laakkonen, E. Ruoslahti, *J. Cell Biol.* **2003**, *163*, 871.

[38] G. R. Reddy, M. S. Bhojani, P. McConville, J. Moody, B. A. Moffat, D. E. Hall, G. Kim, Y. E. L. Koo, M. J. Woolliscroft, J. V. Sugai, T. D. Johnson, M. A. Philbert, R. Kopelman, A. Rehemtulla, B. D. Ross, *Clin. Cancer Res.* **2006**, *12*, 6677.

[39] S. M. Moghimi, A. C. Hunter, J. C. Murray, *Pharm. Rev.* **2001**, *53*, 283.

[40] Z. Tang, N. A. Kotov, *Adv. Mater.* **2005**, *17*, 951.

[41] M. S. Nikolic, M. Krack, V. Aleksandrovic, A. Kornowski, S. Forster, H. Weller, *Angew. Chem. Int. Ed.* **2006**, *45*, 6577.

[42] G. A. DeVries, M. Brunnbauer, Y. Hu, A. M. Jackson, B. Long, B. T. Neltner, O. Uzun, B. H. Wunsch, F. Stellacci, *Science* **2007**, *315*, 358.

[43] X. Montet, M. Funovics, K. Montet-Abou, R. Weissleder, L. Josephson, *J. Med. Chem.* **2006**, *49*, 6087.

[44] S. Hong, P. R. Leroueil, I. J. Majoros, B. G. Orr, J. R. Baker, Jr., M. M. Banaszak Holl, *Chem. Biol.* **2007**, *14*, 107.

[45] P. P. GrassiSchultheiss, F. Heller, J. Dobson, *Biometals* **1997**, *10*, 351.

Biomimetic amplification of nanoparticle homing to tumors

Dmitri Simberg[a], Tasmia Duza[a,b], Ji Ho Park[c,d], Markus Essler[a,e], Jan Pilch[a], Lianglin Zhang[a], Austin M. Derfus[a,f], Meng Yang[g], Robert M. Hoffman[g,h], Sangeeta Bhatia[i,j], Michael J. Sailor[c,d], and Erkki Ruoslahti[a,k,l]

[a]Cancer Research Center, Burnham Institute for Medical Research, 10901 North Torrey Pines Road, La Jolla, CA 92037; [k]Burnham Institute for Medical Research at University of California Santa Barbara, 1105 Life Sciences Technology Building, University of California, Santa Barbara, CA 93106-9610; [c]Department of Chemistry and Biochemistry, University of California at San Diego, 9500 Gilman Drive, La Jolla, CA 92093-0358; [d]Materials Science and Engineering Program, University of California at San Diego, 9500 Gilman Drive, La Jolla, CA 92093-0418; [f]Department of Bioengineering, University of California at San Diego, 9500 Gilman Drive, La Jolla, CA 92093-0412; [g]AntiCancer, Inc., 7917 Ostrow Street, San Diego, CA 92111; [h]Department of Surgery, University of California, 200 West Arbor Drive, San Diego, CA 92103-8820; [i]Harvard–Massachusetts Institute of Technology Division of Health Sciences and Technology, 77 Massachusetts Avenue, Cambridge, MA 02139; and [j]Department of Electrical Engineering and Computer Science, Massachusetts Institute of Technology/Brigham and Women's Hospital, 75 Francis Street, Boston, MA 02115

Nanoparticle-based diagnostics and therapeutics hold great promise because multiple functions can be built into the particles. One such function is an ability to home to specific sites in the body. We describe here biomimetic particles that not only home to tumors, but also amplify their own homing. The system is based on a peptide that recognizes clotted plasma proteins and selectively homes to tumors, where it binds to vessel walls and tumor stroma. Iron oxide nanoparticles and liposomes coated with this tumor-homing peptide accumulate in tumor vessels, where they induce additional local clotting, thereby producing new binding sites for more particles. The system mimics platelets, which also circulate freely but accumulate at a diseased site and amplify their own accumulation at that site. The self-amplifying homing is a novel function for nanoparticles. The clotting-based amplification greatly enhances tumor imaging, and the addition of a drug carrier function to the particles is envisioned.

clotting | liver | peptide | tumor targeting | iron oxide

Nanomedicine is an emerging field that uses nanoparticles to facilitate the diagnosis and treatment of diseases. Notable early successes in the clinic include the use of superparamagnetic nanoparticles as a contrast agent in MRI and nanoparticle-based treatment systems (1, 2). The first generation of nanoparticles used in tumor treatments rely on "leakiness" of tumor vessels for preferential accumulation in tumors; however, this enhanced permeability and retention is not a constant feature of tumor vessels (3) and, even when present, still leaves the nanoparticles to negotiate the high interstitial fluid pressure in tumors (3, 4). An attractive alternative would be to target nanoparticles to specific molecular receptors in the blood vessels because they are readily available for binding from the blood stream and because tumor vessels express a wealth of molecules that are not significantly expressed in the vessels of normal tissues (5–7).

Specific targeting of nanoparticles to tumors has been accomplished in various experimental systems (8–10), but the efficiency of delivery is generally low. In nature, amplified homing is an important mechanism, ensuring sufficient platelet accumulation at sites of vascular injury. Amplified homing involves target binding, activation, platelet–platelet binding, and formation of a blood clot. We have designed a nanoparticle delivery system in which the particles amplify their own homing in a manner that resembles platelets.

Results

CREKA Peptide. We used a tumor-homing peptide to construct targeted nanoparticles. We identified this peptide by *in vivo* screening of phage-displayed peptide libraries (5, 11) for tumor homing in tumor-bearing MMTV-PyMT transgenic breast cancer mice (12).

The most frequently represented peptide sequence in the selected phage preparation was CREKA (Cys-Arg-Glu-Lys-Ala). We synthesized the CREKA peptide with a fluorescent dye attached to the N terminus and studied the *in vivo* distribution of the peptide in tumor-bearing mice. Intravenously injected CREKA peptide was readily detectable in the PyMT tumors, and in MDA-MB-435 human breast cancer xenografts, minutes to hours after the injection. The peptide formed a distinct meshwork in the tumor stroma [supporting information (SI) Fig. 5*A*], and it also highlighted the blood vessels in the tumors. The CREKA peptide was essentially undetectable in normal tissues. In agreement with the microscopy results, whole-body imaging using CREKA peptide labeled with the fluorescent dye Alexa Fluor 647 revealed peptide accumulation in the breast cancer xenografts and in the bladder, reflecting elimination of excess peptide into the urine (SI Fig. 5*B*).

Tumors contain a meshwork of clotted plasma proteins in the tumor stroma and the walls of vessels, but no such meshwork is detectable in normal tissues (13–15). The mesh-like pattern produced by the CREKA peptide in tumors prompted us to study whether clotted plasma proteins might be the target of this peptide. We tested the peptide in fibrinogen knockout mice, which lack the fibrin meshwork in their tumors. Like previously identified clot-binding peptides (15), intravenously injected CREKA peptide failed to accumulate in B16F1 melanomas grown in the fibrinogen null mice but formed a brightly fluorescent meshwork in B16F1 tumors grown in normal littermates of the null mice (Fig. 1 *A* and *B*). In agreement with this result, the CREKA phage, but not the control insertless phage, bound to clotted plasma proteins *in vitro* (Fig. 1*C*). These results establish CREKA as a clot-binding peptide. Its structure makes it an attractive peptide to use in nanoparticle targeting because, unlike our other clot-binding peptides, which are cyclic 10 amino acid peptides (15), CREKA is linear and contains only 5 aa. Moreover, the sulfhydryl group of the single cysteine residue is
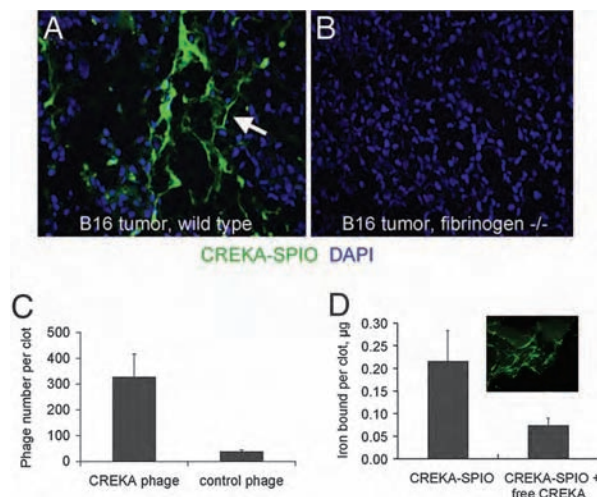
Fig. 1. Tumor homing of CREKA pentapeptide. (*A* and *B*) Fluorescein-conjugated CREKA peptide (200 μg per mouse) was injected into mice bearing syngeneic B16F1 melanoma tumors. Representative microscopic fields are shown to illustrate homing of fluorescein-CREKA to fibrin-like structures in tumors in wild-type mice (*A*, arrow) and lack of homing in fibrinogen null mice (*B*). (*C*) The CREKA phage binds to clotted plasma proteins in a test tube, whereas nonrecombinant control phage shows little binding. (*D*) Dextran-coated iron oxide nanoparticles conjugated with fluorescein-CREKA bind to clotted plasma proteins, and the binding is inhibited by free CREKA peptide. (*D Inset*) The microscopic appearance of the clot-bound CREKA-SPIO. [Magnification: ×200 (*A* and *B*) and ×600 (*D Inset*).]

not required to provide binding activity and can be used to couple the peptide to other moieties.

Peptide-Coated Nanoparticles. We coupled fluorescein-labeled CREKA or fluorescein onto the surface of 50-nm superparamagnetic, amino dextran-coated iron oxide (SPIO) nanoparticles. Such particles have been extensively characterized with regard to their chemistry, pharmacokinetics, and toxicology and are used as MRI contrast agents (16–18). Coupling of the fluorescein-labeled peptides to SPIO produced strongly fluorescent particles. Releasing the peptide from the particles by hydrolysis increased the fluorescence further by a factor of ≈3 (data not shown). These results indicate that the proximity of the fluorescein molecules at the particle surface causes some quenching of the fluorescence. Despite this quenching, fluorescence from the coupled fluorescein peptide was almost linearly related to the number of peptide molecules on the particle (SI Fig. 6), allowing us to track the number of peptide moieties on the particle by measuring particle fluorescence and to use fluorescence intensity as a measure of the concentration of particles in samples. We used CREKA-SPIO with at least 8,000 peptide molecules per particle in our *in vivo* experiments. The CREKA-SPIO nanoparticles bound to mouse and human plasma clots *in vitro*, and the binding was inhibited by the free peptide (Fig. 1*D*). The nanoparticles distributed along a fibrillar meshwork in the clots (Fig. 1*D Inset*). These results show that the particle-bound peptide retains its binding activity toward clotted plasma proteins.

Tumor Homing vs. Liver Clearance of CREKA-SPIO. Initial experiments showed that intravenously injected CREKA-SPIO nanoparticles did not accumulate effectively in MDA-MB-435 breast cancer xenografts. In contrast, a high concentration of particles was seen in reticuloendothelial system (RES) tissues (Fig. 2*A Upper*). Because the free CREKA peptide effectively homes to these tumors (SI Fig. 5), we hypothesized that the RES uptake was a major obstacle to the homing of the nanoparticles. We
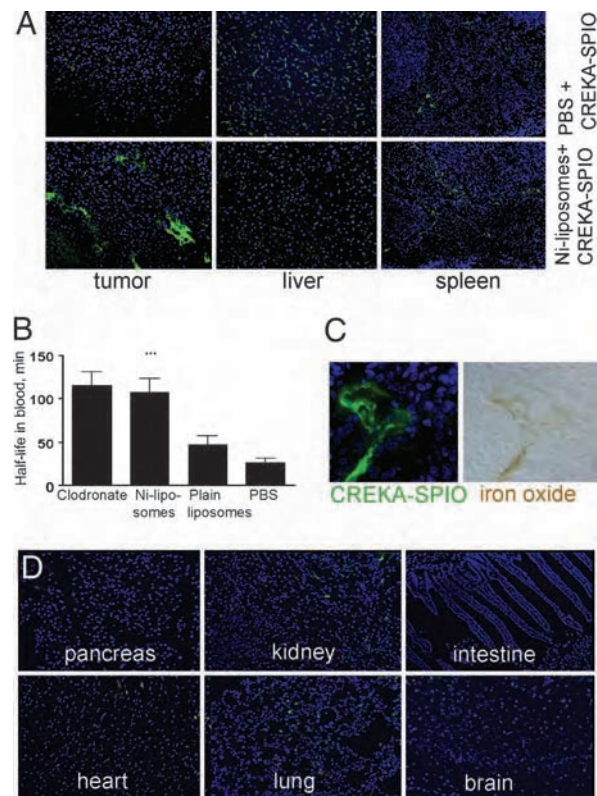

Fig. 2. Tumor homing of CREKA-conjugated iron oxide particles. CREKA-SPIO particles were intravenously injected (4 mg of Fe per kg) into BALB/c nude mice bearing MDA-MB-435 human breast cancer xenograft tumors measuring 1–1.5 cm in diameter. The mice were killed by perfusion 5–6 h later, and tissues were examined for CREKA-SPIO fluorescence (green). Nuclei were stained with DAPI (blue). (*A*) Distribution of CREKA-SPIO in tissues from MDA-MB-435 tumor mice that 2 h earlier had received an injection of PBS (*Upper*) or Ni/DSPC/CHOL liposomes (Ni-liposomes) containing 0.2 μmol Ni in 200 μl of PBS (*Lower*). (*B*) Plasma circulation half-life of CREKA-SPIO after different treatments. At least four time points were collected. Data were fitted to monoexponential decay by using Prizm software (GraphPad, San Diego, CA), and the half-life values were compared in unpaired *t* test (***, $P < 0.0001$ relative to PBS control; $n = 10$). (*C*) Accumulation of CREKA-SPIO nanoparticles in tumor vessels. Mice were injected and tissues were collected as in *A*. Fluorescent intravascular CREKA-SPIO particles overlap with iron oxide viewed in transmitted light. (Magnification: ×600.) (*D*) Control organs of Ni-liposome/CREKA-SPIO-injected mice. Occasional spots of fluorescence are seen in the kidneys and lungs. The fluorescence seen in the heart did not differ from uninjected controls, indicating that it is autofluorescence. Representative results from at least three independent experiments are shown. [Magnification: ×200 (*A* and *D*) and ×600 (*C*).]

confirmed the role of the RES in the clearance of CREKA-SPIO by depleting RES macrophages in the liver with liposomal clodronate (19). This treatment caused an ≈5-fold prolongation in particle half-life (Fig. 2*B*). Particulate material is eliminated from the circulation, because certain plasma proteins bind to the particles and mediate their uptake by the RES (opsonization) (20, 21). Injecting decoy particles that eliminate plasma opsonins is another commonly used way of blocking RES uptake (22, 23). We tested liposomes coated with chelated Ni^{2+} as a potential decoy particle because we surmised that iron oxide and Ni^{2+} would attract similar plasma opsonins, and Ni-liposomes could therefore deplete them from the systemic circulation. Indeed, SDS/PAGE analysis showed that significantly less plasma protein bound to SPIO in the blood of mice that had been pretreated with Ni-liposomes (results not shown).

Intravenously injected Ni-liposomes prolonged the half-life of

the SPIO and CREKA-SPIO in the blood by a factor of ≈5 (Fig. 2B). The Ni-liposome pretreatment, whether done 5 min or 48 h before the injection of CREKA-SPIO, greatly increased the tumor homing of the nanoparticles, which primarily localized in tumor blood vessels (Fig. 2 A Lower and D). The local concentration of particles could be so high that the brownish color of iron oxide was visible in the optical microscope (Fig. 2C Right), indicating that the fluorescent signal observed in tumor vessels was from intact CREKA-SPIO. Fewer particles were seen in the liver after the Ni-liposome pretreatment, but accumulation in the spleen was unchanged or even enhanced (Fig. 2A). Other organs contained minor amounts of CREKA-SPIO particles or no particles at all, whether Ni-liposomes were used or not (Fig. 2D). Although Ni-liposomes were quite effective, they caused some deaths in the tumor mice, prompting us to also test plain liposomes as decoy particles. These liposomes prolonged the blood half-life and tumor homing of subsequently injected CKEKA-SPIO (Fig. 2B and data not shown), suggesting the existence of a common clearance mechanism for liposomes and SPIO. However, although the plain liposomes showed no apparent toxicity, they were less effective as decoy particles than the Ni-liposomes. Reducing the Ni content of the liposomes may provide a suitable compromise between toxicity and efficacy.

Nanoparticle-Induced Blood Clotting in Tumor Vessels. CREKA-SPIO particles administered after liposome pretreatment primarily colocalized with tumor blood vessels, with some particles appearing to have extravasated into the surrounding tissue (Fig. 3A Top). Significantly, up to 20% of tumor vessel lumens were filled with fluorescent masses. These structures stained for fibrin (Fig. 3A Middle), suggesting that they are blood clots impregnated with nanoparticles. In some of the blood vessels, the CREKA-SPIO nanoparticles were distributed along a meshwork (Fig. 3A Middle Inset), presumably formed of fibrin and associated proteins, and similar to the pattern shown in Fig. 1D Inset.

Among the non-RES tissues, the kidneys and lungs contained minor amounts of specific CREKA-SPIO fluorescence (Fig. 2D). However, low-magnification images, which reveal only blood vessels with clots in them, showed no clotting in these tissues, with the exception of very rare clots in the kidneys (SI Fig. 7). Despite massive accumulation of nanoparticles in the liver, we saw no colocalization between fibrin(ogen) staining and CREKA-SPIO fluorescence in liver vessels (SI Fig. 8). Moreover, liver tissue from a noninjected mouse also stained for fibrin(ogen) (SI Fig. 8B), presumably reflecting fibrinogen production by hepatocytes. Thus, the clotting induced by CREKA-SPIO nanoparticles is essentially confined to tumor vessels.

Nanoparticles can cause platelet activation and enhance thrombogenesis (24, 25). Some CREKA-SPIO nanoparticles (<1%) recovered from blood were associated with platelets (SI Fig. 9A), but staining for a platelet marker showed no colocalization between the platelets and CREKA-SPIO nanoparticles in tumor vessels (Fig. 3A Bottom). We also induced thrombocytopenia by injecting mice with an anti-CD41 monoclonal antibody (26) and found no noticeable effect on CREKA-SPIO homing to the MDA-MB-435 tumors (SI Fig. 9B). These results indicate that platelets are not involved in the homing pattern of CREKA-SPIO.

The deep infiltration of clots by nanoparticles suggested that these clots must have formed at the time particles were circulating in blood rather than before the injection. We tested this hypothesis with intravital confocal microscopy, using DiI-labeled erythrocytes as a flow marker. There was time-dependent clot formation and obstruction of blood flow in tumor blood vessels with parallel entrapment of CREKA-SPIO in the forming clots (Fig. 3B; and see SI Movie 1).

We next tested whether the clotting-inducing effect was specific for SPIO particles, or could be induced with a different
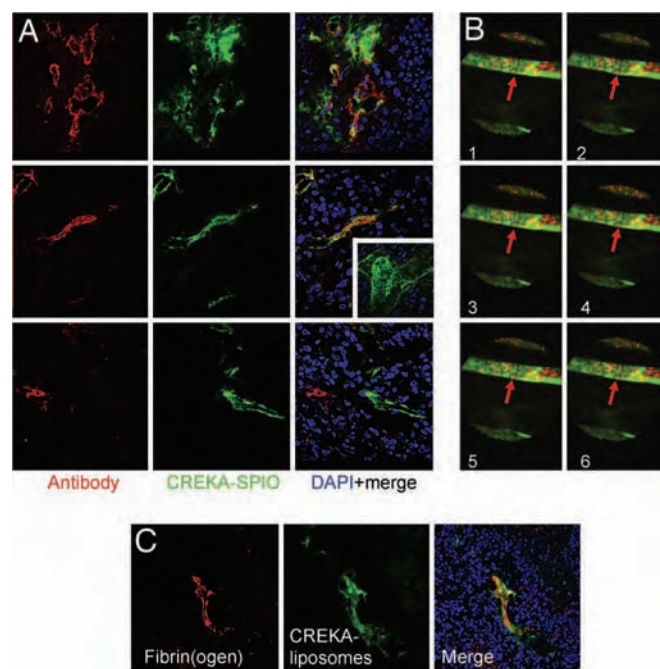

Fig. 3. Accumulation of CREKA-SPIO nanoparticles in tumor vessels. Mice bearing MDA-MB-435 xenografts were injected with Ni-liposomes and CREKA-SPIO nanoparticles as described in the legend to Fig. 2. The mice were perfused 6 h after the nanoparticle injection, and tissues were collected. (A Top) Colocalization of nanoparticle fluorescence with CD31 staining in blood vessels. (A Middle) Colocalization of nanoparticle fluorescence and antifibrin(ogen) staining in tumor blood vessels. (Inset) An image showing CREKA-SPIO distributed along fibrils in a tumor blood vessel. (A Bottom) Lack of colocalization of nanoparticle fluorescence with anti-CD41 staining for platelets. (B) Intravital confocal microscopy of tumors using DiI-stained red blood cells as a marker of blood flow. The arrow points to a vessel in which stationary erythrocytes indicate obstruction of blood flow. Blood flow in the vessel above is not obstructed. Six successive frames from a 1-min movie (SI Movie 1) are shown. (C) CREKA-coated liposomes colocalize with fibrin in tumor vessels. The results are representative of three independent experiments. [Magnification: ×600 (A and C) and ×200 (B).]

CREKA-coated particle. We used liposomes into which we incorporated fluorescein-CREKA peptide that was coupled to lipid-tailed polyethylene glycol. Like CREKA-SPIO, the CREKA-liposomes selectively homed to tumors and colocalized with fibrin within tumor vessels (Fig. 3C), suggesting that CREKA liposomes are also capable of causing clotting in tumor vessels. No clotting was seen when control SPIO or control liposomes were injected in the tumor mice.

Clotting-Amplified Tumor Targeting. We next studied the contribution of clotting to the accumulation of CREKA-SPIO in tumor vessels. Quantitative analysis of tumor magnetization with a superconducting quantum interference device (SQUID) (Fig. 4A), and measurement of the fluorescence signal (data not shown) revealed ≈6-fold greater accumulation of CREKA-SPIO in Ni-liposome-pretreated mice compared with PBS-pretreated mice. Aminated SPIO control particles did not significantly accumulate in the tumors (Fig. 4A).

The SQUID measurements revealed that injecting heparin, which is a strong clotting inhibitor, before injection of CREKA-SPIO reduced tumor accumulation of nanoparticles by >50% (Fig. 4A). Microscopy showed that heparin reduced the fibrin-positive/CREKA-SPIO-positive structures within tumor vessels but that the particles still bound along the walls of the vessels, presumably to preexisting fibrin deposits (a representative image is shown in Fig. 4B). Separate quantification of the homing
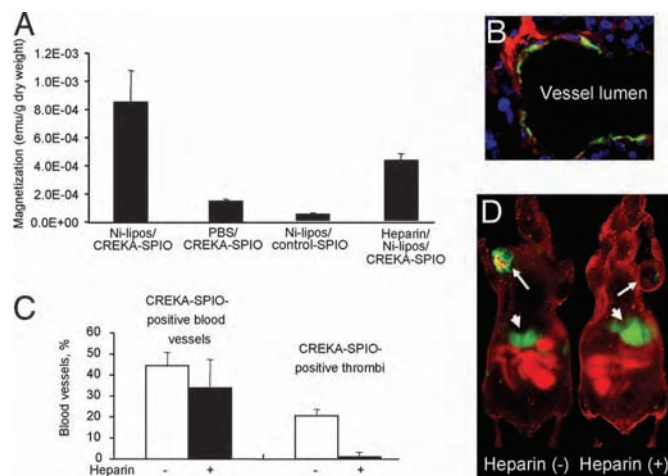
Fig. 4. Effect of blood clotting on nanoparticle accumulation in tumors. Mice bearing MDA-MB-435 human breast cancer xenografts were intravenously injected with PBS or a bolus of 800 units/kg of heparin, followed 120 min later by Ni-liposomes (or PBS) and CREKA-SPIO (or control nanoparticles). The mice received additional heparin by i.p. injections (a total of 1,000 units/kg) or PBS throughout the experiment. (*A*) Tumors were removed 6 h after the nanoparticle injection, and magnetic signal in the tumor after different treatments was determined with SQUID. Aminated dextran SPIO served as a particle control (control SPIO). SPIO nanoparticle concentration in tissues is represented by the saturation magnetization value (electromagnetic unit, emu) of the tissue at 1T magnetic field after the subtraction of the diamagnetic and the paramagnetic background of blank tissue. The magnetization values were normalized to dry weight of the tissue. Results from three experiments are shown. (*B*) Quantification of heparin effect on clotting in blood vessels. Mice were pretreated with PBS (open bars) or heparin (filled bars) as described above, followed by Ni liposomes/CREKA-SPIO nanoparticles. Three sections from two tumors representing each treatment were stained with anti-CD31 for blood vessels, and the percentage of vessels positive for fluorescence and fluorescent clots was determined. Note that heparin did not significantly change the percentage of blood vessels containing particles, but dramatically decreased the incidence of the lumens that are filled with fluorescence. (*C*) A representative example of the appearance of CREKA-SPIO particles in tumor vessels of mice treated with heparin. (*D*) Near-infrared imaging of mice that received Ni-liposomes, followed by Cy7-labeled CREKA-SPIO, with or without heparin pretreatment. The images were acquired 8 h after the injection of the CREKA-SPIO particles by using an Odyssey 2 NIR scanner (Li-COR Biosciences, Lincoln, NE). The images shown are composites of two colors, red (700-nm channel, body and chow autofluorescence) and green (800-nm channel, Cy7). Arrows point to the tumors, and arrowheads point to the liver. Note the strong decrease in signal from the tumor in the heparin-pretreated mouse. One representative experiment of three is shown.

pattern showed that heparin did not significantly reduce the number of vessels with nanoparticles bound to the vessel walls, but essentially eliminated the intravascular clotting (Fig. 4*C*). Thus, the binding of CREKA-SPIO to tumor vessels does not require the clotting activity that is associated with these particles, but clotting improves the efficiency of the tumor homing.

The clotting induced by CREKA-SPIO caused a particularly strong enhancement of tumor signal in whole-body scans. CREKA-SPIO nanoparticles labeled with Cy7, a near-infrared fluorescent compound, effectively accumulated in tumors (Fig. 4*D*, image on the left, arrow), with a significant signal from the liver as well (arrowhead). The reduction in the tumor signal obtained with heparin (Fig. 4*D*, image on the right) appeared greater in the fluorescence measurements than the 50% value determined by SQUID, possibly because the concentrated signal from the clots enhanced optical detection of the fluorescence. These results suggest that the clotting induced by CREKA-SPIO provides a particular advantage in tumor imaging.

Discussion

We describe a nanoparticle system that provides effective accumulation of the particles in tumors. The system is based on four elements: First, coating of the nanoparticles with a tumor-homing peptide that binds to clotted plasma proteins endows the particles with a specific affinity for tumor vessels (and tumor stroma). Second, decoy particle pretreatment prolongs the blood half-life of the particles and increases tumor targeting. Third, the tumor-targeted nanoparticles cause intravascular clotting in tumor blood vessels. Fourth, the intravascular clots attract more nanoparticles into the tumor, amplifying the targeting.

We chose a peptide with specific affinity for clotted plasma proteins as the targeting element for our nanoparticles. The interstitial spaces of tumors contain fibrin and proteins that become cross-linked to fibrin in blood clotting, such as fibronectin (13, 15). The presence of these products in tumors, but not in normal tissues, is thought to be a result of leakiness of tumor vessels, which allows plasma proteins to enter from the blood into tumor tissue, where the leaked fibrinogen is converted to fibrin by tissue procoagulant factors (13, 14). The clotting creates new binding sites that can be identified and accessed with synthetic peptides (15). The present results show that the CREKA-modified nanoparticles not only bind to blood and plasma clots but can also induce localized tumor clotting. The nature of the particle may not be important for this activity, because we found both CREKA-coated iron oxide nanoparticles and micron-sized CREKA-coated liposomes to cause clotting in tumor vessels. The mechanism by which CREKA-SPIO and CREKA-liposomes induce vascular clotting requires further study. We speculate that the binding of one or more clotting products by the CREKA-modified particles may shift the balance of clotting and clot dissolution in the direction of clot formation and that the presence of this activity at the surface of particles may facilitate contact-dependent coagulation.

Some nanomaterials are capable of triggering systemic thrombosis (27), but, here, the thrombosis induced by the CREKA particles was confined to tumor vessels. The high concentration of the targeted particles in tumor vessels partially explains the selective localization of the thrombosis to tumor vessels. However, because no detectable clotting was seen in the liver, where the nanoparticles also accumulate at high concentrations, other factors must be important. The procoagulant environment common in tumors is likely to be a major factor contributing to the tumor-specificity of the clotting (28). It remains to be seen whether CREKA particles might bind to other regions of pathological clotting activity in the body (e.g., wounds) and to induce additional clotting at such sites.

A major advantage of nanoparticles is that multiple functions can be incorporated onto a single entity. We describe here an *in vivo* function for nanoparticles that has not been described previously; self-amplifying tumor homing enabled by nanoparticle-induced clotting in tumor vessels and the binding of additional nanoparticles to the clots. Our nanoparticle system combines several other functions into one particle: specific tumor homing, avoidance of the RES, and effective tumor imaging. We used optical imaging in this work, but the SPIO platform also enables MRI imaging, which does not suffer from the tissue-penetration problems that limit optical imaging in animals larger than mice and in humans. The clotting caused by CREKA-SPIO nanoparticles in tumor vessels serves to focally concentrate the particles in a manner that appears to improve tumor detection by microscopic and whole-body imaging techniques.

Another possibly useful function of our targeted particles is that they cause physical blockade of tumor vessels by local embolism. Blood vessel occlusion by embolism or clotting can reduce tumor growth (29, 30). To date, we have achieved a 20% occlusion rate in tumor vessels. Preliminary tumor treatment

experiments (D.S., L.Z., and E.R., unpublished work) have indicated that this degree of vessel occlusion is not sufficient to reduce the rate of tumor growth. However, future optimization of the procedure may change that. Finally, because of the modular nature of nanoparticle design, the functions we describe here can be incorporated into particles with additional activities. We envision the design of drug-carrying nanoparticles that accumulate in tumor vessels and slowly release the drug payload while simultaneously occluding the vessels.

Materials and Methods

Phage Screening, Tumors, and Peptides. *In vivo* screening of a peptide library with the general structure of CX_7C, where C is cysteine and X is any amino acid, was carried out as described (5) by using 65- to 75-day-old transgenic MMTV PyMT mice (31). These mice express the polyoma virus middle T antigen (MT) under the transcriptional control of the mouse mammary tumor virus (MMTV), leading to the induction of multifocal mammary tumors in 100% of carriers. MDA-MB-435 tumors in nude mice and peptide synthesis have been described (32, 33). B16F1 murine melanoma tumors were grown in fibrinogen null mice (34) and their normal littermates and were used when they reached 0.5–1 cm in size (15).

Nanoparticles and Liposomes. Amino group-functionalized dextran-coated superparamagnetic iron oxide nanoparticles (50-nm nanomag-D-SPIO; Micromod Partikeltechnologie, Rostock, Germany) were coupled with CREKA peptide by using a cross-linker. The final coupling ratio was 30 nmol of fluorescein-labeled peptide molecules per milligram of iron oxide, or 8,000 peptides per particle. For near-infrared labeling with Cy7, ≈20% of the amines were derivatized with Cy7-NHS ester (GE Healthcare Bio-Sciences, Piscataway, NJ), and the remaining amines were used for conjugating the peptide. Details on the SPIO and the preparation of liposomes are described in *SI Materials and Methods*. Clodronate

was purchased from Sigma (St. Louis, MO) and incorporated into liposomes as described (19).

Nanoparticle Injections. For i.v. injections, the animals were anesthetized with i.p. Avertin, and liposomes (2 μmol of DSPC) and/or nanoparticles (1–4 mg of Fe per kg of body weight) were injected into the tail vein. The animals were killed 5–24 h after injection by cardiac perfusion with PBS under anesthesia, and organs were dissected and analyzed for particle homing. To suppress liver macrophages, mice were intravenously injected with liposomal clodronate suspension (100 μl per mouse), and the mice were used for experiments 24 h later. All animal work was reviewed and approved by the Burnham Institute's Animal Research Committee.

Phage and Nanoparticle Binding to Clots. Phage binding to clotted plasma proteins was determined as described (15). CREKA-SPIO and control SPIO were added to freshly formed plasma clots in the presence or absence of free CREKA peptide. After 10 min of incubation, the clots were washed four times in PBS, transferred to a new tube and digested in 100 μl of concentrated nitric acid. The digested material was diluted in 2 ml of distilled water, and the iron concentration was determined by using inductively coupled plasma–optical emission spectroscopy (ICP-OES; PerkinElmer, Norwalk, CT).

Plasma Protein Binding to Nanoparticles, Particle Clearance from the Blood, Intravital Microscopy and Magnetic Measurements. For information on plasma protein binding and the other methods, see *SI Materials and Methods*.

1. Desai N, Trieu V, Yao Z, Louie L, Ci S, Yang A, Tao C, De T, Beals B, Dykes D, et al. (2006) *Clin Cancer Res* 12:1317–1324.
2. Weissleder R, Bogdanov A, Jr, Neuwelt EA, Papisov M (1995) *Adv Drug Delivery Rev* 16:321–334.
3. Sinek J, Frieboes H, Zheng X, Cristini V (2004) *Biomed Microdevices* 6:297–309.
4. Boucher Y, Baxter LT, Jain RK (1990) *Cancer Res* 50:4478–4484.
5. Hoffman JA, Giraudo E, Singh M, Zhang L, Inoue M, Porkka K, Hanahan D, Ruoslahti E (2003) *Cancer Cell* 4:383–391.
6. Oh P, Li Y, Yu J, Durr E, Krasinska KM, Carver LA, Testa JE, Schnitzer JE (2004) *Nature* 429:629–635.
7. Ruoslahti E (2002) *Nat Rev Cancer* 2:83–90.
8. DeNardo SJ, DeNardo GL, Miers LA, Natarajan A, Foreman AR, Gruettner C, Adamson GN, Ivkov R (2005) *Clin Cancer Res* 11:7087s–7092s.
9. Akerman ME, Chan WC, Laakkonen P, Bhatia SN, Ruoslahti E (2002) *Proc Natl Acad Sci USA* 99:12617–12621.
10. Cai W, Shin DW, Chen K, Gheysens O, Cao Q, Wang SX, Gambhir SS, Chen X (2006) *Nano Lett* 6:669–676.
11. Pasqualini R, Ruoslahti E (1996) *Nature* 380:364–366.
12. Hutchinson JN, Muller WJ (2000) *Oncogene* 19:6130–6137.
13. Dvorak HF, Senger DR, Dvorak AM, Harvey VS, McDonagh J (1985) *Science* 227:1059–1061.
14. Abe K, Shoji M, Chen J, Bierhaus A, Danave I, Micko C, Casper K, Dillehay DL, Nawroth PP, Rickles FR (1999) *Proc Natl Acad Sci USA* 96:8663–8668.
15. Pilch J, Brown DM, Komatsu M, Jarvinen TA, Yang M, Peters D, Hoffman RM, Ruoslahti E (2006) *Proc Natl Acad Sci USA* 103:2800–2804.
16. Jung CW, Jacobs P (1995) *Magn Reson Imaging* 13:661–674.
17. Jung CW (1995) *Magn Reson Imaging* 13:675–691.
18. Weissleder R, Stark DD, Engelstad BL, Bacon BR, Compton CC, White DL, Jacobs P, Lewis J (1989) *Am J Roentgenol* 152:167–173.
19. Van Rooijen N, Sanders A (1994) *J Immunol Methods* 174:83–93.
20. Moghimi SM, Hunter AC, Murray JC (2001) *Pharmacol Rev* 53:283–318.
21. Moore A, Weissleder R, Bogdanov A, Jr (1997) *J Magn Reson Imaging* 7:1140–1145.
22. Souhami RL, Patel HM, Ryman BE (1981) *Biochim Biophys Acta* 674:354–371.
23. Fernandez-Urrusuno R, Fattal E, Rodrigues JM, Jr, Feger J, Bedossa P, Couvreur P (1996) *J Biomed Mater Res* 31:401–408.
24. Radomski A, Jurasz P, Alonso-Escolano D, Drews M, Morandi M, Malinski T, Radomski MW (2005) *Br J Pharmacol* 146:882–893.
25. Khandoga A, Stampfl A, Takenaka S, Schulz H, Radykewicz R, Kreyling W, Krombach F (2004) *Circulation* 109:1320–1325.
26. Van der Heyde HC, Gramaglia I, Sun G, Woods C (2005) *Blood* 105:1956–1963.
27. Gorbet MB, Sefton MV (2004) *Biomaterials* 25:5681–5703.
28. Boccaccio C, Sabatino G, Medico E, Girolami F, Follenzi A, Reato G, Sottile A, Naldini L, Comoglio PM (2005) *Nature* 434:396–400.
29. Huang X, Molema G, King S, Watkins L, Edgington TS, Thorpe PE (1997) *Science* 275:547–550.
30. El-Sheikh A, Borgstrom P, Bhattacharjee G, Belting M, Edgington TS (2005) *Cancer Res* 65:11109–11117.
31. Hutchinson JN, Muller WJ (2000) *Oncogene* 19:6130–6137.
32. Laakkonen P, Porkka K, Hoffman JA, Ruoslahti E (2002) *Nat Med* 8:751–755.
33. Laakkonen P, Akerman ME, Biliran H, Yang M, Ferrer F, Karpanen T, Hoffman RM, Ruoslahti E (2004) *Proc Natl Acad Sci USA* 101:9381–9386.
34. Suh TT, Holmback K, Jensen NJ, Daugherty CC, Small K, Simon DI, Potter S, Degen JL (1995) *Genes Dev* 9:2020–2033.

Antiangiogenic Therapy Decreases Integrin Expression in Normalized Tumor Blood Vessels

Virginia J. Yao,[1] Michael G. Ozawa,[1] Amanda S. Varner,[1] Ian M. Kasman,[1] Yvan H. Chanthery,[1] Renata Pasqualini,[3] Wadih Arap,[3] and Donald M. McDonald[1,2]

[1]Department of Anatomy, [2]Cardiovascular Research Institute, Comprehensive Cancer Center, University of California, San Francisco, California; and [3]The University of Texas M.D. Anderson Cancer Center, Houston, Texas

Abstract

Tumor blood vessels normalized by antiangiogenic therapy may provide improved delivery of chemotherapeutic agents during a window of time but it is unknown how protein expression in tumor vascular endothelial cells changes. We evaluated the distribution of RGD-4C phage, which binds $\alpha_v\beta_3$, $\alpha_v\beta_5$, and $\alpha_5\beta_1$ integrins on tumor blood vessels before and after antiangiogenic therapy. Unlike the control phage, fd-tet, RGD-4C phage homed to vascular endothelial cells in spontaneous tumors in RIP-Tag2 transgenic mice in a dose-dependent fashion. The distribution of phage was similar to $\alpha_v\beta_3$ and $\alpha_5\beta_1$ integrin expression. Blood vessels that survived treatment with AG-013736, a small molecule inhibitor of vascular endothelial growth factor and platelet-derived growth factor receptors, had only 4% as much binding of RGD-4C phage compared with vessels in untreated tumors. Cellular distribution of RGD-4C phage in surviving tumor vessels matched the $\alpha_5\beta_1$ integrin expression. The reduction in integrin expression on tumor vessels after antiangiogenic therapy raises the possibility that integrin-targeted delivery of diagnostics or therapeutics may be compromised. Efficacious delivery of drugs may benefit from identification by *in vivo* phage display of targeting peptides that bind to tumor blood vessels normalized by antiangiogenic agents. (Cancer Res 2006; 66(5): 2639-49)

Introduction

The morphologic, organizational, and metabolic diversity of endothelial cells exemplifies the heterogeneity of the microvasculature (1). In the brain, continuous endothelial cells of the blood-brain barrier restrict the movement of solutes, whereas fenestrated endothelial cells of the choroid plexus favor solute flux (2). Signals from endothelial cells influence the formation of bone (3) and the development of the pancreas and liver from the primitive endoderm (4, 5). Compared with quiescent established blood vessels, endothelial cells in angiogenic blood vessels express additional proteins, such as the $\alpha_v\beta_3$, $\alpha_v\beta_5$ (6–8) and the $\alpha_5\beta_1$ integrins (9). Peptides that bind specifically to distinct vascular beds in normal mice and in a human subject, as identified by *in vivo* phage display, show the inherent molecular heterogeneity within the microvasculature (1, 10, 11). Intraorgan vascular heterogeneity has also been shown by two peptide phage that are ephrin A-type ligand mimetics that bind solely to the vasculature of normal murine pancreatic islets with increased

localization to islet tumor blood vessels (12). Given such inherent molecular diversity of the normal and tumor microvasculature, resident receptor proteins for selective targeting of diagnostic and therapeutic agents to specific vascular beds can be identified and exploited.

An example of a tumor-targeting phage is one displaying the sequence, CDCRGDCFC (termed RGD-4C phage). The double cyclic RGD-4C peptide binds with a 200-fold greater *in vitro* affinity to $\alpha_v\beta_3$ and $\alpha_v\beta_5$ integrins and a 50-fold greater affinity to the $\alpha_5\beta_1$ integrin than the linear GRGDSP peptide (13). Moreover, *in vivo* studies show RGD-4C phage have a 40- to 80-fold greater selectivity for tumor blood vessels (8). Tumor burden decreased upon i.v. delivery of the RGD-4C peptide fused to either doxorubicin or to a proapoptotic peptide with reduced host toxicity (14, 15). Other studies revealed FITC-labeled RGD-4C peptide binds to both human MDA-MB-435 tumor xenografts and infiltrating murine tumor endothelial cells (16).

In addition to site-directed targeting, inhibition of proangiogenic factors and their signaling pathways has shown promise as tumor therapies (17, 18). Tumor blood vessel regression is enhanced when therapeutic regimens combine vascular endothelial growth factor receptor (VEGFR)-2 inhibitors, such as SU5416, with platelet-derived growth factor receptor (PDGFR)-β inhibitors, such as SU6668 or Gleevec (19), in implanted rat gliomas and pancreatic islet tumors (20, 21). We have recently shown that VEGF Trap, a soluble VEGFR-1/VEGFR-2 chimeric antibody that binds VEGF-A, VEGF-B, and placental growth factor-1 (22), and AG-013736, a potent small molecule inhibitor of VEGF/PDGF receptor tyrosine kinases (23), cause the disappearance of endothelial fenestrations, tumor vessel regression, and the appearance of basement membrane ghosts in murine pancreatic islet tumors (24). Although combination therapies using antiangiogenic compounds with chemotherapy are successful (25, 26), the timing for administration of secondary therapeutic(s) via the normalized tumor vasculature is likely to be a critical factor (27, 28). Although the surviving normalized tumor vessels are functional, molecular changes to the tumor endothelium following antiangiogenic therapy are less well understood.

In this study, we examined the physiologic distribution of the tumor-targeting RGD-4C phage by immunofluorescence microscopy in blood vessels of the RIP-Tag2 pancreatic islet tumor mouse model (29) and its distribution following AG-013736 therapy. The first objective of this study was to compare the distribution of RGD-4C versus fd-tet phage in tumor blood vessels. We sought to quantify the dose dependency of phage distribution and to corroborate the distribution of $\alpha_v\beta_3$ and $\alpha_5\beta_1$ integrins to that of RGD-4C phage in tumor blood vessels. In addition, we compared the targeted localization of RGD-4C phage in tumor blood vessels to normal blood vessels in the lung, thyroid gland, cerebral cortex, and liver. Our second objective was to determine whether RGD-4C

phage could be used as a biological tool to determine whether endothelial cells that survive antiangiogenic therapy modify their pattern of integrin expression, thereby signaling a phenotypic change in the vasculature.

Materials and Methods

Animals. RIP-Tag2 transgenic mice from a C57BL/6 background contain the insulin promoter–driven SV40 T-antigen and produce spontaneous multifocal and multistage pancreatic islet tumors (29). RIP-Tag2-positive mice were genotyped from tail-tip DNA by PCR. Male and female RIP-Tag2 mice and nontransgenic littermates between 8 and 12 weeks of age were used in these studies. Mice were housed under barrier conditions at the animal care facility at the University of California, San Francisco. The Institutional Animal Care and Use Committee at University of California, San Francisco, approved all experimental procedures.

Phage preparation. Purified single-stranded fd-tet (30) or CDCRGDCFC (13) phage DNA was electroporated into competent MC1061 *Escherichia coli* (31), and plated onto Luria-Bertani agar medium containing 100 mg/L streptomycin and 40 mg/L tetracycline (LB/Strep/TET). Single colonies were picked, peptide inserts were amplified by colony PCR, and sequences were verified (12). Phages were amplified overnight at 37°C with agitation from a single transformed MC1061 colony in 100 mL LB/Strep/TET. Phage were precipitated from the bacterial supernatant with 15% NaCl/PEG 8000 (Fisher Scientific, Tustin, CA) for 1 hour on ice, pelleted by centrifugation for 20 minutes at 4°C at 10,400 × g, gently resuspended in 5 mL sterile PBS, and precipitated with 15% NaCl/PEG 8000 on ice for 30 minutes. The final phage pellet was gently resuspended in 100 μL sterile PBS, centrifuged for 2 minutes at maximum g force, and the supernatant was filtered through a 0.22 μm syringe filter. Infectivity titers were determined using established protocols (32).

Phage and antibody injections and tissue preparation. Purified, titered phage preparations were used within 24 hours of preparation. Serial dilutions of phage at 10^9, 10^8, and 10^7 transforming units (TU) were made with DMEM containing Earle salts (University of California, San Francisco Cell Culture Facility) to a final volume of 200 μL. Twenty-five micrograms hamster CD61 (PharMingen, San Diego, CA), rat CD51 (eBioscience, San Diego, CA), monoclonal rat CD49e antibodies (PharMingen), or corresponding amounts of normal hamster (Jackson ImmunoResearch, West Grove, PA) or rat serum antibodies (Jackson ImmunoResearch) were diluted with sterile saline to a final volume of 125 μL each and filtered through 0.22 μm filters. Phage and antibodies were administered i.v. into Avertin (2,2,2-tribromoethanol, 0.015-0.017 mg/g, injected i.p., Sigma-Aldrich Corp., St. Louis, MO)–anesthetized mice (32) and allowed to circulate for 6 minutes. Body temperatures of anesthetized mice were maintained with a heating pad. Mice were systemically perfused with 1% paraformaldehyde in PBS, pH 7.4, and tissues were frozen (12).

AG-013736 treatment. Nine-week-old male RIP-Tag2 mice (n = 10) were injected with either AG-013736 (25 mg/kg, i.p., BID) or with the vehicle [three parts PEG 400 to seven parts acidified H_2O (pH 2)] for 7 days. AG-013736 is a potent small molecule inhibitor of VEGF/PDGF receptor tyrosine kinases (IC$_{50}$, 1.2 nmol/L for VEGFR-1, 0.25 nmol/L for VEGFR-2, 0.29 nmol/L for VEGFR-3, 2.5 nmol/L for PDGFR-β, 2.0 nmol/L for c-Kit, and 218 nmol/L for FGFR-1; ref. 23), and was provided by Pfizer Global Research and Development (San Diego, CA). Treated mice were injected i.v. with 10^9 TU RGD-4C phage and perfused as described above.

Immunohistochemistry. Details for immunostaining fixed frozen sections and sections of phage injected tissues were previously described (12). For immunostaining antibody-injected tissues, sections were incubated with either monoclonal Armenian hamster anti-mouse CD31 (1:1,000, Chemicon, Temecula, CA) or monoclonal rat antimouse CD31 antibodies (1:500, PharMingen) and 5% normal goat serum (Jackson ImmunoResearch) with 1% Triton X-100 in PBS (PBST; pH 7.4). Rinsed sections were incubated in secondary antibody solutions containing goat FITC-conjugated anti-rat antibodies (1:200, Jackson ImmunoResearch) and goat Cy3-conjugated anti-Armenian hamster antibodies (1:400, Jackson ImmunoResearch), or goat FITC-conjugated anti-Armenian hamster antibodies (1:200, Jackson Immuno Research), or goat Cy3-conjugated anti-rat antibodies (1:400, Jackson ImmunoResearch) and 5% normal goat serum in PBST. Triple stained sections were incubated with monoclonal rat anti-mouse CD31, monoclonal Cy3-conjugated α-smooth muscle actin (α-SMA, 1:2,000, Sigma-Aldrich), rabbit polyclonal anti-fd-bacteriophage antibody (1:5,000, Sigma-Aldrich), and 5% normal mouse serum in PBST. Rinsed sections were incubated in a secondary antibody solution containing mouse FITC-conjugated anti-rat IgGs, mouse Cy5-conjugated anti-rabbit IgGs (1:400, Jackson ImmunoResearch), and 5% normal mouse serum in PBST. For the AG-013736 studies, frozen 80 μm sections from vehicle or AG-013736-treated tissues were incubated with monoclonal Armenian hamster anti-mouse CD31 and monoclonal rat CD49e antibodies (1:500, PharMingen) and 5% normal goat serum in PBST. Rinsed sections were incubated in a secondary antibody solution containing goat FITC-conjugated anti-Armenian hamster antibodies and goat Cy3-conjugated anti-rat antibodies in PBST.

Imaging. Fluorescence images were acquired using an externally coded, three-chip charge-coupled device camera (CoolCam, SciMeasure Analytical Systems, Atlanta, GA) fitted on a Zeiss Axiophot fluorescence microscope with Fluar objectives or with a Zeiss LSM 510 Laser Scanning confocal microscope with krypton-argon and helium-neon lasers at 488, 543, and 633 nm (Carl Zeiss, Jena, Germany) and analyzed with the Zeiss LSM 510 software v. 3.2.2.

Quantification of phage in blood vessels. Densities of phage immunoreactivity in blood vessels, hereafter called phage vessel area density, for the dose-dependent studies were quantified from 20-μm-thick confocal projections of immunostained RIP-Tag2 islets using ImageJ (http://rsb.info.nih.gov/ij/) with the Zeiss LSM Reader plug-in interface (http://rsb.info.nih.gov/ij/plugins/lsm-reader.html). Total blood vessel densities of tumor islets were determined from CD31-immunoreactive blood vessels and calculated from user-defined islet regions after thresholds were empirically determined. Phage vessel area densities were calculated as the number of pixels of phage immunoreactivity divided by the total vessel area represented by CD31 immunoreactivity. Mean phage vessel area density values and SEs were determined from five islet tumors or acinar regions each from three mice injected with 10^9, 10^8, and 10^7 TU RGD-4C phage, and five islet tumors each from three mice injected with 10^9, 10^8, and 10^7 TU fd-tet phage. For the buffer control, five to six islet tumors each were analyzed from five mice. For the AG-013736 studies, phage vessel area densities were quantified from digital Coolcam fluorescence images acquired with a ×10 Fluar objective. Phage vessel area densities were determined as the percentage of red pixels (phage) to the total number of green pixels (CD31) in islets using the threshold setting of 50 for each image. Mean ± SE values were calculated from five images per mouse (n = 5 mice per group). Statistical analyses were determined by the ANOVA Bonferroni-Dunn test. Cy3 anti-rat CD49e fluorescence intensities of 80 μm pancreatic immunostained sections from vehicle and AG-013736-treated mice were measured from digitized Coolcam images acquired with a ×20 Fluar objective. Cy3 digitized images were converted to grayscale 8-bit images using the look-up table importer plug-in in ImageJ. A customized look-up table that defines the boundaries of fluorescence intensities as a spectrum of color from 0 to 255 was applied to each 8-bit image that was then converted to a surface plot. Increased fluorescence intensities correspond to increased peak heights in the Z-plane.

Results

Distribution of RGD-4C phage in tumor blood vessels. Tumors in RIP-Tag2 transgenic mice were used as a model because they are multifocal and multistage, thereby allowing visualization of phage in tumor blood vessels during various stages of tumorigenesis as well as in normal blood vessels in the acinar pancreas. The immunohistochemical staining pattern of i.v. administered 10^9 TU of RGD-4C phage in the tumor vasculature was distinct and punctate (Fig. 1). In RIP-Tag2 tumors, RGD-4C phage was abundant in blood vessels 6 minutes after injection such that the majority of the tumor
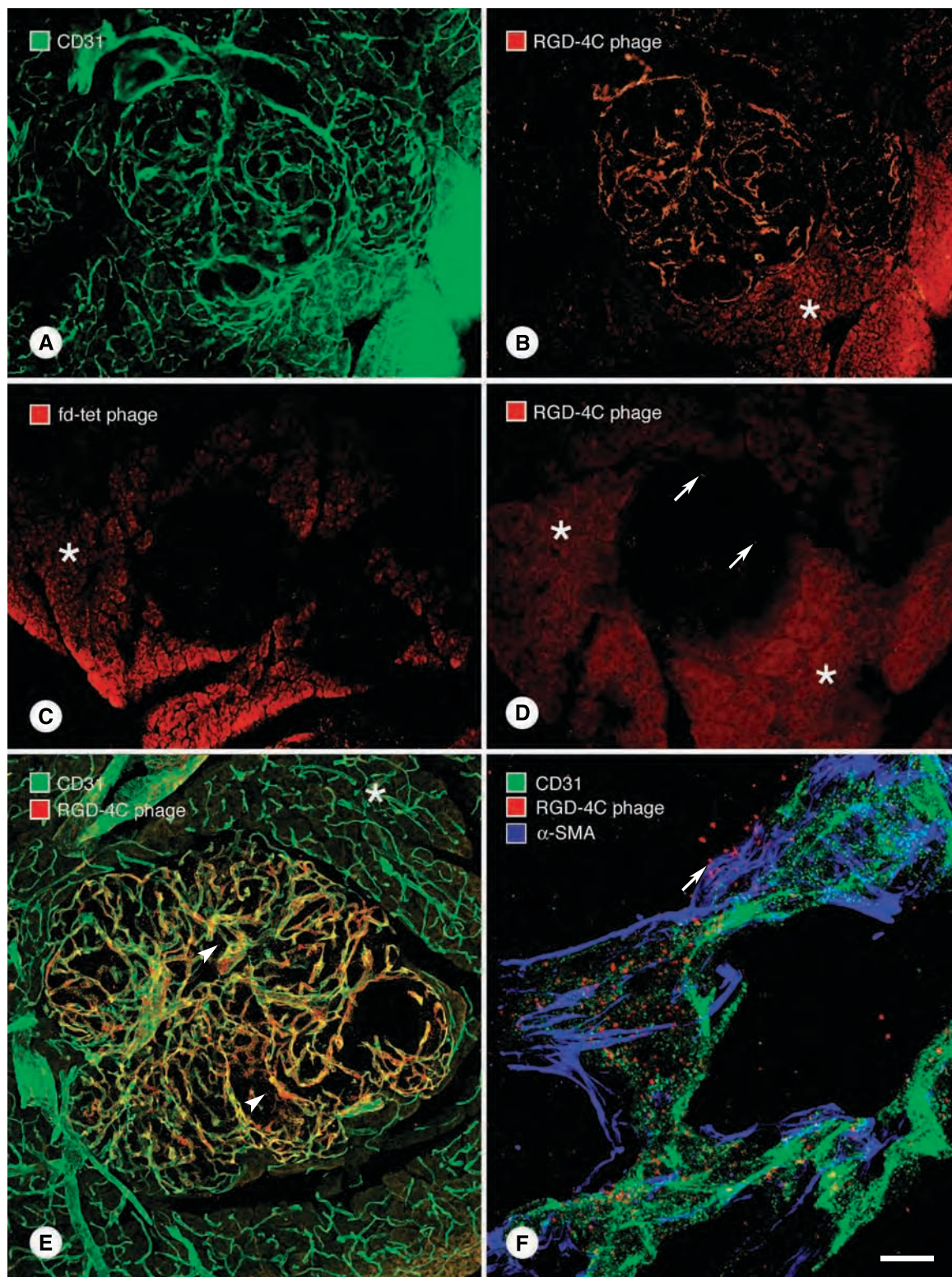
Figure 1. Localization of 10^9 TU RGD-4C phage to RIP-Tag2 islet tumor blood vessels. *A*, blood vessels (CD31, *green*) in two RIP-Tag2 tumors contain (*B*) RGD-4C phage (*red*). RIP-Tag2 tumor blood vessels contain negligible amounts of (*C*) fd-tet phage (*red*), whereas (*D*) vessels in normal islets contain a minimal amount of RGD-4C phage (*red, arrows*). RGD-4C or fd-tet phage show minimal binding to blood vessels in the acinar pancreas from either RIP-Tag2 or C57BL/6 mice (*B-D, asterisks*). *E,* RGD-4C phage (*red*) colocalize with blood vessels (*green*) in a RIP-Tag2 tumor with small focal regions of extravasated phage (*arrowheads*), whereas acinar blood vessels do not contain RGD-4C phage (*asterisk*). *F,* at high magnification, RGD-4C phage (*red*) are primarily confined within tumor blood vessels (*green*); however, extravasated phage (*arrow*) outside blood vessels do not colocalize with associated pericytes (α-SMA, *blue*). Bar in (*F*) applies to all panels: *A* to *C*, 160 μm; *D,* 80 μm; *E,* 60 μm; *F,* 13 μm.

vasculature could be delineated by RGD-4C phage immunoreactivity (Fig. 1*A* and *B*). In contrast, an equivalent amount of the insertless, negative control phage, fd-tet, did not localize to tumor blood vessels (Fig. 1*C*); RGD-4C phage localized much less to blood vessels in normal islets (Fig. 1*D, arrows*). RGD-4C phage accumulation was not influenced by tumor size and was distributed throughout the tumor vasculature with focal regions of extravasation (Fig. 1*E, arrowheads*). Moreover, the amount of RGD-4C phage was comparatively low to none in the acinar pancreas blood vessels of either RIP-Tag2 or normal mice (Fig. 1*B-E, asterisks*). Extravasated RGD-4C phage did not seem to colocalize with α-SMA-immunoreactive pericytes (Fig. 1*F, arrow*).

Quantification of RGD-4C phage in tumor blood vessels. The affinity of RGD-4C phage binding to blood vessels in RIP-Tag2 tumors was examined further by decreasing the injected dose from 10^9 to 10^7 TU (Fig. 2). We reasoned that if *in vivo* binding of RGD-4C

phage was a specific event, then our immunofluorescence studies should show a reduction of phage binding commensurate with decreasing amounts of i.v. administered phage. These experiments should also provide information regarding the threshold for phage detection by immunohistochemistry. The amount of RGD-4C phage in blood vessels in RIP-Tag2 tumors was reduced when the amount of injected phage decreased from 10^9 to 10^7 TU (Fig. 2*A-C*). Background immunostaining in tumor blood vessels from buffer-treated control mice was negligible (data not shown). RGD-4C phage was detectable when injected at 10^7 TU (Fig. 2*C, right*); however, the immunoreactivity was comparable with fd-tet phage injected at 10^7 TU (data not shown). Mean RGD-4C and fd-tet phage vessel area densities were quantified in CD31-immunoreactive tumor blood vessels at each dose (Fig. 2*D*). At 10^9 TU, the mean RGD-4C phage vessel area density was 4-fold greater than that of fd-tet phage in tumor blood vessels and was statistically significant
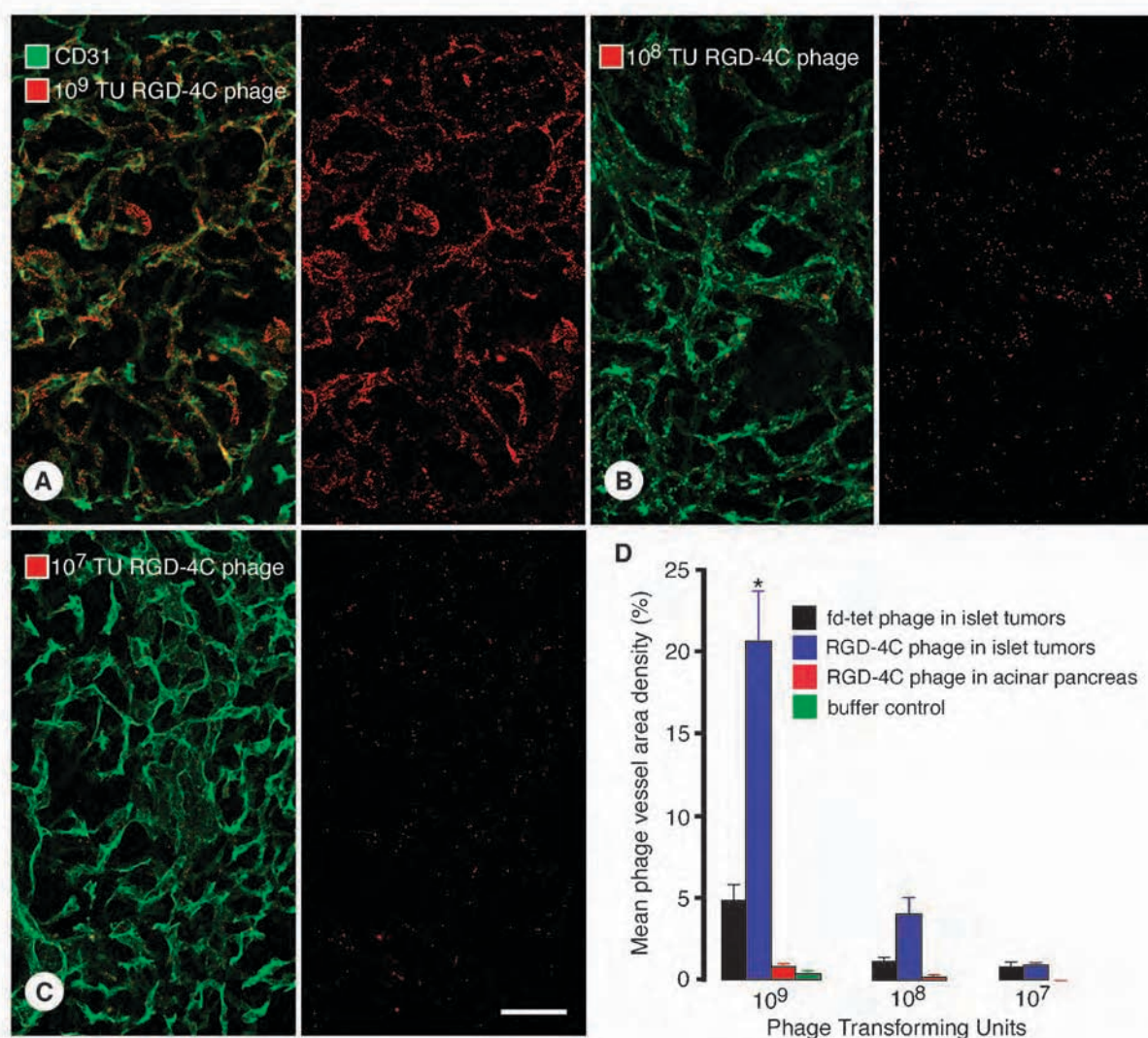

Figure 2. Dose-dependent RGD-4C phage distribution in RIP-Tag2 tumor blood vessels. *A* to *C,* identical confocal images are split: *left,* phage immunoreactivity (*red*) in blood vessels (CD31, *green*); *right,* phage immunoreactivity only. RGD-4C phage distribution in RIP-Tag2 tumor blood vessels from mice receiving (*A*) 10^9, (*B*) 10^8, and (*C*) 10^7 TU RGD-4C phage decreases with decreasing dose. *D,* quantification of mean phage vessel area densities show the amount of RGD-4C phage in the tumor islet vasculature at 10^9 TU was ~4-fold greater than fd-tet phage, whereas mean RGD-4C and fd-tet phage area densities were similar at 10^7 TU. Bonferroni-Dunn analysis of the mean RGD-4C phage area density in islet tumor blood vessels compared with acinar vessels at the 10^9 TU dose was statistically significant (*$P < 0.0027$). Bar in (*C*) applies to all panels (*A-C*), 26 μm.
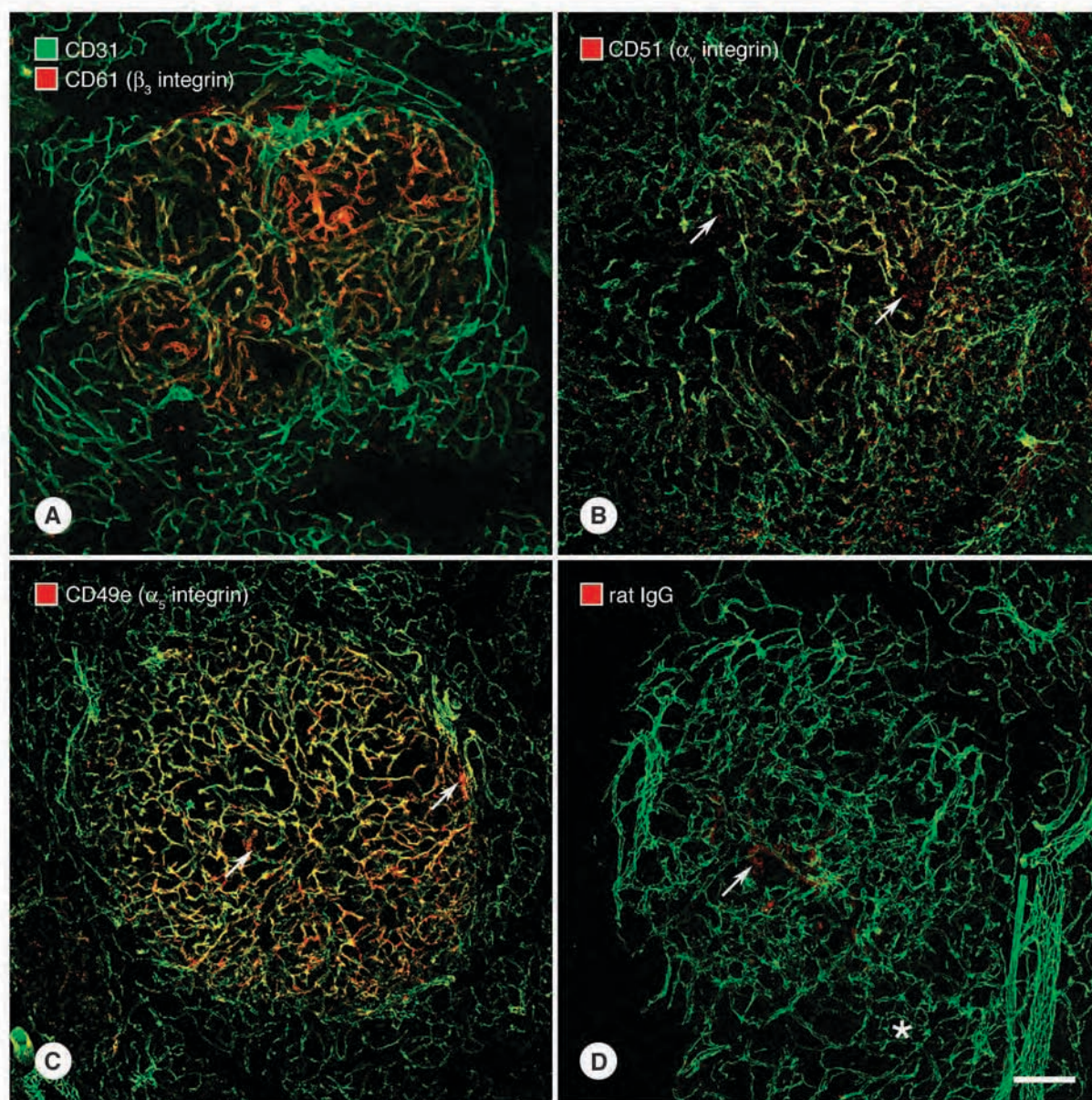
Figure 3. Luminal β_3, α_v, and α_5 integrin expression in RIP-Tag2 tumor vessels. Confocal images of RIP-Tag2 pancreatic islet tumors show heterogeneous expression of (*A*) β_3 integrin (CD61, *red*), and (*B*) α_v integrin (CD51, *red*) in tumor blood vessels (CD31, *green*). Immunoreactivity of α_v integrin is weaker than that of the β_3 integrin in tumor blood vessels. *C*, α_5 integrin expression (CD49e, *red*) is homogenous throughout the islet tumor vasculature (*green*). *D*, immunoreactivity of injected control normal rat serum antibodies (*red*) in tumor blood vessels (*green*) was minimal and similar to their localization in the acinar blood vessels (*asterisk*). Leakage of α_v (*B, arrows*), α_5 integrin antibodies (*C, arrows*), and rat IgGs (*D, arrow*) is apparent outside the tumor vasculature. Bar in (*D*) applies to all panels: *A* and *D*, 53 μm; *B*, 132 μm; and *C*, 64 μm.

compared with the amount of RGD-4C phage found in normal blood vessels of the acinar pancreas. The amount of RGD-4C phage found in the acinar pancreas blood vessels at this dose was similar to the background immunoreactivity measured in islet tumors from buffer-injected RIP-Tag2 control mice. At 10^8 TU, the mean RGD-4C phage area density in tumor blood vessels was 3.4-fold greater than that of fd-tet phage. Mean phage vessel area densities for RGD-4C and fd-tet phages were similar at the injected dose of 10^7 TU. Unlike RGD-4C phage, the mean fd-tet phage vessel area density in tumor blood vessels was similar when injected into RIP-Tag2 mice at either 10^8 or 10^7 TU.

Molecular specificity of RGD-4C phage localization in tumor blood vessels. Given that the RGD peptide is the recognition sequence for many adhesive proteins, such as the $\alpha_v\beta_3$, $\alpha_v\beta_5$, and $\alpha_5\beta_1$ integrins (33), we sought to evaluate the molecular specificity of RGD-4C phage localization by examining the *in vivo* distribution of the α_v, β_3, and α_5 integrins in RIP-Tag2 tumor blood vessels (Fig. 3). Similar to the phage immunostaining pattern, β_3 integrin (CD61, a binding partner of α_v integrin), immunoreactivity in blood vessels of RIP-Tag2 tumors was not uniformly distributed (Fig. 3*A*). Some blood vessels were strongly stained whereas others were devoid of β_3 integrin immunoreactivity.

α_v Integrin (CD51) immunoreactivity was weaker and nonuniformly distributed in tumor blood vessels as well (Fig. 3*B*). Consistent with recent reports (34, 35), α_5 integrin (CD49e) immunoreactivity and, hence, $\alpha_5\beta_1$ integrin expression, because this integrin is a unique heterodimer (33), was strong and uniformly distributed throughout the tumor blood vessels and was not detectable in adjacent normal acinar blood vessels (Fig. 3*C*). Neither control hamster (data not shown) nor rat serum antibodies colocalized with tumor blood vessels or normal blood vessels in the acinar pancreas (Fig. 3*D*, *asterisk*). Extravasation of α_v, α_5, and rat serum antibodies from tumor blood vessels was apparent outside tumor blood vessels (Fig. 3*B-D*, *arrows*).

Distribution of RGD-4C phage in other tissues. In contrast to its distribution in tumor blood vessels, negligible amounts of RGD-4C phage were found in blood vessels of the lung (Fig. 4*A*) and in capillaries surrounding the thyroid follicles (Fig. 4*B*), whereas phages were not detected in the cerebral cortex (Fig. 4*C*). Interestingly, by increasing the input of RGD-4C phage to 5×10^9 TU, we observed phage in blood vessels of the cerebral cortex (data not shown). Phage immunoreactivity was distinct, punctate, and evenly distributed

within the hepatic endothelial sinusoids such that the sinusoids (Fig. 4*D*, *arrow*) surrounding each central vein (Fig. 4*D*, *arrowhead*) were delineated by phage immunoreactivity. Rapid clearance of phage by the reticuloendothelial system and corresponding accumulation of phage in the liver as determined by bacterial infection (8) are consistent with our observations of identical high amounts of RGD-4C phage (Fig. 4*D*) or fd-tet phage immunoreactivity in the murine liver and spleen (data not shown) after a 6-minute circulation time. The half-life of injected fd-tet phage in the blood was ~5.5 minutes and recovery of fd-tet phage from the C57BL/6 mouse liver 6 minutes postinjection was typically 4% of total injected phage in a nonsaturated system (data not shown). After a 60-minute circulation, fd-tet phage was not detected in hepatocytes but were present in Kupffer cells with the majority of fd-tet phage associated with sinusoidal endothelial cells (data not shown).

Reduced RGD-4C phage localization after AG-013736 treatment. Preferential localization of RGD-4C phage to the tumor vasculature prompted us to examine whether the distribution of RGD-4C phage in tumor blood vessels following treatment of
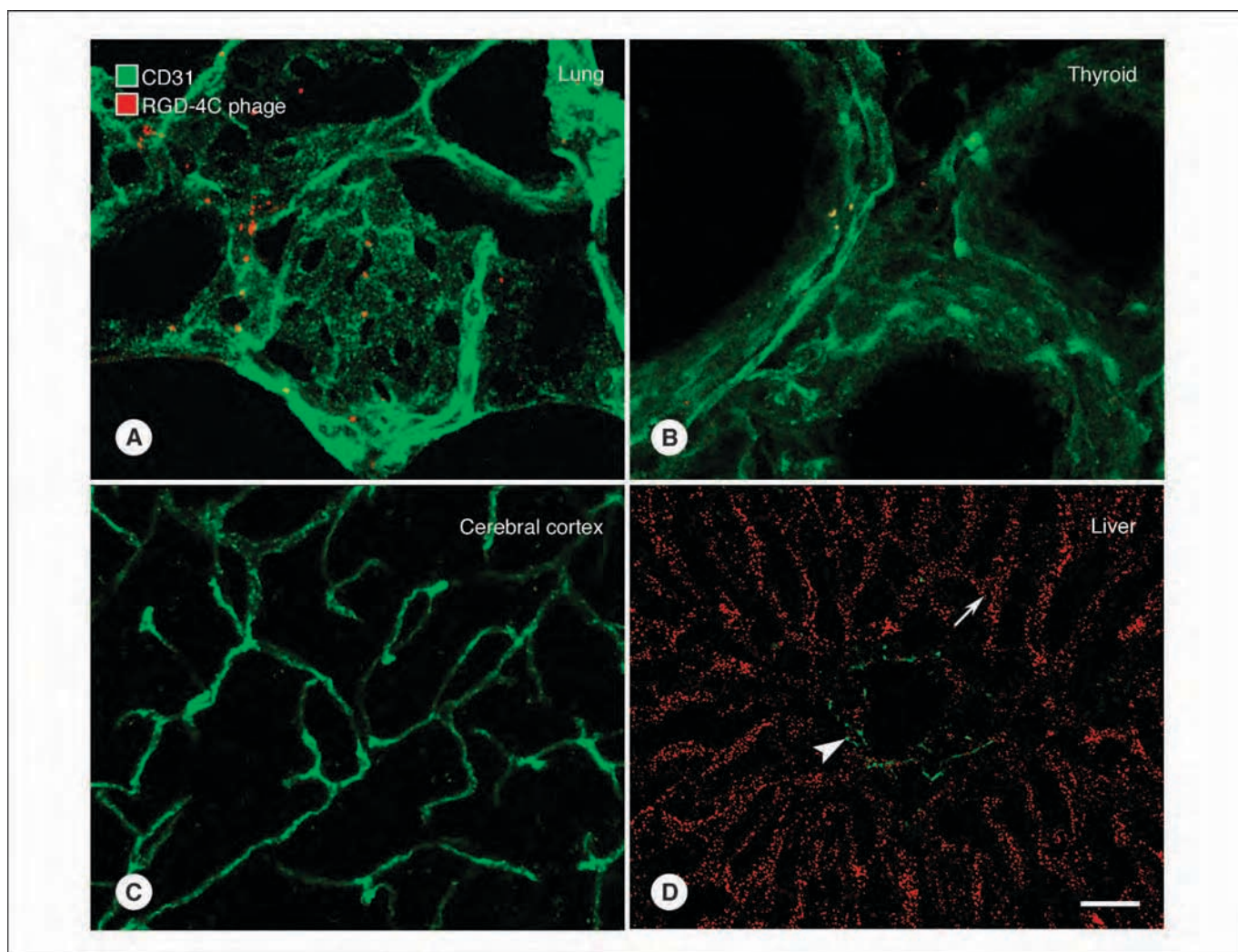

Figure 4. Distribution of RGD-4C and fd-tet phage in normal blood vessels. RGD-4C phage immunoreactivity (*red*) in blood vessels (CD31, *green*) of the RIP-Tag2 (*A*) lung, (*B*) thyroid gland, and (*C*) cerebral cortex is low to none in these normal blood vessels after a 6-minute circulation. *D*, distribution of RGD-4C phage immunoreactivity (*red*) in the liver is largely constrained within the sinusoidal endothelium (*arrow*) that drain toward a central vein whose borders are CD31 immunoreactive (*green, arrowhead*). Bar in (*D*) applies to all panels: *A*, 7 μm; *B* and *D*, 13 μm; *C*, 27 μm.
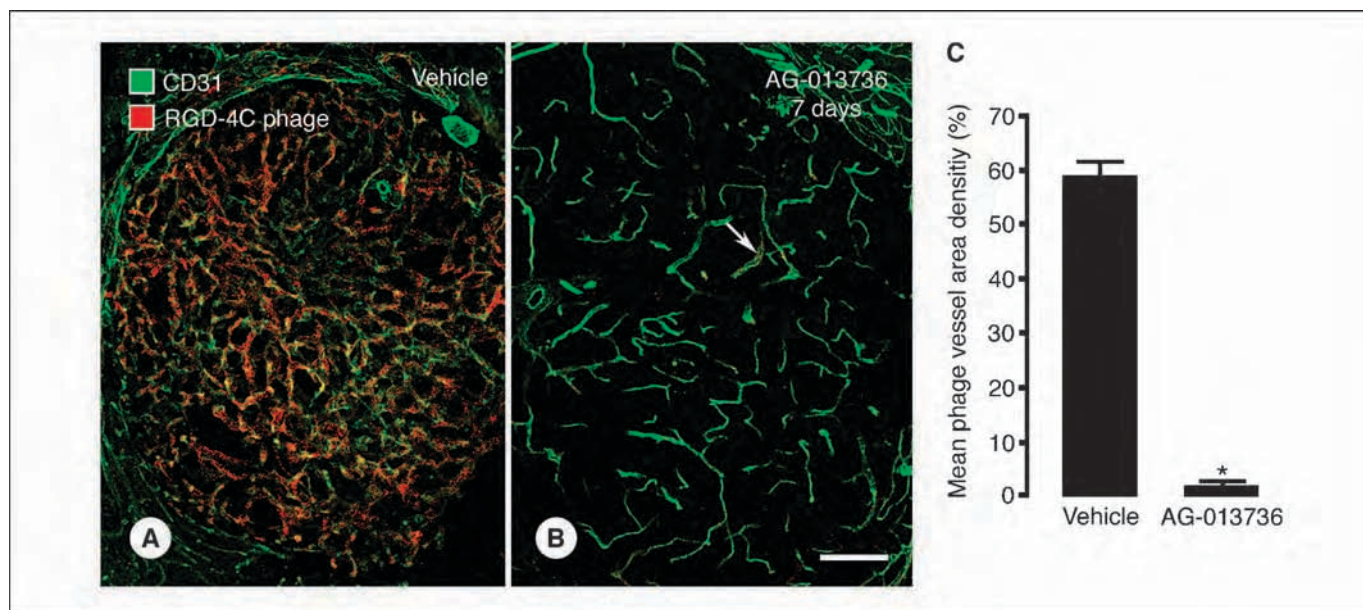
Figure 5. RGD-4C phage localization decreases in blood vessels after AG-013736 treatment. *A*, RGD-4C phage (*red*) colocalize with CD31-immunoreactive tumor blood vessels (*green*) from RIP-Tag2 mice treated with vehicle for 7 days. *B*, surviving blood vessels following AG-013736 treatment for 7 days contain variable and lower amounts of RGD-4C phage (*red, arrow*). *C*, the mean phage vessel area density quantified from islet blood vessels of vehicle versus AG-013736-treated mice show that RGD-4C phage binding is reduced to 4% in the AG-013736-normalized tumor vasculature. Bonferroni-Dunn analysis of the mean phage vessel area density between vehicle-treated and AG-013736-treated islet vasculature was statistically significant (*, $P < 0.0001$). Bar in (*B*) applies to (*A* and *B*): *A*, 106 μm; *B*, 132 μm.

RIP-Tag2 mice with AG-013736 would be altered (Fig. 5). We reasoned that if tumor blood vessels are normalized (28) following AG-013736 treatment, the amount of RGD-4C phage bound *in vivo* would reflect a difference in endothelial cell integrin expression. Pancreatic sections from vehicle-treated mice injected with RGD-4C phage 6 minutes before perfusion showed strong phage immunoreactivity in tumor blood vessels (Fig. 5*A*) that was similar to islet vessels in untreated RIP-Tag2 mice (compare with Fig. 1*B* and *E*). Conversely, RGD-4C phage localization in islet blood vessels was greatly reduced in AG-013736-treated mice (Fig. 5*B*, *arrow*). Blood vessels in the AG-013736-treated tumors had notably uniform diameters and decreased tortuosity than vehicle-treated tumors as previously reported (24). RGD-4C phage area density in the AG-013736-treated islet vasculature was ∼4% of that quantified from vehicle-treated vessels (Fig. 5*C*).

Reduced $\alpha_5\beta_1$ integrin expression in AG-013736-treated tumor blood vessels. To understand the molecular basis for the marked decrease of RGD-4C phage distribution in the surviving islet blood vessels of AG-013736-treated mice, the expression of the $\alpha_5\beta_1$ integrin was evaluated in vehicle versus AG-013736-treated pancreatic sections by immunohistochemistry (Fig. 6). Expression of $\alpha_5\beta_1$ was chosen because its expression was robust and uniform in untreated RIP-Tag2 tumor blood vessels (Fig. 3*C*). In vehicle-treated mice, $\alpha_5\beta_1$ integrin expression in tumor blood vessels was similar to that found in untreated RIP-Tag2 mice (Fig. 6*A* and *B*). Alternatively, $\alpha_5\beta_1$ integrin immunoreactivity in the remaining islet blood vessels from mice treated with AG-013736 for 7 days was much less and heterogeneous (Fig. 6*C* and *D*). In some islet blood vessels, $\alpha_5\beta_1$ integrin expression was strong (Fig. 6*C* and *D*, *arrow*), whereas expression was weak (Fig. 6*C* and *D*, *yellow arrowhead*) or absent in other blood vessels (Fig. 6*C* and *D*, *white arrowhead*). Acinar blood vessels were also $\alpha_5\beta_1$ immunoreactive because the antibody was not administered i.v.. $\alpha_5\beta_1$ Integrin fluorescence

intensity in vehicle versus AG-013736-treated islet blood vessels of large islet tumors was decreased in the latter (Fig. 6*E* and *F*). Qualitative differences of $\alpha_5\beta_1$ integrin fluorescence intensities in the corresponding surface plot illustrate significantly decreased peak heights in surviving islet blood vessels from AG-013736-treated mice (Fig. 6*G*).

Discussion

We show the *in vivo* cellular distribution of RGD-4C phage by immunofluorescence microscopy is highly sensitive and reflects the expression of vascular receptors. We established RGD-4C phage colocalize with CD31-immunoreactive tumor blood vessels and that extravasation of phage from tumor blood vessels occurs in focal regions within a few minutes. Quantification of phage area density in tumor blood vessels showed a dose dependency that is consistent with specific binding and to α_v, α_5, and β_3 integrin expression. Treatment of RIP-Tag2 mice with AG-013736 markedly decreased the amount of RGD-4C phage bound to surviving blood vessels, which was consistent with decreased $\alpha_5\beta_1$ integrin expression. RGD-4C phage binding to the normal endothelium was barely detectable, whereas systemic clearance of phage occurred mainly via the hepatic sinusoidal endothelial cells.

Differential integrin expression in vehicle versus AG-013736-treated blood vessels. Consistent with earlier reports (6–9), our studies show the $\alpha_v\beta_3$ and $\alpha_5\beta_1$ integrins that bind the RGD-4C phage in normal blood vessels were up-regulated in tumor blood vessels. Following AG-013736 treatment, our studies showed endothelial expression of the $\alpha_5\beta_1$ integrin was substantially down-regulated. Studies using primary endothelial cells isolated from human umbilical cord veins show $\alpha_v\beta_3$, $\alpha_5\beta_1$, and $\alpha_2\beta_1$ integrins are physically associated with VEGF$_{165}$-bound VEGFR-2 (36, 37). Moreover, endothelial cell migration and proliferation are

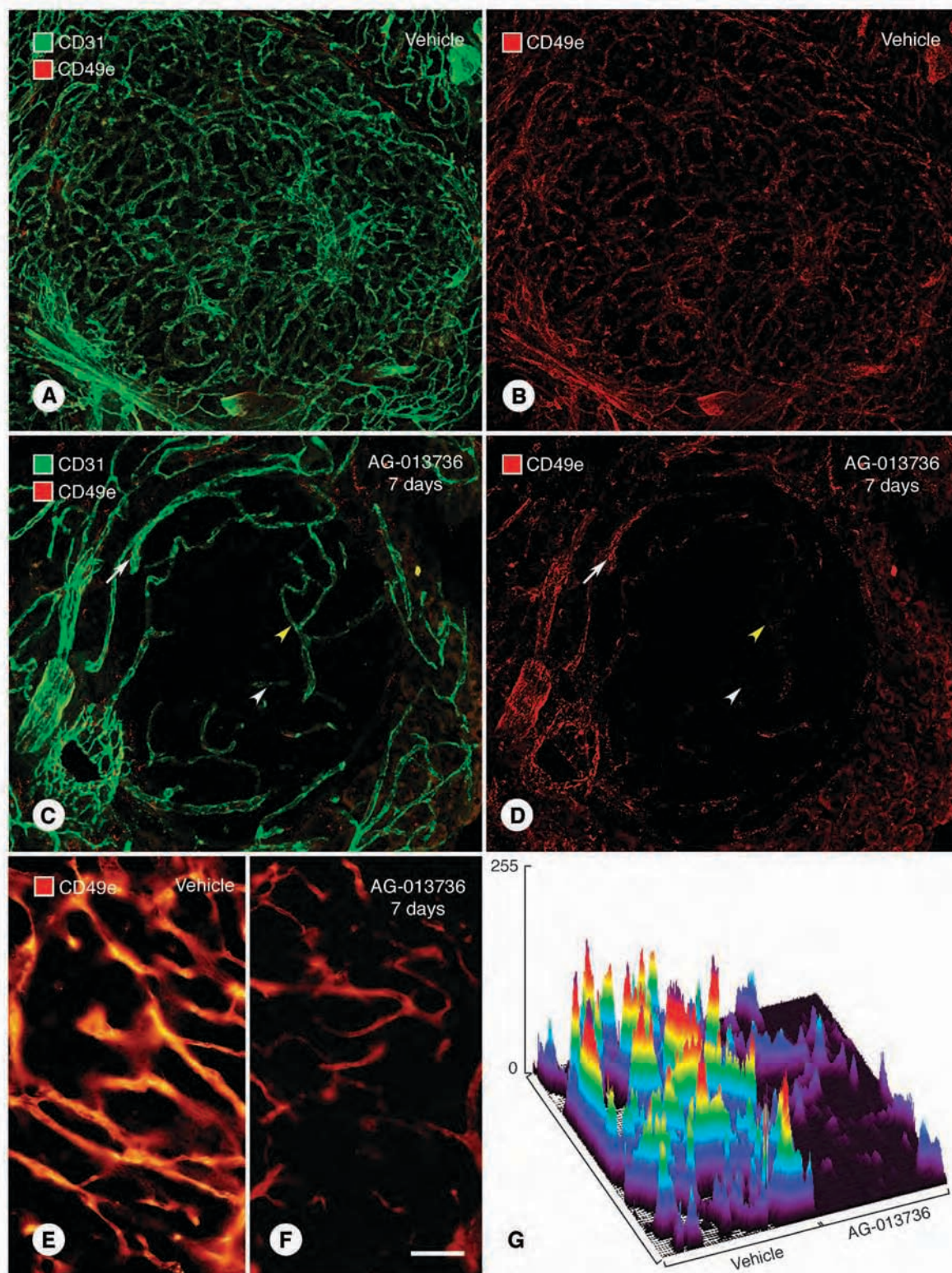**Figure 6.** $\alpha_5\beta_1$ Integrin expression decreases in AG-013736-treated islet blood vessels. *A* and *B,* tumor blood vessels (CD31, *green*) in pancreatic islets from vehicle and AG-013736-treated RIP-Tag2 mice show robust homogeneous $\alpha_5\beta_1$ integrin immunoreactivity (CD49e, *red*) of blood vessels immunostained on pancreatic tissue sections from vehicle-treated mice, whereas (*C* and *D*) surviving islet blood vessels in AG-013736-treated mice show strong (*arrow*), weak (*yellow arrowhead*), or no (*white arrowhead*) $\alpha_5\beta_1$ integrin expression. Qualitative comparison of $\alpha_5\beta_1$ immunofluorescence intensities of blood vessels from large islet tumors between (*E*) vehicle and (*F*) AG-013736-treated mice shows (*G*) markedly decreased vascular $\alpha_5\beta_1$ integrin expression in AG-013736-treated RIP-Tag2 mice. Bar in (*F*) applies to (*A-F*): *A* and *B,* 106 μm; *C* and *D*, 53 μm; *E* and *F,* 60 μm.

enhanced when cells were plated on vitronectin, fibronectin, and type I collagen, the primary cognate ligands for $\alpha_v\beta_3$, $\alpha_5\beta_1$, and $\alpha_2\beta_1$ integrins, respectively. Adhesion proteins, such as fibronectin, vitronectin, laminin, as well as collagen, contain the RGD binding motif as recognized by the $\alpha_v\beta_3$, $\alpha_5\beta_1$, and $\alpha_2\beta_1$ integrins, respectively (33). The presence of basement membrane ghosts lacking endothelial cells in AG-013736-treated RIP-Tag2 islet tumors (24) is consistent with our current finding of integrin down-regulation because integrins mediate cell adhesion to the basement membrane. Others have shown decreased endothelial cell expression of integrins such as $\alpha_2\beta_1$ may account for the loss of capillary lumen maintenance and tube formation (38). We have shown decreased expression of VEGFR-2 and VEGFR-3 in AG-013736-treated RIP-Tag2 tumors (24). Thus, down-regulation of VEGF receptors by AG-013736 and decreased RGD-4C binding to AG-013736-treated tumors may have effectively disrupted the crosstalk between VEGF and adhesion receptors (39, 40). Whether integrin expression is down-regulated as a result of inhibiting VEGFR-2 signaling cascades or by directly inhibiting integrin transcription is unknown. The net effect of AG-013736 treatment in RIP-Tag2 tumors indicates that the surviving tumor blood vessels are functional and have decreased levels of integrin expression despite the high VEGF concentration in these tumors (41). Our results suggest that AG-013736 therapy may act synergistically with integrin antagonists (42) in combination therapy to effect a faster rate of tumor blood vessel regression.

Pericyte changes associated with AG-013736 treatment. Comparison of pericyte morphology in wild-type mice to the RIP-Tag2 tumor mouse model (43) and a mouse model of prostate cancer (44) show pericytes are loosely associated with tumor blood vessels, have processes that extend away from the vessel wall, overlap with other pericytes, and accompany and extend beyond endothelial sprouts. Due to the heterogeneity of islet tumors in the RIP-Tag2 model, the amount of α-SMA-immunoreactive pericytes increases with tumor size, whereas vessels in hyperplastic islets have mostly desmin-immunoreactive pericytes (43). Subsequent to this work, Inai et al. (24) showed pericyte processes are more tightly associated with normalized blood vessels in tumors from RIP-Tag2 mice treated with AG-013736 for 7 days by scanning electron microscopy. An interesting finding of this work is that although the area density of CD31-immunoreactive blood vessels decreases by 79% following AG-013736 treatment, the reduction of α-SMA-immunoreactive pericyte area density (33%) is not coincident with vessel regression but is similar to the reduction of basement membrane area density. Indeed, immunohistochemistry with all three marker proteins, α-SMA, CD31, and type IV collagen, shows the α-SMA-immunoreactive pericytes associate with either normalized blood vessels or with basement membrane sleeves that do not contain endothelial cells. Recent studies showed that pericytes of RIP-Tag2 mice treated with AG-013736 for 7 days and then withdrawn from treatment for 4 days reverted to that morphology described by Morikawa et al (43).[4] Immunohistochemical studies using antibodies that recognize PDGFR-β showed the area density of PDGFR-β-immunoreactive pericytes was unchanged in the absence or presence of AG-013736 and after AG-013736 treatment was withdrawn. Consistent with earlier studies (24), however, the ratio of α-SMA and PDGFR-β area

densities decreased during AG-013736 treatment and returned to baseline levels 7 days after withdrawal of AG-013736. These results suggest sustained AG-013736 treatment reverted pericyte protein expression to a normal phenotype rather than decreased the total number of pericytes. The biochemical transformation of pericytes following AG-013736 treatment corresponds with their gross morphologic changes to a more normal phenotype (24). Whether vessel normalization and pericyte transformation occurs concurrently or in a sequential fashion is unknown. Decreased endothelial expression of $\alpha_5\beta_1$ integrin and the findings of pericyte transformations upon treatment with a broad-spectrum compound, such as AG-013736, lends further support for effective treatment of tumors with combination therapies.

Physiologic evaluation of tumor blood vessels by RGD-4C phage. Recent reports show that combination therapies of antiangiogenic inhibitors are more efficacious when used with low-dose chemotherapy (25–27). In addition, because tumors activate multiple angiogenic pathways, others propose that clinical therapies should include cocktails of angiogenic inhibitors that target multiple angiogenic pathways (18, 28). The paradox of abrogating tumor blood vessels in antiangiogenic therapy when delivery of therapeutics is dependent on a functional vasculature can be resolved because angiogenic inhibitors gradually "prune" the dysfunctional tumor vasculature to a more "normalized" state (28). The period in which the normalized functional vasculature can be effectively used to deliver appropriate therapeutics, however, is a critical temporal window (26). Accurate assessment of the tumor vasculature during antiangiogenic therapy by peptide phage such as RGD-4C may provide one variable by which the rate and extent of tumor blood vessel normalization can be evaluated for appropriate application of secondary treatment regimens.

Targeting specificity of RGD-4C phage. The distribution of 10^9 TU RGD-4C in islet tumor blood vessels reflected the expression patterns of $\alpha_v\beta_3$, $\alpha_2\beta_1$, and $\alpha_5\beta_1$ immunoreactivity. Our results do not contradict the fact that many different integrins recognize the RGD binding motif (33). Nevertheless, it would be difficult to unequivocally assign RGD-4C binding to be exclusively limited to either α_v integrins or $\alpha_5\beta_1$ integrins based on the current findings described here until reliable mouse $\alpha_v\beta_3$ and $\alpha_v\beta_5$ antibodies become available. Although α_v integrins are also expressed on pericytes and tumor cells, the limited amount of RGD-4C phage extravasation we observed here may be insufficient to detect on these perivascular cell types and/or may be confined within the vascular basement membrane to allow binding to surrounding tumor cells.

We found, however, that decreasing the dose of RGD-4C phage by 10-fold did not alter its specificity for tumor blood vessels. These findings support the targeting specificity of RGD-4C phage to angiogenic tumor blood vessels and corroborates previous reports of decreased toxicity to normal tissues of RGD-4C-based delivery of targeted therapeutics (14, 15). Although targeting peptide sequences outside the context of phage confers an improved specificity, phage display is an appealing tool by which small peptides can be rapidly propagated by bacterial amplification and screened *in vivo* due to its low toxicity to mammalian cells. Given our experimental variables, we show by immunofluorescence microscopy that 10^9 TU is an optimal dose for visualization of targeting phage and may be the optimal dose for identifying peptides from a random phage library in *in vivo* phage display.

Localization of RGD-4C phage in other tissues. Although RGD-4C phage bind to tumor blood vessels, we were interested in

---

[4] M.R. Mancuso, et al. Rapid vascular regrowth in tumors after reversal of VEGF inhibition, submitted for publication.

exploring this further by examining normal blood vessels of other tissues from RIP-Tag2 mice that represent a variety of endothelial cell types. Given the extensive vascularity of the lung, the small amount of phage detected indicates that RGD-4C phage binding to tumor blood vessels was not determined by the concentration of endothelial cells. To address whether binding of RGD-4C phage was specific to fenestrated endothelial cells, which are abundant in RIP-Tag2 tumors and in the thyroid gland, we found a minimal amount of RGD-4C phage in the follicular capillaries of the thyroid. These results indicate that endothelial cell type was also not a key determinant in RGD-4C phage binding in the RIP-Tag2 tumor blood vessels. The brain and liver are typically treated as negative and positive control organs, respectively, in *in vivo* phage display experiments, and our results confirmed this. Identical amounts of fd-tet or RGD-4C phage in the liver suggests phage localization in the hepatic endothelial sinusoids seems to be a property of the phage protein coat and not determined by the peptide targeting sequence thereby confirming previous findings (8).

Although *in vitro* phage display was originally developed to map antigenic sites on antibodies *in vitro* (45), this method was successfully adapted to identify *in vivo* vascular addresses in mice and in a human subject (1, 12, 46–49). Our studies here show that visualization of targeting phage in blood vessels at the cellular level by immunofluorescence microscopy allows direct identification and quantification of phage homing to the endothelium of tumor blood vessels. Decreased vascular localization of RGD-4C phage following AG-013736 treatment is consistent with down-regulation of integrin expression during normalization of surviving tumor blood vessels. Decreased integrin expression on tumor vascular endothelial cells raises the possibility of impaired targeting of chemotoxins that are dependent on integrin overexpression. These findings also illustrate the use of phage-displayed peptides as tools to probe the vascular addresses of abnormal blood vessels in disease and identify changes in the microvasculature in response to antiangiogenic treatment. Phage-displayed peptides that exploit the molecular changes in the normalized tumor endothelium may be judiciously used for targeted delivery of secondary chemotherapeutics.

Acknowledgments

References

1. Pasqualini R, Arap W, McDonald DM. Probing the structural and molecular diversity of tumor vasculature. Trends Mol Med 2002;8:563–71.
2. Risau W. Differentiation of endothelium. FASEB J 1995;9:926–33.
3. Gerber HP, Ferrara N. Angiogenesis and bone growth. Trends Cardiovasc Med 2000;10:223–8.
4. Lammert E, Cleaver O, Melton D. Induction of pancreatic differentiation by signals from blood vessels. Science 2001;294:564–7.
5. Matsumoto K, Yoshitomi H, Rossant J, Zaret KS. Liver organogenesis promoted by endothelial cells prior to vascular function. Science 2001;294:559–63.
6. Ruoslahti E. Specialization of tumour vasculature. Nat Rev Cancer 2002;2:83–90.
7. Eliceiri BP, Cheresh DA. Role of α_v integrins during angiogenesis. Cancer J 2000;6 Suppl 3:S245–9.
8. Pasqualini R, Koivunen E, Ruoslahti E. α_v Integrins as receptors for tumor targeting by circulating ligands. Nat Biotechnol 1997;15:542–6.
9. Kim S, Bell K, Mousa SA, Varner JA. Regulation of angiogenesis *in vivo* by ligation of integrin $\alpha_5\beta_1$ with the central cell-binding domain of fibronectin. Am J Pathol 2000;156:1345–62.
10. Marchiò S, Lahdenranta J, Schlingemann RO, et al. Aminopeptidase A is a functional target in angiogenic blood vessels. Cancer Cell 2004;5:151–62.
11. Kolonin MG, Pasqualini R, Arap W. Teratogenicity induced by targeting a placental immunoglobulin transporter. Proc Natl Acad Sci U S A 2002;99:13055–60.
12. Yao VJ, Ozawa MG, Trepel M, Arap W, McDonald DM, Pasqualini R. Targeting pancreatic islets with phage display assisted by laser pressure catapult microdissection. Am J Pathol 2005;166:625–36.
13. Koivunen E, Wang B, Ruoslahti E. Phage libraries displaying cyclic peptides with different ring sizes: ligand specificities of the RGD-directed integrins. Bio/ Technology 1995;13:265–70.
14. Ellerby HM, Arap W, Ellerby LM, et al. Anti-cancer activity of targeted pro-apoptotic peptides. Nat Med 1999;5:1032–8.

15. Arap W, Pasqualini R, Ruoslahti E. Cancer treatment by targeted drug delivery to tumor vasculature in a mouse model. Science 1998;279:377–80.
16. Zitzmann S, Ehemann V, Schwab M. Arginine-glycine-aspartic acid (RGD)-peptide binds to both tumor and tumor-endothelial cells *in vivo*. Cancer Res 2002;62:5139–43.
17. Folkman J. Endogenous angiogenesis inhibitors. APMIS 2004;112:496–507.
18. Hicklin DJ, Ellis LM. Role of the vascular endothelial growth factor pathway in tumor growth and angiogenesis. J Clin Oncol 2005;23:1–17.
19. Dash AB, Williams IR, Kutok JL, et al. A murine model of CML blast crisis induced by cooperation between BCR/ABL and NUP98/HOXA9. Proc Natl Acad Sci U S A 2002;99:7622–7.
20. Erber R, Thurnher A, Katsen AD, et al. Combined inhibition of VEGF and PDGF signaling enforces tumor vessel regression by interfering with pericyte-mediated endothelial cell survival mechanisms. FASEB J 2004; 18:338–40.
21. Bergers G, Song S, Meyer-Morse N, Bergsland E, Hanahan D. Benefits of targeting both pericytes and endothelial cells in the tumor vasculature with kinase inhibitors. J Clin Invest 2003;111:1287–95.
22. Holash J, Davis S, Papadopoulos N, et al. VEGF-Trap: a VEGF blocker with potent antitumor effects. Proc Natl Acad Sci U S A 2002;99:11393–8.
23. Wickman G, Hallin M, Dillon R, et al. Further characterization of the potent VEGF/PDGF receptor tyrosine kinase inhibitor, AG013736, in preclinical tumor models for its antiangiogenesis and antitumor activity. Proc Am Assoc Cancer Res 2003;44:A3780.
24. Inai T, Mancuso M, Hashizume H, et al. Inhibition of vascular endothelial growth factor (VEGF) signaling in cancer causes loss of endothelial fenestrations, regression of tumor vessels, and appearance of basement membrane ghosts. Am J Pathol 2004;165:35–52.
25. Pietras K, Hanahan D. A multitargeted, metronomic, and maximum-tolerated dose "chemo-switch" regimen is antiangiogenic, producing objective responses and survival benefit in a mouse model of cancer. J Clin Oncol 2005;23:939–52.

26. Willett CG, Boucher Y, di Tomaso E, et al. Direct evidence that the VEGF-specific antibody bevacizumab has antivascular effects in human rectal cancer. Nat Med 2004;10:145–7.
27. Winkler F, Kozin SV, Tong RT, et al. Kinetics of vascular normalization by VEGFR2 blockade governs brain tumor response to radiation: role of oxygenation, angiopoietin-1, and matrix metalloproteinases. Cancer Cell 2004;6:553–63.
28. Jain RK. Normalization of tumor vasculature: an emerging concept in antiangiogenic therapy. Science 2005;307:58–62.
29. Hanahan D. Heritable formation of pancreatic β-cell tumours in transgenic mice expressing recombinant insulin/simian virus 40 oncogenes. Nature 1985;315: 115–22.
30. Zacher AN III, Stock CA, Golden JW II, Smith GP. A new filamentous phage cloning vector: fd-tet. Gene 1980;9:127–40.
31. Smith GP, Scott JK. Libraries of peptides and proteins displayed on filamentous phage. Methods Enzymol 1993;217:228–57.
32. Pasqualini R, Arap W, Rajotte D, Ruoslahti E. *In vivo* selection of phage display libraries. In: Barbas CF III, Burton DR, Scott JK, Silverman GJ, editors. Phage display: a laboratory manual. Cold Spring Harbor (New York): Cold Spring Harbor Laboratory Press; 2001. p. 22.9.
33. Ruoslahti E. RGD and other recognition sequences for integrins. Annu Rev Cell Dev Biol 1996;12:697–715.
34. Parsons-Wingerter P, Kasman IM, Norberg S, et al. Uniform overexpression and rapid accessibility of $\alpha_5\beta_1$ integrin on blood vessels in tumors. Am J Pathol 2005;167:193–211.
35. Magnussen A, Kasman IM, Norberg S, Baluk P, Murray R, McDonald DM. Rapid access of antibodies to $\alpha_5\beta_1$ integrin overexpressed on the luminal surface of tumor blood vessels. Cancer Res 2005;65: 2712–21.
36. Byzova TV, Goldman CK, Pampori N, et al. A mechanism for modulation of cellular responses to VEGF: activation of the integrins. Mol Cell 2000;6: 851–60.

37. Soldi R, Mitola S, Strasly M, Defilippi P, Tarone G, Bussolino F. Role of $\alpha_v\beta_3$ integrin in the activation of vascular endothelial growth factor receptor-2. EMBO J 1999;18:882–92.

38. Davis GE, Camarillo CW. An $\alpha_2\beta_1$ integrin-dependent pinocytic mechanism involving intracellular vacuole formation and coalescence regulates capillary lumen and tube formation in three-dimensional collagen matrix. Exp Cell Res 1996;224:39–51.

39. Senger DR, Claffey KP, Benes JE, Perruzzi CA, Sergiou AP, Detmar M. Angiogenesis promoted by vascular endothelial growth factor: regulation through $\alpha_1\beta_1$ and $\alpha_2\beta_1$ integrins. Proc Natl Acad Sci U S A 1997;94:13612–7.

40. Giancotti FG, Ruoslahti E. Integrin signaling. Science 1999;285:1028–32.

41. Christofori G, Naik P, Hanahan D. Vascular endothelial growth factor and its receptors, flt-1 and flk-1, are expressed in normal pancreatic islets and throughout islet cell tumorigenesis. Mol Endocrinol 1995;9:1760–70.

42. Hwang R, Varner J. The role of integrins in tumor angiogenesis. Hematol Oncol Clin North Am 2004;18: 991–1006.

43. Morikawa S, Baluk P, Kaidoh T, Haskell A, Jain RK, McDonald DM. Abnormalities in pericytes on blood vessels and endothelial sprouts in tumors. Am J Pathol 2002;160:985–1000.

44. Ozawa MG, Yao VJ, Chanthery YH, et al. Angiogenesis with pericyte abnormalities in a transgenic model of prostate carcinoma. Cancer 2005;104:2104–15.

45. Smith GP. Filamentous fusion phage: novel expression vectors that display cloned antigens on the virion surface. Science 1985;228:1315–7.

46. Kolonin MG, Saha PK, Chan L, Pasqualini R, Arap W. Reversal of obesity by targeted ablation of adipose tissue. Nat Med 2004;10:625–32.

47. Zurita AJ, Troncoso P, Cardó-Vila M, Logothetis CJ, Pasqualini R, Arap W. Combinatorial screenings in patients: the interleukin-11 receptor α as a candidate target in the progression of human prostate cancer. Cancer Res 2004;64:435–9.

48. Joyce JA, Laakkonen P, Bernasconi M, Bergers G, Ruoslahti E, Hanahan D. Stage-specific vascular markers revealed by phage display in a mouse model of pancreatic islet tumorigenesis. Cancer Cell 2003;4: 393–403.

49. Essler M, Ruoslahti E. Molecular specialization of breast vasculature: a breast-homing phage-displayed peptide binds to aminopeptidase P in breast vasculature. Proc Natl Acad Sci U S A 2002;99:2252–7.

Lymphatic Zip Codes in Premalignant Lesions and Tumors

Lianglin Zhang,[1] Enrico Giraudo,[4] Jason A. Hoffman,[2,3]
Douglas Hanahan,[4] and Erkki Ruoslahti[1]

[1]Cancer Research Center and [2]Program in Molecular Pathology, Burnham Institute for Medical Research; [3]Department of Pathology,
University of California San Diego, School of Medicine, La Jolla, California; and [4]Department of Biochemistry and Biophysics,
and the Diabetes and Comprehensive Cancer Centers, University of California at San Francisco, San Francisco, California

Abstract

Blood vessels in tumors are morphologically and functionally distinct from normal resting blood vessels. We probed lymphatic vessels in premalignant lesions and tumors by *in vivo* screening of phage-displayed peptide libraries, asking whether they too have distinctive signatures. The resulting peptides begin to define such signatures. One peptide identified the lymphatics in a human melanoma xenograft. Another recognized the lymphatics in prostate cancers but not in premalignant prostate lesions; this peptide similarly identifies human prostate cancer lymphatics. A third was selective for the lymphatics in the premalignant prostate lesions. A fourth identified the lymphatics in dysplasias and squamous carcinomas of the cervix and skin. None recognize lymphatics in normal tissues. Thus, tumor development is associated with organ- and stage-specific changes in lymphatics. Systemic treatment of mice with fusions of a lymphatic homing peptide and a proapoptotic motif reduced the number of tumor lymphatics in prostate tumor and melanoma, forecasting future lymphatic targeting agents for detection and therapeutic intervention. (Cancer Res 2006; 66(11): 5696-706)

Introduction

The endothelial lining of blood vessels is highly diversified. Many, and perhaps all, normal tissues impart a tissue-specific "signature" on their vasculature, and tumor vessels differ from normal vessels both in morphology and molecular composition (1). Tumors induce angiogenesis to support expansive growth (2) and many of the changes in tumor vessels are angiogenesis related (3–6). Moreover, tumor blood vessels have tumor type–specific and, in some stages, stage-specific characteristics; *in vivo* screening of phage libraries has yielded distinct sets of homing peptides selectively recognizing angiogenic signatures in two transgenic mouse models of organ-specific tumorigenesis. Homing peptides can also distinguish the angiogenic blood vessels of premalignant lesions from those of fully malignant lesions in the same tumor

model (7, 8), indicating that vascular changes mirror the stage of tumor development.

The lymphatic system constitutes a second vascular system, one that has only an efferent arm. Tumors frequently induce lymphangiogenesis, as well as co-opt existing lymphatics (9–11). Tumors may contain intratumoral lymphatics, but, more commonly, an extensive network of lymphatic vessels is present around tumor tissue (12–14). The lymphatics within tumors, when present, are generally nonfunctional in fluid transport (14), possibly reflecting compression by interstitial pressure and blockage by intraluminal tumor cells. The lymphatic vessels in and around tumors are an important conduit of metastasis. Indeed, growth factor–stimulated enhancement of lymphatic vessel expression in tumors increases metastasis (15, 16). Conversely, inhibiting lymphangigenesis suppresses lymphatic metastasis, but generally does not affect tumor growth (17).

A peptide that selectively binds to the endothelial cells of lymphatics associated with a xenotransplanted human breast tumor has been described (13). This was the first demonstration that tumor lymphatics can differ from normal lymphatics, but the larger question of whether tumor lymphatics are generally distinguishable from normal lymphatics has been unanswered.

Here, we identify homing peptides that specifically recognize tumor lymphatics or lymphatics in premalignant lesions in a set of distinctive organ-specific tumor models in mice. Our results show that tumor lymphatics, like tumor blood vessels, express specific markers, and that these lymphatic markers are tumor type specific and distinct from blood vessel markers in the same tumors. The tumor-specific lymphatic vessel markers may be useful in early detection and tumor targeting.

Materials and Methods

Cell Lines, Mice, and Tumors

The following cell lines were maintained in DMEM supplemented with 10% FCS: C8161 human melanoma, MDA-MB-435 human breast cancer, KRIB human osteosarcoma, and human prostate cancer cells PPC1 and DU145. LNCaP human prostate cancer cell line was grown in RPMI 1640 with 10 mmol/L HEPES, 1 mmol/L sodium pyruvate, and 1.5 g/L sodium bicarbonate supplemented with 10% FCS. M12 human prostate cancer cell line was cultured in RPMI 1640 with 5 μg/mL insulin-transferrin-sodium selenite, 2.5 μg/mL fungizone, 50 μg/mL gentamicin, 0.2 μmol/L dexamethasone, 10 ng/mL epidermal growth factor, and 5% FCS (18). To produce tumors, nude BALB/c and C56BL/6 mice were s.c. (C8161, KRIB, and PPC1) or orthotopically (MDA-MB-453, PPC1, DU145, M12, and LNCaP) injected with 1×10^6 tumor cells. Transgenic mouse tumor models included transgenic adenocarcinoma of the mouse prostate (TRAMP), mouse mammary tumor virus (MMTV)-PyMT breast cancer, and K14-HPV16 cervical cancer. To initiate cervical carcinogenesis, female K14-HPV16 mice (19) were treated with 17β-estradiol (E₂; refs. 20, 21). Briefly, 1-month-old virgin female transgenic (heterozygous K14-HPV16, 1203#1) and non-transgenic (FVB/n) mice were anesthetized with isoflurane, and continuous release pellets that deliver E₂ at doses of 0.05 mg over 60 days (Innovative

Research of America, Sarasota, FL) were implanted s.c. in the dorsal back skin. Subsequent pellets were implanted at 3 and 5 months of age for a total of 6 months of hormone treatment. K14-HPV16 mice were maintained in the FVB/n background (FVB/n; The Jackson Laboratory, Bar Harbor, ME). The mice were maintained in accordance with the University of California, San Francisco, institutional guidelines governing the care of laboratory mice. The animal experimentation was approved by Animal Research Committees at University of California, San Francisco, or Burnham Institute for Medical Research.

Phage Library and Screening

A NNK-encoded CX7C library display on T7Select415-1 phage (Novagen, Madison, WI) was prepared as previously described (13). Phage selection and validation have been described (22). A two-step procedure was designed for the selection of peptides targeting the tumor lymphatic vessels of premalignant prostate lesions and prostate tumor. First, the phage library was incubated with cells derived from normal prostate to subtract the phage that bind to normal prostate. Second, the antipodoplanin magnetic beads were used to isolate lymphatic endothelial cells. We did two to three rounds of *ex vivo* selection and two to three rounds of *in vivo* selections.

For the *ex vivo* selections, cell suspensions were prepared from normal prostates of tumor-free littermates of TRAMP mice, premalignant prostates of 14- to 16-week-old TRAMP mice, and tumor tissues of 25- to 28-week-old TRAMP mice. The C57BL6 TRAMP mice display mild to severe hyperplasia by the time they are 12 weeks of age, and severe hyperplasia has developed by 18 weeks (23, 24). Thus, the premalignant lesions of prostate we used represent a mixture of mild or severe hyperplasia. Collagenase IA (1 mg/mL; Sigma, St. Louis, MO) was used to disperse the tissues. About 1×10^7 normal prostate cells were incubated at 4°C for 3 hours with 5×10^{10} plaque-forming units (pfu) of T7 phage displaying a CX7C peptide library. The samples were centrifuged at 1,200 rpm for 10 minutes; the supernatant (the normal prostate-subtracted phage library) was recovered and then incubated overnight at 4°C with 5×10^7 cells derived from premalignant prostate tissue or prostate tumor. The cells were washed to remove unbound phage, incubated with rat anti-mouse podoplanin for 45 minutes at 4°C, and washed thrice with cold PBS containing 0.5% bovine serum albumin (BSA). Podoplanin-positive cells were then isolated using M450 sheep anti-rat IgG Dynabeads (M450; Dynal, Oslo, Norway). Phage that bound to the podoplanin-positive cell population were rescued and amplified in *Escherichia coli*. *In vivo* phage library screening was done as described (13).

Homing Specificity of Phage

In vivo homing specificity of phage was tested as described (22). Briefly, mice bearing tumors were anesthetized and i.v. injected with 5×10^9 pfu phage. After 7 minutes, the mice were perfused through the heart with PBS containing 0.5% BSA. The tumor and control organs were dissected from each mouse and the phage were rescued and tittered. For histology analysis, the mice were perfused with 4% PFA 30 minutes after the injection of phage. Tissues were embedded in Tissue-Tek OCT (Tissue-Tek, Elkhart, IN) and 5 μm sections were prepared for phage immunostaining.

Antibodies and Immunohistology

Custom immunization to produce a rabbit antiserum against mouse Prox-1 was done by Proteintech, Inc. New Zealand White rabbits were immunized with a fusion protein of glutathione *S*-transferase (GST)–COOH-terminal fragment of Prox-1 protein. The antibody was affinity purified on the fusion protein and absorbed with GST. The resulting antibody preparation (1.8 mg/mL) gave a titer of 1:10,000 against the fusion protein in ELISA. Immunofluorescence staining of tissue sections with the anti-Prox-1 antibody gave a pattern of nuclear staining. Antibodies against the lymphatic markers anti-LYVE-1 (13) and antipodoplanin (kindly provided by T. Petrova and K. Alitalo), rat monoclonal anti-mouse CD31 (BD PharMingen, San Diego, CA), rat anti-mouse MECA-32 (BD PharMingen), rabbit polyclonal anti-T7 phage, rabbit anti-mouse cleaved caspase-3 (ASP175; Cell Signaling Technology, Danvers, MA), and rat anti-mouse vascular endothelial growth factor receptor 3 (VEGFR; provided by H. Kubo and K. Alitalo) were used for immunohistochemical staining of frozen tissue sections as described (8, 13).

The corresponding secondary antibodies were added and incubated for 1 hour at room temperature: AlexaFluor-488 goat anti-rat or rabbit IgG (1:1,000; Molecular Probes, Eugene, OR), AlexaFluor-594 goat anti-rat or rabbit IgG (1:1,000; Molecular Probes), AlexaFluor-594 donkey anti-mouse or goat IgG (1:1,000; Molecular Probes), and AlexaFluor-488 donkey anti-mouse or goat IgG (1:1,000; Molecular Probes). The slides were washed thrice with PBS and mounted in Vectashield Mounting Medium with 4′,6-diamidino-2-phenylindole (DAPI; Vector Laboratories, Burlingame, CA). Blood vessels were also visualized by i.v. injecting *Lycopersicon esculentum* (tomato) lectin conjugated to fluorescein (100 μg of lectin in 200 μL PBS; Vector Laboratories).

Tissue distribution of fluorescein-labeled peptides (25) was studied by i.v. injecting the peptide (100-150 μg in 200 μL PBS) into the mice. The injected peptides were allowed to circulate 30 minutes to 2 hours, and the mice were perfused with 4% paraformaldehyde through the left ventricle of heart. Tissues were dissected and frozen in OCT embedding medium (Tissue-Tek). The frozen sections were prepared for immunohistologic analysis.

Peptide Synthesis

Peptides were synthesized in our peptide facility using Fmoc chemistry in a solid-phase synthesizer. The peptides were purified by high-performance liquid chromatography and confirmed by mass spectrometry. Fluorescein-conjugated peptides were synthesized as described (25). The LSD and REA peptides were synthesized as the chimera with the proapoptotic motif $_D(KLAKLAK)_2$ (26).

Targeted Proapoptotic Peptide Treatment of Tumor-bearing Mice

Prostate cancer model. Orthotopic xenografted prostate tumors were established by injecting 1×10^6 PPC1 human prostate cancer cells into the mouse prostate. Fifteen days postinoculation, the mice were i.v. injected with $_D(KLAKLAK)_2$-CREAGRKAC, an equimolar mixture of $_D(KLAKLAK)_2$ and CREAGRKAC, or PBS. Mice were given 200 μg of the conjugate per week divided into two injections (26, 27).

Melanoma model. Nude BALB/c mice were s.c. injected with 1×10^6 C8161 human melanoma cells. Treatment started when mean tumor volumes reached ~100 mm³. Mice with size-matched tumors were randomized into three groups. The therapeutic group received a chimera of tumor-homing peptide with the proapoptotic motif [$_D(KLAKLAK)_2$-CLSDCGKRKC]. The control groups received an equimolar mixture of CLSDGKRKC and $_D(KLAKLAK)_2$, or PBS alone. The tumor-bearing mice were i.v. injected with 200 μg/dose/mouse weekly for 3 weeks (26, 27).

The mice were monitored for weight loss, and tumors were dissected and weighed at the termination of the experiment. Histologic analysis was done to evaluate the density of tumor lymphatics and blood vessels. Apoptotic lymphatic endothelial cells were visualized by double staining with anticleaved caspase-3 and antipodoplanin antibodies. The animal experiments reported here were approved by the Animal Research Committee of Burnham Institute for Medical Research.

Phage Overlay of Tissue Sections From Human Cancer

The frozen sections of human prostate tumor specimens were obtained from Dr. Daniel Mercola (Sidney Kimmel Cancer Center, La Jolla, CA). The sections (5 μm) were preincubated with blocking buffer (5% normal goat serum and 0.5% BSA in 1× PBS) for 1 hour at room temperature, washed thrice with diluted blocking buffer (1:10), and phage (3×10^9 pfu) were incubated on the section for 4 hours. After three washes, rabbit anti-phage antibody (10 μg/mL) was added and the phage incubated for 2 hours. The slides were washed and incubated with AlexaFluor-488 goat anti-rabbit IgG for 1 hour. After further washes, the slides were mounted with Vectashield (Vector Laboratories).

Statistical Analysis

Student's *t* test was used in statistical analysis of the results. The bar diagrams show mean and SD.

Results

Phage targeting of lymphatics in C8161 melanoma. We chose the C8161 human melanoma as the first topic because xenografts of tumors generated with this cell line in nude mice contain lymphatic vessels that are not recognized by the homing peptide LyP-1, which binds to lymphatic endothelial cells in breast carcinomas (13). Our experimental design was aimed to determine whether lymphatic homing peptides having analogous specificity for the melanoma-associated lymphatics could be identified. We modified our earlier protocols to increase the probability of obtaining peptides that recognize tumor lymphatics. We incubated a phage display library with a cell suspension of whole C8161 tumor tissue, allowing phage to bind, and then used immunomagnetic beads to isolate lymphatic endothelial cells that carried along any phage bound to these cells. This enrichment step yielded a phage pool that bound 250-fold more efficiently to the isolated cells than nonrecombinant phage (Supplementary Fig. S1*A*). The enriched phage pool was used in subsequent *in vivo* rounds to select phage that homed to C8161 xenograft tumors. Two rounds of selection *in vivo* produced a 40-fold enrichment of phage (Supplementary Fig. S1*B*). There was no enrichment in the several control organs tested.

The 48 phage clones from the second *in vivo* round of phage pool selection included five clones that appeared most frequently, and these were analyzed further. Two clones displaying peptides with related amino acid sequences (CLSDGKRKC and CLDGGRPKC)

bound to cell suspensions prepared from C8161 tumors; the stronger binder, CLSDGKRKC, bound 100-fold more than control phage. I.v. injection of phage into nude mice bearing C8161 tumors showed that both phage homed selectively to the tumors; CLSDGKRKC was about twice as efficient as CLDGGRPKC (the results for CLSDGKRKC are shown in Fig. 1*A*). The CLSDGKRKC peptide (referred to below as LSD) was chosen for further study.

To establish that the homing ability of LSD phage is due to the displayed peptide sequence, we chemically synthesized the peptide as a fluorescein conjugate peptide and i.v. injected the conjugate into C8161 tumor mice. After 2 hours of circulation, the peptide was detected within the tumors (Fig. 1*B*), but not in control organs (Supplementary Fig. S1*C*). Staining of tissue sections with the lymphatic vessel markers podoplanin, Prox-1, LYVE-1, and VEGFR3 showed colocalization of the LSD fluorescence with them (Fig. 1*C*), whereas there was no colocalization with the blood vessel markers MECA-32 and CD31 (Fig. 1*D*). Quantification showed that 85% of the lymphatic vessels that were positive for the peptide were also positive for podoplanin.

We further tested the homing of LSD phage to other types of cancer, including the MDA-MB-435 human breast cancer xenografts recognized by the previously described lymphatic homing peptide, LyP-1 (13). I.v. injected LSD phage did not appreciably home to MDA-MB-435 tumors (see below). These data show that LSD-peptide selectively homes to the lymphatic vessels in C8161 melanoma.
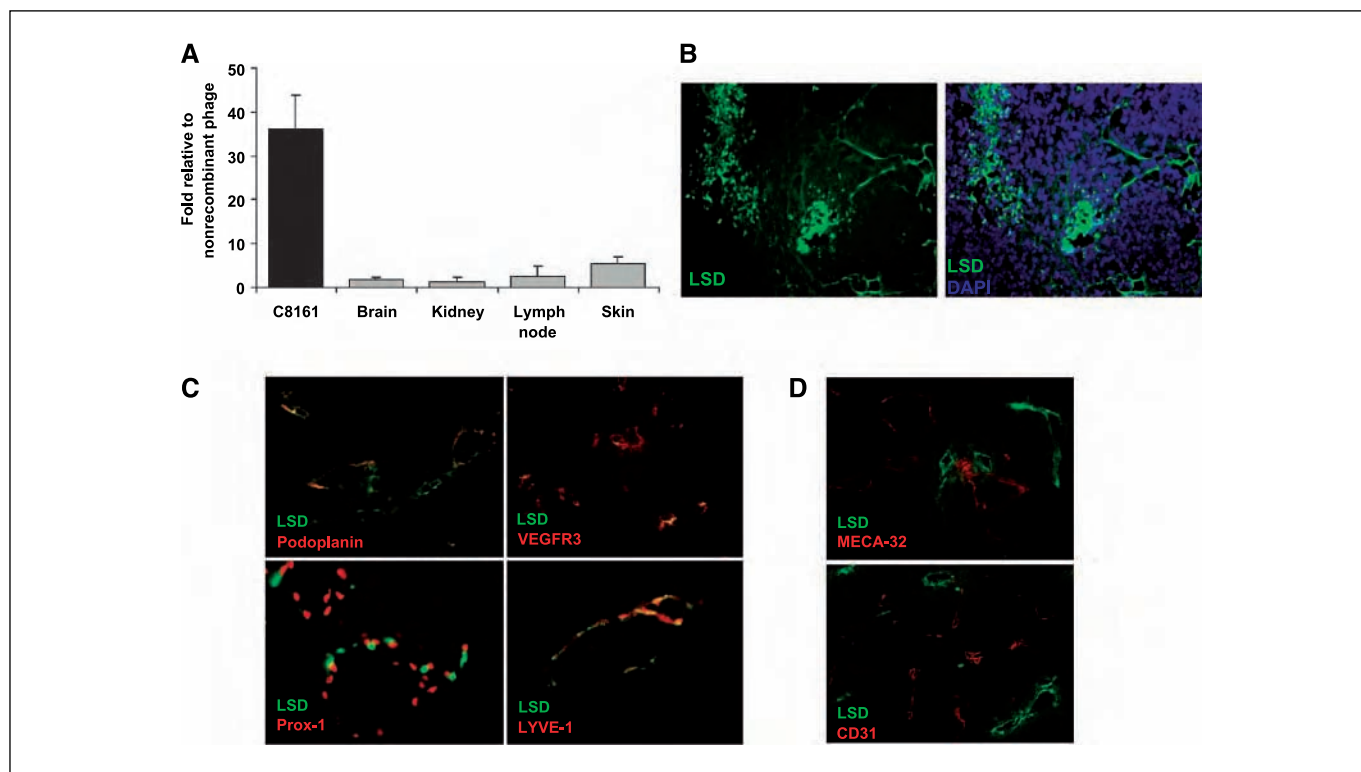

Figure 1. A homing peptide recognizes C8161 melanoma lymphatics. *A,* homing of LSD phage to C8161 xenografts. The LSD phage clone (2×10^9 pfu) was injected i.v. into mice bearing C8161 xenograft tumors and allowed to circulate for 7 minutes. Phage titers recovered from tumors and control tissues are shown. Phage accumulation in C8161 tumor tissue was significantly higher than in normal tissues ($P < 0.03$ relative to the normal tissue with the highest phage uptake, the skin; $n = 3$). *B, in vivo* localization of fluorescein-labeled LSD peptide. The peptide (150 µg) was i.v. injected into C8161 tumor mice, and the tumors and various control tissues were collected for histologic analysis 2 hours after the injection. *Green fluorescence,* presence of the peptide; *blue,* nuclei (DAPI staining). Original magnification, ×200. *C,* colocalization of the LSD peptide with lymphatic markers. The green FITC fluorescence colocalizes with red staining for the lymphatic vessel markers podoplanin, VEGFR3, Prox-1, and LYVE-1 in vessel-like structures within the tumor tissue and at tumor periphery (*bottom left*). *D,* LSD peptide does not colocalize with blood vessel markers. Tumor blood vessels were stained with anti-MECA-32 or anti-CD31 (*red*). Original magnification (*C* and *D*), ×400.

Phage targeting of lymphatics in premalignant lesions and tumors of prostate. Seeking to further generalize the proposition that tumor-associated lymphatics might have organ-specific signatures, we selected lymphatic homing peptides in the TRAMP transgenic mouse model of *de novo* prostate carcinogenesis (28). Immunohistochemical analysis had revealed abundant lymphatics associated both with premalignant lesions and tumors in this model (Supplementary Fig. S2A). As it is possible to access premalignant lesions in this system, we also explored the possibility of distinguishing the lymphatics of such lesions from those of fully developed tumors. We studied TRAMP mice inbred into C57BL6, a genetic background wherein prostate tumorigenesis occurs over a 30-week time course to terminal disease, with a discernable premalignant phase (~10-20 weeks).

To isolate peptides that selectively home to fully developed tumors in the TRAMP model, we first pretreated the phage library with cell suspensions derived from normal prostate to decrease the abundance of phage that bind to normal prostate. The normal prostate-subtracted library was then enriched by two rounds of *ex vivo* selection on lymphatic endothelial cells immunopurified from tumors of 25- to 28-week-old TRAMP mice. Three subsequent *in vivo* selection rounds yielded a phage pool that showed nearly 50-fold enrichment for tumor homing. Five peptide sequences were represented more than once in this pool. Three of these phage clones with amino acid sequences CREAGRKAC, CSMSAKKKC, and CKTRVSCGV showed robust binding to tumor-derived cell suspensions and were further tested *in vivo*. I.v. injected CREAGRKAC phage became 50-fold enriched in TRAMP tumors relative to nonrecombinant phage, whereas the other two phage showed ~30-fold enrichment. We chose the CREAGRKAC (REA) for further study.

To screen for peptides recognizing the premalignant lymphatics, we first treated the phage library with cell suspensions derived from normal prostate, and the subtracted library was then enriched on immunopurified lymphatic endothelial cell suspensions derived from prostates containing premalignant lesions, the so-called prostatic intraepithelial neoplasia, or PIN (in 14- to 16-week-old mice). The sequential *ex vivo* selections yielded a phage pool that was 60-fold enriched for binding to the target cells, and a 30-fold enrichment for homing to prostate with PIN lesions was obtained in a subsequent *in vivo* selection. Five phage clones were chosen for evaluation of *in vivo* homing based on their frequent appearance among 64 clones sequenced (32 clones each from the second *ex vivo* round and the third *in vivo* round). Of these, three clones with amino acid sequences CAGRRSAYC, CASLSCR, and CSGGKVLDC, bound to cell suspension derived from PIN lesions (data not shown). These candidates were further tested *in vivo* individually. Phage-displayed peptides CAGRRSAYC, CSGGKVLDC, and CASLSCR showed 24-, 14-, and 12-fold enrichment to PIN lesions relative to nonrecombinant phage, respectively. The CAGRRSAYC (AGR) was chosen for further study.

To evaluate the specificity of the REA and AGR peptides, we i.v. injected the phage into TRAMP mice with either premalignant PIN lesions or prostate tumors, or into their tumor-free (transgene negative) male littermates with normal prostates. The results showed that the REA phage homes to tumors, but not to PIN lesions or normal prostate, whereas the AGR phage homes only to PIN (Fig. 2A). Neither phage was found in other tissues, including lymph nodes, kidneys, lungs, skin, or intestine, at levels higher than the nonrecombinant control phage.

In vivo distribution of fluorescein-conjugated REA and AGR peptides after i.v. injection confirmed the phage results. The REA peptide accumulated in prostate tumors, showing 90% overlap with podoplanin-positive lymphatic vessels, whereas PIN lesions, normal prostate (Fig. 2B), and control organs (Supplementary Fig. S2B) were negative. The AGR peptide selectively homed to PIN lesions, but little or no peptide was seen in prostate tumors, normal prostate tissue (Fig. 2B), or in control tissues (Supplementary Fig. S2C).

To study the association of REA and AGR peptides with the vasculature, the phage or fluorescein-labeled peptides were i.v. injected into TRAMP mice and phage and peptide localization was compared with lymphatic and blood vessel markers localized with antibodies. The phage and their cognate peptides each showed substantial colocalization with the lymphatic markers podoplanin, VEGFR3, LYVE-1, and Prox-1 in their respective lesions, whereas their localization was entirely distinct from that of the blood vessel markers CD31 and MECA-32. The overlap of the peptides with Prox-1 was less obvious than with the other markers, presumably because Prox-1 is nuclear, whereas the peptides associate with the cell membrane. The results for the REA and AGR peptides are shown in Fig. 2C and D, and for the REA phage in Supplementary Fig. S2D.

Homing peptide for lymphatic vessels in cervical cancer. In a previous study from our laboratories, we identified a homing peptide for dysplastic skin lesions in K14-HPV16 transgenic mice, which develop skin cancers (7). This peptide, CNRRTKAGC, is similar to LyP-1 (CGNKRTRGC), which selectively recognizes lymphatic vessels and tumor cells in breast cancers (13). Because of this similarity, we asked whether the CNRRTKAGC peptide (LyP-2) also recognizes tumor lymphatics. We tested the LyP-1 and LyP-2 peptides in skin and cervical cancers of the K14-HPV16 transgenic mice. In addition to spontaneously developing angiogenic dysplasias and then squamous cell carcinomas of the skin (29), female K14-HPV16 mice develop cervical cancers when their normally cyclic estrogen levels are sustained with time release pellets (20). The estrogen-treated females undergo neoplastic progression in the cervix mimicking, that inferred for human cervical carcinogenesis (20, 21, 29). The premalignant cervical lesions (also called cervical intraepithelial neoplasia, CIN) and cervical tumors of these mice contain abundant lymphatic vessels as detected by immunostaining for lymphatic markers (Supplementary Fig. S3A).

I.v. injected LyP-2 phage showed robust homing both to the premalignant and malignant lesions in the cervix, but not to normal cervix (Fig. 3A). Fluorescein-labeled LyP-2 peptide also accumulated in the cervical lesions, colocalizing with LYVE-1 (Fig. 3B, *top*) and podoplanin (82% overlap; data not shown), but not with MECA-32 (Fig. 3B, *bottom*). Additionally, occasional foci of scattered cells in the stroma were labeled, with some apparent intracellular localization; the identity of these cells is currently unresolved. No peptide accumulation was observed in normal cervix (Fig. 3B) or in other control tissues, either in lymphatics or in nonvascular cells (Supplementary Fig. S3B). LyP-2 also homed to the lymphatics associated with dysplasias and squamous cell carcinomas of the skin in male and female K14-HPV16 mice, but not to normal skin lymphatics (data not shown).

Specificity of lymphatic homing peptides for different types of tumors. Having isolated phage-displayed peptides that homed to the lymphatics of melanoma, prostate, or cervix (the origin and specificity of these peptides is summarized in Table 1), we asked whether they recognized common determinants of the
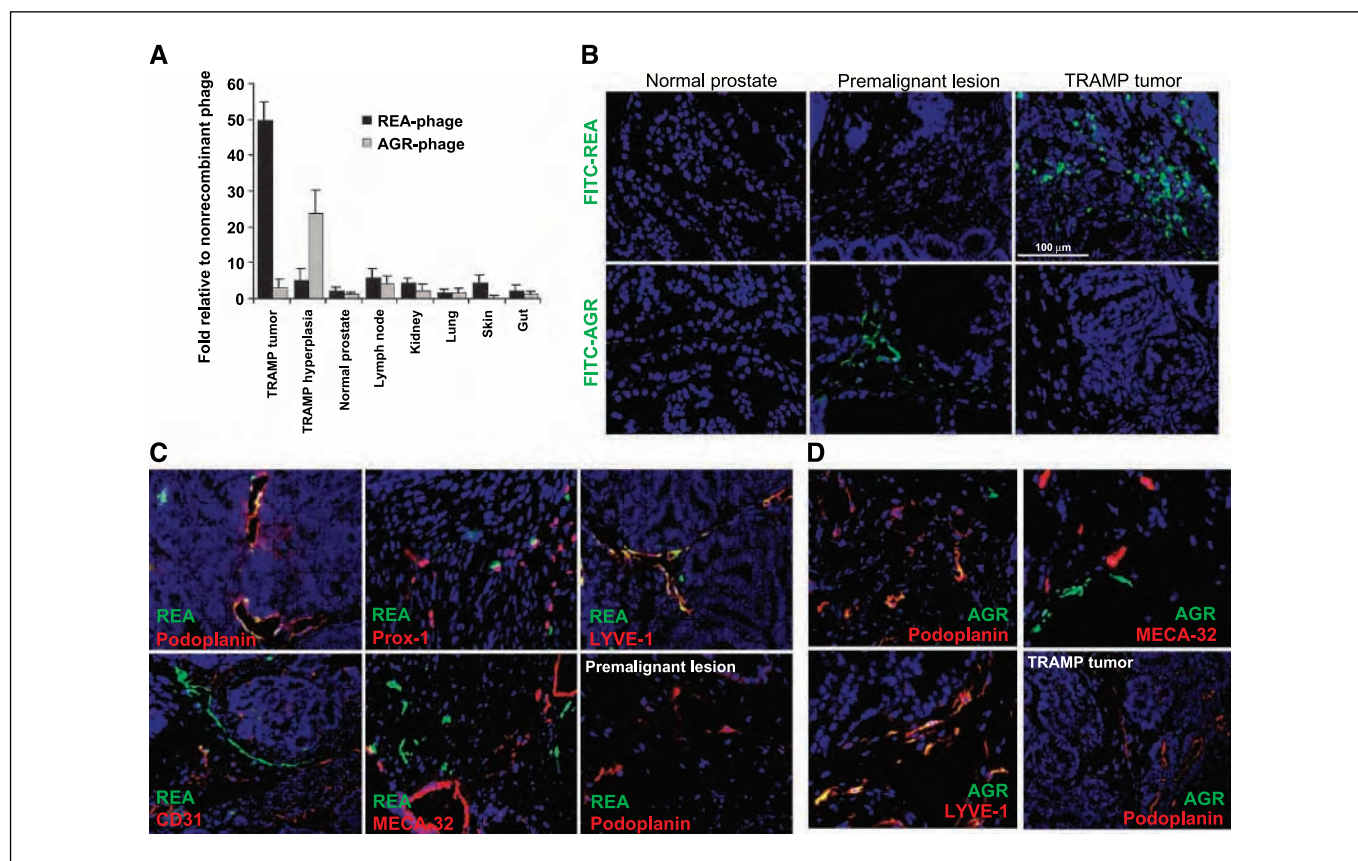
Figure 2. Stage-specific peptides distinguish premalignant lesions and tumors in the prostate of TRAMP mice and colocalize with lymphatic vessels. Phage isolated by screening for homing to TRAMP tumors (REA) or to TRAMP premalignant lesions (AGR) were individually tested in TRAMP mice bearing tumors, or premalignant lesions, and in tumor-free littermates of TRAMP mice with normal prostate. TRAMP mice were i.v. injected with phage or fluorescein-conjugated peptides, and the localization of the phage was studied by phage titration or immunohistochemistry in frozen tissue sections. The peptides were detected in tissue sections by examining fluorescence. The REA phage (*A, black columns*) and peptide (*B, top*) accumulate in TRAMP tumors, whereas the AGR phage (*A, gray columns*) and peptide (*B, bottom*) selectively home to premalignant lesions. The difference between tumor tissue and premalignant tissue was significant for both peptides ($P < 0.01$; n = 3-6) Original magnification, ×400. *C*, i.v. injected fluorescein-labeled REA peptide (*green*) colocalizes TRAMP tumor sections with the lymphatic vessel markers podoplanin, Prox-1, and LYVE-1 (*top row*), but not with blood vessel markers (*bottom row*); a premalignant TRAMP lesion does not bind the REA peptide (*bottom row, right*). Original magnification, ×400. *D*, fluorescein-labeled AGR peptide (*green*) colocalizes with podoplanin and LYVE-1 (*red*) in dysplastic prostate lesions, but there is no colocalization with blood vessels detected with MECA-32 staining; a TRAMP tumor does not bind the AGR peptide. Original magnification, ×400.

tumor-associated lymphatic vasculature or organ/tumor selective signatures. The lymphatic homing peptides derived from the different tumor models were tested for their ability to recognize the lymphatics of other tumors. I.v. injected LSD phage did not home to xenotransplant tumors derived from the MDA-MB-435 breast tumor cell line (Fig. 4*A, left*). This phage also did not appreciably home to transgenic mouse tumors of the breast or prostate, or to PPC1 human prostate cancer xenografts; possible low-level homing was seen to squamous carcinomas of the skin in K14-HPV16 mice, and to KRIB human osteosarcoma xenografts. *In vivo* injection of fluorescein-labeled LSD peptide, followed by histologic analysis of peptide distribution, agreed well with the phage results. As shown in Fig. 4*A* (*right*), strong LSD peptide fluorescence was seen in the C8161-derived tumors, the model in which the peptide was selected. The C8161 tumors were positive in nude mice representing two different genetic backgrounds (BALB/c and C57BL/6; shown for the BALB/c strain in Fig. 4*A, right*). In agreement with the phage data, KRIB tumors were weakly positive with the fluorescent peptide, and the other tumors, including the skin cancers, were negative. These results show that the LSD peptide selectively recognizes the lymphatics in the C8161 melanoma–derived tumors.

To profile the homing peptide specificity of the AGR peptide in different types of premalignant lesions, we used three transgenic mouse models, TRAMP, K14-HPV16/E$_2$, and MMTV-PyMT, which, respectively, develop prostate, cervical, or breast neoplasias that subsequently progress to overt cancer. Both AGR phage (Figs. 2*A* and 4*B*) and fluorescent peptide (Fig. 2*B* and *D*) showed marked preference for the PIN lesions in TRAMP mice; there was little homing of the phage and no detectable homing of the peptide to similar premalignant lesions or malignant tumors in the other two models (Fig. 4*B* and Supplementary Fig. S2*G*).

The REA phage, which was identified in the TRAMP model, also homed to xenografts obtained by orthotopically inoculating into nude mice cells from the human prostate cancer cell lines PPC1, M12, DU145, and LNCaP (Fig. 4*C*). These xenografted tumors were also positive with the fluorescein-conjugated REA peptide (the results for PPC1 are shown in Fig. 4*D*). In contrast, the MDA-MB-435, C8161, and KRIB xenografts, as well as the *de novo* breast and skin cancers arising in MMTV-PyMT or K14-HPV16 mice, respectively, were negative for REA binding (Fig. 4*C* and *D*). The cervical tumors of K14-HPV16/E$_2$ mice were slightly positive for REA peptide binding, but markedly less so than the prostate tumors. Immunohistochemical analysis showed that FITC-REA

peptide colocalized with lymphatic vessels both within tumor tissues (Fig. 4D, *first row, middle*) and tumor periphery (Fig. 4D, *first row, right*). This was the case with orthotopic prostate tumor xenografts arising from multiple human prostate tumor-derived cell lines (results for PPC1 tumors are shown in Fig. 4D). This peptide homed to a lesser extent to K14-HPV16/E_2 cervical tumors (Fig. 4D). Interestingly, REA phage homed less efficiently to s.c. xenografts of PPC1 than to orthotopic xenografts of the same tumor cell line (Supplementary Fig. S2E). The REA phage strongly bound to PPC1 tumor-derived cell suspensions, but did not bind to cultured PPC1 cells (Supplementary Fig. S2F). Thus, REA seems to primarily recognize prostate cancer lymphatics.

We also asked whether the REA peptide recognizes human prostate cancers by using phage overlay of tissue sections. Immunohistochemical staining with antibodies against lymphatic markers Prox-1 and podoplanin revealed abundant lymphatic vessels in human prostate tumors (Fig. 4D, *bottom row, red*). Overlay of tissue sections from two primary human prostate cancers with REA phage indicated that this phage recognizes the lymphatics of human prostate tumors (Fig. 4D, *bottom row, green*). The AGR phage did not bind to the human tumor sections (not shown).

LyP-1 and LyP-2 have different specificities. Given the similar amino acid sequences of the LyP-1 and LyP-2 peptides, and the fact that they both bind to tumor lymphatics, we were interested in comparing their specificities. Surprisingly, these peptides recognize different tumors. Although both peptides homed to the K14-HPV16 skin cancer lymphatics (data not shown), LyP-1 phage homed to MDA-MB-435 breast tumors growing s.c. but not to the *de novo* cervical tumors, whereas the opposite was true of LyP-2 (Fig. 5A). Both phage did not home to the normal cervix or normal breast tissue. To confirm these differences in specificity, we coinjected one peptide as a fluorescein conjugate and the other conjugated to rhodamine and vice versa. Both LyP-2 conjugates homed to cervical tumors, whereas neither LyP-1 conjugate did so. The opposite result was obtained when the same conjugates were tested in MDA-MB-435 tumor-bearing mice (Fig. 5B). These data indicate that different binding sites exist for the two LyP peptides in different types of tumors.

Lymphatic homing peptide conjugates destroy tumor lymphatics. One potential application of peptides that home and bind to the distinctive lymphatic vasculature of tumors is to target delivery of toxic payloads aiming to disrupt the tumor lymphatics, thereby assessing their functional importance and prospects as a therapeutic target. We began this assessment by linking two of our signature-finding peptides to a toxic agent, assessing its effects on the tumor lymphatics. As a toxic agent, we used conjugates with an apoptosis-inducing peptide, $_D$(KLAKLAK)$_2$. In a previous study,

Figure 3. LyP-2 peptide homes to lymphatics in premalignant lesions and tumors of cervix in K14-HPV16/E_2 transgenic mice. *A*, LyP-2 phage (1.5 × 10^9 pfu) was i.v. injected into mice bearing CIN-3 lesions or tumors of the cervix, and phage titers from the indicated tissues were determined. Significantly more of the LyP-2 phage accumulated in the tumors and dysplastic lesions than in normal cervix ($P < 0.005$; $n = 3$). *B*, FITC-LyP-2 peptide (100 μg) was injected into the tail vein of mice bearing dysplastic lesions or tumors of the cervix and allowed to circulate for 2 hours. FITC-LyP-2 selectively localized within premalignant lesions and tumors, colocalizing with lymphatic vessel markers (shown for LYVE-1; *top row*), but not with the blood vessel markers (shown for MECA-32; *bottom row*). Original magnifications, ×400 (*top*) and ×200 (*bottom*).
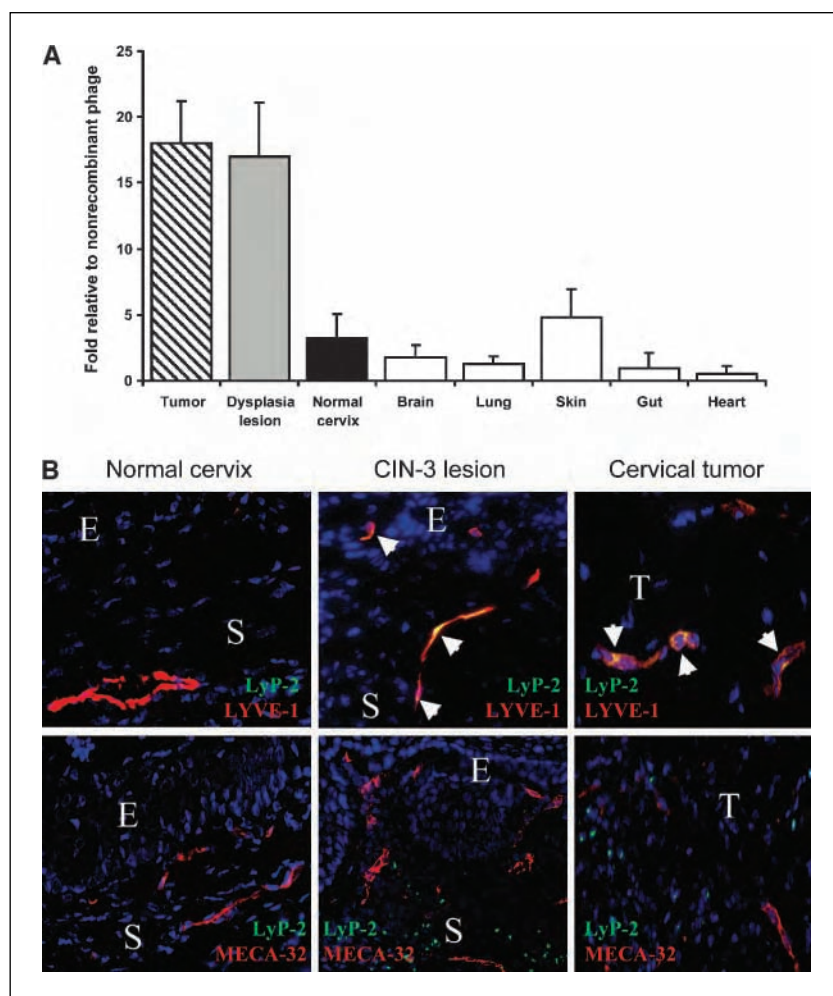
this peptide was linked to blood vascular tumor-homing peptides and shown to be selectively cytotoxic to angiogenic endothelial cells and to have demonstrable antitumor activity (26). To determine whether peptides recognizing tumor lymphatics could be used to target those lymphatics, we synthesized the REA and LSD peptides as conjugates with $_D$(KLAKLAK)$_2$ and systemically treated mice bearing PPC1 or C8161 xenografts.

Treatment with the REA conjugate had no effect on tumor blood vessel density in the PPC1 tumors, but significantly reduced the number of tumor lymphatics; the uncoupled mixture had no effect on the lymphatics compared with the PBS control (Fig. 6*A*). The conjugate had no effect on tumor growth (Fig. 6*B*), indicating (perhaps not surprisingly) that the tumor-associated lymphatics were not essential for primary tumor growth. Examination of lymphatics in normal skin revealed no discernible effect by the REA or LSD conjugates, and no significant differences were observed in the weight of the mice belonging to the various treatment groups, indicating lack of general lymphatic effects or overt toxicity (data not shown). Reduced density of tumor lymphatics was also seen in C8161 melanoma xenografts of mice treated with the LSD conjugate (data not shown).

To study the mechanism of the lymphatic disruption by the REA conjugate, we examined the frequency of apoptosis in lymphatic endothelial cells in PPC1 tumors using caspase-3 as a marker. The tumors of the mice treated with the REA conjugate had a significant increase in lymphatic endothelial cells expressing active caspase-3 compared with tumors of mice treated with PBS, REA, or a mixture of REA and $_D$(KLAKLAK)$_2$ (Fig. 6*C*). These data indicate that the REA conjugate reduced the lymphatic vessel counts by inducing apoptosis in lymphatic endothelial cells.

Discussion

In this article, we show an extensive heterogeneity of tumor lymphatics. We have identified peptides that recognize the lymphatics of individual tumor types, including transgenic mouse tumors arising *de novo* in different organs, as well as human tumor xenografts. We also describe a peptide that distinguishes the lymphatics of premalignant prostatic lesions, both from normal lymphatics and from those of fully developed tumors in the same transgenic mouse model of prostate carcinogenesis. The lymphatic

Table 1. Main characteristics of lymphatic homing peptides

Peptide	Tumor used to isolate homing peptide	Tumors tested for phage homing *in vivo**	Specific homing[†]	Fold over control phage
LSD	C8161 s.c. xenografts	C8161 xenografts	Yes	39
		KRIB xenografts	Yes	7[‡]
		K14-HPV16 skin cancer	No	5
		MDA-MB-435 orthotopic xenografts	No	3
		MMTV-PyMT breast tumors	No	3
		PPC1 orthotopic xenografts	No	3
		TRAMP prostate tumors	No	1
REA	TRAMP prostate tumors	TRAMP prostate tumors	Yes	46
		PPC1 orthotopic xenografts	Yes	25
		M12 orthotopic xenografts	Yes	24
		LNCaP orthotopic xenografts	Yes	20
		DU145 orthotopic xenografts	Yes	14
		MMTV-PyMT breast tumors	Yes	8[‡]
		K14-HPV16/E$_2$ cervical cancer	Yes	7[‡]
		KRIB xenografts	Yes	7[‡]
		PPC1 s.c. xenografts	No	6
		C8161 s.c. xenografts	No	5
		K14-HPV16 skin cancer	No	4
		MDA-MB-435 orthotopic xenografts	No	4
AGR	TRAMP PIN lesions	TRAMP PIN lesions	Yes	18
		TRAMP prostate tumors	No	4
		K14-HPV16/E$_2$ cervical dysplasia	No	5
		K14-HPV16/E$_2$ cervical tumors	No	4
		MMTV-PyMT premalignant lesions	No	2
		MMTV-PyMT breast tumors	No	4
LyP-2	K14-HPV16 skin cancer	K14-HPV16/E$_2$ cervical dysplasia	Yes	17
		K14-HPV16/E$_2$ cervical tumors	Yes	22
		MDA-MB-435 orthotopic xenografts	No	3

*TRAMP, MMTV-PyMT, and K14-HPV16 are genetically engineered mouse models of organ-specific carcinogenesis, each of which presents first with angiogenic dysplasia and subsequently carcinoma.
[†]The specific homing of phage is considered to be strong (>10-fold compared with control), weak (between 5- and 10-fold), or nonspecific (below 5-fold).
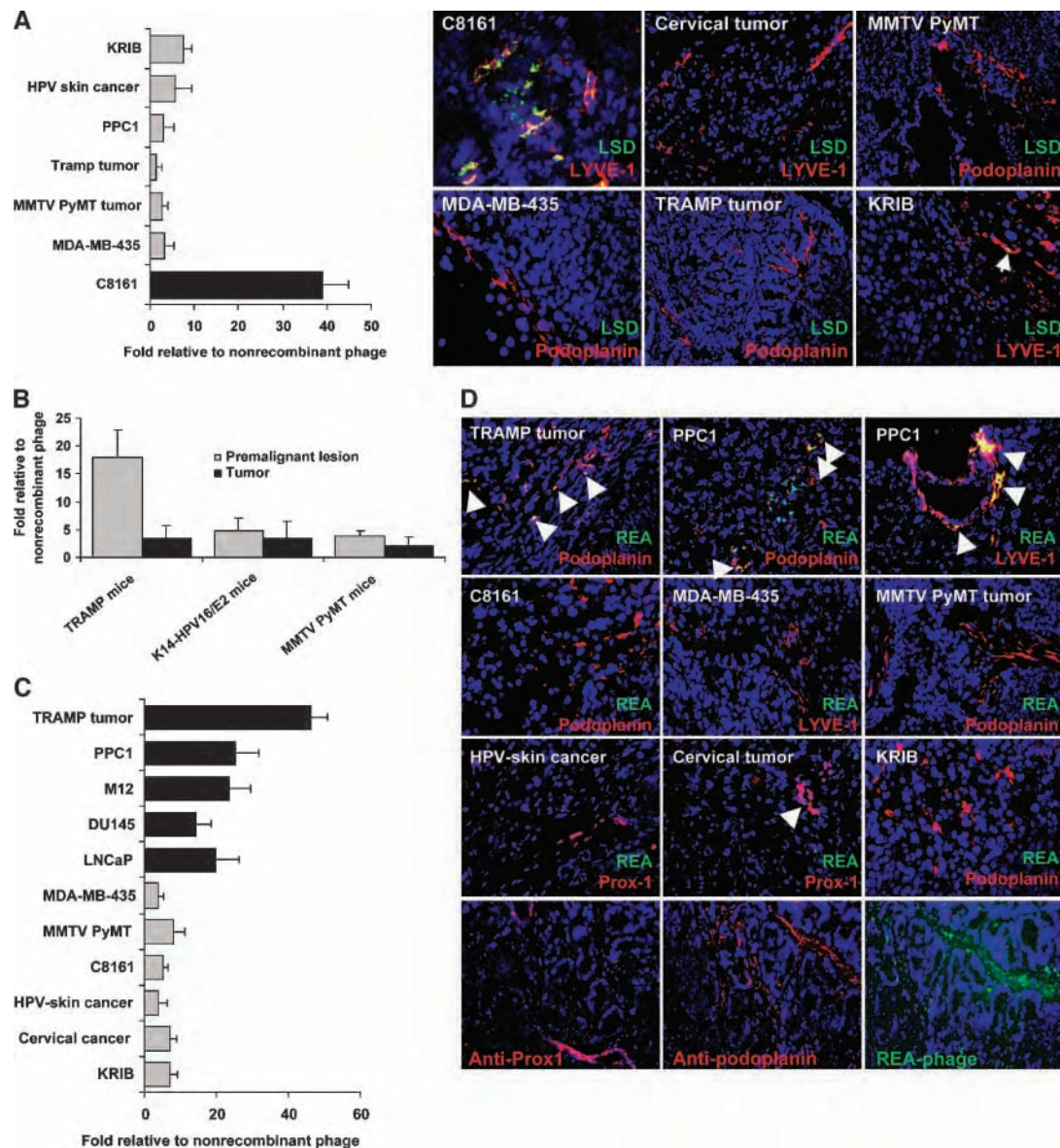[‡]Phage homing corroborated by fluorescent peptide homing.

Figure 4. Homing specificity of the LSD, REA, and AGR peptides in different types of tumors and premalignant lesions. *In vivo* homing of the LSD phage (*A, left*) and fluorescein-labeled LSD peptide (*A, right*) to six types of tumors was tested as in Fig. 1 (*n* = 3-6). Robust phage homing and peptide fluorescence was only observed in C8161 tumors. KRIB xenograft tumors were slightly positive for phage and peptide homing, but phage homing to C8161 tumors was significantly higher than to this or any of the other tumors (*P* < 0.005). Original magnification, ×400. *B, in vivo* homing of i.v. injected AGR phage in TRAMP mice, K14-HPV16/E$_2$ mice bearing CIN-3 lesions or tumors (*n* = 3), and MMTV-PyMT mice with dysplastic lesions or breast tumors. The AGR phage homed significantly more to TRAMP premalignant lesions than to comparable lesions in the other tumor models (*P* < 0.03). *In vivo* homing of the REA phage (*C*) and fluorescein-labeled REA peptide (*D*) to 11 types of tumors was tested (*n* = 3-6). Significant phage homing and peptide fluorescence was observed in prostate tumors of TRAMP mice, and in PPC1, M12, DU145, and LNCaP human prostate cancer xenograft tumors (peptide fluorescence is shown for PPC1 in *D*). Four of five prostate cancers (DU145 was the exception) accumulated significantly more REA phage than the other types of tumors (*P* < 0.03). Cervical tumors in K14-HPV16/E$_2$ mice were slightly positive. REA phage overlay of primary human prostate cancer is shown in *D* (*bottom row*). Human tumor tissue sections were stained with Prox-1 or antipodoplanin. A serial section from the podoplanin staining was used for REA phage overlay showing correspondence of the podoplanin and the REA phage localization.

markers detected by the homing peptides are specific for lymphatic vessels (i.e., the peptides do not bind to the blood vessels of the same tumors or premalignant lesions). Several prostate cancers shared the same lymphatic marker. These results show that the lymphatics express a zip code system that is akin to the one in blood vessels, but distinct from it. In beginning, to assess the applications of this knowledge, we showed that systemic treatment of tumor-bearing mice with a lymphatic homing peptide

linked to a proapoptotic compound could selectively destroy tumor lymphatics.

We used a new screening method based on the immuno-isolation of lymphatic endothelial cells from whole tumor cell suspensions that had been preincubated with phage display libraries, thereby enriching for phage bound to this rare cell type. This method allowed us to focus on the selection of phage-displayed peptides that identify specific features in the lymphatics

of the target tissue. We show in each of the tumor models that peptides strongly represented in the selected phage pools specifically homed to tumors, and extensively colocalized with markers of lymphatic endothelial cells in the tumor tissue after an i.v. injection. In contrast, there was no colocalization with blood vessel endothelial markers. Costaining with the lymphatic markers LYVE-1, podoplanin, Prox-1, and VEGFR3 were consistent in supporting this result. The use of multiple markers is an important standard, as none of the lymphatic endothelial markers is completely specific for lymphatics (30, 31). In aggregate, however, they provide strong evidence for a lymphatic vessel identity of the structures that our peptide recognizes in tumors.

We have now shown lymphatic vessel specialization in every one of the five tumor types studied. These tumors consisted of xenograft models of melanoma, breast, and prostate carcinomas, as well as transgenic mouse models developing prostate, skin, and cervical cancers. In addition, the LSD, REA, and LyP peptides each recognized tumor lymphatics in more than one inbred mouse strain. For example, the REA peptide homed to prostate cancers in TRAMP mice (C57BL/6 background) and prostate cancer xenograft tumors grown in nude mice (BALB/c), demonstrating that their specificity is not limited to any given mouse strain. Previous studies have defined a peptide that distinguishes the lymphatics of MDA-MB-435 breast cancer xenografts tumors from normal lymphatics (13, 25). The present results show that such molecular specialization of tumor lymphatics is not limited to this tumor, but is likely to be a generalized phenomenon. The peptides we identified in this study as being specific for lymphatic vessels in the various tumor models were essentially specific for the tumor type used in the screening. Interestingly, the only other tumors with lymphatics recognized by the TRAMP tumor-homing peptide REA were xenograft tumors generated with four different human prostate cancer cell lines. This result suggests that the changes detected by our peptides in tumor lymphatics may be tumor type specific. Similar experiments with tumor blood vessels have revealed two classes of peptides identifying signatures of the angiogenic neovasculature. One pan-specific class recognizes markers that are generally associated with angiogenesis in most tumor types and organs (1, 4, 32, 33), whereas a second class of peptides detected tumor type–specific vascular signatures (7, 8). Although we did not isolate any peptides that identified pan-specific markers of tumor (but not normal) lymphatics, we anticipate that additional screens could reveal such entities.

Stage-specific lymphatic signatures during tumorigenesis. We obtained two stage-specific lymphatic homing peptides using different neoplastic lesions in the TRAMP model. The REA peptide selectively recognizes the lymphatics in fully developed TRAMP tumors, whereas the AGR peptide was only reactive with the lymphatics in PIN lesions. Our laboratories have previously obtained homing peptides that distinguish the blood vessels of premalignant lesions from normal blood vessels and those of malignant tumors arising subsequently in the same transgenic mouse models (7, 8). The present results suggest that lymphatic vessels display a similar evolution of molecular specificities as tumorigenesis progresses.
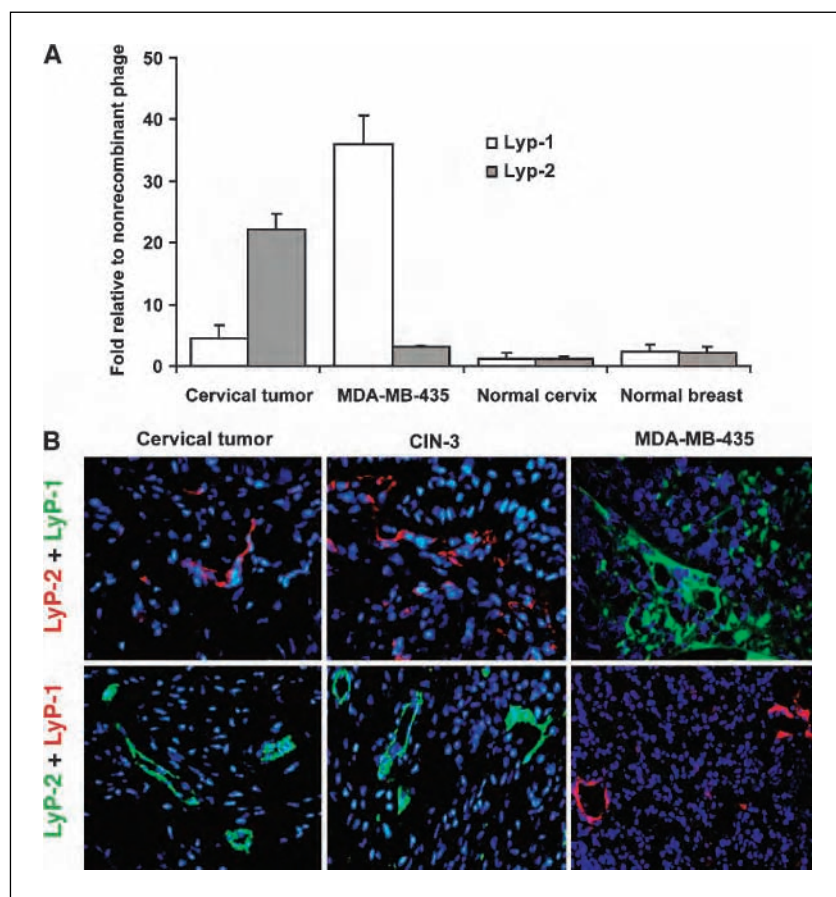

Figure 5. Differential tumor-homing specificity of LyP-1 and LyP-2 peptides. *A,* LyP-1 and LyP-2 phage were i.v. injected into mice bearing MDA-MB-435 breast cancer xenografts or K14-HPV16/E_2 tumors (*n* = 3). *B,* fluorescein-labeled LyP-1 and rhodamine-labeled LyP-2 (*top row*) were i.v. injected (100 μg of each peptide) into the mice bearing tumors or premalignant lesions. Alternatively, the injection consisted of rhodamine-labeled LyP-1 and fluorescein-labeled LyP-2 (*bottom row*). Tissues were collected and processed for histologic analysis 2 hours later. LyP-1 homes to the MDA-MB-435 tumors, whereas LyP-2 homes to the cervical cancers and premalignant lesions. Phage homing to the premalignant lesions was significantly higher than to the corresponding tumors in both models (*P* < 0.01). Original magnification, ×400.
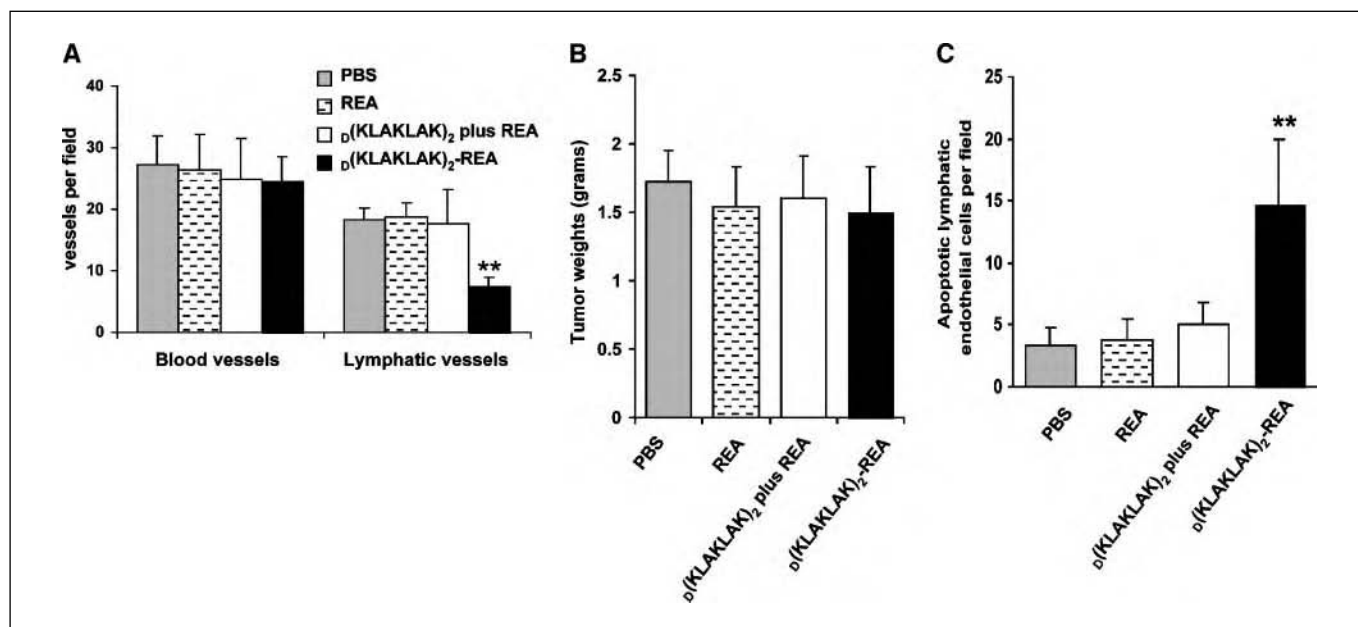
Figure 6. Targeting the tumor-associated lymphatics with homing peptides linked to a proapoptotic peptide. The PPC1 orthotopic xenografted mice (10 mice per group) were systemically treated with 100 μg/dose/mouse/biweekly of $_D$(KLAKLAK)$_2$-CREAGRKAC, equimolar amounts of the uncoupled peptides, or with the vehicle (PBS). At termination, tumor weights were recorded and frozen tissue sections were prepared for immunohistochemical analysis. *A,* the $_D$(KLAKLAK)$_2$-CREAGRKAC chimeric peptide greatly reduces the number of tumor lymphatics (*P* < 0.01) as determined from podoplanin staining, whereas the blood vessel count (MECA-32 staining) and tumor volume (*B*) were unaffected. *C,* $_D$(KLAKLAK)$_2$-CREAGRKAC induced apoptosis of lymphatic endothelial cells in PPC1 tumors. The apoptotic lymphatic endothelial cells were detected by double staining with antiactive caspase-3 and antipodoplanin antibodies. A significant increase in apoptosis of lymphatic endothelial cells in PPC1 tumors was observed in tumors of mice treated with the $_D$(KLAKLAK)$_2$-CREAGRKAC conjugate compared with controls (*P* < 0.001).

A prospective family of lymphatic signatures? The mutually exclusive tumor specificity of the LyP-1 and LyP-2 peptides is interesting given the close sequence similarity of these peptides (CGNKRTRGC versus CNRRTKAGC). LyP-1 recognizes lymphatics and tumor cells in MDA-MB-435 and MMTV-PyMT breast cancers (8). Careful comparison of the ability of the two peptides to accumulate in MDA-MB-435 tumors and cervical carcinomas after i.v. injection showed that MDA-MB-435 tumors were positive for LyP-1, whereas cervical carcinomas were not, whereas LyP-2 had the opposite specificity. Interestingly, both peptides bound to other cell types in the neoplastic lesions: LyP-1 binds to and is internalized by breast tumor cells, whereas LyP-2 binds to scattered cells in the neoplastic cervix. The bases for and the implications of these distinctive lymphatic and non-lymphatic binding specificities are presently unclear and deserve future investigation. We have encountered a third peptide in the LyP series, CNKRTRGGC. We did not include that peptide in this study but its specificity seems to parallel that of LyP-1 (25). Comparison of the three sequences indicates that shifting the glycine residue from the NH$_2$-terminal to the COOH-terminal end is not important to the specificity of the peptide, but that the arrangement of the basic residues in the K/RRTR/K motif can alter specificity. Our attempts to identify the binding molecules (receptors) for the LyP peptides (and indeed for other of the lymphatic signature–finding peptides identified in this study) have not been successful thus far, and this remains an agenda for future studies. The closely related sequences of the LyP peptides predict the existence of a family of related receptors with tumor type–specific expression in lymphatics. The distinctive specificity of peptides containing the RGD motif in different sequence contexts for individual integrins (34) exemplifies the archetype.

Prospects for therapeutic and diagnostic targeting of the lymphatics. The peptides we describe here have potentially important uses. Early targeting of the tumor lymphatics for destruction may serve to reduce metastatic spread, as lymphatic vessels provide one of the main routes for the spreading of many types of cancer (15–17, 35, 36). In the present study, we were able to reduce the abundance of lymphatics in melanoma xenograft tumors by using lymphatic homing peptides to direct a toxic peptide to the lymphatics in these tumors. In agreement with earlier studies (36), the destruction of the lymphatics had little effect on the growth of the melanoma tumors. These data support the proposition that primary tumor growth is not in general dependent on the lymphatic neovasculature. However, targeted destruction of tumor lymphatics with homing peptide conjugates has prospect to limit metastatic dissemination as has been exemplified in other studies that genetically manipulated lymphatic growth factors to eliminate tumor lymphatics (15–17, 35, 36).

Although studying the effect of the lymphatic homing peptide-drug conjugates on metastasis is one of our long-term aims, we foresee considerable potential in more general applications aimed at producing antitumor effects with homing peptides for tumor lymphatics. Lymphatic homing peptides can be harnessed to deliver a payload into the tumor, as illustrated herein for fluorescein and for the $_D$(KLAKLAK)$_2$ proapototic peptide. Targeted drug conjugates can potentially have broader effects than what can be obtained by destroying peritumoral lymphatics. Homing peptides for tumor blood vessels have been used in targeted delivery of therapeutic agents into tumors. As a result of such targeting, the efficacy of the drug increased, whereas its side effects were reduced (26, 32, 37, 38). Our lymphatic homing peptides present another potential route for targeted delivery of drugs into tumors.

Tumor-specific changes in the lymphatics may also have applications in diagnostic molecular imaging of tumor growth, progression, and response to therapy, as well as for early detection of incipient organ-specific cancers (or premalignant progenitor lesions) that evidently have both blood and lymphatic vascular signatures.

Acknowledgments

References

1. Ruoslahti E. Specialization of tumour vasculature. Nat Rev Cancer 2002;2:83–90.
2. Hanahan D, Weinberg RA. The hallmarks of cancer. Cell 2000;100:57–70.
3. Brooks PG, Clouse J, Morris LS. Hysterectomy vs. resectoscopic endometrial ablation for the control of abnormal uterine bleeding. A cost-comparative study. J Reprod Med 1994;39:755–60.
4. Christian S, Pilch J, Akerman ME, Porkka K, Laakkonen P, Ruoslahti E. Nucleolin expressed at the cell surface is a marker of endothelial cells in angiogenic blood vessels. J Cell Biol 2003;163:871–8.
5. Ferrara N, Alitalo K. Clinical applications of angiogenic growth factors and their inhibitors. Nat Med 1999;5:1359–64.
6. Pasqualini R, Koivunen E, Kain R, et al. Aminopeptidase N is a receptor for tumor-homing peptides and a target for inhibiting angiogenesis. Cancer Res 2000;60:722–7.
7. Hoffman JA, Giraudo E, Singh M, et al. Progressive vascular changes in a transgenic mouse model of squamous cell carcinoma. Cancer Cell 2003;4:383–91.
8. Joyce JA, Laakkonen P, Bernasconi M, Bergers G, Ruoslahti E, Hanahan D. Stage-specific vascular markers revealed by phage display in a mouse model of pancreatic islet tumorigenesis. Cancer Cell 2003;4:393–403.
9. Cao R, Bjorndahl MA, Religa P, et al. PDGF-BB induces intratumoral lymphangiogenesis and promotes lymphatic metastasis. Cancer Cell 2004;6:333–45.
10. Cassella M, Skobe M. Lymphatic vessel activation in cancer. Ann N Y Acad Sci 2002;979:120–30.
11. Stacker SA, Achen MG, Jussila L, Baldwin ME, Alitalo K. Lymphangiogenesis and cancer metastasis. Nat Rev Cancer 2002;2:573–83.
12. Jackson DG, Prevo R, Clasper S, Banerji S. LYVE-1, the lymphatic system and tumor lymphangiogenesis. Trends Immunol 2001;22:317–21.
13. Laakkonen P, Porkka K, Hoffman JA, Ruoslahti E. A tumor-homing peptide with a targeting specificity related to lymphatic vessels. Nat Med 2002;8:751–5.
14. Padera TP, Kadambi A, di Tomaso E, et al. Lymphatic metastasis in the absence of functional intratumor lymphatics. Science 2002;296:1883–6.
15. Mandriota SJ, Jussila L, Jeltsch M, et al. Vascular endothelial growth factor-C-mediated lymphangiogenesis promotes tumour metastasis. EMBO J 2001;20:672–82.
16. Skobe M, Hawighorst T, Jackson DG, et al. Induction of tumor lymphangiogenesis by VEGF-C promotes breast cancer metastasis. Nat Med 2001;7:192–8.
17. Saharinen P, Tammela T, Karkkainen MJ, Alitalo K. Lymphatic vasculature: development, molecular regulation and role in tumor metastasis and inflammation. Trends Immunol 2004;25:387–95.
18. Bae VL, Jackson-Cook CK, Maygarden SJ, Plymate SR, Chen J, Ware JL. Metastatic sublines of an SV40 large T antigen immortalized human prostate epithelial cell line. Prostate 1998;34:275–82.
19. Arbeit JM, Munger K, Howley PM, Hanahan D. Progressive squamous epithelial neoplasia in K14-human papillomavirus type 16 transgenic mice. J Virol 1994;68:4358–68.
20. Arbeit JM, Howley PM, Hanahan D. Chronic estrogen-induced cervical and vaginal squamous carcinogenesis in human papillomavirus type 16 transgenic mice. Proc Natl Acad Sci U S A 1996;93:2930–5.
21. Giraudo E, Inoue M, Hanahan D. An amino-bisphosphonate targets MMP-9-expressing macrophages and angiogenesis to impair cervical carcinogenesis. J Clin Invest 2004;114:623–33.
22. Hoffman J, Laakkonen P, Porkka K, Bernasconi M, Ruoslahti E. *In vivo* and *ex vivo* selections using phage-displayed libraries. In: Clackson T, Lowman HB, editors. Phage display. New York: Oxford University Press; 2004. p. 171–92.
23. Greenberg NM, DeMayo F, Finegold MJ, et al. Prostate cancer in a transgenic mouse. Proc Natl Acad Sci U S A 1995;92:3439–43.
24. Gingrich JR, Greenberg NM. A transgenic mouse prostate cancer model. Toxicol Pathol 1996;24:502–4.
25. Laakkonen P, Akerman ME, Biliran H, et al. Antitumor activity of a homing peptide that targets tumor lymphatics and tumor cells. Proc Natl Acad Sci U S A 2004;101:9381–6.
26. Ellerby HM, Arap W, Ellerby LM, et al. Anti-cancer activity of targeted pro-apoptotic peptides. Nat Med 1999;5:1032–8.
27. Arap W, Haedicke W, Bernasconi M, et al. Targeting the prostate for destruction through a vascular address. Proc Natl Acad Sci U S A 2002;99:1527–31.
28. Hsu CX, Ross BD, Chrisp CE, et al. Longitudinal cohort analysis of lethal prostate cancer progression in transgenic mice. J Urol 1998;160:1500–5.
29. Coussens LM, Hanahan D, Arbeit JM. Genetic predisposition and parameters of malignant progression in K14-16 transgenic mice. Am J Pathol 1996;149:1899–917.
30. Mouta Carreira C, Nasser SM, di Tomaso E, et al. LYVE-1 is not restricted to the lymph vessels: expression in normal liver blood sinusoids and down-regulation in human liver cancer and cirrhosis. Cancer Res 2001;61:8079–84.
31. Valtola R, Salven P, Heikkila P, et al. VEGFR-3 and its ligand VEGF-C are associated with angiogenesis in breast cancer. Am J Pathol 1999;154:1381–90.
32. Arap W, Pasqualini R, Ruoslahti E. Chemotherapy targeted to tumor vasculature. Curr Opin Oncol 1998;10:560–5.
33. Yao VJ, Ozawa MG, Trepel M, Arap W, McDonald DM, Pasqualini R. Targeting pancreatic islets with phage display assisted by laser pressure catapult microdissection. Am J Pathol 2005;166:625–36.
34. Ruoslahti E. The RGD story: a personal account. Matrix Biol 2003;22:459–65.
35. Stacker SA, Caesar C, Baldwin ME, et al. VEGF-D promotes the metastatic spread of tumor cells via the lymphatics. Nat Med 2001;7:186–91.
36. Lin J, Lalani AS, Harding TC, et al. Inhibition of lymphogenous metastasis using adeno-associated virus-mediated gene transfer of a soluble VEGFR-3 decoy receptor. Cancer Res 2005;65:6901–9.
37. Curnis F, Gasparri A, Sacchi A, Longhi R, Corti A. Coupling tumor necrosis factor-α with αV integrin ligands improves its antineoplastic activity. Cancer Res 2004;64:565–71.
38. Curnis F, Sacchi A, Borgna L, Magni F, Gasparri A, Corti A. Enhancement of tumor necrosis factor α antitumor immunotherapeutic properties by targeted delivery to aminopeptidase N (CD13). Nat Biotechnol 2000;18:1185–90.